Measuring J/ψ yields as a function of the charged-particle multiplicity in regions of J/ψs azimuth angle in pp collisions with ALICE

Ailec de la Caridad Bell Hechavarria

Münster, 2025

Experimentelle Physik

Measuring J/ψ yields as a function of the charged-particle multiplicity in regions of J/ψs azimuth angle in pp collisions with ALICE

Inaugural-Dissertation
zur Erlangung des Doktorgrades
der Naturwissenschaften im Fachbereich Physik
der Mathematisch-Naturwissenschaftlichen Fakultät
der Universität Münster

vorgelegt von
AILEC DE LA CARIDAD BELL HECHAVARRIA
aus HAVANNA, KUBA

– Münster, 2025 –

Abstract

The study of J/ψ production as a function of the charged-particle multiplicity offers a unique opportunity to probe the interplay between hard and soft Quantum Chromodynamics (QCD) processes in proton-proton (pp) collisions. On the one hand, J/ψ mesons provide a well-established playground for investigating hard scattering (perturbative QCD) and hadronization mechanisms. On the other hand, the charged-particle multiplicity, representing the number of primary charged particles produced in a collision, is a relatively straightforward observable to measure experimentally but that remains challenging to model accurately due to its sensitivity to soft, non-perturbative QCD processes that are not yet fully understood within existing theoretical frameworks.

Previous measurements have explored the dependency between J/ψ yields and the charged-particle multiplicity in pp and p–Pb collisions. In particular, results at midrapidity in pp collisions revealed deviations from the approximately linear trend with slope = 1 observed for analogous measurements at forward rapidities and predicted by theoretical models incorporating Multi-Parton Interactions (MPI). Thus, the microscopic origin of the observed stronger-than-linear increase of J/ψ yields with the charged particle multiplicity at midrapidity remains an open question.

This thesis addresses this question by measuring experimentally the first differential in azimuthal angle J/ψ–charged-particle multiplicity correlation by sorting per analyzed collision the produced charged particles into Toward, Transverse, and Away regions defined relative to the J/ψ mesons. The study uses data of pp collisions at $\sqrt{s} = 13$ TeV collected by the ALICE experiment with both J/ψ mesons and the charged-particle multiplicity measured at midrapidity ($|\eta| < 0.9$). The results are compared to available PYTHIA8 predictions.

PYTHIA8 Monasch 2013 tune simulations for inclusive transverse momentum (p_{T}) J/ψ mesons predict a region-dependent behavior: a slightly stronger-than-linear increase of the J/ψ yield with charged-particle multiplicity in the Toward region, an approximately linear trend in the Away region, and a weaker-than-linear increase in the Transverse region. However, the experimental results presented in this thesis show no significant variation among the three azimuthal regions for inclusive-p_{T} J/ψ mesons. Instead, a consistently stronger-than-linear correlation between the J/ψ yield and the charged-particle multiplicity is observed in all regions Toward, Transverse, and Away.

As the region-dependent behavior predicted by PYTHIA8 is also expected to depend on the J/ψs p_{T}, this thesis further investigates the correlation of J/ψ and multiplicity through a p_{T} differential analysis. Indeed, a more refined picture emerges: in the Toward region, the correlation shows a pronounced p_{T} dependence, with high-p_{T} J/ψ mesons exhibiting a notably steeper

increase with multiplicity. In contrast, the Transverse and Away regions show no significant p_{T} dependence, with the analyzed p_{T} intervals displaying a stronger-than-linear increase. Thus, the measurements confirm that the Toward region is particularly sensitive to autocorrelation effects, especially at high p_{T} as predicted by the PYTHIA8 Monasch 2013 tune simulations. However, they do not confirm the expectation that these autocorrelation effects should not be observed in the J/ψ Transverse region, as a weaker-than-linear increase is not observed. In PYTHIA8 simulation studies, this behavior in the J/ψ Toward region is mainly attributed to the non-prompt J/ψ fraction as a result of B-hadrons decays producing additional charged particles that could be spatially correlated with the J/ψ, thereby enhancing the multiplicity in the Toward direction. Therefore, a key recommendation from this study is to perform a prompt/non-prompt separation of J/ψ yields in future analyses, which could disentangle the contributions from the different production mechanisms.

Zusammenfassung

Die Untersuchung der J/ψ-Produktion in Abhängigkeit von der Multiplizität geladener Teilchen bietet eine einzigartige Möglichkeit, das Zusammenspiel zwischen harten und weichen Prozessen der Quantenchromodynamik (QCD) in Proton-Proton (pp)-Kollisionen zu untersuchen. Einerseits bieten J/ψ-Mesonen eine etablierte Möglichkeit um harte Streuung (perturbative QCD) und Hadronisierungsmechanismen zu untersuchen. Andererseits ist die Teilchenmultiplizität, welche die Anzahl der in einer Kollision erzeugten primären geladenen Teilchen darstellt, eine relativ einfach zu messende Observable, deren genaue theoretische Beschreibung jedoch aufgrund ihrer Empfindlichkeit gegenüber weichen, nicht-pertubativen QCD-Prozessen, die in bestehenden theoretischen Rahmenwerken noch nicht vollständig verstanden werden, eine Herausforderung darstellt.

Frühere Messungen haben die Abhängigkeit zwischen der J/ψ-Ausbeute und der Anzahl der geladenen Teilchen in pp- und p–Pb-Kollisionen untersucht. Insbesondere zeigten die Ergebnisse bei zentraler Rapidität in pp-Kollisionen Abweichungen von dem annähernd linearen Trend mit Steigung = 1, der für analoge Messungen bei vorwärts gerichteter Rapidität beobachtet und durch theoretische Modelle, die sogenannte Multi-Parton Interactions (MPI) berücksichtigen, vorhergesagt wurde. Der mikroskopische Ursprung des beobachteten, stärker als linearen Anstiegs der J/ψ-Ausbeute mit der Teilchenmultiplizität bei zentraler Rapidität bleibt daher eine offene Frage.

Die vorliegende Arbeit geht dieser Frage nach, indem erstmals experimentell die Korrelation zwischen J/ψ und Teilchenmultiplizität differentiell nach dem azimutalen Winkel gemessen wird. Dies geschieht indem für jede analysierte Kollision die erzeugten geladenen Teilchen in die Regionen „Toward", „Transverse" und „Away" sortiert werden, die relativ zu den J/ψ-Mesonen definiert sind. Die Studie verwendet Daten von pp-Kollisionen bei $\sqrt{s} = 13$ TeV, die vom ALICE-Experiment aufgenommen wurden, wobei sowohl die J/ψ-Mesonen als auch die Teilchenmultiplizität bei zentraler Rapidität ($|\eta| < 0.9$) gemessen wurden. Die Ergebnisse werden mit verfügbaren PYTHIA8-Vorhersagen verglichen.

PYTHIA8 Simulationen mit Monash 2013 Tune von J/ψ-Mesonen mit inklusivem Transversalimpuls (p_T) sagen ein regionsabhängiges Verhalten voraus: einen etwas stärker als linearen Anstieg der J/ψ-Ausbeute mit der Multiplizität der geladenen Teilchen in der Toward-Region, einen annähernd linearen Trend in der Away-Region und einen schwächer als linearen Anstieg in der Transversal-Region. Die in dieser Arbeit vorgestellten experimentellen Ergebnisse zeigen jedoch keine signifikanten Unterschiede zwischen den drei azimutalen Regionen für p_T-inklusive J/ψ-Mesonen. Stattdessen wird in allen Regionen (Toward, Transverse und Away) eine

durchgängig stärker als lineare Korrelation zwischen der J/ψ-Ausbeute und der Teilchenmultiplizität beobachtet.

Da erwartet wird, dass das von PYTHIA8 vorhergesagte regionsabhängige Verhalten auch vom p_T der J/ψ abhängt, wird in dieser Arbeit die Korrelation zwischen J/ψ und Teilchenmultiplizität durch eine p_T-abhängige Analyse näher untersucht. Tatsächlich ergibt dies ein differenzierteres Bild: In der Toward-Region zeigt die Korrelation eine ausgeprägte p_T-Abhängigkeit, wobei J/ψ-Mesonen mit hohem p_T einen deutlich steileren Anstieg mit der Multiplizität aufweisen. Im Gegensatz dazu zeigen die Transversal- und Away-Regionen keine signifikante p_T-Abhängigkeit, wobei die analysierten p_T-Intervalle einen stärker als linearen Anstieg aufweisen. Somit bestätigen die Messungen, dass die Toward-Region besonders empfindlich auf Autokorrelationseffekte reagiert, insbesondere bei hohen p_T, wie es die Simulationen von PYTHIA8 Monash 2013 vorhersagen. Sie bestätigen jedoch nicht die Erwartung, dass diese Autokorrelationseffekte in der J/ψ Transversalregion nicht beobachtet werden sollten, da ein schwächer als linearer Anstieg nicht beobachtet wird. In PYTHIA8-Simulationsstudien wird dieses Verhalten in der J/ψ Toward-Region hauptsächlich auf den nicht-prompten J/ψ-Anteil als Ergebnis von B-Hadron-Zerfällen zurückgeführt, die zusätzliche geladene Teilchen erzeugen, die räumlich mit dem J/ψ korreliert sein könnten, wodurch die Multiplizität in der Toward-Richtung erhöht wird. Daher ist eine wichtige Empfehlung dieser Studie, in zukünftigen Analysen eine Trennung der prompten/nicht prompten J/ψ-Ausbeuten vorzunehmen, was die Beiträge der verschiedenen Produktionsmechanismen aufklären könnte.

Contents

Introduction

A state of matter, known as the Quark-Gluon Plasma (QGP), believed to have existed approximately one microsecond after the Big Bang, can be produced under laboratory conditions by colliding heavy nuclei at higher center-of-mass energies. Studies with the ALICE experiment at LHC provide insights into this state of the early universe by analyzing the products of colliding heavy nuclei (Pb-Pb). The QGP presents a unique opportunity to study Quantum Chromodynamics (QCD) under extreme conditions, as quarks and gluons in this phase are no longer strongly coupled, exhibiting deconfined behavior, contrasting with their usual confined state. To better interpret the signatures of QGP formation, ALICE also studies proton–proton (pp) collisions as a baseline and proton–lead (p–Pb) collisions to probe cold nuclear matter effects. Among the collision products and key probes of QCD in these environments are J/ψ mesons, which consist of a charm quark and its antiquark. As their production involves both perturbative (heavy quark production) and non-perturbative (hadronization) QCD processes, measurements of J/ψ mesons in pp, p–Pb, and Pb–Pb collisions are critical for disentangling QCD dynamics and advancing our understanding of the Standard Model.

At the LHC, where protons collide at center-of-mass energies on the order of several TeV, collisions producing higher numbers of charged particles have been observed. In these environments, observations have emerged suggesting collective-like effects traditionally associated with QGP formation. As a result, pp collision studies have gained renewed attention, particularly in searching for novel observables exploring the interplay between soft and hard QCD processes. One such observable is the correlation between the number of J/ψ mesons and charged particles produced in a collision (the charged-particle multiplicity). Initially, a linear dependence between J/ψ production and charged-particle multiplicity was anticipated, based on the expectation that both are influenced by multiparton interactions (MPI). However, ALICE measurements have revealed a more complex picture: while the correlation remains approximately linear at forward rapidity, a stronger-than-linear, nearly quadratic dependence is observed at midrapidity.

Several theoretical models have been proposed to describe this behavior. Although most include MPI as a core mechanism, they differ in the microscopic interpretation of the J/ψ-charged particle multiplicity correlation. Some models invoke initial-state effects such as parton saturation or Color Glass Condensate (CGC) dynamics. In contrast, others focus on final-state effects like the interaction and overlap of color strings. Meanwhile, complex event generators like PYTHIA8 and EPOS combine initial and final states to reproduce the correlation. Therefore, as all these models can generally reproduce, at least qualitatively, the correlation behavior observed at mid- and forward rapidities, further experimental constraints are needed to disentangle these competing mechanisms.

This thesis investigates the origin of the stronger-than-linear increase in the J/ψ-Nch correlation observed at midrapidity in pp collisions. To this end, the analysis works on $\sqrt{s}$=13 TeV pp data collected by the ALICE experiment, and studies the correlation in three regions of the azimuthal plane: Toward, Transverse, and Away. These regions, defined relative to the J/ψ meson direction, offer a way to isolate potential autocorrelation effects by spatially distributing particle production around the emitted J/ψ. This methodology was initially proposed in the study conducted by [1] with PYTHIA8 Monasch 2013 tune simulations to investigate autocorrelation effects associated with J/ψ meson production mechanisms that could influence particle production in pp collisions. Therefore, the analysis proposed in this thesis reconstructs J/ψ mesons and measures the charged-particle multiplicity per event at midrapidity. Subsequently, the Toward, Transverse, and Away regions are constructed event-by-event around each detected J/ψ, and the correlation between the J/ψ yield and the event multiplicity in each region is systematically studied.

Thus, this thesis is organized as follows: Chapter 1 introduces the theoretical foundations on which this thesis is based. Chapter 2 reviews relevant theoretical models and summarizes existing experimental results on J/ψ-Nch correlations. Chapter 3 presents the ALICE detector and the data-taking conditions, while Chapters 4 and 5 detail the analysis methodology, intermediate results, and systematic uncertainties evaluation. Finally, Chapter 6 presents the main results of this work and compares them with the Monte Carlo simulations discussed by [1]. Lastly, is also offered a summary of the primary findings and suggestions for further studies.

1. Basic Theoretical Concepts

This chapter provides the theoretical foundation necessary to understand this thesis project's motivation and main goal. Particularly, the chapter summarizes the essential particle and heavy-ion physics concepts that will be deepened throughout this thesis project.

The chapter is organized into three main sections. The first introduces the Standard Model of particle physics as the theoretical framework that gathers the well-established knowledge of elementary particles, with particular emphasis on Quantum Chromodynamics (QCD) theory. The second section focuses on the J/ψ meson, discussing its fundamental properties, experimental detection, and relevance within high-energy physics. Lastly, the third section addresses the physics of heavy-ion collisions, from the motivation behind these experiments, to the experimentally observed QGP signatures focusing on the role of the J/ψ meson as a QGP probe. This final section also includes a brief representation of the reference system and the definition of the main kinematic variables used in this thesis.

1.1. The Standard Model

The Standard Model, formulated in the 1970s, provides a comprehensive framework for describing fundamental particles and their interactions. It incorporates all known elementary particles, categorizing them into fermions, which constitute matter, and bosons, which mediate fundamental forces. Specifically, the model consists of twelve fermions (along with their antiparticles) and six bosons, five of them experimentally confirmed: the photon, gluon, $W^{\pm}$, Z^0, and the Higgs boson. The sixth boson remains unobserved and lies outside the model's scope. This boson proposed as the hypothetical mediator of gravity within the Standard Model is the graviton. Fermions obey Fermi-Dirac statistics and are subject to the Pauli exclusion principle, which states that no two identical fermions can simultaneously occupy the same quantum state. This statistical behavior was established by Enrico Fermi, Paul Dirac, and Wolfgang Pauli. In contrast, bosons follow Bose-Einstein statistics, formulated by Satyendra Bose and Albert Einstein, allowing multiple bosons to coexist in the same quantum state. The fermions of the Standard Model are divided into quarks and leptons. Dominated by the strong interaction, quarks are found forming bound states, whereas leptons can exist as free particles. Quarks combine into composite particles classified as baryons (three-quark states) and mesons (two-quark states). Collectively, quarks, baryons, and mesons are referred to as hadrons. Fermions possess an intrinsic spin of 1/2, while bosons carry integer spin values: 1 for gauge bosons and 0 for the Higgs boson. Particles composed of multiple fermions exhibit composite spin states resulting from their constituents' spin coupling.

The Standard Model organizes quarks and leptons into three generations, each comprising two particles. The first generation consists of the lightest and most stable particles, while the second and third generations contain progressively heavier and less stable states. Stable matter in the universe is exclusively composed of first-generation particles, as heavier states decay into lighter, more stable ones. The quark sector follows the following generational structure. The first-generation quarks, Up and Down, discovered in 1968, form the valence components of protons and neutrons. The second-generation quarks, Strange and Charm, were discovered in 1968 and 1974, respectively. Lastly, the third-generation quarks, Bottom (or Beauty), and Top, are the heaviest. The Bottom quark was discovered in 1977, while the Top quark, with the shortest lifetime of all quarks, was observed in 1995. Experimental confirmation of quarks came through Deep Inelastic Scattering experiments, which provided indirect evidence of their existence.

Furthermore, the lepton sector follows a similar three-generation hierarchy, with each generation including a charged lepton and a corresponding neutrino: the Electron and the Electron Neutrino, the Muon, and the Muon Neutrino, followed by the Tau and the Tau Neutrino. Charged leptons (electron, muon, tau) carry electric charge and significant mass, while neutrinos are electrically neutral and have a tiny but nonzero mass. The Tau neutrino was the last discovered lepton, identified in 2000, while the Higgs boson, the latest identified particle of the Standard Model, was observed in 2012.
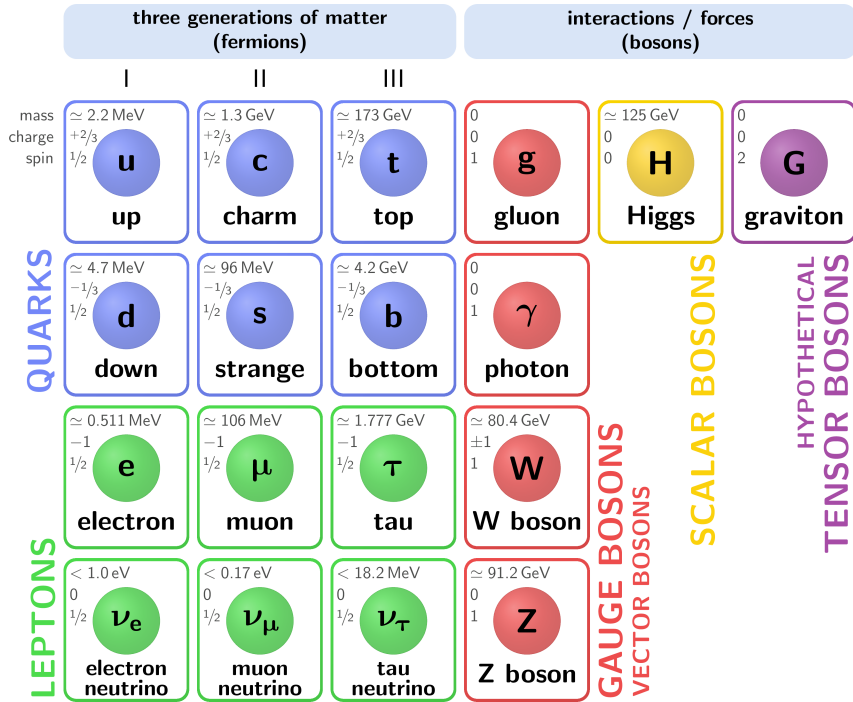
Figure 1.1.: The Standard Model of of particle physics.

Beyond the above schematic representation of the fundamental particles, the Standard Model is a quantum field theory ([2], [3]) that, by incorporating special relativity and quantum mechanics, provides a unified description of three of the four fundamental interactions: the electromagnetic, weak, and strong forces. Although proposing a boson for the inclusion of the gravitational force stil gravity The Standard Model describes the strong and electroweak (electromagnetic

+ weak forces) interactions via a gauge symmetry group, $G_{SM} = SU(3)_C \times SU(2)_W \times U(1)_Y$ where $U(1)_Y$ is an Abelian symmetry, while $SU(2)_W$ and $SU(3)_C$ are non-Abelian. Chirality is another ingredient of the Standard Model theory, as only left-handed fermions participate in weak interactions, while right-handed fermions transform as singlets under $SU(2)_W$. Moreover mass generation in the Standard Model occurs through the Higgs mechanism, which assigns electroweak gauge bosons and fundamental fermions with mass via spontaneous symmetry breaking, and spontaneous chiral symmetry breaking, respectively.

Despite its success, the Standard Model is incomplete, leaving several fundamental questions unanswered. It fails to provide valid candidates for the observation of dark matter. Moreover, it does not incorporate dark energy, which represents 68% of the universe's energy density, by not accounting for a boson candidate for it. Furthermore, the Standard Model predicts massless neutrinos, but experimental evidence confirms that they have small, nonzero masses. It does not explain the observed dominance of matter over antimatter in the universe. Finally, the model requires 27 free parameters, such as coupling constants and particle masses, which must be experimentally determined rather than theoretically derived. Therefore, while the Standard Model remains one of the most successful theories in physics, it needs extensions for addressing these open questions, motivating Beyond Standard Model studies such as Supersymmetry (SUSY), Grand Unified Theories (GUTs), or String Theory.

1.1.1. Quantum Chromodynamics (QCD)

Quantum Chromodynamics (QCD) is a non-Abelian gauge field theory that describes the strong interaction, a fundamental force responsible for binding quarks into hadrons. It is a central component of the Standard Model and is governed by the property of color charge, which comes in three types: red, green, and blue. In analogy to additive color mixing in human vision, QCD ensures that bound states of quarks always combine into color-neutral configurations.

The gauge-invariant QCD Lagrangian is given by:

$$L_{QCD} = \sum_f \bar{\psi}_f (i\gamma^\mu (\partial_\mu - ig_s T^a A_\mu^a) - m_f)\psi_f - \frac{1}{4} G_{\mu\nu}^a G^{a,\mu\nu} \tag{1.1}$$

where the sum runs over the six quark flavors, and m_f represents their respective masses. The first term encodes the quark-gluon interaction, and contains the covariant derivative defined as:

$$D_\mu = \partial_\mu - ig_s T^a A_\mu^a \tag{1.2}$$

where A_μ^a are the gluon fields, T^a are the generators of the SU(3) gauge group, and g_s is the gauge coupling constant. The second term, $\frac{1}{4} G_{\mu\nu}^a G^{a,\mu\nu}$, corresponds to the kinetic term of the gluon fields (Yang-Mills term), with the field strength tensor given by:

$$G_{\mu\nu}^a = \partial_\mu A_\nu^a - \partial_\nu A_\mu^a + g_s f^{abc} A_\mu^b A_\nu^c \tag{1.3}$$

The final term $g_s f^{abc} A_\mu^b A_\nu^c$ describes the self-interaction of gluons (gluons would interact even if quarks did not exist), which is a direct consequence of the non-Abelian structure of the SU(3) gauge symmetry.

Additionally, the gauge coupling constant g_s in the QCD Lagrangian is basically responsible for one of the defining properties of QCD: asymptotic freedom, which implies that the interaction strength between quarks and gluons, collectively called partons, decreases as their momentum exchange increases. This behavior is encoded in the strong coupling constant defined as $\alpha_s = g_s^2/4\pi$, and varying with the energy scale μ of the given physical process following the renormalization group equation, given by the QCD β-function:

$$\beta(g_s) = \mu \frac{dg_s}{d\mu}. \tag{1.4}$$

In non-Abelian gauge theories like QCD Eq. 1.4 can be negative, causing a logarithmic decrease of the coupling constant. Solving this equation to the first quantum correction (only one closed loop in Feynman diagrams) gives for the strong coupling constant the following expression:

$$\alpha_s(\mu) = \frac{4\pi}{\beta_0 ln(\mu^2/\lambda_{QCD}^2)} \tag{1.5}$$

where λ_{QCD} is the QCD scale parameter with a value around 200-300 MeV. The result of renormalizing the strong coupling constant, Eq 1.5, implies that at high momentum transfers ($\mu \gg \lambda_{QCD}$), where α_s is small, QCD interactions can be analyzed using perturbative QCD (pQCD), which allows for a systematic expansion in powers of α_s, with only the lowest orders significantly contributing. Conversely, at low energy scales ($\mu < \lambda_{QCD}$), α_s grows large, making perturbation theory inapplicable.

This non-perturbative regime is key for describing essential additional features of the strong interaction, such as confinement and spontaneous chiral symmetry breaking. Confinement, for instance, ensures that quarks and gluons can never be observed in isolation, as they are permanently bound within color-neutral hadrons. Meanwhile, spontaneous chiral symmetry breaking generates the dominant contribution to the mass of hadrons, including protons and neutrons. Since perturbative methods break down in these regimes, alternative approaches, such as Lattice QCD and Effective Field Theories (EFTs), are employed instead to study these features.

1.2. J/ψ meson

The J/ψ meson belongs to the quarkonium family, consisting of a heavy quark Q and its corresponding antiquark $\bar{Q}$. Two distinct types of quarkonia have been observed: charmonium, consisting of a charm quark (c) and an anticharm quark ($\bar{c}$), and bottomonium, composed of a bottom quark (b) and an antibottom quark ($\bar{b}$).

Within the charmonium spectrum, the J/ψ is a ground state, characterized by quantum numbers $n = 1$, $L = 0$, and $S = 1$. Another ground state in this spectrum is the η_c meson, sharing with the J/ψ the same radial and orbital quantum numbers ($n = 1, L = 0$) but differing in spin ($S = 1$). Excited charmonium states include the $\psi(2S)$, the χ_c states, and the higher ψ states. The $\psi(2S)$ is the first radial excitation ($n = 2$), while the χ_c mesons correspond to P-wave states ($L = 1$). Higher charmonium states are usually denoted by the letter ψ referring to D-wave states ($L = 2$) or higher orbital excitations ($n \geq 3$). To date, 17 confirmed charmonium states have been observed, including the discovery of the spin-3 charmonium state $X(3842)$ in 2019. This state identified via D-meson pair decays at LHCb ($\psi_3(1^3D_3)$), filled the gap in the predicted charmonium spectrum.

The discovery of the J/ψ meson in November 1974, independently observed at Brookhaven National Laboratory and the Stanford Linear Accelerator Center, provided the first direct confirmation of the charm quark's existence. The unexpectedly large mass of the J/ψ meson ($m_{J\psi} = 3.1$ GeV/c), combined with its anomalously long lifetime ($\approx 10^{-20}$ s), strongly suggested the presence of a new quark flavor. This quark was later identified as the charm quark, predicted in 1970 by the GIM mechanism (Glashow-Iliopoulos-Maiani) as a solution to anomalies in weak interaction theory. Therefore, the discovery of the J/ψ meson marked a turning point in high-energy physics, solidifying the quark model and accelerating the development of the Standard Model. Beyond confirming the charm quark, the J/ψ meson became a crucial testing ground for Quantum Chromodynamics (QCD). Studies of its production and decay provided direct evidence for asymptotic freedom and serve as a theoretical laboratory for testing perturbative QCD (pQCD) calculations. In this context, quarkonium states are particularly valuable due to two key factors that facilitate theoretical analysis. First, the large mass (m_Q) of the heavy quark relative to the QCD scale parameter (Λ_{QCD}) suppresses nonperturbative effects, allowing perturbative techniques to be applied in certain kinematic regimes. Second, at sufficiently high transverse momentum ($p_T \geq \Lambda_{QCD}$), inclusive quarkonium production is dominated by short-distance dynamics, reducing sensitivity to hadronization effects. These characteristics make heavy-quarkonium systems invaluable probes of QCD in both perturbative and nonperturbative regimes.

Experimentally the identification of resonances such as the J/ψ meson is achieved through their invariant mass (M_{inv}) calculation derived from relativistic kinematics:

$$M_{inv}^2 c^4 = (\sum_i E)^2 - (\sum_i \mathbf{p}c)^2 \tag{1.6}$$

where E is the total energy and $\mathbf{p}$ is the vector 3-momentum of the system (with Cartesian components p_x, p_y, p_z). The invariant mass is a fundamental property of all particles, remaining independent of the observer's reference frame.

The J/ψ meson, being significantly heavier than light mesons (e.g., pions), can transition between excited states by emitting photons and predominantly decays through annihilation into gluons or lepton pairs (e.g., $J/\psi \to e^+e^-$ or $\mu^+\mu^-$). Experiments using the above equation summing over the decay products reconstruct the J/ψ invariant mass. At high-energy heavy-ion collisions, such

as those conducted at CERN, J/ψ mesons can be detected as prompt or non-prompt. Prompt J/ψ mesons production includes the contributions from the directly produced J/ψs during the hard partonic collision in addition to the J/ψs coming from the decays of heavier charmonium states, such as the χ_c and $\psi(2S)$. In contrast, non-prompt J/ψ mesons are coming from the weak decays of bottom hadrons (primarily B-mesons) leading to a measurable displacement of their decay vertex from the primary collision point.

Quarkonium mesons, including the J/ψ, play a critical role in high-energy physics for multiple reasons. They serve as probes of QCD, allowing for tests of the strong interaction at various energy scales. They are considered key signatures of the Quark-Gluon Plasma (QGP), as in the extreme conditions of heavy-ion collisions quarkonia can suppress and regenerate (see Sec. 1.3.1), providing insight into QCD at these high temperatures and densities. Lastly, their formation and decay processes contribute to studies in Non-Relativistic QCD (NRQCD), refining our understanding of quark dynamics beyond the relativistic regime.

1.3. Heavy nuclei collisions

Current scientific evidence suggests that the early universe emerged from a rapidly expanding, highly dense, and hot state in an event known as the Big Bang. In the first 10 microseconds of the universe's life, the high energy density in this medium was sufficient for finding deconfined quarks and gluons into a phase of matter called Quark-Gluon Plasma (QGP). In this deconfined phase, partons (quarks and gluons) behave as nearly free constituents of a strongly interacting medium, contrasting with their usual bound state as color-neutral hadrons. Therefore, the QGP is particularly attractive as it represents a regime of Quantum Chromodynamics (QCD) fundamentally different from that observed in everyday matter. Experimentally, in the laboratory, the conditions necessary for QGP formation can be recreated by accelerating and colliding heavy nuclei, such as lead (Pb) or gold (Au). The first experimental hints of QGP were reported at CERN's Super Proton Synchrotron (SPS). Subsequently, these observations have been confirmed by numerous results from the Relativistic Heavy Ion Collider (RHIC) and from the Large Hadron Collider (LHC), primarily via the ALICE experiment, which specifically analyzes Pb–Pb collisions focusing on QGP studies.

Figure 1.2 schematically illustrates the space-time evolution of an average heavy-ion collision at LHC, remarking the fifth more important phases of it: the initial state, the QGP formation, hadronization, freeze-out of the system, and finally, the arrival of particles to the detectors. The initial state of the process is characterized by the partonic wave functions of the incoming nuclei, which are governed by universal parton distribution functions (PDFs) and are independent of the specific scattering process. During the collision, interactions at both large and small momentum transfers occur, producing a dense system of partons, marking the pre-equilibrium stage. As the system evolves, it rapidly reaches a local thermal equilibrium, forming the Quark-Gluon Plasma (QGP), which undergoes collective expansion and is usually described by relativistic hydrodynamics assuming thermal and sometimes chemical equilibrium. This QGP phase eventually cools down and transitions into a hadronic phase where quarks and gluons recombine to form hadrons. As the system expands, dilutes, and goes out of thermal equilibrium,

inelastic interactions cease at the chemical freeze-out, fixing the relative abundances of different hadron species. This is followed by the kinetic freeze-out, where elastic scatterings also cease, and particles decouple from the system. Subsequently, hadrons free-stream toward the detector, where their final momentum and identity are determined.
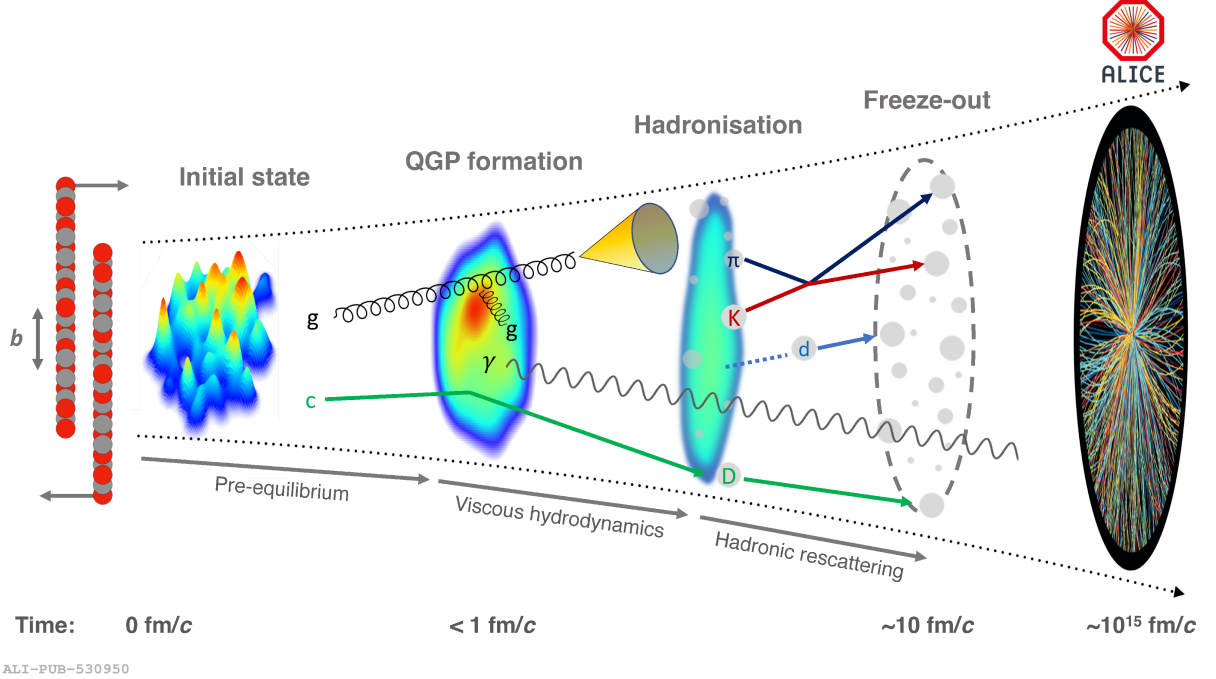

Figure 1.2.: The evolution of a heavy-ion collision at LHC energies. Taken from [4]

In heavy-ion collision experiments, the ultimate goal is to reconstruct the full ensemble of particles produced in the aftermath of the collision and, with it, to learn reversely key properties of the initial colliding nuclei and their constituents. Therefore, experimentalists defined a coordinate system and variables to facilitate the analysis of the produced particles and their kinematics. The following briefly sketches and summarizes the principal kinematic variables, such as momentum, rapidity, and azimuthal angle, that characterize the emitted particles in heavy-ion collisions. These variables are at the base of this thesis analysis and will be used and referred to several times in this manuscript.

Usually, in heavy ion experiments, the z-axis of an Euclidean coordinates system coincides with the beam direction representing the colliding ion's trajectory. This alignment ensures momentum conservation along the beamline, with initial momentum exclusively in the z-direction before collision. Perpendicular to the beam direction is the transverse plane (x-y plane), where the generated particles' transverse momentum (p_{T}), a key observable, is defined. Thus the momentum of a produced particle is computated as $\mathbf{p} = \boldsymbol{p}_{\mathrm{T}} + \boldsymbol{p}_{\mathrm{L}}$ where $\boldsymbol{p}_{\mathrm{T}}$ stands for the vectorial adittion of p_x and p_y components while $\boldsymbol{p}_{\mathrm{L}} = p_z$.

Two angular coordinates are essential to describe the angular distribution of emitted particles: the azimuthal angle (φ) and the polar angle (θ). Defined as the angle between a particle's momentum projection in the transverse plane (p_{T}) and the beam axis (z-axis), φ measurements are central to analyses of anisotropic flow and particle correlations. At the same time, the polar

angle (θ), as the angle between a particle's three-momentum vector (**p**) and the beam axis, is used when determining the pseudorapidity (η) which is defined in the high-energy limit by $\eta = -\ln\left[\tan\left(\frac{\theta}{2}\right)\right]$. Pseudorapidity is a spatial coordinate commonly used in collider experiments as a convenient spatial variable that approximates to rapidity for highly relativistic particles. As a function of the three-momentum components, it can be written as: $\eta = \frac{1}{2}\ln\left(\frac{|\boldsymbol{p}|+p_\mathrm{L}}{|\boldsymbol{p}|-p_\mathrm{L}}\right)$. In the ultra-relativistic limit where $m \ll \mathbf{p}$, the pseudorapidity converges to the rapidity y when expressed as: $y = \frac{1}{2}\ln\left(\frac{E+p_\mathrm{L}}{E-p_\mathrm{L}}\right)$. Unlike velocity, rapidity provides a natural variable for describing boosts along the beam direction, with rapidity differences remaining invariant under Lorentz transformations in that direction. At low velocities, rapidity is approximately proportional to velocity, but it increases logarithmically at high energies, diverging as approaching to the value of the speed of light.

Figure 1.3 schematically illustrates the coordinate system and, the above-discussed, relevant kinematic variables. Two colliding nuclei are shown approaching the interaction point (I.P.), after which multiple particles are emitted, although only one is represented. The direction of this representative outgoing particle is aligned with its momentum vector (blue arrow), from which the azimuthal and polar angles are defined. The figure also outlines the rapidity segmentation of the detector acceptance, with midrapidity corresponding to small values of η (perpendicular to the beam) and forward/backward rapidity regions lying closer to the beam direction. The coordinate system is offset in the illustration purely for better visualization.
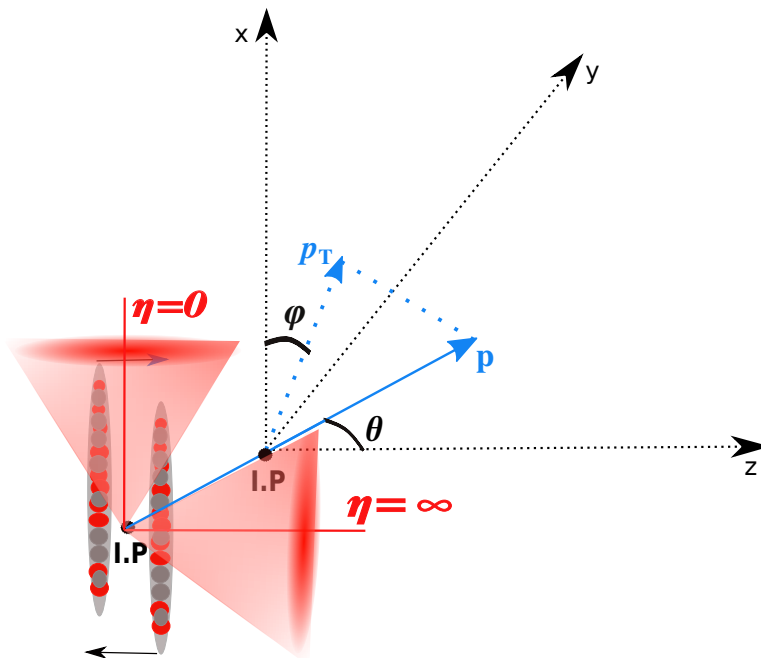

Figure 1.3.: Schematic representation of the coordinate system used in heavy-ion collisions.

1.3.1. J/ψ yields measurements as a QGP signature

The analysis of the produced final-state particles in heavy-ion collisions enables to investigate the formation of the Quark-Gluon Plasma (QGP). While the QGP cannot be observed directly

due to its extremely short lifetime, it can be infered through the so-called QGP signatures which are a set of indirect yet solid evidence confirming the existence of this deconfined, strongly interacting partonic medium after a heavy-ion collision. These signatures are often compared with measurements from systems where no QGP is presumed to form, such as proton-proton or proton-nuclei collisions. Among these signatures are strangeness enhancement as an indicative of rapid chemical equilibration in a high-temperature gluon-rich environment; quarkonium suppression and regeneration, which probe color screening effects and recombination mechanisms in the medium; thermal radiation, manifested as excess direct photons and dileptons carrying information about the temperature and lifetime of the plasma; and chiral symmetry restoration, expected to modify hadron spectral functions and mass degeneracies. Additional signatures include jet quenching, where high-energy partons lose energy while traversing the medium; anisotropic collective flow, providing insight into the strongly coupled, low-viscosity nature of QGP; and chemical equilibration, revealed through particle yield ratios that match predictions from thermal models. Further indicators involve charge balance functions, femtoscopy measurements that explore spatial and temporal scales of the emitting source, and the production of light nuclei and hypernuclei, which inform on coalescence mechanisms and baryon density. A more detailed discussion on these QGP signatures can be found in the 2023 review [5] where the authors focus on the up-to-date status and interpretation of these signatures by discussing the experimental progress that have reinforced the evidence for QGP formation in laboratory conditions when colliding heavy ions at high energies.

Given the central role of the J/ψ meson in this thesis, it is important to highlight the QGP signature of quarkonium suppression and regeneration, as supported by recent ALICE results (see Fig. 1.4). Essentially, quarkonium suppression refers to the observed reduction in quarkonium yields in heavy-ion collisions, primarily due to the color screening effect in the QGP. This phenomenon leads to a sequential suppression of quarkonium states according to their binding energies, with more weakly bound states melting at lower temperatures. Suppression is most prominent at low transverse momentum (p_{T}), where the $Q\bar{Q}$ pair remains longer in the deconfined medium and is more susceptible to color screening. At higher p_{T}, quarkonium states are also suppressed, albeit to a lesser extent, consistent with expectations based on shorter formation times. Furthermore, at the high energies achieved at the LHC, the large abundance of $c\bar{c}$ pairs enables significant regeneration of charmonium during the hadronization stage, activating a new charmonium production mechanism. This regeneration component is predicted to be small for bottomonium states due to the lower production rate of $b\bar{b}$ pairs compared to $c\bar{c}$ pairs; recent ALICE measurements of bottomonium states are reported in [4].

Figure 1.4 presents in the left panel midrapidity measurements of the J/ψ meson nuclear modification factor (R_{AA}) as a function of the charged-particle pseudorapidity density ($\frac{dN_{\mathrm{ch}}}{d\eta}$), while the right panel presents the measurements of the J/ψ nuclear modification factor as a function of the number of participants (N_{part}) at forward rapidity and compared with the data points obtained for $\psi(2S)$ mesons. The nuclear modification factor quantifies the deviation of particle yields in heavy-ion collisions from those in proton-proton collisions scaled by the number of binary nucleon-nucleon interactions. The $\frac{dN_{\mathrm{ch}}}{d\eta}$ is the number of charged particles produced per unit pseudorapidity (η) while N_{part} represents the number of nucleons from the colliding

nuclei that actually interact; although it is not directly measurable it can be estimated using a Glauber model [6]. The charged-particle pseudorapidity density increases with the number of participants, since more participating nucleons tend to produce more particles. The left panel shows the recent ALICE measurements together with the RHIC (STAR) and SPS(NA50) measurements, spanning a broad range of collision energies. These results demonstrate that the J/ψ meson is more suppressed at lower center-of-mass energies, consistent with the picture of color screening being dominant in that energy region. At LHC energies, however, it is observed from the figure that the abundance of $c\bar{c}$ pairs leads to a substantial regeneration contribution, mitigating the suppression effects at high multiplicities or more central collisions. The right panel comparing R_{AA} for J/ψ and $\psi(2S)$ as a function of N_{part}, illustrates the stronger suppression for $\psi(2S)$ as expected for more weakly bound excited states of J/ψ, thereby supporting the sequential melting idea. The results of Fig. 1.4 confirmed existing ideas about J/ψ suppression and, more importantly, about its regeneration mechanism, constituting a significant step toward understanding the production of J/ψ in heavy ion collisions.
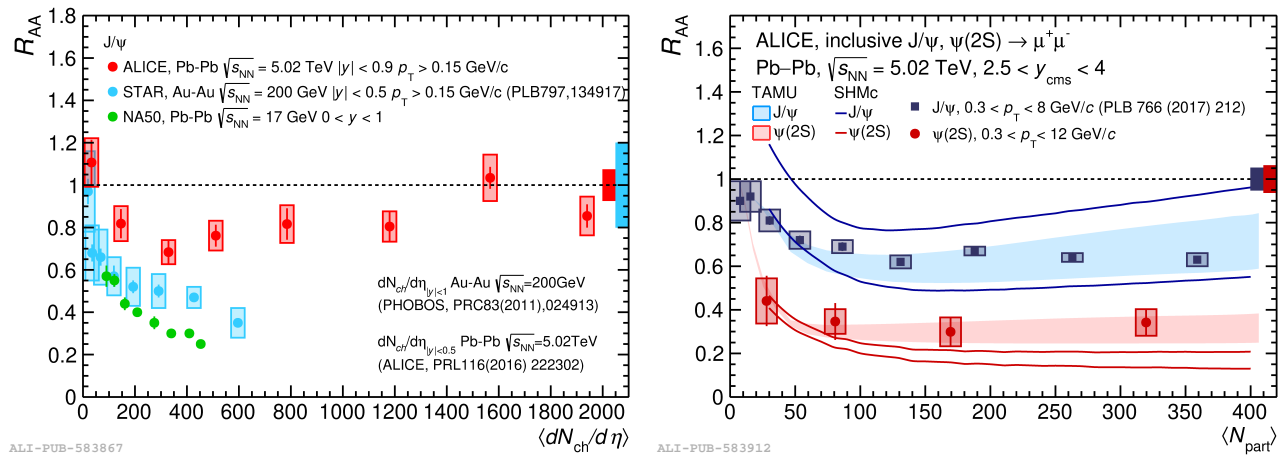

Figure 1.4.: Left: Comparison between SPS (NA50), RHIC (STAR) and LHC (ALICE) results on the nuclear modification factor as a function of the charged hadron multiplicity. **Right:** The nuclear modification factor for inclusive $\psi(2S)$ and J/ψ, as a function of N_{part}, at forward rapidity. Predictions from the TAMU [7] and SHMc [8] models are also included. Taken from [4]

2. Reviewing J/ψ mesons production as a function the Charged-Particle Multiplicity

This chapter aims to consolidate key phenomenological principles and recent experimental results from the ALICE collaboration, which lead to the analysis presented in this thesis. While Chapter 1 provided an overview of the foundational theoretical concepts in particle physics and the general motivation for this work, this chapter shifts towards a detailed introduction to quarkonium (J/ψ) production as a function of the charged-particle multiplicity.

The chapter is divided into three sections, each building on the previous one. The first section explores the significance and increasing interest in studying pp collisions, focusing on theoretical descriptions and recent measurements conducted by the ALICE experiment using pp collision data at $\sqrt{s} = 13$ TeV. This section is divided into three parts. The first subsection reports briefly about the simulation of proton-proton collisions as an essential theoretical component in the particle physics community; the second subsection discusses some of the main theoretical ideas for understanding charged-particle production and presents ALICE's latest measurements of the charged-particle multiplicity in pp collisions while the third subsection reviews theoretical models for J/ψ production and compares them to ALICE's latest experimental results.

The second section dives into the correlations between hard components, such as J/ψ mesons, and soft components, such as the charged-particle multiplicity, within a pp collision. This section reviews theoretical/phenomenological models attempting to describe the correlation between hard and soft components in a pp collision, and it also highlights the latest ALICE measurements of J/ψ mesons, $\psi(2S)$, open heavy flavor, and bottomonium mesons as functions of the charged-particle multiplicity. Finally, the third section discusses the importance of the azimuthal J/ψ-$\mathrm{N_{ch}}$ correlation analysis as the natural next step towards an attempt to understand the remaining open questions on the interplay between hard and soft components in a pp collision.

2.1. High multiplicity proton-proton (pp) collisions

Describing particle production in proton-proton (pp) collisions is essential to identify the QGP-like signatures manifested in nucleus-nucleus collisions, as these are mostly indirectly inferred by taking pp collisions as a baseline reference, assuming no QGP formation in those. However, high-multiplicity pp and pPb collisions at LHC energies have been raising considerable interest due to the emergence of QGP-like signatures within these collisions. At these energies, high multiplicity pp collisions could produce ten times more particles than a minimum-bias pp collision (a collision without any selection bias caused by the presence of a hard scattering), which is closer to the

number of particles produced after a peripheral heavy-ion collision. Phenomenological models introduce the idea of multiparton interactions trying to explain such high-multiplicity events. This possibility of multiple hard and soft interactions among the proton's constituents is the result of increasing the collision energy, which leads to a more accessible denser sea of partons within the protons, consequently raising the probability of multiple inelastic partonic interactions with high momentum transfer during a single pp collision, as roughly depicted in Fig. 2.1. As the initial system volume is fixed (two protons), these hard partonic interactions could then achieve energy densities exceeding the QGP formation threshold.
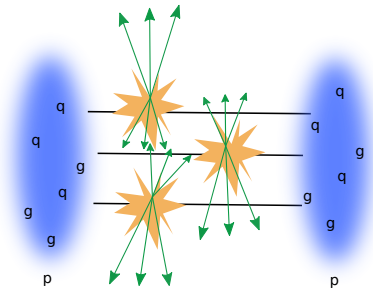

Figure 2.1.: Sketch of multi-partonic interactions in a pp collision.

Some recent QGP-like observations in pp collisions at LHC energies are a large radial flow velocity [9], a strangeness enhancement [9], a collective hadrodynamic behavior [10], and multiparticle Ridge-like correlations [11]. Despite these observations, whether or not a QGP medium forms remains an open question since several phenomena observed in heavy-ion collisions (see Sec. 1.3.1) still require thorough investigation. Phenomena such as jet quenching, medium-induced energy loss, high-p_{T} hadron suppression, and suppression of charmonia and bottomonia have not been observed in pp collisions. The upcoming high interaction rate and luminosity of the LHC experiments will enable enhanced access to high-multiplicity events, short-lived particles, exotica, and heavy-flavor physics, thus providing the perfect scenario to investigate these open questions.

2.1.1. Simulations of pp collisions

Simulating high-energy hadronic collisions is fundamental to modern particle physics. These simulations rely on Monte Carlo (MC) event generators [12], which are essential for interpreting experimental data, optimizing detector designs, and refining theoretical models in collider experiments such as those at the Large Hadron Collider (LHC).

MC event generators simulate high-energy hadronic interactions by integrating random numbers generation with theoretical models, producing events that closely replicate real collisions. A key strength of these tools is their ability to model the parton-to-hadron transition, a process that cannot be entirely derived from first principles. As a result, current simulation frameworks rely on phenomenological models to connect theoretical predictions with experimental observables. Furthermore, simulations of high-energy pp collisions are governed by frameworks that incorporate factorization theorems. These theorems enable the decomposition of cross-sections

and other observables into short-distance components, such as parton-level scattering matrix elements, which can be computed using perturbative QCD, and long-distance components, including parton distribution functions (PDFs) and fragmentation functions, which describe non-perturbative effects. The complexity of these factorization theorems increases when incorporating transverse-momentum dependence or considering less-inclusive observables.

PYTHIA([13], [14], [15], [16]) and EPOS ([17], [18], [19]) are the most widely used MC event generators for pp collision simulations at the LHC. These frameworks provide a coherent description of hadronic collisions, modeling the evolution from an initial hard-scattering process to the complex multiparticle final state. While some aspects of these models are rigorously derived from theory, others rely on phenomenological parameters that must be tuned using experimental data. LHC experimentalists employ PYTHIA and EPOS for various purposes, including exploring the experimental consequences of theoretical models, developing search strategies for new physics, interpreting experimental results, and evaluating detector performance. Different PYTHIA tunes correspond to specific parameter sets, with PYTHIA 8.2 Monash 2013 as one of the most stable for comparisons with experimental measurements. Similarly, EPOS has multiple versions, with EPOS-LHC designed explicitly for analyzing high-energy hadronic collisions at the LHC.

The following subsections present the latest ALICE experimental results for the key observables in this thesis: the J/ψ yield and the charged particle multiplicity. These measurements are systematically compared to theoretical predictions from MC-simulation frameworks, incorporating various models and physics concepts discussed in the subsequent sections. PYTHIA and EPOS, for example, include many of these theoretical concepts to describe the production of J/ψ mesons and the charged particle multiplicity.

2.1.2. Charged-Particle Multiplicity (N_{ch}) in pp collisions

A fundamental observable in high-energy physics is the charged-particle multiplicity (N_{ch}), defined as the number of charged particles produced in a collision. In pp collisions at LHC energies, this multiplicity, although influenced by the hard scatterings (high transfer momentum) between the proton's constituents, is predominantly governed by soft QCD processes. The transition between soft and hard interactions occurs around a momentum transfer threshold of 2 GeV/c. This value is not a strict theoretical cutoff but a boundary based on experimental observations showing that particle spectra and event properties change character around this value. Theoretically, charged-particle production in collisions is typically modeled in QCD-based event generators by combining perturbative QCD, describing the hard interactions between partons, with phenomenological models such as the Quark-Gluon String Model [20] and the Dual Parton Model [21] to describe the enormous bulk of produced charged particles via soft interactions processes or underlying events. These phenomenological models based on Regge Field Theory [22] describe the produced particle spectra by introducing multiple Pomerons exchanges with cylinder topology to estimate the particle production cross sections. Additionally, they relied on fitting a few parameters to the experimental data. Therefore, due to the interplay between hard and soft QCD processes and the complexity involved in

describing hadronization, theoretical reproduction of the charged particle multiplicity is a complex task calling for a detailed understanding of the collision's final state. In contrast, the distribution of charged particles ($P(N_{ch})$) is one of the most straightforward observables to measure experimentally, making the measurements of this observable crucial in constraining theoretical and phenomenological particle-production models.

The dependency of $P(N_{ch})$ on N_{ch} in pp collisions has been the focus of extensive research. Assuming that particle production is independent, meaning that each produced particle is independent of previously produced particles, the resultant distribution could theoretically approximate a statistical Poisson distribution. However, correlations among final-state particles introduce deviations from this assumption. In pp collisions, additional fluctuations and final-state correlations make the multiplicity distribution better described by a Negative Binomial Distribution (NBD) or, at LHC energies, by a double NBD [23]. While there is no fully established physical justification for using NBDs, their application is interpreted as reflecting the combination of different classes of events rather than distinct particle-production mechanisms. Recent measurements of $P(N_{ch})$ vs. N_{ch} in pp collisions at center-of-mass energies from $\sqrt{s}$ = 2.76 TeV to $\sqrt{s}$ = 13 TeV are presented in [24] and depicted in the left panel of Fig. 2.2. The maximum of these distributions consistently appears around $N_{ch} \approx 2$, while the distribution shapes exhibit a steep fall-off, with the slope becoming progressively steeper at higher collision energies, likely due to increased momentum transfer in hard scatterings. Additionally, the $P(N_{ch})$ vs. N_{ch} measurements were compared to simulations from PYTHIA with the Monash 2013 tune [25] and EPOS LHC ([17], [18], [19]) event generators. The models and the ALICE data agree within 25%, with larger discrepancies observed at higher multiplicities, as shown in the right panel of Fig 2.2.
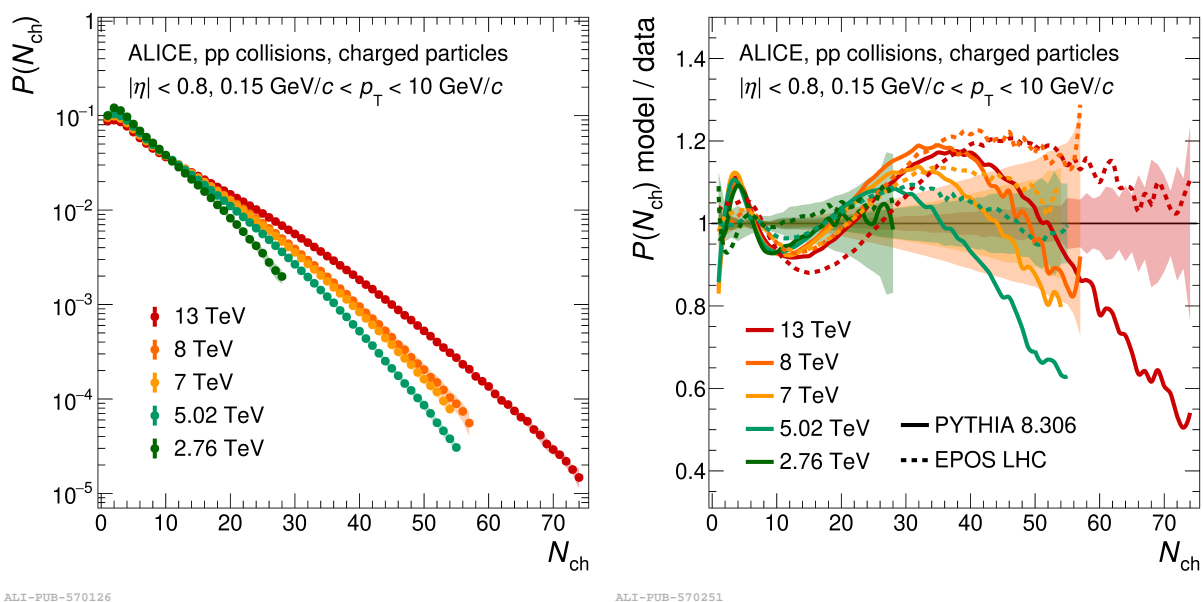

ALI-PUB-570126   ALI-PUB-570251

Figure 2.2.: Left: Probability density of charged-particle multiplicity in pp collisions at different centre-of-mass energies per nucleon pair. **Right:** Ratio model predictions to data of the multiplicity distributions for pp collisions at different centre-of-mass energies per nucleon pair. Figures taken from [24].

In addition to $P(N_{ch})$ vs. N_{ch}, other key observables frequently analyzed by experiments and models are the charged-particle multiplicity as a function of pseudorapidity density, (η) $(dN_{ch}/d\eta$ vs. $\eta)$, the dependence of the average transverse momentum (p_T) on the charged-particle multiplicity $(\langle p_T \rangle$ vs. $N_{ch})$, and the energy dependence by looking at the mean charged-particle multiplicity as a function of the collision center-of-mass energy $(\langle N_{ch} \rangle$ vs. $\sqrt{s}$ or $dN_{ch}/d\eta$ vs. $\sqrt{s})$. The latest measurements of these observables by the ALICE experiment and their comparison with models and event generators such as PYTHIA and EPOS are reported in [26], revealing discrepancies ranging from 3% to 20% for the different analyzed cases. Likewise the Koba, Nielsen, and Olesen (KNO) scaling behavior is also investigated in measurements and simulations by expressing the charged particle multiplicity distribution as $\langle N_{ch} \rangle P(N_{ch})$ and as a function of the mean charged-particle multiplicity $\langle N_{ch} \rangle$ across different collision center-of-mass energies and by pseudorapidity regions. Based on the Feynman postulate [27], which connects the average number of produced particles $(\langle N \rangle)$ with the center-of-mass energy of a collision, as $\langle N \rangle \propto ln\sqrt{s}$, the KNO scaling proposes that the charged-particle multiplicity distribution $P(N_{ch})$ can be expressed as a rescaled version of the universal distribution, $\Psi(z)$, where z represents the scaled multiplicity defined as $z = N_{ch}(\sqrt{s})/\langle N_{ch}(\sqrt{s}) \rangle$ predicting the overlap of rescaled $P(N_{ch})$ distributions for different center-of-mass energies while measured at the same pseudorapidity. Moreover, KNO scaling implies energy-independent moments of the multiplicity distribution in the limit of $s \to \infty$. Recent ALICE measurements [24] in pp collisions report that KNO scaling holds within 20% for the reported distributions.

In summary, while the existing theoretical/phenomenological simulation frameworks grounded in distinct physics principles offer relatively accurate descriptions, they do not offer exact agreement with the experimental data. The persistent discrepancies accentuate the necessity of refining the current description of the charged-particle production in hadronic interactions, remarking the importance of continuing to analyze high-precision data from experiments like ALICE to constrain further and comprehensively understand the existing theoretical frameworks.

2.1.3. J/ψ production in pp collisions

Measurements of particle production in proton-proton (pp) collisions, when compared to those in proton-nucleus and nucleus-nucleus collisions, are essential for investigating Cold Nuclear Matter (CNM) effects and quantifying the influence of the Quark-Gluon Plasma (QGP), respectively. Mainly, quarkonia production, especially J/ψ meson, is a key observable in heavy-ion collisions, where its suppression and subsequent regeneration are considered compelling evidence of a QGP formation, as previously discussed in 1.3.1.

In pp collisions, J/ψ production measurements are critical for understanding hadronization processes within the QCD framework. This complexity arises from the distinct energy scales involved in quarkonium production. The initial production of the heavy $c\bar{c}$ pairs is typically modeled using perturbative QCD, as $m_c \gg \Lambda_{QCD}$, while nonperturbative QCD governs the subsequent binding of the pair into a J/ψ meson. Therefore, theoretically describing the production of quarkonium states resulting from quarks and gluons interactions remains a challenging topic, requiring the disentangling of two stages: the production of the heavy quark

pair during the hard scattering process and its subsequent hadronization into a bound state. As a result, the theoretical/phenomenological calculations of the charmonium production cross-section rely on the factorization theorem: one factor includes the perturbative effects, and another encloses nonperturbative contributions. Prominent theoretical approaches in this direction are the Color Singlet Model (CSM), the Color Evaporation Model (CEM), and the Non-Relativistic Quantum Chromodynamics (NRQCD) and the Color Glass Condensate (CGC) frameworks. The CGC has been recently incorporated as a complementary framework for modeling J/ψ production, particularly at high parton densities. The following summarizes these models' main ideas and key concepts originally formulated for J/ψ production, but that can generally also describe quarkonia production.

The Color Singlet and Color Evaporation models ([28], [29], [30], [31]) were introduced in the 1970s to describe the inclusive production of heavy quarkonium. These models fundamentally differ in their treatment of the color and spin configurations of the heavy quark (Q) and its antiquark ($\bar{Q}$) during the charmonium production process. The CSM, for instance, assumes that the $Q\bar{Q}$ pairs and the resulting charmonium state share identical angular-momentum quantum numbers and exist exclusively in a color singlet configuration. In contrast, the CEM assumes the probability of forming a specific quarkonium state independent of the $Q\bar{Q}$ pair color and the spin. In the CSM for the $Q\bar{Q}$ pair to have a significant probability of binding it must be produced with small relative momentum ($v \to 0$) compared to the mass of the charm quark, when in the rest frame of the pair. Otherwise, in the case of J/ψ, the c and $\bar{c}$ would fly apart and ultimately form D mesons. The evolution of the $Q\bar{Q}$ pair into charmonium in color singlet state then occurs by emitting a gluon ($gg \to c\bar{c} + g$). The CSM provides a framework for calculating the quarkonium production cross-sections as a factorized expression of the production rate of a $Q\bar{Q}$ pair in a color singlet state (S_1^3) state multiplied by the probability that a point-like $Q\bar{Q}$ pair forms a J/ψ bound in the S_1^3 state. The CSM predicts the cross-section dependence with the polarization of quarkonium states and that the ratios $\sigma(H)/\sigma(J/\psi)$—the cross-sections of different charmonium states (H) relative to J/ψ—should vary significantly between processes based on angular momentum selection rules. However, these predictions have not been seen experimentally, and there is little evidence of spin asymmetries in the effective cross-sections.

On the other hand, charmonium production takes place under the CEM when a $Q\bar{Q}$ pair with an invariant mass below the D-meson threshold transitions into a charmonium state through the emission of soft gluons. The model considers that the emission of these soft gluons eliminates any correlation between the color and spin states of the heavy quark pairs and the quantum numbers of the final charmonium state. The quarkonium production cross-section is also estimated in this model following the factorization theorem: a factor proportional to the $Q\bar{Q}$ production cross-section in an invariant mass region where its hadronization into a quarkonium is possible, that is, between the kinematics threshold to produce a quark pair, $2m_Q$ and that to create the lightest open-heavy-flavor hadron pair, $2m_H$; multiplied by a second factor of phenomenological roots related to a process-independent probability that the pair eventually forms a bound state. A key feature of the Color Evaporation Model is stating quarkonium production cross-sections independent of the quarkonium polarization, predicting the transversely polarized fraction of J/ψ equal to 2/3. At the same time, this model also makes predictions about the differential

cross-section ratio of charmonium states to J/ψ ($\sigma(H)/\sigma(J/\psi)$), considering it to be independent of both kinematics and the colliding species. Experimental results, however, have long shown that this ratio varies with transverse momentum, making this discrepancy clear evidence against the validity of the CEM. Since its proposal to date the CEM has undergone modifications, evolving into the Improved Color Evaporation Model (ICEM) [32], [33], during the past decade. While the ICEM does not address the issue of the J/ψ polarization, it estimates the charmonium production cross-sections. By distinguishing between the momentum of the $Q\bar{Q}$ pair and that of the resulting charmonium state, the ICEM produces smoother predictions for the p_T spectra, providing a better match to the experimental data of the J/ψ double-differential cross-section, particularly at high p_T, as it is observed in Fig. 2.3.

Despite their fundamentally different assumptions, both the Color Singlet Model (CSM) and the Color Evaporation Model (CEM) achieved significant phenomenological success during the 1980s and 1990s. However, by the early 1990s, it became evident that the CSM alone was insufficient to explain experimental observations. In response, a more comprehensive theoretical framework emerged to address charmonium production: Nonrelativistic Quantum Chromodynamics (NRQCD) ([29], [28]). Positioned between the Color Singlet and the Color Evaporation models in its treatment of spin and color, the NRQCD model introduces a significant advancement: it does not restrict the charmonium-bound state to form exclusively in a color-singlet configuration. Instead, it also considers the contributions from color-octet mechanisms, where the $Q\bar{Q}$ pair is produced at short distances in a color-octet state and subsequently transitions to a bound charmonium state via the emission of soft gluons. This approach improved agreement between models and experimental data, particularly in describing the fraction of J/ψs coming from χ_{c1} and χ_{c2} (P-wave charmonium states). In general, three main momentum scales could be considered while describing the dynamics of mesons containing a heavy quark and antiquark: the heavy quark mass (M), its typical three-momentum (Mv), and its kinetic energy (Mv^2). The NRQCD model leverages from separating these momentum scales, and by assuming the hierarchy $(Mv^2)^2 << (Mv)^2 << M^2$, it proposes a nonrelativistic treatment of the heavy quark-antiquark pair in their center-of-mass frame. This nonrelativistic QCD formalism implies formulating the Lagrangian with a nonrelativistic Schrödinger field theory (two-component Pauli spinor field) instead of using the traditionally relativistic Dirac field theory (four-component Dirac spinor field). Subsequently, the NRQCD framework relies on the factorization theorem, which separates the production cross section into two components: a short-distance part describing the production of $Q\bar{Q}$ pairs and a long-distance part accounting for the subsequent formation of the bound state. The effect of the heavy quark mass M momentum scale allows a QCD perturbative description as expansions in the strong-coupling constant α_s when describing the short-distance part responsible for the production of the heavy quark pairs after the collision. Meanwhile, the effects of the Mv, Mv^2, and Λ_{QCD} momentum scales are encapsulated in the long-distance matrix elements (LDME), which is the term describing the long-distance part in the factorized expression of the charmonium production cross-section. In practice, these LDMEs are determined by fits to experimental data and are assumed to be universal across different processes. Although the NRQCD formalism does not fully align with experimental observations, mainly when predicting charmonium polarization, it remains a

crucial tool for interpreting quarkonium production, as illustrated in Fig. 2.3, which compares its theoretical predictions with the experimental J/ψ production spectra at midrapidity.

The Color Glass Condensate (CGC) Model [34], introduced in the early 21st century, was developed to describe particle production in Au-Au collisions at the Relativistic Heavy Ion Collider (RHIC). The model is based on the observation that at high energies—or equivalently, at small values of the Bjorken-x variable (fraction of momentum carried by a parton) —parton densities in the colliding hadrons become extremely large. In this regime, the parton distribution functions (PDFs) saturate at a critical value of x, denoted as $x_s(Q^2)$, for a given momentum scale. This characteristic scale, known as the saturation scale $Q_s^2(x)$, represents the squared average color charge per unit transverse area and rapidity. At high energies, gluon densities increase more rapidly than quark densities, leading to gluon saturation. This saturation occurs when gluons begin to recombine rather than only splitting, effectively limiting their density. The CGC model treats small-x gluons as classical fields radiated by higher-x gluons. Consequently, the dense gluonic environment can be described using a many-body QCD framework characterized by weakly coupled partons but exhibiting strong nonperturbative effects due to high gluon densities. Furthermore, the evolution of partons with $Q^2 > Q_s^2$ follows linear differential equations, such as the Dokshitzer-Gribov-Lipatov-Altarelli-Parisi (DGLAP) or Balitsky-Fadin-Kuraev-Lipatov (BFKL) equations. Saturation effects will become important when Q^2 approaches Q_s^2 from above meaning that the gluon distribution "flattens" in this region ceasing to grow rapidly with decreasing x. Thus conversely, partons with $Q^2 \leq Q_s^2$ are in a saturated regime with nonlinear evolution as described by the Jalilian-Marian-Iancu-McLerran-Weigert-Leonidov-Kovner (JIMWLK) equations ([35]). A commonly used criterion for gluon saturation is the Gribov-Levin-Ryskin condition ([36]), which leads to a parameterized expression for Q_s^2 yielding values in the range of 0.5-1 GeV/c. The CGC model provides a practical framework for describing the small-x regime, particularly for studying the initial stages of high-energy hadronic collisions. Although initially developed for AA collisions, the CGC model has been successfully extended to pA and pp collisions, especially in quarkonium production. In these cases, factorization-based models incorporate the CGC framework to describe the perturbative production of heavy quark pairs ([37], while the subsequent hadronization of these pairs is typically modeled using the Color Evaporation Model (CEM)[38]) or the Non-Relativistic QCD (NRQCD) framework ([39]), as illustrated in Fig. 2.3.

On the other hand, experimentally the latest measurements of J/ψ meson production by the ALICE experiment are reported in [40] and [41]. The plots in Fig. 2.3 taken from [40] show the double differential J/ψ production cross-section as a function of transverse momentum. The left panel of the figure shows the measurements at midrapidity and forward rapidity in pp collisions at $\sqrt{s} = 13$ TeV, while the right panel compares the midrapidity data points with theoretical predictions from the above-discussed models. Experimentally, the double differential J/ψ production cross-section is determined using the expression:

$$\frac{\mathrm{d}^2\sigma_{J/\psi}}{\mathrm{d}y dp_\mathrm{T}} = \frac{N_{J/\psi}}{BR(J/\psi \to e^+e^-) \times \langle A \times \epsilon \rangle \times \Delta y \times \Delta p_\mathrm{T} \times L_{int}} \tag{2.1}$$
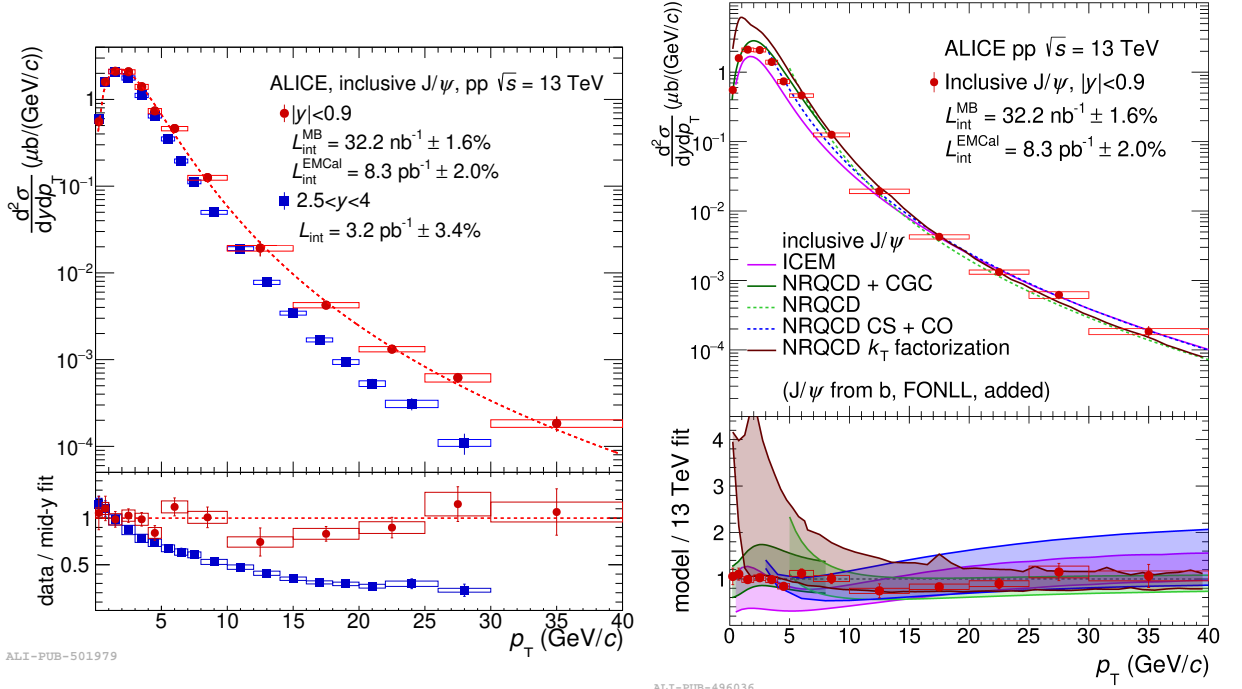
Figure 2.3.: Left: Inclusive J/ψ production cross section at midrapidity compared with the J/ψ production cross section at forward-rapidity in pp collisions at $\sqrt{s} = 13$ TeV . **Right:** Inclusive J/ψ production cross section compared with the corresponding calculations obtained as the sum of the prompt J/ψ component predicted by the ICEM, NLO NRQCD, LO NRQCD+CGC models and the non-prompt contribution from FONLL. The bottom panel shows the ratios between the model calculations and a fit to the data points. Figures taken from [40].

where $N_{J/\psi}$ is the number of reconstructed J/ψ in a given interval of rapidity Δy and transverse momentum Δp_T, $BR(J/\psi \to e^+e^-)$ is the decay branching ratio into the dielectron channel, $\langle A \times \epsilon \rangle$ is the average acceptance and efficiency and lastly L_{int} is the integrated luminosity of the data sample.

The data reveal that at midrapidity, J/ψ mesons are produced with higher p_T values compared to forward rapidity, indicating enhanced production at higher transverse momenta in the central region. Comparisons of the measured midrapidity cross-sections with theoretical models show that, overall, all models reasonably describe the data. However, the best agreement is observed for the Improved Color Evaporation Model (ICEM) and the NRQCD+CGC framework, highlighting their effectiveness in capturing the dynamics of J/ψ production.

2.2. Correlating hard (N_Q) and soft components (N_ch) in a collision

At LHC energies, the average transverse momentum, $\langle p_T \rangle$, of the charged particles produced in pp collisions is relatively low, ranging from approximately 0.3 GeV/c to 1 GeV/c [24]; with light mesons, such as pions dominating the particle composition of the final state. Thus, most charged particles in hadronic collisions result from partonic interactions characterized by low momentum exchange (soft interactions or underlying events). In contrast, quarkonia, such as J/ψ, are produced far less frequently since producing the heavy quarks forming these mesons requires high momentum exchange partonic interactions (hard interactions). Therefore, correlating the

production of quarkonia (N_Q) with the charged-particle multiplicity (N_{ch}) in hadronic collisions could provide valuable insight into the interplay between hard and soft mechanisms governing particle production in a pp collision. Specifically, this correlation aims to understand how the charged-particle multiplicity behaves in collisions producing a heavy meson, such as the J/ψ, compared to the majority of the pp collisions when selected without the bias of producing a J/ψ or any other hard probe. Furthermore, studies in p–Pb and nucleus-nucleus collisions have shown that final state interactions influence quarkonia production ([4], [42]). Analyzing this correlation in pp collisions, especially high multiplicity pp collisions, could help determine whether quarkonium production depends on its kinematics and the initial state of the colliding hadrons or if, similarly to heavy-ion collisions, final state interactions play a significant role in modifying quarkonia production rates.

The axes, when depicting this correlation, are consistently presented in a self-normalized form: $dN_Q/\langle dN_Q \rangle$ as a function of $dN_{ch}/\langle dN_{ch} \rangle$. Here, the number of counts corresponding to the measured number of quarkonium (N_Q) and charged particles (N_{ch}) are divided by their respective multiplicity-integrated values. This normalization provides observables indicating how many times their absolute quantities deviate from their average values across the analyzed collisions.

Correlating J/ψ with N_{ch} was initially proposed in [43], predicting two possible scenarios: a flat ratio or a linear ($f(x) = x$) increase. The correlation is anticipated to yield a flat ratio if quarkonium production is completely independent of multiparton interactions. However, as discussed in the previous sections, multiparton interaction mechanisms significantly influence quarkonium and the charged-particle production. Therefore, a linear relationship between quarkonium yield and the charged-particle multiplicity was initially expected.

The correlation between quarkonium production and the charged-particle multiplicity has been experimentally measured by CMS ([44], [45]), STAR ([46])and ALICE collaborations when using Run 1 data ([47]). These studies observed a linear increase in quarkonium production with charged-particle multiplicity, attributing this trend to multiparton interaction mechanisms and the hadronic activity accompanying quarkonium production. The following focuses on a review and analysis of the latest reported measurements using the Run 2 data from the ALICE experiment alonside the theoretical predictions by the different models.

2.2.1. Measurements of J/ψ yields as a function of N_{ch} with ALICE

The latest ALICE results on J/ψ production as a function of the charged-particle multiplicity ([48], [49]) are presented in Fig. 2.4. The figure presents the J/ψ yield as a function of the charged-particle multiplicity, with J/ψ mesons detected in their dielectron and dimuon decay channels. The electron-positron decay channel corresponds to J/ψ production at midrapidity, while the dimuon decay channel corresponds to J/ψ production at forward rapidity. In both cases, the J/ψ yields are correlated with the charged-particle multiplicity measured at midrapidity. The results reveal a significantly stronger-than-linear increase in the J/ψ yield as a function of charged-particle multiplicity when both observables are measured at midrapidity. In contrast with the almost linear increase observed for this exact correlation but when the J/ψ is at forward rapidity in pp collisions with $\sqrt{s} = 5.02$ and 13 TeV center-of-mass energies.

Furthermore, the figure also presents two sets of data points with the J/ψ measurements at midrapidity (electron-positron decay channel), but the charged-particle multiplicity is estimated using different detector configurations. In the first set of data points, the charged-particle multiplicity is obtained directly from a detector with midrapidity acceptance, the inner tracking system (ITS), see Chapter 3 for further details, which provides an experimental estimator (SPD tracks). The second set of data points uses the V0 detector configuration, which has a forward rapidity acceptance, and subsequently, the multiplicity is converted to the midrapidity bins. Despite the differing rapidity ranges for measuring charged-particle multiplicity, the pronounced stronger-than-linear increase is observed when the J/ψ is measured at midrapidity, suggesting that the physical mechanisms governing J/ψ production might differ between forward and midrapidity. Another possible explanation of this difference includes autocorrelations effects associated with particle production mechanisms differing between mid and forward rapidity, potentially influencing the soft components in a collision.

ALI−PUB−501851
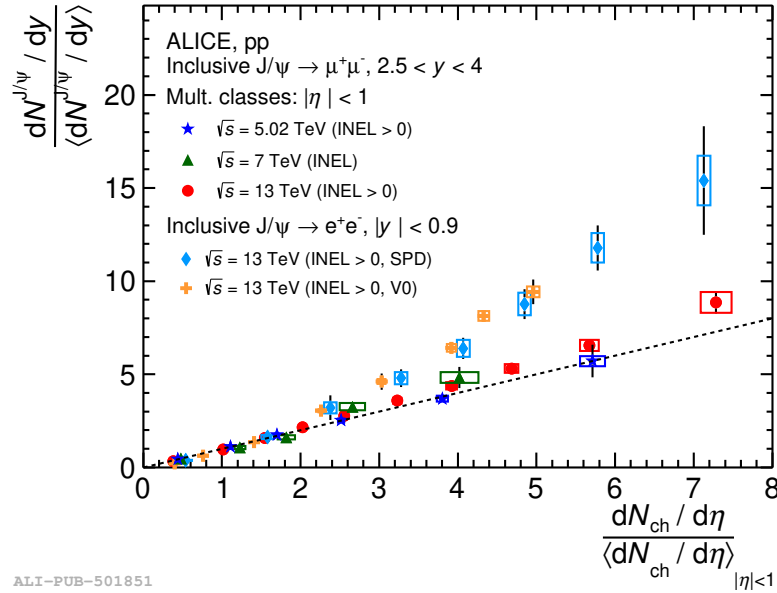
Figure 2.4.: Relative J/ψ yields measured at forward rapidity at $\sqrt{s} = 5.02$ TeV, 7 and 13 TeV compared with similar measurements at midrapidity at $\sqrt{s} = 13$ TeV, the latter corresponding to the event selection based on SPD tracklets at midrapidity and on V0 amplitude at forward rapidity.
Figure taken from [49]

2.2.2. Latest theoretical predictions on J/ψ yields as function of N_{ch}

Comparisons of the above-discussed results with the available theoretical predictions are depicted in Fig. 2.5. The models offering the best descriptions among all the reported measurements are the 3-Pomeron Color Glass Condensate (CGC), the Coherent Particle Production (CPP), and the Percolation models. In contrast, PYTHIA 8.2 and EPOS3 event generator predictions underestimate all the measurements. At forward rapidity, the CGC+ICEM model overestimates the experimental results, while the Percolation, the 3-Pomeron CGC, and the CPP models are in good agreement with the experimental measurements, especially at $\sqrt{s} = 13$ TeV. On the other hand, at midrapidity, the CGC+ICEM model, alongside the 3-Pomeron CGC and the CPP models, provides a satisfactory description of the data, whereas the Percolation model,

in this case, overestimates the correlation at high multiplicities. All these models incorporate phenomenological components and rely on distinct physical assumptions to describe the J/ψ-N_{ch} correlation. The following provides an overview of these theoretical models, highlighting their primary physical assumptions.
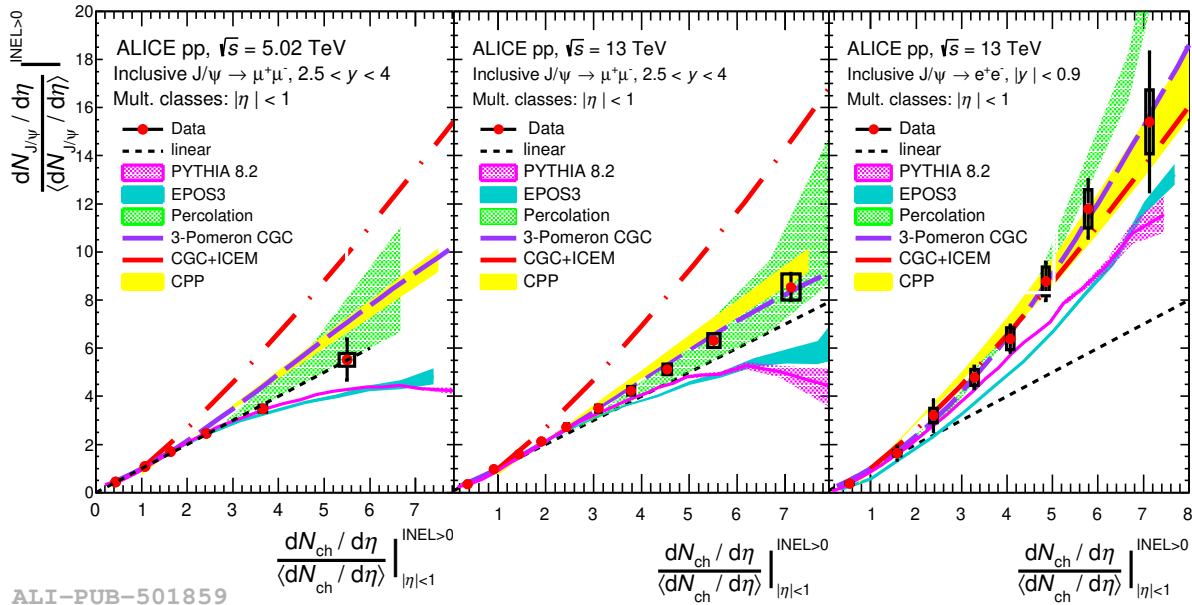

Figure 2.5.: Relative J/ψ yield as a function of the relative charged-particle multiplicity compared to model predictions by CPP, CGC with ICEM, 3-Pomeron CGC, Percolation, EPOS3 and PYTHIA 8.2 event generators, at forward rapidity in pp collisions at $\sqrt{s} = 5.02$ TeV (left panel) and 13TeV (middle). The right panel shows the results from midrapidity compared to the corresponding theoretical model estimations for pp collisions at $\sqrt{s} = 13$ TeV. Figure taken from [49].

PYTHIA 8.2 [15]: Describes light-charged particle production through a comprehensive set of physics models that simulate the entire evolution from initial partonic scattering to the final multiparticle state. The process unfolds through several key stages. During the Partonic Interaction and Showers stage, the parton-parton interactions are accompanied by initial- and final-state parton showers, where quarks and gluons radiate additional partons through QCD processes. Multiparton Interactions (MPI) mechanisms are also implemented in PYTHIA models, including 2-to-2 parton-parton interactions within a single collision event, which can be either soft or hard. Subsequently, PYTHIA includes the treatment of Beam Remnants after the primary interactions, where the valence quarks and companion quarks interact. This latest process is followed by Color Reconnection (CR) to rearrange the color connections between partons, forming color-singlet systems (strings). The following stage is hadronization, which occurs through the Lund string model, where colored partons are transformed into color-neutral hadrons. Lastly is the Particle Decay stage, where initially unstable particles decay into lighter ones, including charged particles, contributing to the overall multiplicity. In addition to light-particle production, PYTHIA 8.2 models heavy quark production through several perturbative QCD processes as gluon fusion ($gg \rightarrow Q\bar{Q}$), quark-antiquark annihilation ($q\bar{q} \rightarrow Q\bar{Q}$), and flavor excitation ($Qg \rightarrow Qg$). Additionally, heavy quark pairs can also emerge from parton showers (e.g., $g \rightarrow Q\bar{Q}$) and multiparton interactions. For quarkonium production

specifically, PYTHIA 8.2 implements leading-order perturbative QCD calculations within the Non-Relativistic QCD (NRQCD) framework, in addition to the non-prompt fraction and the Cluster Collapse mechanism during the hadronization stage. PYTHIA has demonstrated success in reproducing many experimental features of J/ψ production. Of particular relevance to this thesis is its ability to describe the hardening of the J/ψ-N_{ch} correlation with increasing J/ψ transverse momentum (p_T), as observed in Fig. 2.6. Causes for the stronger-than-linear increase of the J/ψ yield with the charged particle multiplicity with PYTHIA were investigated in [1] and this discussion is included in the following section of this chapter 2.3.

ALI-PUB-348257
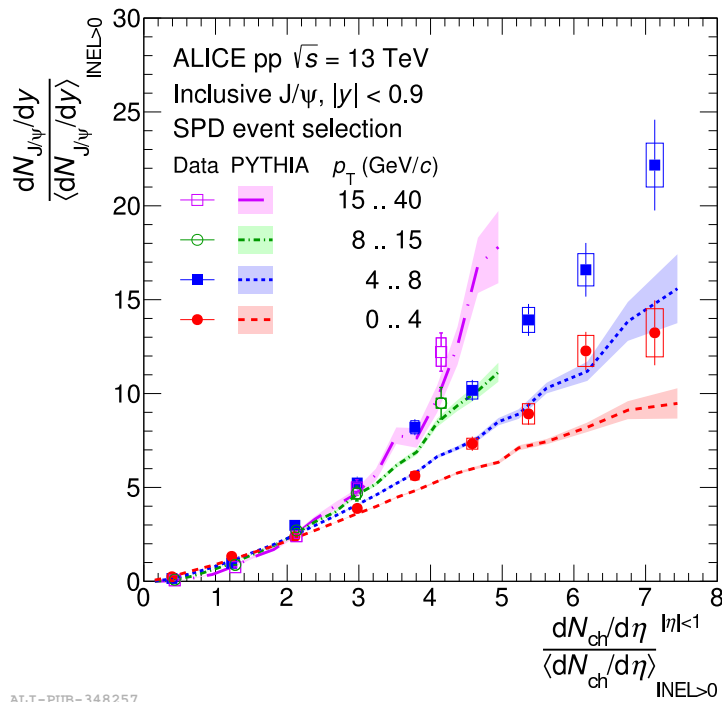
Figure 2.6.: Normalized inclusive J/ψ yield at midrapidity as a function of normalized charged-particle multiplicity at midrapidity for different p_T intervals; the data are compared to theoretical model predictions from PYTHIA 8.2.
Figure taken from [48].

EPOS3 [50]: Event generator is designed to model light particle production in proton-proton and heavy-ion collisions. The production process is independent of the collision system (same considerations for pp, pA, and AA collisions) and is structured into five sequential stages. First, the initial conditions, which are defined within the parton-based Gribov-Regge theory (PBGRT) framework, describe the formation of the objects: Pomerons. These pomerons are treated as parton ladders with a characteristic saturation scale and evolved according to the DGLAP equations. The second stage is the core-corona separation, where the system is divided into a dense core (fluid-like region) and a dilute corona (hadron escape region) based on the momentum and density of string segments. The third stage is the hydrodynamic evolution, which describes how the core undergoes viscous hydrodynamic expansion, governing the system's collective dynamics. The fourth stage is hadronization, which describes hadron formation at the end of the quark-gluon plasma (QGP) phase or during the mixed phase using a statistical approach. Lastly is the hadronic cascade, where the final-state hadronic interactions are modeled

using an Ultra-relativistic Quantum Molecular Dynamics (UrQMD) framework. On the other hand, the heavy quark production was incorporated into the initial stage of EPOS, being created similarly to the light quarks from gluon radiation at the initial or final state or coming from very energetic gluon splitting. The production of heavy quarks also contains cold nuclear matter effects, modeled by a saturation picture. At the same time, the propagation of the heavy flavors through the medium is carried out also employing an UrQMD framework, allowing the heavy quarks to suffer elastic collisions.

Percolation model [51]: Considering coherence effects in high-energy pp collisions, this model introduces color ropes or strings as the fundamental variables and sources of particle production. Within this framework, the number of partonic collisions (N_{coll}) is proportional to the number of produced strings (N_s). However, interactions and overlaps among these strings reduce the effective number of sources available for particle production, thus directly influencing the soft mechanisms of particle production. The framework then works with the rapidity distribution ($dN/d\eta$) of soft particles expressing it as the product of the number of parton-parton collisions (N_s), the multiplicity produced by a single string, and a damping factor that accounts for the interactions of the produced strings. Thus making the $dN/d\eta$ distribution proportional to the number of participants rather then number of collisions. On the other hand, the model assumes that the number of initially produced hard probes, such as J/ψ mesons ($N_{J/\psi}$), remains proportional to the number of collisions (N_s). Therefore, the correlation between soft and hard components at low multiplicities where the number of strings is small, is predicted to be linear and to subsequently transition to an almost quadratic dependence at high multiplicities. Furthermore, interestingly, the model predicts that the number of strings $\langle N_s \rangle$ is significantly larger at midrapidity, approximately double, compared to forward rapidity. This rapidity gap in the correlation is explained by long strings contributing simultaneously to both the central and forward regions, whereas, short strings are mostly created and solely contribute to the central region, thus enhancing the contribution in this region. In summary, this model attributes the behavior of the J/ψ-N_{ch} correlation primarily to final-state interactions. It operates under the assumption of coherent effects in high-multiplicity pp collisions to formulate color strings that predominantly impact the soft mechanisms governing charged-particle production in collisions where J/ψ mesons are produced.

3-Pomeron CGC [52]: Proposes the production of J/ψ primarily via a multi-gluon fusion mechanism, specifically through 3-gluon fusion, rather than the conventional gluon-gluon fusion accompanied by soft gluon emission. The model states that the 3-pomeron contribution, unlike in previous approaches, should not be neglected and thus should not be suppressed when estimating the heavy quark pairs production cross-section perturbatively. This assumption is based on the charm quark mass suppression when gluon densities increase in the small-x kinematic region. Consequently, the contribution from the 3-pomeron mechanism becomes comparable to that from the 2-pomeron mechanism. In this framework, pomerons are treated as either gluon fields or gluon ladders, where a gluon ladder represents multiple exchanged gluons between interacting entities. According to the model, J/ψ production at a given rapidity y originates from

the same number of ladders as those responsible for soft hadron production. The multiplicity dependence in events containing J/ψ is expected to be enhanced due to the increased number of particles produced per pomeron cascade, with each pomeron satisfying the nonlinear Balitsky-Kovchegov (BK) equation. This enhanced multiplicity modifies the dipole amplitude, whose phenomenological description within the model depends explicitly on the saturation scale Q_s^2. The model provides rapidity-dependent predictions for the J/ψ-N_{ch} correlation, considering two scenarios: first when J/ψ and N_{ch} are measured in the same rapidity interval (overlapping case), and second, when they are measured in separate rapidity intervals (non-overlapping case). In the non-overlapping case, the model predicts a weaker stronger-than-linear increase of the normalized J/ψ yield with the charged particle multiplicity, N_{ch}, due to the ability to distinguish between different possible production configurations (1-pomeron or 2-pomeron ladders) contributing to N_{ch}. Conversely, in the overlapping case, where J/ψ and N_{ch} are measured within the same rapidity range, it becomes impossible to differentiate the contributions of individual configurations. To resolve this ambiguity, the model sums the contributions of all possible configurations to N_{ch}, leading to an enhanced J/ψ-N_{ch} correlation dependency. While this model successfully reproduces experimental observations of the J/ψ-N_{ch} correlation in rapidity ranges and for p_T integrated J/ψ yield, it fails to accurately predict the hardening of the correlation when increasing the p_T of the J/ψ yield.

CGC with ICEM [53]: Includes saturation effects by combining the CGC effective field theory when estimating the heavy quarks pair production cross section with the ICEM to describe the heavy quark pair hadronization. The primary consideration is that the production of heavy quarks is affected by groups of gluons in the colliding hadrons that are strongly correlated, causing the dynamics between hard and soft mechanisms to be energy and centrality of the collision dependent. High multiplicities collision configurations under this CGC framework are implemented by increasing the value of the saturation scale in multiplies of $Q_0^2 = 0.168$ GeV^2, taking into account an initial saturation scale at $x = 0.001$ which was determined by fits to the Minimum bias $e+p$ deep inelastic scattering (DIS) data. Under this framework, the contributions from the color octet mechanisms ($^3S_1^8$) to the J/ψ hadronization are higher, suggesting the importance of hard gluon fragmentation in J/ψ hadronization. The framework accomplished interesting results when describing the J/ψ-N_{ch} correlation at midrapidity but utterly fails when describing it at forward rapidity.

Coherent Particle Production [54]: Postulates that the environment generated in high-multiplicity pp collisions resembles that of proton-nucleus and nucleus-nucleus collisions. Consequently, it attributes the observed behavior of the J/ψ-N_{ch} correlation to a combination of shadowing and gluon saturation effects. Shadowing effects, arising from quantum coherence phenomena, suppress gluon radiation and are expected to impact light-quark dipoles more strongly than heavy-quark dipoles. This distinction follows the assumption that hadronic gluons, which carry lower energy than those in the quark-gluon plasma (QGP), are less effective at breaking heavy-quark dipoles than light-quark dipoles. A key aspect of this model is incorporating a parametrization method, with the parameter β fitted to experimental data,

to estimate the normalized multiplicities of light hadrons (charged particles) and J/ψ yields. In addition to shadowing, gluon saturation further enhances the J/ψ production rate, leading to a steeper-than-linear increase in J/ψ yield as a function of normalized multiplicity. This enhancement results from a mutual amplification of gluon densities and saturation scales in the colliding protons, similar to effects observed in nucleus-nucleus collisions. Thus, the gluon saturation effects are included as a correction factor in the parametrized calculation of J/ψ production rates. The model successfully reproduces the experimentally observed steeper stronger-than-linear increase of the J/ψ-N_{ch} correlation when increasing p_T by incorporating the value of mean p_T from experimental measurements into their calculations. Regarding the rapidity dependence of the J/ψ-N_{ch} correlation, where a stronger-than-linear increase is observed at midrapidity compared to forward rapidity, this model attributes the effect to the parametrization rather than a fundamental physical mechanism. Specifically, the rapidity-dependent difference arises because the fitted β value for J/ψ yields is just slightly higher than that for light hadrons, leading to an almost linear increase of the correlation at forward rapidity.

Summarizing: The Percolation Model, considering predominantly final state effects to predict the behavior of the J/ψ-N_{ch} correlation, poses the formation of color strings, driven by coherent effects, as the cause enhancing soft processes responsible for charged-particle production. Models like the CPP, the 3-Pomeron CGC, and the CGC+ICEM consider initial state effects such as Color Glass Condensate and parton saturation in the colliding protons primarily responsible for the experimental observations. Meanwhile, EPOS3 and PYTHIA 8.2 offer a combination of initial and final state effects to be responsible for the observed J/ψ-N_{ch} correlation. A common denominator in all these models is the inclusion of multiparton interactions (MPI) to reproduce the experimental observations. However, except for PYTHIA, all the predictions given by the models do not account for the J/ψs non-prompt fraction (J/ψs from B-meson decays).

2.2.3. ALICE measurements of Quarkonia yields as a function of N_{ch}

The ALICE experiment with the $\sqrt{s}$ = 13 TeV pp collision data extended its studies of quarkonium production as a function of the charged-particle multiplicity beyond J/ψ mesons. Measurements of the $\psi(2S)$ excited state of charmonium, [55], as well as the ground ($\Upsilon(1S)$) and excited states ($\Upsilon(2S)$, $\Upsilon(3S)$) of bottomonium, [56], could also provide deep insight into the interplay between hard and soft processes in pp collisions. Studies of quarkonia excited states in high charged-particle multiplicity environments are particularly relevant, as they possess lower binding energies than their ground states. Consequently, they are more susceptible to dissociation mechanisms arising from the formation of a hot and dense medium (QGP) or from final-state interactions. Furthermore, as previous experimental analyses observed a stronger suppression of excited charmonium and bottomonium states compared to their respective ground states (J/ψ and $\Upsilon(1S)$), these latest ALICE studies, [55] and [56], have also looked into the ratios of excited-to-ground quarkonium states as a function of the charged-particle multiplicity. This suppression of the excited quarkonium states cannot be explained solely by initial-state effects, indicating that final-state interactions could influence quarkonium survival probabilities in high-multiplicity pp collisions.

Measurements of $\psi(2S)$ as a function of the charged-particle multiplicity are presented in the left panel of Fig. 2.7. The figure also includes a comparison with theoretical predictions from the PYTHIA 8.2 event generator, both with and without the color reconnection (CR) mechanism, showing the PYTHIA description independent of this (CR) mechanism to describe the $\psi(2S)$-N_{ch} correlation. Similarly, Fig. 2.8 presents the measured yields of bottomonium mesons as a function of charged-particle multiplicity in the left panel. Meanwhile, the right panel compares these measurements with available theoretical models.
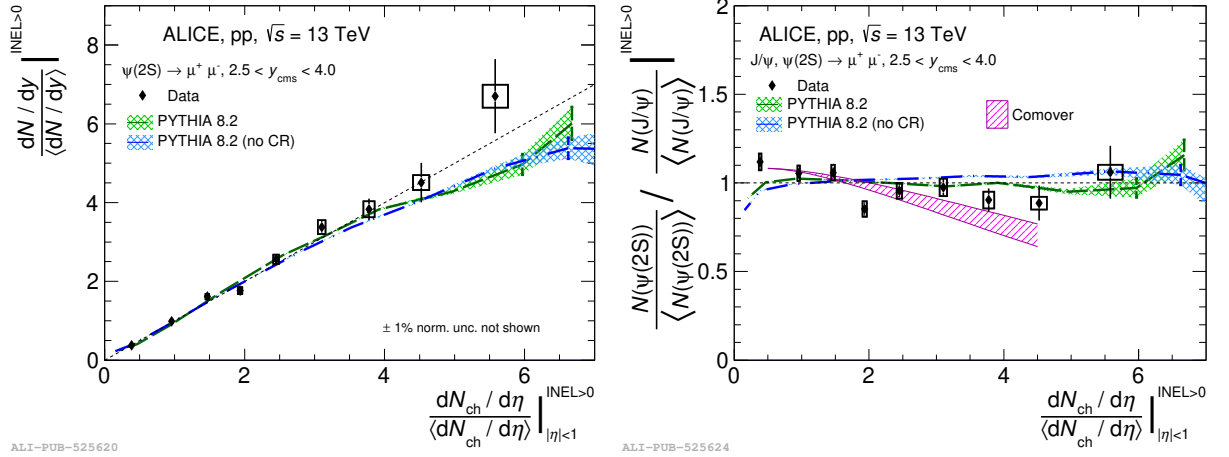
Figure 2.7.: The self-normalized $\psi(2S)$ yield (**Left**) and the ratio of normalized $\psi(2S)$-over-J/ψ yields (**Right**) as a function of the self-normalized charged-particle multiplicity. Measurements are compared to predictions by comovers and PYTHIA 8.2 with and without color reconnection (no CR). Figures taken from [55].
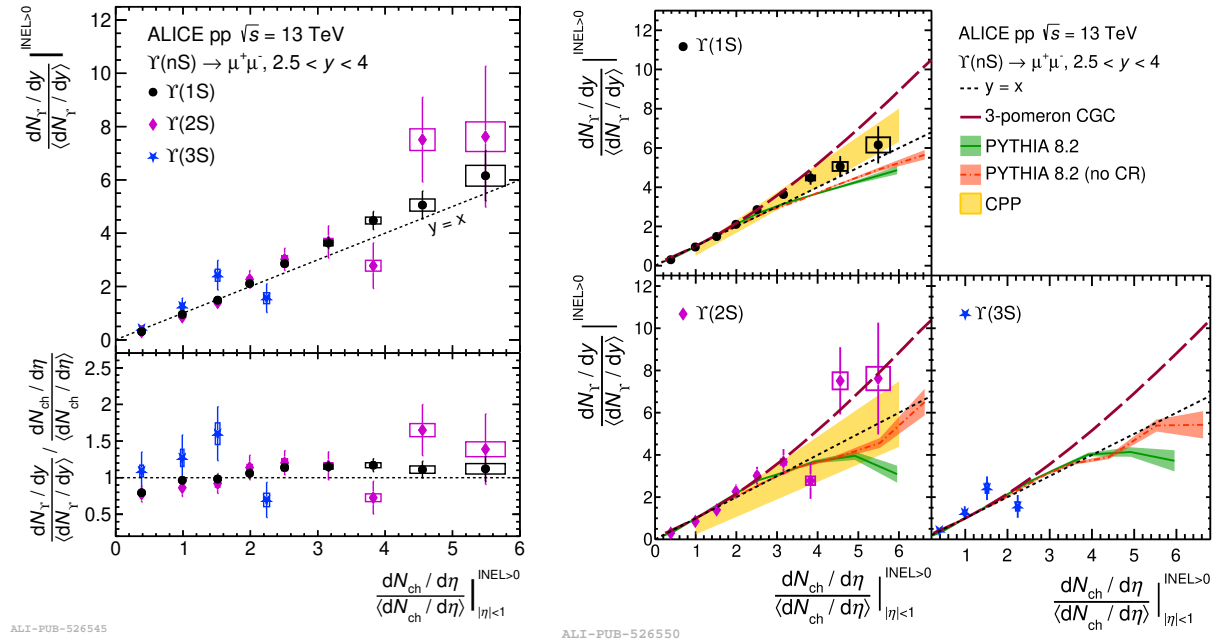
Figure 2.8.: Left: Self-normalized yield of $\Upsilon(nS)$ states as a function of normalized charged-particle multiplicity for $p_T > 0$. **Right:** Self-normalized yield of $\Upsilon(1S)$ states as a function of normalized charged-particle multiplicity for $p_T > 0$, compared to 3-pomeron CGC, PYTHIA 8.2 and CPP models. Figures taken from [56].

The data points of the $\psi(2S)$-N_{ch} and $\Upsilon(nS)$-N_{ch} correlations correspond to quarkonium mesons measured at forward rapidity via their dimuon decay channel, whereas the charged-particle multiplicity is detected at midrapidity. These correlations follow an approximately slope-close-to-unity linear behavior, consistent with the trend observed in the J/ψ-N_{ch} correlation when J/ψ mesons are also detected at forward rapidity. Similarly, when comparing with theoretical models, it is evident that PYTHIA underestimates the experimental data at high multiplicities for all the discussed correlations except for the $\Upsilon(3S)$ case where, due to statistical uncertainties, it is difficult to make predictions. In contrast, the CPP model provides a better description of the $\Upsilon(1S)$ and $\Upsilon(2S)$ data points, while the 3-Pomeron CGC model overestimates the $\Upsilon(1S)$ results at the same time that offers a more accurate description of $\Upsilon(2S)$. However, as the measurements of the excited bottomonium state, $\Upsilon(2S)$ and $\Upsilon(3S)$ are affected by statistical uncertainties, drawing definitive conclusions is challenging.

Additionally, to assess possible differences in their production mechanisms, the ratios of the normalized yields of excited-to-ground states are evaluated as a function of charged-particle multiplicity. The $\psi(2S)$ to J/ψ ratio is shown in the right panel of Fig. 2.7. This ratio remains consistent with unity across the explored multiplicity range within uncertainties, exhibiting a similar multiplicity dependence of these two charmonium states. The figure also compares the ratio with the theoretical predictions from PYTHIA 8.2 and the final-state-effects driven Comover model [57], [58]. Meanwhile, the $\Upsilon(2S)$ and $\Upsilon(3S)$ to $\Upsilon(1S)$) ratios are shown in Fig. 2.9. These ratios are also compatible with unity within the large statistical uncertainties, results that agree with PYTHIA 8.2, CPP, and 3-Pomeron CGC predictions.

ALI-PUB-526555   ALI-PUB-526560
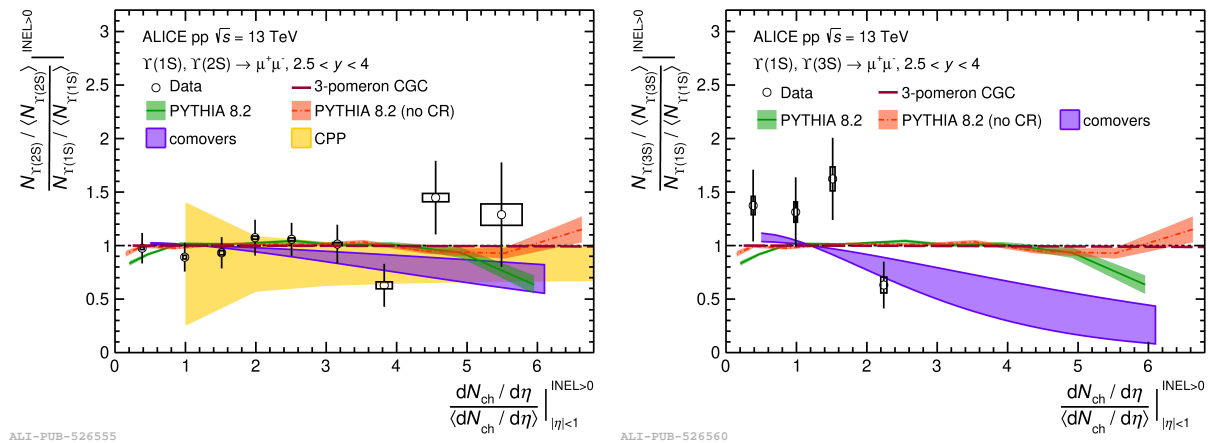
Figure 2.9.: Left: Excited-to-ground state self-normalized yield ratio ($\Upsilon(2S)$ over $\Upsilon(1S)$) as a function of the self-normalized charged-particle multiplicity, compared to model predictions from 3-pomeron CGC, PYTHIA 8.2, comovers, and CPP. **Right:** Excited-to-ground state self-normalized yield ratio ($\Upsilon(3S)$ over $\Upsilon(1S)$) as a function of self-normalized multiplicity, compared to PYTHIA 8.2 and comovers predictions. Figures taken from [56]

Motivated by the assumption that if quarkonium mesons (charmonium and bottomonium) follow the same behavior as the standard hard processes, then their multiplicity dependence should exhibit similar trends, the ALICE experiment with the $\sqrt{s} = 13$ TeV pp collisions data also measured open heavy-flavor production via the dielectron decay channel as a function of the charged particle multiplicity at midrapidity. The measurements reported initially in [59], and in

Fig. 2.10, show the same stronger than the linear increase observed for J/ψ at midrapidity and subsequently the hardening of this behavior when increasing the p_T of the electrons.

This study also concluded that the slope of the self-normalized yield of electrons from heavy-flavor hadronic decays as a function of self-normalized multiplicity at midrapidity matches that observed for J/ψ, charged particles, strange mesons, and D mesons within similar p_T ranges. This suggests that at high and intermediate p_T, hadron production is dominated by hard particle scattering processes, regardless of particle species, and is accompanied by jet activity in the event. Therefore, observing that the multiplicity dependence of detected charm and beauty mesons is similar to that of open charm and beauty hadrons confirms a common underlying mechanism governing their production and the independence of this mechanism from the hadronization process.

ALI–PUB–538980
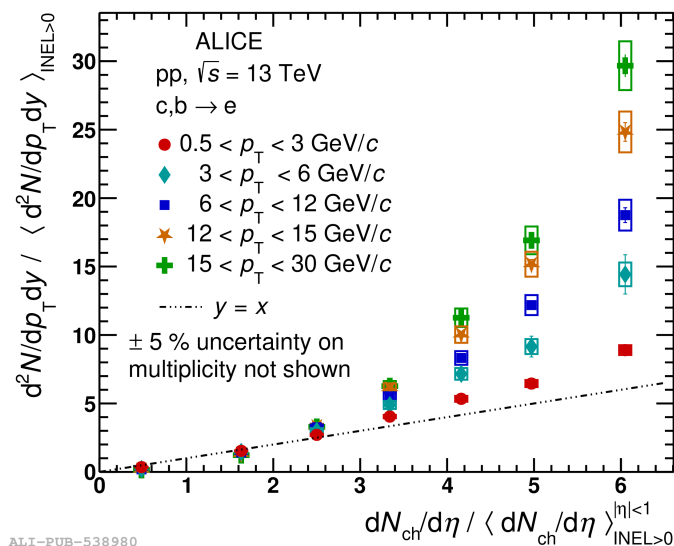
Figure 2.10.: Self-normalised yield of electrons from heavy-flavour hadron decays as a function of normalised charged-particle pseudorapidity density at midrapidity computed in pp collisions at $\sqrt{s} = 13$ TeV in different p_T intervals.
Figure taken from [59].

2.3. J/ψ **production as a function of the N$_{ch}$ in** J/ψ **azimuthal regions**

The previous section discussed the stronger-than-linear increase of the J/ψ yields with the charged-particle multiplicity observed in high multiplicity pp collisions, showing that when J/ψs are produced, the multiplicity could reach values up to seven times the mean multiplicity observed commonly in pp collisions (Minimum Bias collisions specifically). Furthermore, from the previous section, was also seen, the stronger-than-linear increase of the J/ψ-N$_{ch}$ correlation when both the J/ψ yields and the charged particle multiplicity are measured in the same rapidity interval in contrast to its observed linear increase when measured in different rapidity intervals. Several of the theoretical models based on initial state effects, final state effects, or a combination of both, discussed in the previous section, offer different possible explanations to predict the

experimentally observed behavior of the J/ψ-N$_{\text{ch}}$ correlation. This section is devoted to the studies conducted in PYTHIA searching for the causes of this behavior. These studies with PYTHIA led to the proposal of the azimuthal analysis in relation to the emitted J/ψ that the experimental data of this thesis aim to reproduce.

Using PYTHIA8 Monasch 2013 tune [25] was intended by [1] to investigate the possible causes of the observed stronger-than-linear increase of the J/ψ yield with the charged particle multiplicity when measured in the same rapidity interval and its dependence on p_{T}. The study simulating pp collisions at $\sqrt{s} = 13$ TeV analyzed the J/ψ-N$_{\text{ch}}$ correlation with and without Multiparton Interactions (MPI) and color reconnection (CR). Simulating with PYTHIA allows the decomposition of the J/ψ yields by production mechanisms (non-relativistic Quantum Chromodynamics (NRQCD), non-prompt (J/ψs from B-hadron decays), and Cluster Collapse), which facilitates the investigation of the J/ψ yield given by each mechanism as a function of the charged particle multiplicity and the number of MPIs. The study reported, when analyzing the J/ψ-N$_{\text{ch}}$ correlation by production mechanism, a linear increase for NRQCD-produced J/ψ, whereas both non-prompt and Cluster Collapse contributions exhibited a stronger-than-linear increase. Furthermore, as it is interesting to see which mechanism is predominant as a function of the J/ψ transverse momentum, since the slope of the correlation is p_{T} dependent, the study also analyzed J/ψ yields by production mechanisms as a function of p_{T} (ranging from 0 to 16 GeV/c) revealing that low-p_{T} J/ψ mesons predominantly originate from NRQCD processes, while at higher p_{T}, the non-prompt fraction becomes increasingly significant. In contrast, the Cluster Collapse mechanism contributes a constant fraction across the p_{T} range. The role of CR as a possible final state effect influencing the J/ψ-N$_{\text{ch}}$ correlation was examined by comparing correlations with and without this mechanism. While CR had no significant effect on the NRQCD and non-prompt J/ψ yields as a function of charged particle multiplicity, it introduced a quadratic dependency for the Cluster Collapse mechanism. Further, disabling MPI resulted in an almost linear NRQCD-produced J/ψ yield at low multiplicities, transitioning into a weaker-than-linear increase at higher multiplicities, highlighting the essential role of MPI in PYTHIA when describing the experimental J/ψ-N$_{\text{ch}}$ correlation. Conversely, the non-prompt fraction showed a stronger-than-linear increase with charged particle multiplicity when MPI was disabled, and a similar, though less pronounced, trend was observed for Cluster Collapse production.

The study suggested several autocorrelation effects associated with the different J/ψ production mechanisms in PYTHIA to further interpret the above-mentioned observations:

- Multiplicity bias from decay products: The inclusion of J/ψ decay daughters in the N$_{\text{ch}}$ count.

- NRQCD contribution: J/ψ mesons from the color-octet mechanism are typically produced with the emission of soft gluons, which will subsequently hadronize increasing the charged particle multiplicity.

- Cluster Collapse mechanism: As this process involves the coalescence of a quark and antiquark that were not necessarily produced together, additional c and $\bar{c}$ undergo hadronization, contributing to the charged particle multiplicity.

- Non-prompt production: The recoil *B*-meson and the associated particles from the decayed B-meson, besides the *J/ψ* itself, could contribute to the charged particle multiplicity.

In order to test these autocorrelation effects, the study subsequently proposed investigating the *J/ψ*-N$_{ch}$ correlation across different regions of the emitted *J/ψ*s azimuthal angle φ. The azimuthal collision plane was divided into three regions, see Fig. 2.11: Toward, Transverse, and Away, where the expected behaviors within PYTHIA8 are as follows:

- Toward region of the emitted *J/ψ*s: A steep stronger-than-linear increase of the *J/ψ*-N$_{ch}$ correlation which becomes steeper at higher p_{T}. In this region it is expected the steeper increase of the *J/ψ* yield with the charged particle multiplcity since mainly three of the above-mentioned autocorrelation effects are expected to enhance the charged particle multiplicity. First an increase in multiplicity from the non prompt *J/ψ* fraction due to the associated particles from the decayed B-meson. Aditionally, the NRQCD contribution is also relevant, as the emitted soft gluons are likely to have a small opening angle relative to the produced *J/ψ*, and finally the *J/ψ* decay daughters directly contributing to the charged-particle multiplicity.

- Transverse region of the emitted *J/ψ*s: A correlation slope close to unity, with no significant p_{T} dependence, as the autocorrelation effects are not expected to play a role in this region.

- Away region of the emitted *J/ψ*s: A stronger-than-linear correlation, though milder than in the toward region primarily driven by the non-prompt *J/ψ* fraction. This behavior arises as the recoil *B*-meson is typically emitted in the direction opposite to the *J/ψ* parent *B*-meson, contributing with additional particles to this region.
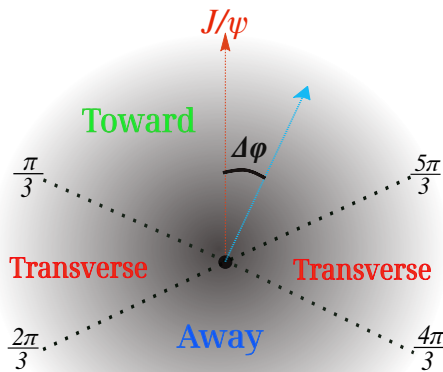
Figure 2.11.: Schematic view in the azimuthal collison plane of the three defined regions with respect to the emitted *J/ψ* direction.

Determining the charged-particle multiplicity in different azimuthal regions relative to the emitted *J/ψ*, or more generally quarkonium, enables a detailed tomography of the distribution of charged particles in collisions producing quarkonium or in different words, this analysis could provide insights into the spatial characteristics of particle production associated with quarkonium formation.

The [1] study also investigates the separation of prompt and non-prompt J/ψ production in their respective dependencies on the charged particle multiplicity. The expectation is that the above-suggested autocorrelation effects will become stronger when assessing the non-prompt fraction. As PYTHIA allows for the decomposition of non-prompt J/ψ yields by production mechanism, the study also correlates these contributions with the charged particle multiplicity in the regions finding that the transverse region is not affected by autocorrelation effects when the J/ψ yield and the charged particle multiplicity are measured in the same rapidity interval. The study declared all the findings aplicable not only to J/ψ mesons but also bottomonium mesons.

Therefore, the CMS collaboration reported the first experimental measurements of this type of analysis using pp collisions at $\sqrt{s} = 7$ TeV [60]. The analysis, measuring both observables at forward rapidity, correlated $\Upsilon(nS)$ production with the charged-particle multiplicity in regions of the $\Upsilon(nS)$ azimuthal angle. The results, while including the two decay muons in the toward region, counted fewer tracks in the transverse region than in the toward and away regions giving a first hint of the predictions made by [1] and discussed along this section .

This thesis aims to reconstruct the charged-particle multiplicity in three azimuthal regions relative to the emitted J/ψ mesons and to correlate this observable with the J/ψ yields using pp collision data at $\sqrt{s} = 13$ TeV from Run 2 of the ALICE experiment. The ultimate objective is to determine whether autocorrelation effects associated with the J/ψ production mechanism or contributions from soft particle production account for the observed steeper stronger-than-linear increase when correlating the J/ψ yield with charged-particle multiplicity at midrapidity.

3. ALICE Experiment

This chapter describes the experimental setup for collecting the data that produced the results of this thesis. Three sections divide this chapter; the first part gives information about The Large Hadron Collider (LHC) as the giant experiment containing ALICE, while the second describes ALICE's detectors, focusing on those used to achieve the upcoming results in Chapter 6. Subsequently, the third section centers on ALICE's analysis framework, the machinery responsible for reconstructing the collisions, mainly explaining the primary vertex reconstruction, the tracking, and the particle identification techniques.

3.1. ALICE's home: The Large Hadron Collider (LHC)

CERN (Conseil Européen pour la Recherche Nucléaire), located in Geneve and also known as the European Organization for Nuclear Research, is the host of the LHC that aims to reveal and study particle physics by analyzing the collision products of protons and heavy ions. At the CERN's accelerator complex, proton beams firstly enter the linear accelerator Linac 2 and then into three other accelerators: the Proton Synchroton Booster (PSB), the Proton Synchroton (PS), and the Super Proton Synchroton (SPS). Once the proton beams have reached the energy of 450 GeV, they are finally injected into the LHC. On the other hand, heavy ion beams are first accelerated with the linear accelerator Linac 3, then with the Low Energy Ion Ring (LEIR) before entering the PS and the SPS accelerator. With this mechanism for injecting the beams, it is possible to collide protons with protons (p-p), heavy ions with heavy ions (Pb–Pb), and also protons with heavy ions (p–Pb), see Fig. 3.1.

LHC is under its third running period (Run 3), which started in July 2022 and is expected to end in 2025. During this period, LHC will collide protons at a maximum energy of $\sqrt{s}$=13.6 TeV and plans to deliver an integrated luminosity of $\sim$400 fb^{-1}, increasing the amount of data in almost the double. Other running periods preceded the current one: Run 1 and Run 2, lasting from 2009 to 2013 and from 2015 to 2018, respectively. During Run 1, the collisions reached center-of-mass energies of $\sqrt{s}$=8 TeV for pp, $\sqrt{s_{NN}}$=5.02 TeV for p–Pb and $\sqrt{s_{NN}}$=2.76 TeV for Pb–Pb, while Run 2 saw an increase in the center-of-mass energies, reaching $\sqrt{s}$=13 TeV, $\sqrt{s_{NN}}$=8.16 TeV, $\sqrt{s_{NN}}$=5.02 TeV and $\sqrt{s_{NN}}$=5.44 TeV for pp, p–Pb, Pb–Pb, and Xe–Xe, respectively.

There are four interaction points where the two injected beams collide in the LHC, and precisely at those points are located the four major LHC experiments, as depicted in Fig. 3.1: ATLAS (A Toroidal LHC Apparatus), CMS (Compact Muon Solenoid), LHCb (The Large Hadron Collider beauty), and ALICE (A Large Ion Collider Experiment). Information about ATLAS, CMS,

and LHCb detectors can be found in [61], [62], [63], respectively. The next sections will briefly describe the Run 2 ALICE experiment.
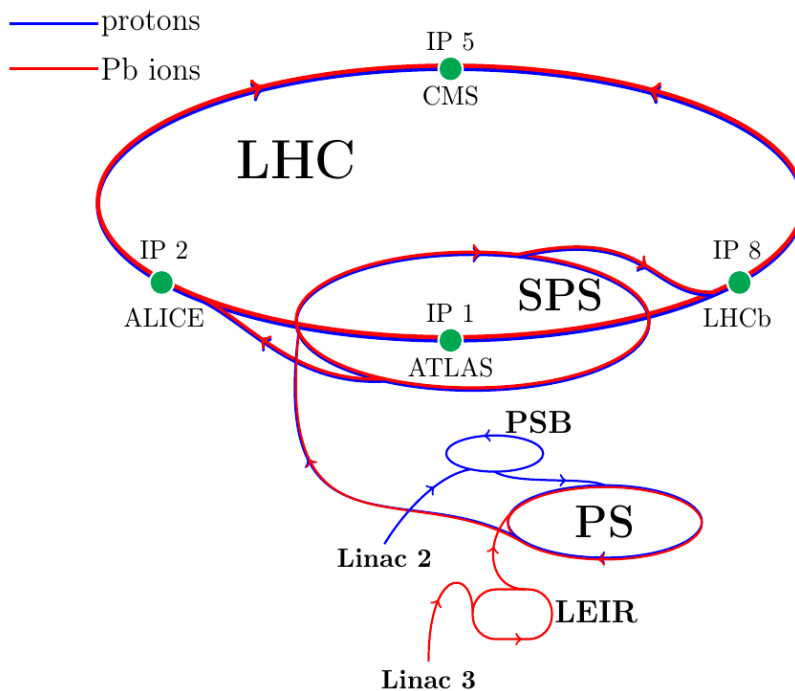
Figure 3.1.: Figure adapted from [64]. LHC injection chain: acceleration of protons (blue) and Pb ions in different stages of the accelerator complex before entering the LHC ring.

3.2. ALICE's detectors

The physical motivation for ALICE in LHC is to study the QCD phase diagram's structure, the QGP phase's properties, and its evolution towards hadronization in a dense nuclear environment. Heavy ion collisions are a perfect scenario for these studies, so the prime concern of ALICE is to accomplish excellent tracking in high multiplicity density mediums, which leads to highly granular detectors with high performance at low luminosity values, especially when compared with the three other main LHC experiments. ALICE has excellent measuring and identifying capabilities, going from very low-p_T (~ 0.1 GeV) to high-p_T for all detected particle types: electrons, muons, photons, and hadrons. Combining a low magnetic field (~ 0.5 T) with its thin detectors, ALICE identifies particles towards the low-p_T region, making the experiment complementary to CMS and ATLAS for pp collisions physics analyses. At large momenta (high-p_T), a good resolution is achieved by measuring a long track length that compensates for the low magnetic field. Fig. 3.2 shows a sketch of the ALICE experiment during Run 2.

A red solenoid L3 magnet, providing a uniform magnetic field, is covering ALICE's central barrel, and on top lies an array of scintillators (ACORDE) that triggers cosmic rays. Inside the L3 magnet, at midrapidity acceptance and covering full azimuth angle, four detectors are found: the Inner Tracking System (ITS), used for finding and reconstruction of the primary and secondary vertices; the Time Projection Chamber (TPC), essential for tracking and

THE ALICE DETECTOR

a. ITS SPD (Pixel)
b. ITS SDD (Drift)
c. ITS SSD (Strip)
d. V0 and T0
e. FMD

1. ITS
2. FMD, T0, V0
3. TPC
4. TRD
5. TOF
6. HMPID
7. EMCal
8. DCal
9. PHOS, CPV
10. L3 Magnet
11. Absorber
12. Muon Tracker
13. Muon Wall
14. Muon Trigger
15. Dipole Magnet
16. PMD
17. AD
18. ZDC
19. ACORDE
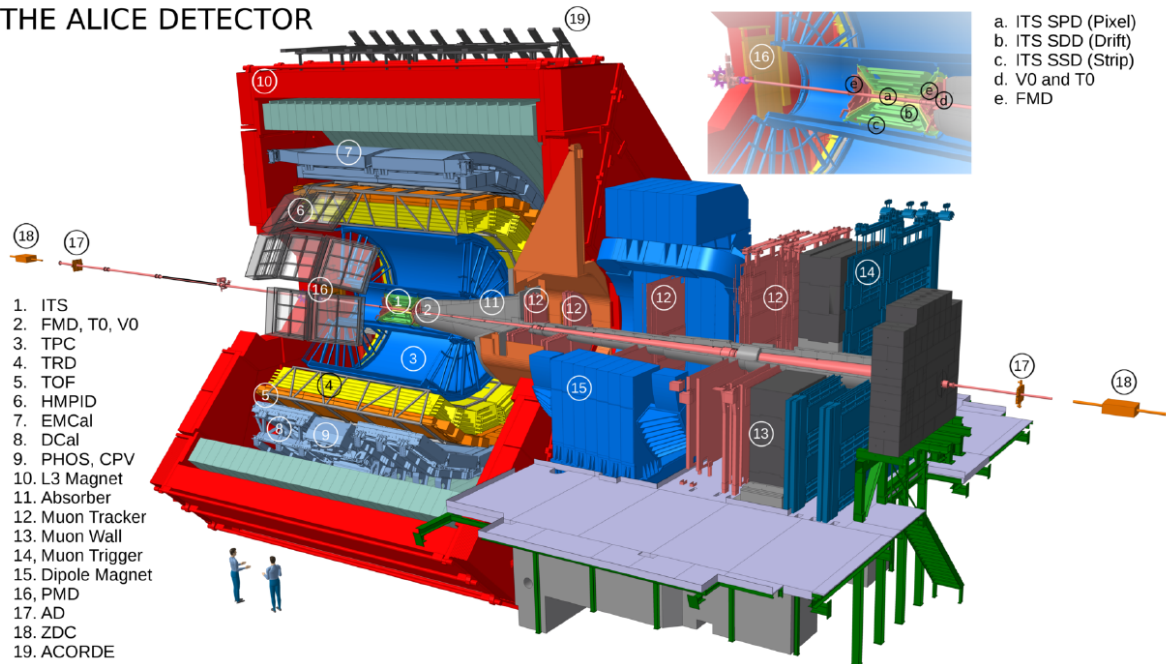
Figure 3.2.: Sketch of ALICE experiment during Run2.

particle identification, the Transition Radiation Detector (TRD), and the Time of Flight (TOF) detector. These last two provide particle identification complementing the TPC information for medium to high-p_T tracks. The High Momentum Particle Identification Detector (HMPID), the Photon Spectrometer (PHOS), and the electromagnetic calorimeters: EmCal (ElectroMagnetic Calorimeter), DCal (Di-Jet Calorimeter) are also in the central barrel, but identifying particles at limited pseudorapidity and azimuth coverage. The Photon Multiplicity Detector (PMD), the Forward Multiplicity Detector (FMD), the V0, the T0, and the Zero-Degree Calorimeter (ZDC) for triggering, event characterization, and multiplicity studies are located at both sides of the beam interaction point and cover a forward pseudorapidity acceptance. Also, in the forward direction, at one side, is the muon arm consisting of a thick hadron absorber (Absorber) followed by five tracking stations (Muon Tracker) and by the trigger chambers (Muon Trigger) that identify muons measuring their time-of-flight. Next is a brief description of the three main detectors involved in this thesis's analysis: ITS, TPC, and V0, as they were during Run 2.

3.2.1. Inner Tracking System (ITS)

The Inner Tracking System is a six-layer detector surrounding the beam pipe with an inner radius of 4 cm, which is the minimum allowed by the 3 cm radius of the beam pipe. It is essential for almost all physics analyses with ALICE, and among its functions are localizing the primary vertex (with a resolution better than 100 μm), the reconstruction of secondary vertices, tracking, and particle identification at very low transverse momenta ($p_T < 0.1$ GeV) [65].

The two innermost layers are covered by Silicon Pixel Detectors (SPD), which are a perfect fit due to the high particle density hitting these layers ($\sim$50 cm^{-2}) and the aim of achieving excellent primary and secondary vertices reconstruction. A basic SPD module of the ITS consists of a

two-dimensional array of reverse-biased silicon detector diodes strongly connected to readout chips. Each readout chip contains the electronics, such as pre-amplifiers and discriminators, that process the induced signal into binary data packages [65]. Since the readout is binary, no particle identification is possible with these layers.

Silicon Drift Detectors (SDD) are in the two middle layers of the ITS, where the charged particle density reaches the 7 cm^{-2} approximately. Its modules have a drift sensor of 300 μm thickness and a total sensitive area of 70.17 x 75.26 mm^2 divided into two drift regions by a central cathode along the bending direction. Three rows of 33 point-like Metal-Oxide Semiconductor (MOS) charge injectors monitor the drift velocity in each region. Contrarily to the SPD layers, the readout of these layers is analog, which allows them to contribute to two of the four energy loss (dE/dx) samples used for particle identification with the ITS [65], [66]. Furthermore, the SSD also provides high energy resolution in short processing times, allowing an outstanding multitrack capability.

The two outermost layers of the ITS consist of Silicon micro-Strip Detectors (SSD) mounted on carbon-fiber support structures. The SSD sensors, with an active area of 73 x 40 mm^2, provide particle identification information (via dE/dx) at low transverse momenta and are double-sided detectors allowing to match the tracks from the TPC to the ITS during the tracking reconstruction algorithms [65], [66].

3.2.2. Time Projection Chamber (TPC)

The TPC is an essential detector of the ALICE's central barrel due to its excellent capabilities for particle identification, tracking, and charged-particle momentum measurements with two-track separation. The necessity for good performance in high multiplicities environments resulting from Pb–Pb central collisions was considered while designing ALICE TPC. The resulting multiplicity was thought to be around 8000 per unit of rapidity, which results in 20,000 charged primary and secondary tracks, leading to maximum occupancies in the inner and outermost radius of 40% and 15%, respectively. These conditions supposed multiple software challenges for accomplishing tracking efficiencies larger than 90%. For pp collisions, where the average multiplicity is 10^3 lower than in Pb–Pb central collisions, the TPC memory's time is the limiting factor for the luminosity due to its ~90 μs drift time [65], [66].

With a cylindrical shape, the ALICE TPC has an inner radius of 85 cm and an outer radius of 500 cm, a length in beam direction of 510 cm, and 88 m^3 of active volume filled with a gas mixture of Ar-CO$_2$ (90%/10%). A central high-voltage electrode divides the active volume into two drift regions, ensuring a uniform electrostatic field along the beam direction. The end-caps of the drift regions are divided into 18 sectors, each containing an inner and an outer multi-wire proportional readout chamber. Inactive areas between neighboring inner and outer chambers are aligned, optimizing the momentum precision for high-p_{T} tracks but creating dead zones or cracks in the acceptance. Excluding these dead zones (the detector is non-sensitive in about 10% of the total azimuthal angle), the TPC has full azimuth coverage and a pseudorapidity acceptance of $|\eta| < 0.9$ for full radial tracks (matches in ITS, TRD, and TOF detectors). Distributed between 36 inner and 36 outer readout chambers are about $560{\times}10^3$ readout pads collecting the charge

that will input the TPC front-end electronics where the signals are transformed into differential semi-Gaussian voltage signals and continuously digitized and processed [65], [66].

3.2.3. V0

The V0 detector is useful for triggering the collected data using its excellent temporal resolution and its track multiplicity measurements. In particular, when having pp beams, triggering with V0 allows to select events coming from actual pp collisions and to veto interactions of the beam with the residual gas in the beam pipe since the particles' arrival time to the scintillators is different in pp collisions than in beam–gas interactions. V0 detector is the name for the two arrays of scintillator counters, V0A and V0C, positioned at either side of the ALICE beam interaction point. On one side, at a 340 cm distance, is V0A, while on the opposite side, placed at 90 cm and fixed to the front of the Absorber, is V0C. Covering a pseudorapidity range of $2.8 > \eta > 5.1$, V0A is inside a box that occupies a volume of 100 cm in diameter, 6 cm in thickness, and has a central hole with a diameter of 8 cm. V0C, on the other side, covering a pseudorapidity range of $-3.7 < \eta < -1.7$, has 76 cm in diameter, 4.7 cm in thickness, and a central hole of 8.4 cm in diameter [66], [67]. Each array of scintillators, V0A and V0C, consists of 32 counters distributed in four rings, covering between 0.5 and 0.6 units in pseudorapidity, and split into eight sectors (45°) in azimuth. For this thesis's analysis, the V0 detector provides the collision triggers Minimum Bias and High Multiplicity.

Minimum Bias Trigger (MB): During Run 2, this trigger is defined as the simultaneous detection of a signal in each scintillator array (V0A and V0C) during a collision, which is possible thanks to the excellent temporal resolution ($\sim$ 1 ns) and high acceptance for detecting charged particles of the V0 scintillators.

High Multiplicity Trigger (HM): Event charged-particle multiplicity selections are possible with the V0 detector due to the monotonic dependence of the number of particles recorded in the scintillators and the number of primary particles emitted during a pp collision. Denoting V0M as the sum of V0A and V0C signals, during Run 2, the High-Multiplicity trigger requires a V0M signal exceeding five times the mean value measured in a Minimum Bias collision, representing about 0.1% of all MB events.

3.3. ALICE's analysis framework

The ALICE analysis framework is the set of computer tools and software needed to process the data collected by the detectors (real-raw data) and convert them into physical results. It first contains the ALICE online system that interacts with the detectors during data collection. Secondly, being responsible for the offline processing of the data are the software AliRoot [65] and AliPhysics. Also part of the framework is the ALICE Environment (AliEn) in GRID (Global Research Identifier Data) [68] and the train system Lightweight Environment for Grid Operators

(LEGO) [69] that is coupled to the user-interactive web interface MonALISA (Monitoring Agents in a Large Integrated Services Architecture) [70].

ALICE online system is active during data-taking, connecting the readout coming from the detectors with the data's offline processing stage. The five online systems are the Central Trigger Processor (CTP), the High-Level Trigger (HLT), the Data Acquisition (DAQ), the Detector Control System (DCS) and lastly the Experiment Control System (ECS) [71]. The CTP allows the read-out of each detector based on their busy status while the HLT filters out the non-interested collisions or events. The DAQ handles the data flow from the detector to the storage system of the CERN computing center, while the DCS, having user-interactive software, controls each detector. Finally, the ECS monitors the other four systems, providing a simplified view of the experiment's complexity.

AliRoot and AliPhysics carry out the offline processing stage of the data, reconstructing the collisions and arriving at the physical results, respectively. AliRoot software reconstructs the collisions and estimates the detector's response by coupling Monte Carlo (MC) event generators like HIJING [72], PYTHIA [13] [14], [15], EPOS [17], [18], or DPMJET [73] with detector simulation packages like GEANT3 [74], GEANT4 [75], or FLUKA [76]. In the AliRoot analysis chain, the MC event generators first generate MC data, and to simulate the particles' behavior as they pass through the ALICE detectors, this data is reduced and reconstructed to produce simulated "raw" data. From then on, the part of the analysis chain that includes a full simulation of all detectors is activated, accepting simulated and real-raw data as input. In the next step, reconstruction algorithms analyze each collision or event (independently of whether they are simulated or not) to reconstruct it, along with the trajectory and mass information of all the emitted particles. AliRoot evaluates these procedures and the detector performance by processing the simulated events throughout the cycle and comparing the particles reconstructed from the simulated raw data with the MC-generated particles since their particle identification and momentum information are well known. Deriving in an essential utility of AliRoot while processing real-raw data: to provide the playground to estimate efficiencies and detector effects corrections influencing the yields and reconstruction of the different particles.

The offline AliPhysics software, on the other hand, is mainly in charge of the physical analysis of the collected data. The AliPhysics code is linked to the AliRoot code, and contributions to the main code by the analysts are possible through subgroups called Physics Working Groups (PWG), each corresponding to a specialized type of analysis: photon detection, particle correlations, jet analysis, heavy flavor (...).

Run 1 and Run 2 ALICE's data is organized into two types of data objects: Event Summary Data (ESD) or its subset Analysis Object Data (AOD). The ESD format contains information about all reconstructed collisions: their number of events, triggers, reconstructed vertexes, tracking, plus all detector-specific information, while the AOD format is the results of filtering from ESD all the specific information needed for a particular physics analysis. Using AliRoot and AliPhysics, it is possible to create jobs (analysis tasks) to run over these data formats in AliEn-GRID, which, with a ROOT interface, allows the possibility to run them in parallel. The execution of these jobs is further optimized with another tool: the LEGO train system, which processes the jobs

with higher CPU efficiency using the same data set for multiple jobs. The LEGO framework also allows hiding the GRID complexity from the user since the jobs configuring, submission, and checking are done through the web interface MonALISA.

The results described in this thesis, directly or indirectly, will make use of all the tools mentioned above. Taking the information provided by the online systems as input to AliRoot, each collision or event is fully reconstructed, and with it, three essential features that are at the base of this thesis' analysis: the primary interaction vertex, the tracking, and the particle identification in the central barrel. The following sections will provide a summary describing the techniques used to determine them in ALICE. The code in the PWG-DQ (Dielectron and Quarkonium) in AliPhysics allowed the creation of ROOT trees by running it over ESD sets in the LEGO train system. The further processing of these trees occurred locally, under a PWGDQ's subset of codes: The Reduced Tree Framework.

3.3.1. Primary Vertex and Track Reconstruction

During the event reconstruction in AliRoot, the primary vertex determination and the tracking procedure are interconnected in a loop. The starting point is the estimation of a preliminary primary interaction vertex with only ITS information, followed by the complete track length reconstruction procedure, and ending with a new and final determination of the primary interaction vertex from fully reconstructed tracks (ITS-TPC tracks).

3.3.1.1. Preliminary reconstruction of the primary interaction vertex

Within the ALICE analysis framework, two main algorithms are implemented to reconstruct the primary interaction vertex with the help of the first two layers of the ITS. The first is a three-dimensional algorithm, while the second is a one-dimensional algorithm, mainly used in events or collisions where the first fails because of a low amount of produced particles. Both approximate tracks to lines, ignoring the curvature effect resulting from the uniform magnetic field in the central barrel.

The three-dimensional procedure estimating the preliminary primary interaction vertex consists of three steps repeated twice: a first iteration with looser selection criteria and a second with stricter selection criteria. The starting point in both iterations is the definition of a referential region, followed by the selection of tracks according to their azimuth coordinates while crossing the SPD layers and concluding by pairing these tracks and selecting them minding their Distance of Closest Approach (DCA) and the distance between their intersection point and the center of the referential region. During the first iteration, the referential region is centered around the mean beam position with a radius of 2.5 cm and a width of 40 cm. The tracklets (only SPD information tracks) passing the selection are near the center of the referential region, hitting each SPD layer with azimuth coordinates within a window $\Delta\varphi = 0.5$ rad. After pairing these tracklets, the selected pairs will have a DCA < 1 mm plus an intersection point no more than 8 mm away from the center of the referential region. During the second iteration, the referential region is around the just estimated in the first iteration primary vertex, at 0.5 cm radius and width. The cut based on the azimuth coordinates of the tracklets hitting the SPD is also stricter, requiring

$\Delta\varphi = 0.025$ rad. Extra checks guarantee that the vertex position is inside the beam pipe and that the multiplicity of tracklets pointing to the primary vertex is larger than zero. Lastly, the exact coordinates for a preliminary primary interaction vertex are the result of minimizing the square sum of all the distances between each tracklet and the vertex coordinates, considering possible sources of errors affecting the precise measurement of the tracklets. For detailed information, see [77].

The above-described method highly depends on the amount of particles produced in an event (the event multiplicity). Events with low multiplicity (mostly only one SPD tracklet) require a slightly different procedure to find a preliminary primary interaction vertex. This alternative procedure depends on knowing the beam position in the transverse plane ($< 200~\mu$m) and on the value of the azimuth window (set to $\Delta\varphi = 0.01$ rad by default) between two points in each SPD layer, which will define the candidate tracklets. The computation of the intersection point with the beam axis for each tracklet candidate and the estimation of their mean value inside a referential region gives the first possibility of a primary interaction vertex. Next, several iterations centered around the previously found point will eventually derive a symmetrical region around the mean value of all the candidate tracklets, which will be the preliminary primary interaction vertex [77].

3.3.1.2. Track reconstruction

Track reconstruction in the ALICE experiment is a complicated task that starts in the outermost layers of the TPC. The entire procedure follows an inward-outward-inward scheme, applying the Kalman filter technique in every step. The Kalman filter technique reconstructs an unknown track trajectory by measuring several of its spacial points, considering that all the measured points are equidistant and the possible curvature of the track. The fitting algorithm expresses each track as a parametrized vector state, requiring a well-defined initial set of its kinematical parameters (seeds) and their covariance matrices. The idea is to propagate them to the next spatial point, adding a noise term to account for unwanted processes. If compatible with the track prolongation, the new spatial point is added, updating the track parameters and their covariance matrices. [78].

Within the TPC, the first seeds are the parameters associated with the center of gravity of the space-point positions left by a track in the time and the pad-rows directions (TPC clusters) of the outermost layers of the detector. Since there are 159 tangential pad rows in the TPC, a track could produce a maximum of 159 clusters in its pass throughout the TPC active volume. During the first inward part, the track seeding repeats many times while following two hypotheses: first, considering the track originated in the primary interaction vertex, for which is required information on two TPC clusters constrained by the previously found primary interaction vertex; and second considering the track is the result of decays or secondary interactions for which is only needed information on three TPC clusters. For both hypotheses, the general procedure involves applying the Kalman filter at each step while propagating each seed towards the center of the TPC, adding the nearest cluster that fulfills a proximity cut. The accepted tracks have a minimum of 20 clusters while matching 50% of the predicted clusters. Next, taking the

reconstructed TPC tracks candidates as the starter seeds, the track propagation extends to the outer layer of the ITS (ITS-TPC reconstruction), where the propagation is still inwards its center while considering the two hypotheses introduced above. Each TPC track produces a tree of track hypotheses in the ITS, but only the track candidate with the highest quality, according to a χ^2 criteria, from each tree passes the cut. Furthermore, within the ITS, an additional reconstruction is performed considering only the clusters that were not included in the previously explained ITS-TPC reconstruction. Finally, all hypotheses are refitted with Kalman filtering, selecting the track with the best χ^2 and eliminating its clusters from further searches. The whole process repeats several times to increase the tracking efficiency. Lastly, the track candidates propagate to the preliminary primary interaction vertex to start the outwards part of the procedure. Refitting the track candidates from the preliminary interaction vertex outwards the detectors placed outside the TPC in the central barrel: TRD, TOF, EmCal, PHOS, and HMPID, makes it possible to match them with the encountered tracklets in each of these detectors. The information these detectors give does not update the kinematics parameters of the propagated track candidates, although their valuable particle identification information is stored.

The final stage of the track reconstruction is the second inwards part, where all the track candidates are propagated from the outer layer of the TPC to the inner layer in the ITS while saving each track's position, direction, inverse curvature, and covariance matrix.

Detailed information about the tracking procedure can be found in the references [79], [80].

3.3.1.3. Final determination of the primary interaction vertex

Once the tracking procedure finishes, employing the reconstructed tracks, the vertex finding and fitting algorithms will determine the final primary interaction vertex. The vertex finding algorithm will follow a procedure similar to the one explained above for the three-dimensional preliminary reconstruction of the primary interaction vertex, considering that at the final stage during the minimization, the errors to include will now correspond to ITS-TPC tracks instead of SPD tracklets. The fitting algorithms determine the best-fit coordinates of the vertex and its covariance matrix in an iterative process until the distance among successively fitted vertices is below 10 μm and no more vertices are found along the beam direction. With TOF's information, the tracks are associated with bunch crossings, and to increase the probability of reconstructing the primary interaction vertex correctly, only tracks with the same bunch crossing or undefined bunch crossing can contribute to the same vertex. For detailed information, see [77].

3.3.2. Particle IDentification (PID) in the central barrel

The ALICE experiment can identify and reconstruct a wide range of particle species. At forward rapidity, the muon arm specializes in muon detection, while in the central barrel, different PID techniques allow the exact identification of charged hadrons, electrons, and photons. Within the ALICE central barrel, the general idea is to combine different PID techniques provided by the different detectors to complement their information over the achievable transverse momentum range of the experiment.

With the first two detectors of the central barrel, ITS and TPC, PID information is extracted similarly: truncating the mean of each track's estimated specific energy loss ($\mathrm{d}E/\mathrm{d}x$) according to the Bethe-Bloch formula. Thus, the resulting distribution can approximate a Gaussian distribution at a given momentum and for a specific particle species, with a standard deviation determined by the detector properties and the quality of the reconstructed track. ALICE ITS provides PID information in the low-p_T region (< 0.1 GeV) with a resolution of 11%. Fig. 3.3-left shows simulations of the charged particles average $\mathrm{d}E/\mathrm{d}x$ vs. their momentum, measured by the ITS alone in pp collisions at 13 TeV. Good separation of kaons from pions and protons is observed up to 450 MeV/c and 1 GeV/c, respectively. With the TPC, excellent PID is also possible in the low momentum range, as shown in the performance plot of Fig. 3.3-right. The clear separation among the Bethe-Bloch lines of the different particles progressively worsens as the momentum increases. However, at higher momentum values (higher than 80 GeV/c), thanks to the relativistic rise of the $\mathrm{d}E/\mathrm{d}x$ in the TPC, up to the Fermi plateau, the resolution to separate particles increases again [80].
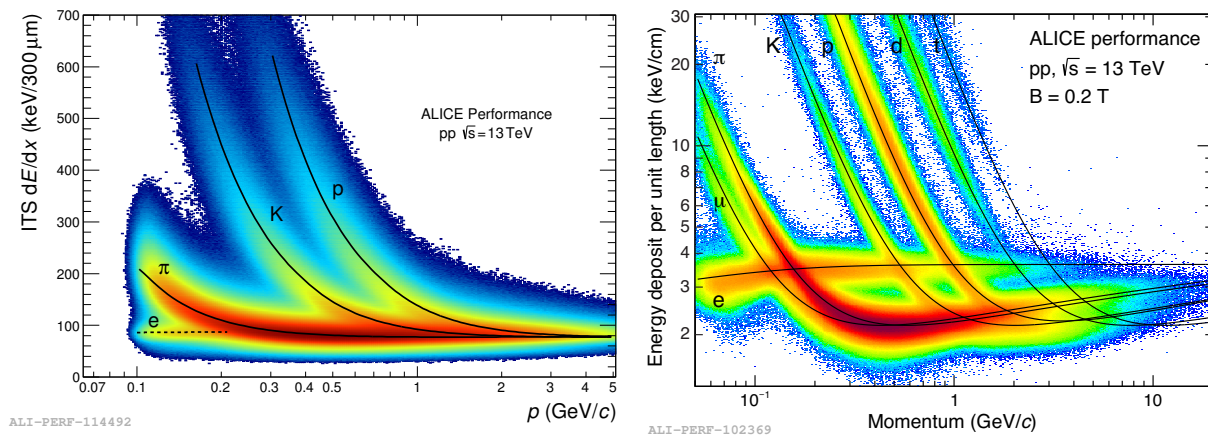
Figure 3.3.: Particle identification with ITS (left) and TPC (right).

The next detector in line is the TRD, which, within ALICE, is meant to complement the TPC capabilities when identifying electrons with a $p_\mathrm{T} > 1$ GeV/c. A charged particle traversing the boundary surface between two media with different dielectric constants emits transition radiation, an effect that becomes relevant for highly relativistic particles. Thus, adding the information on the emitted transition radiation while passing throughout the TRD to the specific energy loss ($\mathrm{d}E/\mathrm{d}x$) enables particularly, the disentanglement of electrons from pions, two of the most abundant particles resulting from hadronic collisions, see the simulation plot of Fig. 3.4-left depicting the phenomena.

TOF detector following the TRD in the central barrel of ALICE, measures the particle's time-of-flight, providing PID at the intermediate momentum range, separating pions and kaons up to 2.5 GeV/c and protons up to 4 GeV/c as shown the simulation plot on the right part of Fig. 3.4. Next, covering the higher momentum range is the HMPID, which, by employing a different PID technique based on the Cherenkov angle of an emitted charged particle passing throughout the ring-imaging Cherenkov modules composing the detector, can separate kaons from pions and protons up to 3 GeV/c and 5 GeV/c respectively as shown in Fig. 3.5.

Lastly, since electrons deposit their whole energy in the calorimeter while hadrons only lose a small fraction of it, the photon spectrometer PHOS and the electromagnetic calorimeters EmCal and DCal can identify electrons by measuring their deposited energy while traversing the clusters of the calorimeters composing these detectors. By reconstructing the ratio $E/\mathbf{p}$, where E stands for the energy deposited in the cluster and $\mathbf{p}$ is the momentum of a reconstructed track that points to the cluster, the ALICE calorimeters identify electrons and photons in the low and intermedia p_{T} range, with an efficiency of almost 100% in low multiplicity environments and of 80% to 90% in heavy ion collisions.
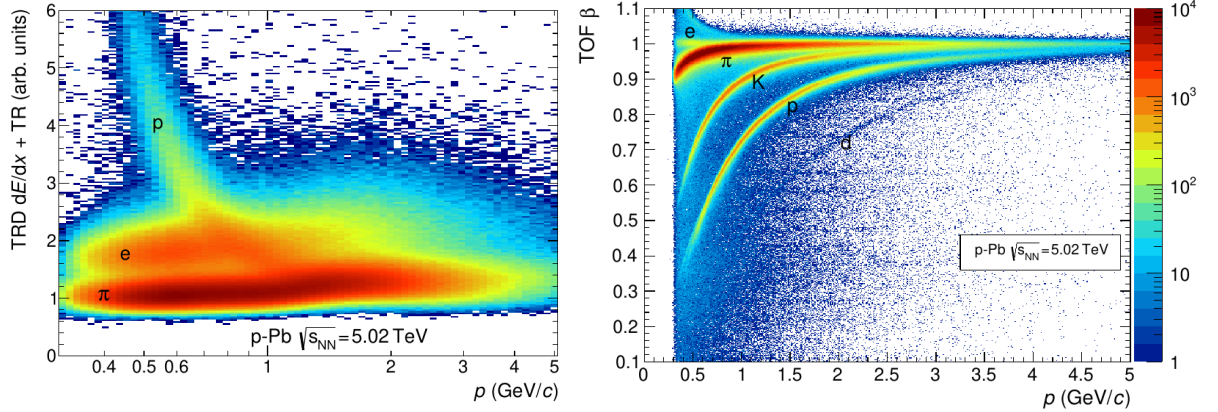
Figure 3.4.: Particle identification TPC+TRD (left) and TOF (right). Figure taken from [79].
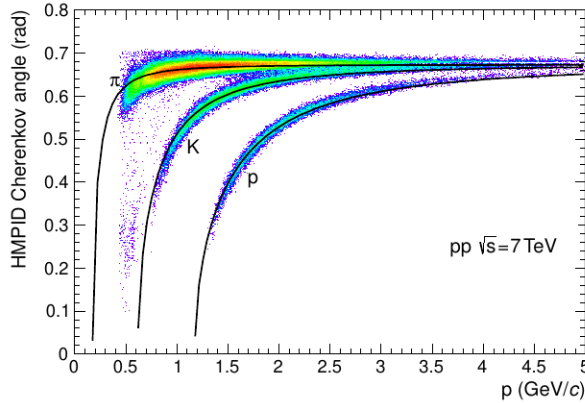
Figure 3.5.: Particle identification HMPID detector. Figure taken from [79].

3.3.2.1. PID with the TPC

The Time Projection Chamber is the sole detector considered for PID purposes in the analysis of this thesis. Fig. 3.3-right illustrating the specific energy loss curves $(\mathrm{d}E/\mathrm{d}x)$ in the TPC, along with the expected mean energy loss $(\langle\mathrm{d}E/\mathrm{d}x\rangle)$ as a function of particle momenta allows to visualize how particle identification takes place in the TPC.

The colored curves depicted in 3.3-right represent the specific energy loss $\mathrm{d}E/\mathrm{d}x$ within the active volume of the TPC. The TPC $\mathrm{d}E/\mathrm{d}x$ for each track is calculated from the amount of charge collected in the track clusters, although not all the clusters of a track contribute to PID

purposes. The charge deposited in a cluster follows a Landau distribution, with a characteristic tail towards higher values. Unlike a Gaussian distribution, the integral of a Landau distribution diverges, making the average energy loss not a good estimate of the mean energy loss. Therefore, the adopted approach is the estimation of the truncated mean S^α of several deposited charge measurements, as defined in Eq. 3.1 according to [81].

$$S^\alpha = \frac{1}{m} \sum_{i=0}^{m} Q_i \tag{3.1}$$

Here, m is defined as $m = \alpha * n$, where n is the total number of clusters assigned to a track for particle identification, and Q_i is the deposited charge in each cluster. S^α of a track, in bins of momentum, follows a Gaussian distribution with a standard deviation σ, and this is the actual quantity used for PID purposes in the TPC showing the best resolution for $\alpha = 0.6$.

On the other hand, the $\langle dE/dx \rangle$ black solid lines in 3.3-right are the final parametrization of the Bethe-Bloch equation for different particle species. This parametrization formula, initially proposed by the ALEPH collaboration [82] is outlined in Equation 3.2, where β is the relativistic particle velocity, γ is the Lorentz factor, and P_{1-5} are fit parameters. The fit parameters are obtained through simulations that include detector effects, using clean samples of electrons, pions, and kaons covering the regions of the Bethe-Bloch curve. Further details on this parametrization procedure are available in [83].

$$f(\beta\gamma) = \frac{P_1}{\beta^{P_4}} (P_2 - \beta^{P_4} - ln(P_3 + \frac{1}{(\beta\gamma)_5^P})) \tag{3.2}$$

Lastly, the final track identification is based on the number of standard deviations from the PID hypothesis: the so-called "*nsigma* cut". The cut expresses the difference between the track-specific energy loss in the TPC and the Bethe-Bloch fits. The number of standard deviations quantifies this difference as:

$$n\sigma_{TPC,i} = \frac{dE/dx_{TPC} - \langle dE/dx \rangle_{i,fits}}{\sigma} \tag{3.3}$$

where i denotes a given particle species and σ is the resolution (or standard deviation) of the track-specific energy loss in the TPC, dE/dx_{TPC}.

4. Analysis Description

The analysis proposed in this thesis is developed within the Reduced Tree Framework located in the PWGDQ folder of AliPhysics. It aims to convert the raw observables obtained from proton-proton collisions at $\sqrt{s}$=13 TeV, recorded by the ALICE experiment, into physically interpretable quantities. Specifically, the analysis explores the correlation between the mean number of J/ψ mesons and the mean number of primary charged particles in three distinct azimuthal regions relative to the emitted J/ψs. To this end, the chapter is structured into five sections, each detailing a step in the data analysis process, from selecting events and tracks to defining the azimuthal regions.

The initial section outlines the criteria for selecting the analyzed collisions among all the recorded collisions. The subsequent sections elaborate on detecting the two main observables in the analysis: the multiplicity of primary charged particles and the J/ψ mesons. Specifically, the second section introduces the experimental charged particle multiplicity estimator considered for this analysis, which differs from the one used by prior ALICE analyses on the J/ψ and the charged particle multiplicity correlation. This section also comprehensively covers the corrections necessary to translate this estimator into the accurate number of produced primary charged particles per collision by discussing the corrections validated in previous studies, such as the z-coordinate of the vertex position and the alpha factor correction, alternatively to the unfolding technique implemented in the azimuthal regions analysis of this thesis. On the other hand, the third section dives into the strategy for detecting J/ψ mesons, from the track selection to the reconstruction and extraction of the J/ψ invariant mass signal.

The fourth section presents the methodology used to obtain the azimuth-inclusive correlation between the number of detected J/ψs and the charged-particle multiplicity produced per event at midrapidity. It also compares the resulting azimuth-inclusive correlations between the J/ψ yields and the charged-particle multiplicity when under three conditions: uncorrected, corrected for the z-coordinate of the vertex position and alpha factor, and corrected by the unfolding technique.

The subsequent section focuses on this thesis's primary objective: defining three distinct regions in the azimuthal plane relative to the beam axis and establishing the correlation between J/ψ yields and primary charged particle multiplicity within these regions. It comprehensively analyzes the J/ψ signal extraction in each azimuthal region and the unfolding process for the azimuthal-charged particle multiplicity estimator.

The last step of the analysis is the assessment of the systematic uncertainties, which will be discussed at length in Chapter 5.

4.1. Event Selection

This thesis analysis selects proton-proton (pp) collisions that, according to the V0 configuration, are triggered by Minimum Bias (MB) and High Multiplicity (HM), see Chapter 3. The MB trigger allows recording higher amounts of tracks in the low multiplicity region while adding the HM trigger provides statistical significance towards the higher multiplicity regions.

The selected collisions must also have a reconstructed primary interaction vertex not exceeding the 10 cm displacement around the nominal point in the beam direction. Besides, collisions with no actual physical meaning, like those assigned to calibration purposes or contamination due to inelastic beam-gas interactions, are discarded by a Physics Selection cut. Pile-up effects are considered by removing collisions with more than one primary interaction vertex reconstructed from three SPD tracklets in low multiplicity collisions or five SPD tracklets in high multiplicity collisions.

See table 4.1 for a summary of the discussed event selection.

Selection	Value
Minimum Bias Trigger	required
High Multiplicity Trigger	required
Physics Selection	required
$|\text{vtx}_z|$	< 10 cm
Pile-up rejection	required

Table 4.1.: Events selection criteria.

In summary, this thesis focuses on the analysis of proton-proton collisions candidates (events) at a center-of-mass energy of $\sqrt{s}$=13 TeV, recorded during Run 2 in 2016, 2017, and 2018. The dataset, passing simultaneously all the conditions mentioned above, comprises approximately 2.8 billion events.

4.2. Multiplicity Estimator (N_{trk})

The ALICE experiment denotes a charged particle as primary [84] if it is produced directly in the collision and has a lifetime larger than $1\text{cm}/c$ or if it comes from decays of particles that have a lifetime smaller than $1\text{cm}/c$. If considering tracks as the trajectories described by particles when traversing the detectors, the number of primary charged particles produced in a collision (charged-particle multiplicity) could be estimated by the number of detected tracks per event matching the ALICE definition of a primary charged particle. Therefore, in the analysis of this thesis, the number of detected tracks reconstructed in the ITS and TPC detectors (N_{trk}) fulfilling the criteria stated in table 4.2 is taken as an experimental estimator indicating the number of primary charged particles produced in a collision.

Prior ALICE studies exploring the correlation between the inclusive J/ψ yield and the charged-particle multiplicity ([49], [48]) considered the number of tracks at midrapidity reconstructed in only the first two layers of the ITS detector (SPD tracklets) as the experimental multiplicity

estimator in the selected events. However, as discussed above, the analysis presented in this thesis adopts a different approach by taking tracks reconstructed in the ITS and the TPC detectors as the experimental multiplicity estimator. Besides enhancing the quality of the reconstructed tracks, this decision also allows the knowledge of the track's angular information, which is crucial for the azimuthal angular analysis of the J/ψ as a function of the charged particle multiplicity developed in this thesis.

Selection	Value
pseudorapidity	$|\eta| < 0.9$
transverse momentum	$p_{\mathrm{T}} > 0.15$ GeV/c
ITS refit	required
TPC refit	required
geometric length (dead TPC area)	3 cm
geometric length (track length)	130 cm
crossed rows/findable clusters	0.8
max. fraction of shared TPC clusters	0.4
$\chi^2/N_{cls.TPC}$	< 2.5
$\chi^2/N_{hit.ITS}$	< 36
max. $\chi^2_{TPC-ITS}$	36
DCA_z	< 2cm
DCA_{xy}	$< 7\sigma_0$
Hit in SPD	required in at least one layer
kink topologies	daughters rejected

Table 4.2.: ITS+TPC track selection criteria.

The selections of table 4.2 have been proposed and optimized by previous ALICE analyses([85], [24]), minding to include the best-reconstructed tracks and to reject tracks belonging to different physical processes that do not fulfill the ALICE definition of a primary charged-particle. The track kinematics selections in the pseudorapidity range and transverse momentum are possible due to the optimal momentum resolution and uniform tracking efficiency in the central barrel region of the ALICE detectors. Requiring ITS and TPC, refit guarantees track information coming from these detectors after passing completely the inward-outward-inward scheme followed in the experiment for track reconstruction. Additionally, the geometric constraints applied to the TPC address the length of the measured track within its active volume, discounting a 3 cm margin to account for its dead zones. The criterion of crossed rows to findable clusters ratio filters out tracks crossing two TPC sectors' boundaries, and a low maximum of shared TPC cluster fraction ensures distinct tracks in an event do not share clusters. The χ^2 requirements provide quality criteria during track reconstruction in each detector and the TPC-ITS matching process. Stricter DCA cuts reduce the inclusion of secondary and decay particle tracks, while only including tracks with at least one hit in any of the SPD layers of the ITS increases the chances of accepting tracks originating in the collision's primary interaction vertex. The exclusion of kink topologies further eliminates tracks from weakly decaying hadrons categorized as non-primary charged particles.

The implementation of these criteria on tracks from the selected MB and HM events leads to distributions of the track multiplicity (N_{trk}) depicted in Fig. 4.1. These distributions reveal that, on average, approximately seven tracks are produced in MB-triggered events, whereas HM-triggered events typically have around 22 tracks.
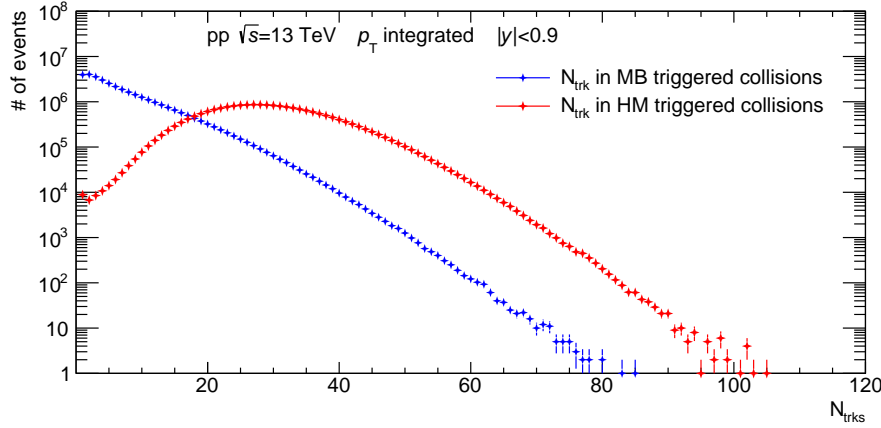
Figure 4.1.: Distributions of the selected tracks (N_{trk}) in MB and HM-triggered events.

4.2.1. From the track multiplicity (N_{trk}) to the charged-particle multiplicity (N_{ch})

The track multiplicity obtained in the previous section (N_{trk}) is susceptible, among other effects, to the tracking efficiencies of the involved detectors (ITS and TPC) and the contamination from particles smeared into these detectors' kinematic acceptance range. In contrast, the distribution of the primary charged particle multiplicity (N_{ch}) given by an MC event generator like PYTHIA8 is free from all these detector effects, allowing to take its dependencies with detectors and experiment features (like the *z*-vertex position) as a reference for correcting N_{trk} and find the true distribution of primary charged particles for the selected events with the ALICE experiment. Moreover, PYTHIA8 event generators, when coupled to a detector simulation package as GEANT3, enable the reconstruction of a charged particle multiplicity estimator mirroring the experimental track multiplicity (N_{trk}). In the following, this estimator is called the MC-reconstructed track multiplicity ($N_{MC\text{-}trk}$) and is depicted in Fig 4.2 together with the MB-triggered track multiplicity given by the experimental measurements and the true charged particle multiplicity (N_{ch}) from PYTHIA8. In figure Fig 4.2, the y-axis is expressed in terms of probability by normalizing each distribution to the total number of analyzed events. At the same time, the x-axis is obtained by normalizing the number of tracks per event to the distribution's mean value, illustrating the likelihood of observing collisions with track counts above or under the average number of tracks per collision in the analyzed data.

A comparison of the N_{trk} in MB events with the $N_{MC\text{-}trk}$ distributions from Fig 4.2 reveals an alignment between these distributions. This correspondence, illustrated in Fig 4.3, indicates that the simulations of collisions through the ALICE detectors effectively mirror the experimental data. Consequently, corrections applied to the MC-reconstructed track multiplicity can be reliably transferred to the MB-triggered track multiplicity, ensuring minimal errors.
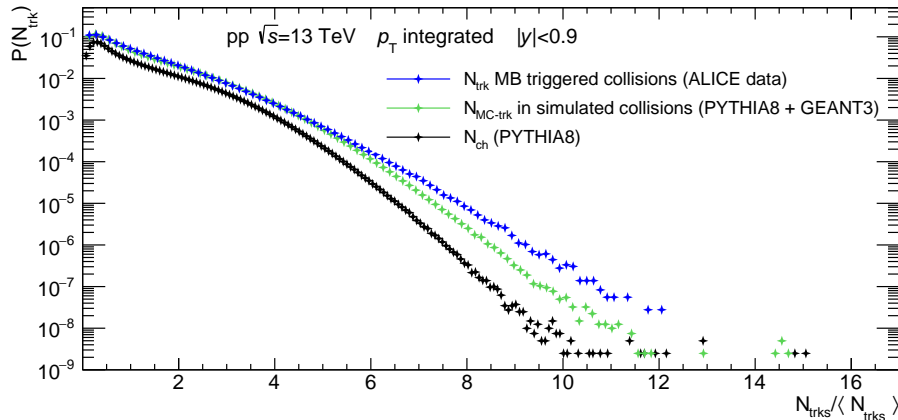
Figure 4.2.: The MB-triggered track multiplicity (N_{trk}) from the experimental measurements and the MC-reconstructed track multiplicity ($N_{MC\text{-}trk}$) resulted by simulating the collisions with PYTHIA8 and the ALICE detectors with GEANT3, and the true charged-particle multiplicity given by only PYTHIA8 (PYTHIA8-N_{ch}).
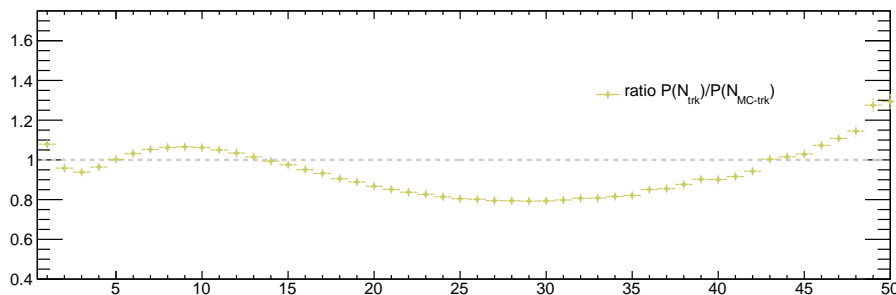
Figure 4.3.: Ratio between the MB-triggered track multiplicity (N_{trk}) and the MC-reconstructed track multiplicity ($N_{MC\text{-}trk}$).

Latest ALICE published analyses ([49], [48]) on the correlation between the inclusive J/ψ yield and the charged particle multiplicity have mainly considered two effects to correct the N_{trk} distribution. Firstly, the dependency of the mean number of tracks with the z-position of the primary interaction vertex, effect illustrated in Fig.4.4 (top). Secondly, the non-linear correlation (in the form $f(x) = x$) between the mean value of the previous-effect-corrected distribution ($N_{trk,corr}$) and the primary charged-particle multiplicity distribution given by PYTHIA8 (see Fig.4.4 bottom). The first effect is corrected following a data-driven approach known as "vertex correction," while the so-called "alpha factor", implemented to correct the second effect, relies on MC studies. In contrast, another recent ALICE study [24] - analyzing the charged particle multiplicity and its p_T spectrum across various collision systems (pp, p–Pb, Pb–Pb, and Xe–Xe) at different center-of-mass energies - employed a two-dimensional unfolding procedure of the measured distribution N_{trk} with the PYTHIA8-N_{ch} distribution to correct N_{trk} due to detector effects. Although this unfolding technique can not provide an event-by-event correction of the experimental track multiplicity, it accounts for both effects mentioned above while potentially reducing the systematic uncertainties in estimating the true charged-particle multiplicity.

These corrections aiming to refine the experimental charged particle multiplicity estimator, N_{trk}, to accurately reflect the true charged particle multiplicity in the events under study are detailed in the coming parts of the present section. Leaving for next sections of this chapter, the further
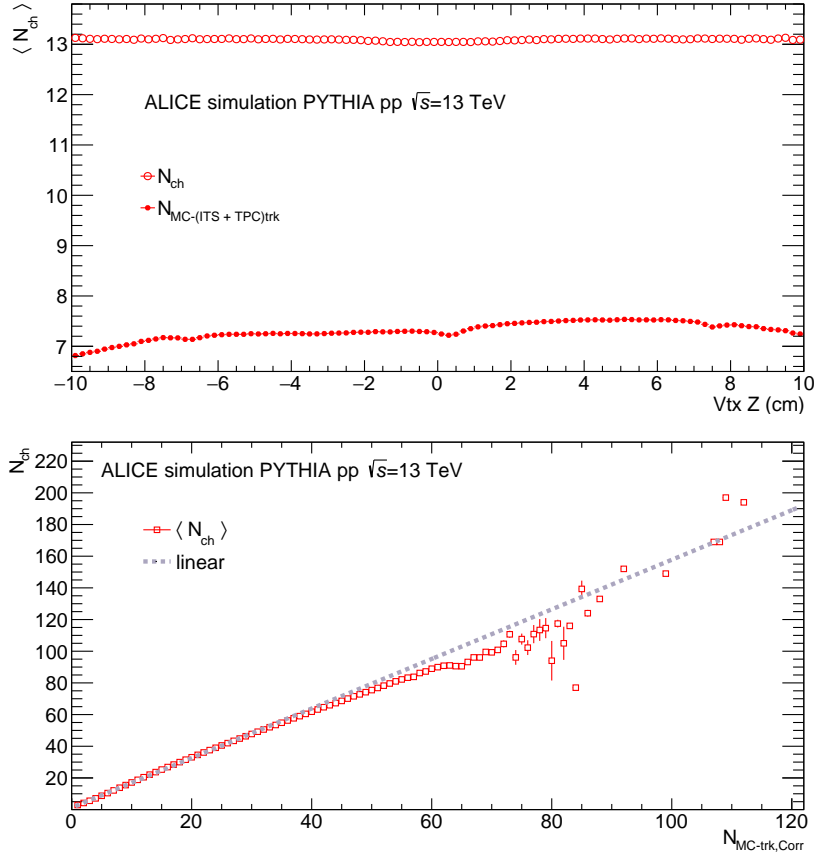
Figure 4.4.: Top: Dependency of PYTHIA8-N_{ch} and MC reconstructed selected tracks with the z-coordinate of the primary interaction vertex. **Bottom:** Correlation between the mean of PYTHIA8-N_{ch} as a function of the MC-reconstructed-vertex-corrected number of selected tracks.

examination of the azimuth-inclusive correlation between the self-normalized J/ψ yield and the true charged-particle multiplicity, when obtained through vertex correction and the alpha factor compared to when derived using the unfolding of the distributions.

4.2.1.1. Vertex and Alpha-factor corrections

Vertex Correction: The process of vertex correction addresses the relationship between the average number of tracks in the analyzed events and the z-coordinate of the primary interaction vertex (Vtx_Z). This dependency arises due to inefficiencies and inactive channels in the SPD detector, restricting its acceptance coverage during data-taking. Additionally, the map of these inactive channels varies between different run periods —the intervals during which the ALICE experiment records collision data— introducing a time-dependent aspect to this effect. This temporal variation is observed in Fig 4.5 produced by grouping run periods displaying similar SPD performance and plotting their average number of SPD tracklets as a function of the z-coordinate of the primary interaction vertex. This figure also shows the relevance of the vertex correction for previous analyses, where the experimental estimator for the charged particle multiplicity was derived from SPD tracklets. However, for tracks reconstructed using the ITS and TPC detectors, the impact of vertex correction is substantially reduced. Figure 4.6 illustrates a smoother dependency between the average number of tracks and the z-coordinate of the primary

interaction vertex despite it not being constant. Additionally, time dependence is minimal, as the average number of tracks remains consistent across different run groups.
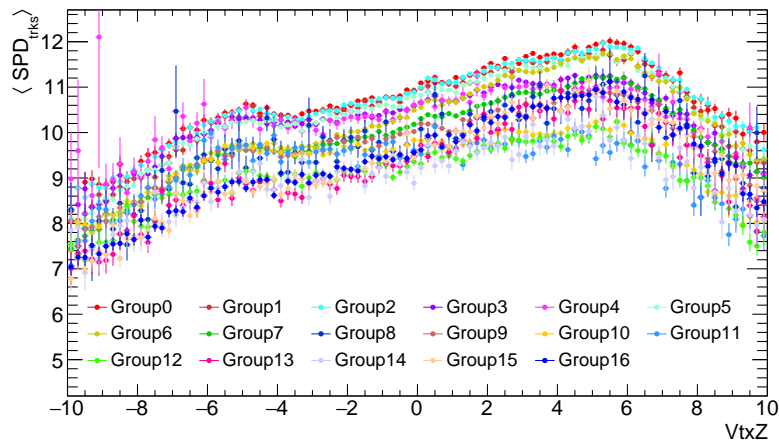
Figure 4.5.: Average number of SPD-tracks in $|\eta| < 0.9$ as a function of the z-coordinate of the primary interaction vertex in bins of runs with similar SPD performance.
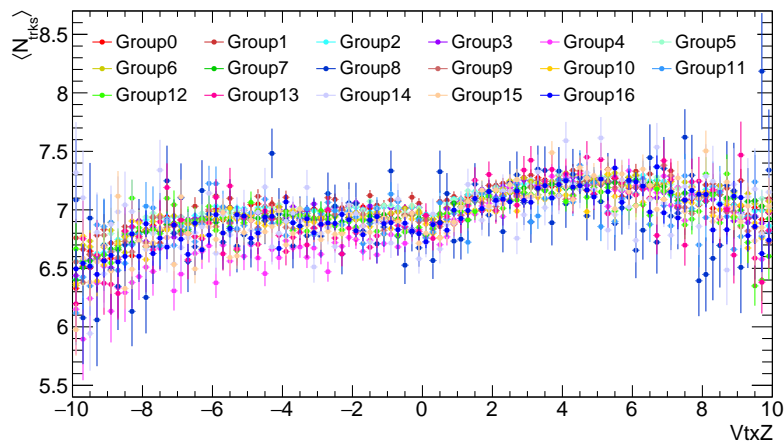
Figure 4.6.: Average number of SPD-TPC tracks in $|\eta| < 0.9$ as a function of the z-coordinate of the primary interaction vertex in bins of runs with similar SPD performance.

The vertex correction as developed by prior analyses on the topic is reflected in equations 4.1 and 4.2 allowing the event-by-event correction of the track multiplicity, giving $N_{trk,corr}$ by:

$$N_{trk,corr} = N_{trk} + Poisson(\Delta N_{trk}) \tag{4.1}$$

where

$$\Delta N_{trk} = \left(\frac{N_{trk,ref}}{\langle N_{trk} \rangle (Vtx_Z, run)} - 1 \right) * N_{trk} \tag{4.2}$$

In the above equations, N_{trk} is the raw number of tracks in the event, while the term $Poisson(\Delta N_{trk})$ smears the correction, meaning that the correction factor per event is randomly generated from a Poisson distribution centered at the ΔN_{trk} estimated value. The choice of a statistical Poissonian distribution is meant to approximate the distribution of the number of missing tracks regarding the generated number of charged particles ($N_{trk} - N_{ch}$) at a given z-vertex as discussed in [86]. The correction factor expressed as ΔN_{trk} accounts for the missing

tracks at the primary interaction point regarding a reference value. In the numerator $N_{trk,ref}$ is the reference number, which in this analysis is the maximum value of the average N_{trk} in bins of Vtx_Z and $runGroup$. The factor in the denominator $\langle N_{trk} \rangle (Vtx_Z, run)$, stands for the average number of tracks in bins of the Vtx_Z and run variables. Applying this correction to the number of selected tracks per event results in a corrected multiplicity estimator $N_{trk,corr}$ independent of the z-coordinate of the primary interaction vertex and the run group. This effect can be observed in Fig 4.7, where the corrected distributions have a flat dependency regarding the position of the primary interaction vertex in the analyzed collisions. This behavior reproduces the dependency of the PYTHIA8-N_{ch} distribution as a function of Vtx_Z depicted in the top plot of Fig 4.4.
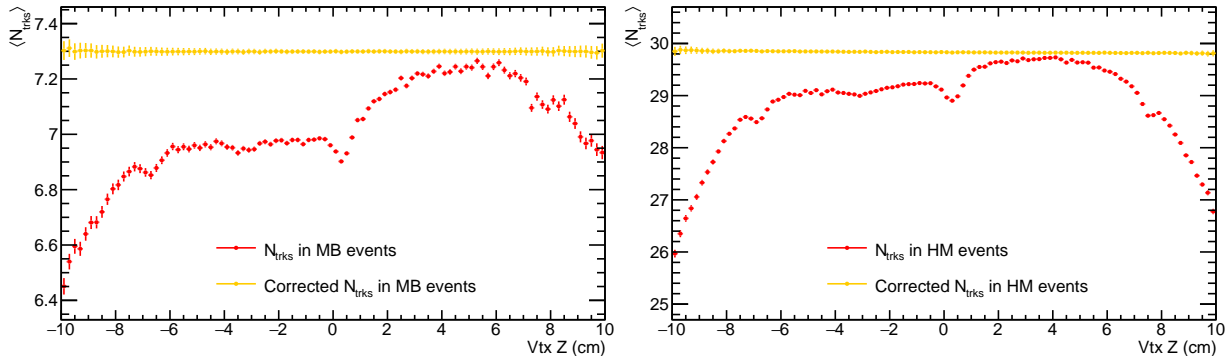
Figure 4.7.: Average number of selected tracks and average number of vertex corrected selected tracks as a function of the z-coordinate of the primary interaction vertex in MB (**right**) and HM (**left**) triggered events.
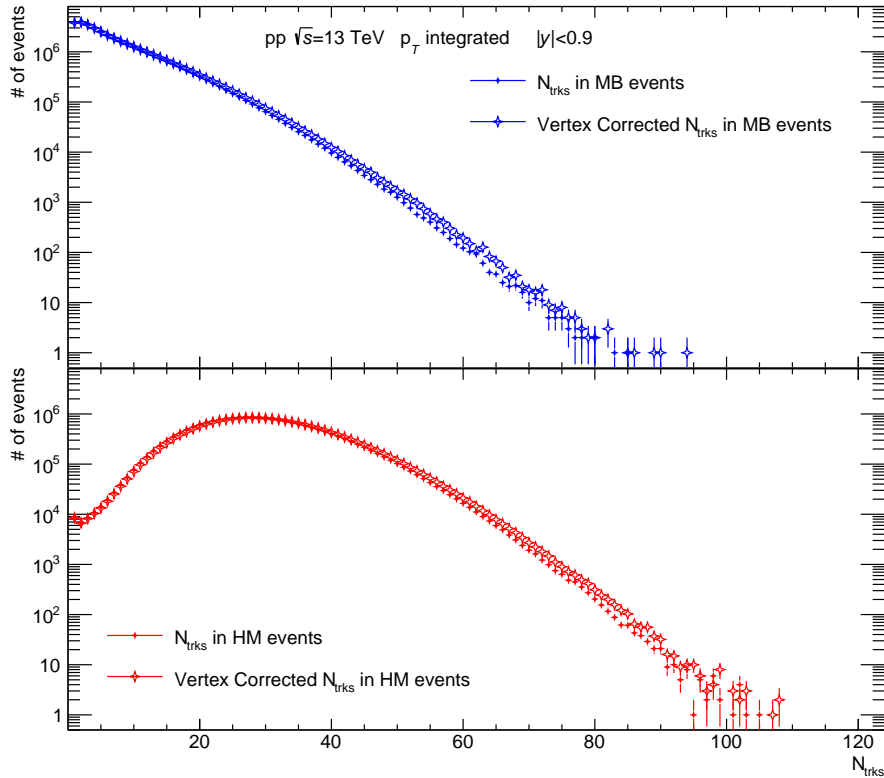
Figure 4.8.: Distributions of the selected tracks (N_{trk}) and the vertex corrected selected tracks ($N_{trk,Corr}$) in MB (**Top**) and HM (**Bottom**) triggered events.

The corrected track multiplicity distributions, $N_{trk,corr}$, for minimum bias (MB) and high multiplicity (HM) triggered events are illustrated in Figure 4.8. As expected, these distributions exhibit higher values at increased multiplicities since the taken reference value is the maximum average multiplicity in each run group. Prior studies ([49], [86]) have explored the adoption of different reference values and smearing functions, concluding that these do not significantly influence the final correlation between the J/ψ yield and the charged particle multiplicity.

Alpha-factor: Assuming each track as the trajectory described by a charged particle when moving through the detectors may lead to the expectation of a perfect linear relationship, in the form x=y, between the MC-reconstructed ($N_{MC\text{-}trk}$) and the solely PYTHIA8-N_{ch} distribution in the simulated events. However, as illustrated at the bottom plot of Fig. 4.4, even after applying the vertex correction, there is a minor but noticeable deviation from linearity in the correlation of these two distributions. This deviation lead, in previous analysis, to estimate an "alpha factor" to rectify other possible unknown detector effects influencing the $N_{MC\text{-}trk}$ distribution. Defined in Eq. 4.3, the alpha factor expresses the ratio between the average PYTHIA8-generated charged particle multiplicity and the MC-reconstructed vertex-corrected track multiplicity.

$$\alpha(N_{MC-trk,corr}) = \frac{\langle N_{ch} \rangle}{N_{MC-trk,z-corr}} \tag{4.3}$$

Recomputing the alpha factor with the analyzed MC-data leads to the curve observed in Fig. 4.9. This figure shows the curve correspoding to the variation of the alpha factor with the number of vertex-corrected tracks, indicating a change acounting to 0.3 of the alpha factor across multiplicities ranging from 20 to 60 tracks.
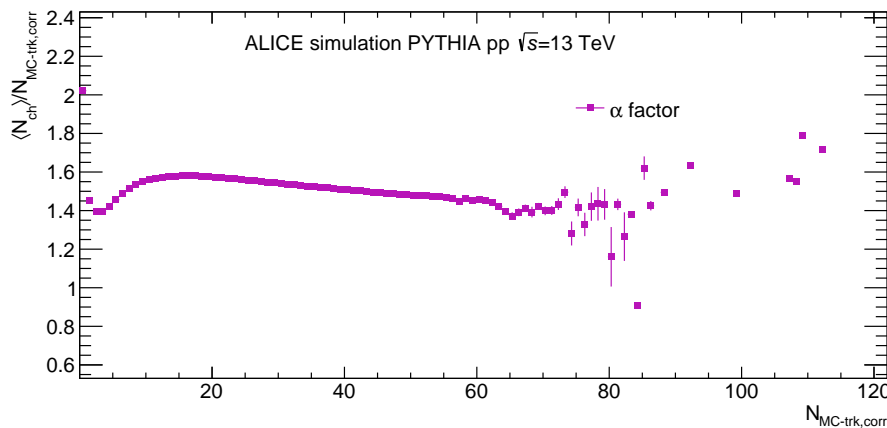
Figure 4.9.: alpha factor as a function of the reconstructed vertex-corrected track multiplicity ($N_{trk,corr}$).

When applied to the experimental vertex-corrected track distributions, this factor produces the actual charged-particle multiplicity distributions computing $N_{ch} = \alpha \times N_{trk,z-corr}$ for each analyzed event. Fig. 4.10 illustrates the expected shift in the resultant distributions towards higher multiplicity values, with no significant changes in the shape for both MB and HM-triggered events.
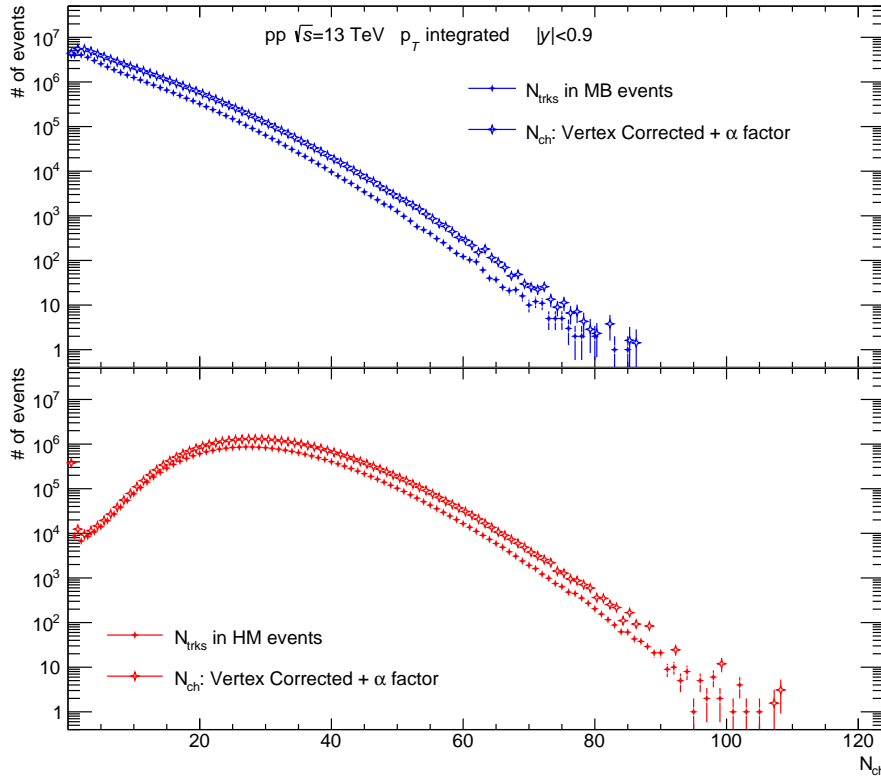
Figure 4.10.: Distributions of the selected tracks (N_{trk}) and their corresponding true charged particle multiplicity distribution (N_{ch}) for MB (**Top**) and HM (**Bottom**) triggered events after the vertex and alpha corrections.

4.2.1.2. Unfolding

As discussed along this section, the detector's variable impact on the track multiplicity leads to a non-linear correlation between N_{trk} and N_{ch}. Specifically, this variability implies that an event with a particular N_{ch} value does not consistently correspond to the same N_{trk}. Conversely, two events with identical N_{trk} values may yield different N_{ch} values. The unfolding procedure by deconvoluting detector-related effects aims to correct this situation. The unfolding framework used in this analysis is adapted from the framework initially developed for the ALICE study of [24] addressing the analytical needs of the J/ψ as a function of the charged particle multiplicity studies. The framework requires MC-simulated data from coupling an event generator with an ALICE detector model. These events simulations generate the 2D detector response matrix, plotting the MC-reconstructed N_{trk} on the x-axis as a function of the PYTHIA8-generated charged particle multiplicity (PYTHIA8-N_{ch}) on the y-axis as depicted in Fig. 4.11.

While employing the iterative Bayesian D'Agostini unfolding algorithm [87], the unfolding framework aims to estimate the true charged particle probability distribution $P(N_{true})$ by improving its computations using recursively the updated values from the previous iteration. Each iteration of the Bayesian D'Agostini unfolding algorithm consists of two key steps. The first step estimates the unfolding matrix $P(N_{true} \mid N_{trk})$ using the Bayes theorem. The second step deduces $P(N_{true})$ using the unfolding matrix. The algorithm is described in the following.
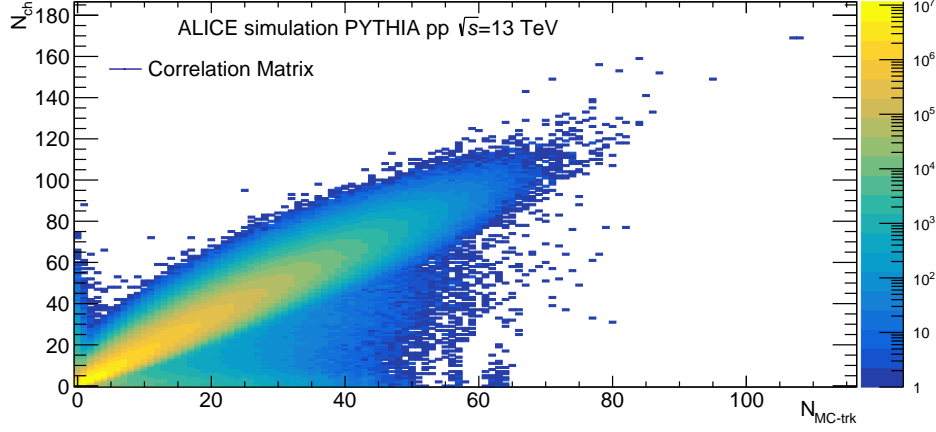
Figure 4.11.: Correlation between PYTHIA8 charged-particle multiplicity (PYTHIA8-N_{ch}) at mid-rapidity and the MC reconstructed track multiplicity ($N_{MC\text{-}trk}$).

With $P(N_{trk})$ as the probability distribution of the measure multiplicity and $P(N_{true} \cap N_{trk})$ as the probability of having an N_{true} paired with an N_{trk} then the conditional probabilities between these two can be expressed as:

$$P(N_{trk} \mid N_{true}) = \frac{P(N_{true} \cap N_{trk})}{P(N_{true})} \tag{4.4a}$$

$$P(N_{true} \mid N_{trk}) = \frac{P(N_{true} \cap N_{trk})}{P(N_{trk})} \tag{4.4b}$$

As first step the Bayes theorem is adapted to the problem in question to obtain the unfolding or smearing matrix as:

$$P(N_{true} \mid N_{trk}) = \frac{P(N_{trk} \mid N_{true}) * P(N_{true})}{P(N_{trk})} \tag{4.5}$$

Where $P(N_{trk} \mid N_{true})$ is derived from the detector response matrix depicted in Fig 4.11. During the first iteration, $P(N_{true})$ is the PYTHIA8-N_{ch} and $P(N_{trk})$ is the MC-reconstructed track multiplicity. Having the first computation of $P(N_{true} \mid N_{trk})$ it is time to calculate $P(N_{true})$, which can be expressed as follows:

$$P(N_{true}) = \frac{A}{\varepsilon(N_{true})} * \sum_N P(N_{true} \mid N_{trk}) * P(N_{trk}) \tag{4.6}$$

Here A is a normalization factor ensuring $\sum_N P(N_{true}) = 1$, $\varepsilon(N_{true})$ represents the trigger efficiency, $P(N_{true} \mid N_{trk})$ is the previously found detector response matrix while $P(N_{trk})$, in this case, is the experimental track multiplicity.

Since the total probability to measure an event with a multiplicity $P(N_{trk})$ can be constructed by summing over all the N_{true} multiplicities, for subsequent iterations $P(N_{trk})$ is expressed as $P(N_{trk}) = \sum_{N_{ch}} P(N_{trk} \mid N_{true}) * P(N_{true})$, and re-writting Eq. 4.5 is obtained:

$$P(N_{true} \mid N_{trk}) = \frac{P(N_{trk} \mid N_{true}) * P(N_{true})}{\sum_{N} P(N_{trk} \mid N_{true}) * P(N_{true})} \tag{4.7}$$

From this point on, $P(N_{true})$ is always the true probability estimated by Eq. 4.6 in the previous iteration, updating subsequently the unfolding matrix $P(N_{true} \mid N_{trk})$ computation. This loop iterates until the χ^2 change between the two most recent estimated $P(N_{true})$ falls below one ($\chi^2 < 1$).

Results from applying this iterative unfolding framework over the experimental track multiplicity are illustrated in Fig. 4.12 and Fig. 4.13, displaying the unfolding matrix for events using the two triggers simultaneously, and the true charged particle multiplicity distributions, respectively.

The unfolding procedure achieves a more accurate representation of the charged particle production per event compared to the previous method of vertex correction with the alpha factor. The resulting unfolding matrix provides a correlation between N_{trk} and N_{ch} for all the analyzed events, facilitating the estimation of N_{ch} distributions within multiplicity bins in the subsequent sections. As illustrated in Fig. 4.13, the unfolding process leads to an increase in event multiplicity, with the corrected distributions having their mean values at approximately 12 and 51 tracks for MB and HM-triggered events, respectively-a nearly 40% difference with the mean values of the experimental track multiplicity N_{trk}. Moreover, the unfolding procedure also refines the distribution shape into a distribution almost free from detector-related effects, as evidenced by the close resemblance between the unfolded distribution for MB-triggered events and the PYTHIA8-N_{ch} distribution (previously shown in Fig 4.2).
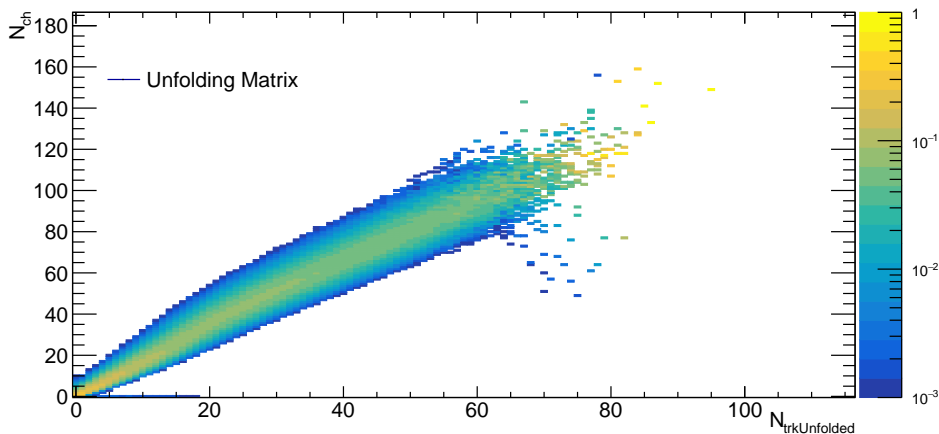
Figure 4.12.: Unfolding matrix ($P(N_{true} \mid N_{trk})$) obtained after unfolding the N_{trk} distribution into N_{ch} for all the analyzed MB and HM-triggered events.
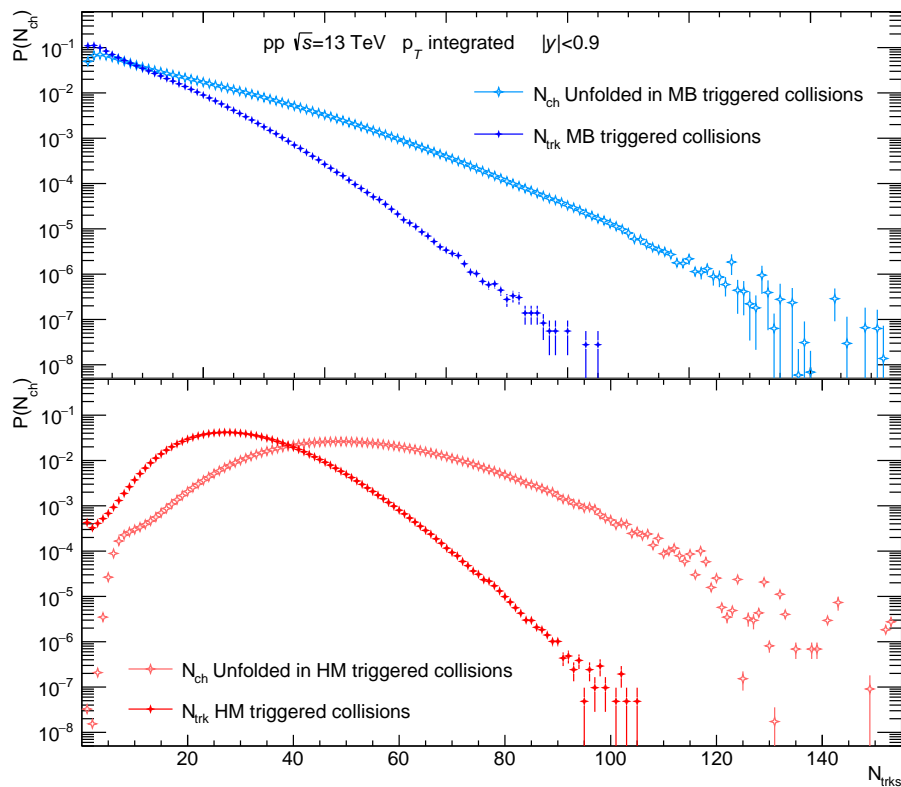
Figure 4.13.: Distributions of the selected tracks (N_{trk}) and their corresponding unfolded distributions (N_{ch}) for MB (**Top**) and HM (**Bottom**) triggered events.

4.3. *J/ψ* **meson detection**

In this analysis, the detection of J/ψ mesons is achieved by their reconstruction in the dielectronic decay channel, specifically through their decay into electron-positron pairs ($J/\psi \rightarrow e^+e^-$). By employing a set of selection criteria, it is possible to identify the tracks corresponding to these electron-positron pairs among the produced tracks per event. These criteria are concisely summarized in Table 4.3.

A kinematic cut in pseudorapidity of $|\eta| < 0.9$ ensures selecting tracks in the TPC full acceptance coverage region. While a transverse momentum requirement of $p_T > 1.0$ GeV/c guarantees the exclusion of electron and positron tracks originating from different physical processes than the J/ψ decay. This criterion is particularly relevant given the large invariant mass of the J/ψ, which typically results in its decay products having relatively high momentum. Notably, about 85% of these products are emitted with a p_T exceeding 1.0 GeV/c.

The tracks corresponding to J/ψ pair candidates reconstructed in the ITS and TPC detectors are characterized by having at least 70 out of 159 possible clusters in the TPC. Additionally, requiring the refitting ensures that these tracks undergo the entire tracking procedure within ALICE. Similar to the track selection criteria for the multiplicity estimator discussed in the previous section, the χ^2 requirement provides a quality criterion per cluster used during the track reconstruction procedure. At the same time, contamination by secondary particles is reduced

Selection	Value
pseudorapidity	$\|\eta\| < 0.9$
transverse momentum	$p_{\mathrm{T}} > 1.0 \ \mathrm{GeV}/c$
ITS refit	required
TPC refit	required
DCA_z	< 3.0 cm
DCA_{xy}	< 1.0 cm
$\chi^2/N_{cls.TPC}$	< 4
$N_{cls.TPC}$	> 70
Hit in SPD	required in at least one layer
kink topologies	daughters rejected
PID electron inclusion	$-3.0 < n\sigma_{TPC,e} < 3.0$
PID proton exclusion	$n\sigma_{TPC,p} > 3.0$
PID pion exclusion	$n\sigma_{TPC,\pi} > 3.0$

Table 4.3.: J/ψ's daughters track selection criteria.

by applying cuts in the Distance of Closest Approach (DCA), requesting a hit in at least one layer of the SPD detector, and rejecting the daughters of kink topologies. Only accepting tracks that hit any of the ITS SPD layers excludes, from the selection, tracks that may not come from the primary interaction vertex of the collision, while rejecting the daughters in kink topologies ensures the removal of tracks from weakly decaying hadrons.

The last three track selection criteria in the above table are particle identification (PID) cuts. These are based on the specific energy loss ($\mathrm{d}E/\mathrm{d}x$) in the TPC (Fig. 3.3) and the subsequent PID via the number of standard deviations from the PID hypothesis, as discussed in Sec. 3.3.2.1. Tracks corresponding to electrons and positrons are required to have the specific energy loss expected for electrons within a range of 3σ below and 3σ above this value. This selection aims to reduce the contamination by pions, which exhibit lower values of specific energy loss at the same transverse momentum than electrons. In addition, to further mitigate the hadronic background, cuts of 3σ and 3.5σ are implemented around the expected $\mathrm{d}E/\mathrm{d}x$ values for pions and protons, respectively, effectively reducing potential contamination by not only pions and protons but also kaons as well. Fig 4.14 depicting the map of the $n\sigma_{TPC}$ applied cuts as a function of the track momentum in the analyzed events gives a visual representation of this discussion.

The selected tracks are randomly paired in the next step, and their invariant mass is calculated as discussed in Sec. 1.2, resulting in a dielectron invariant mass histogram shown in the upper part of Fig. 4.15. This histogram exhibits a notable peak at a value of approximately 3.1 GeV/c^2, which is aligned with the expected invariant mass of the J/ψ meson. The asymmetric shape of the peak, broad towards lower values of the invariant mass, is due to the bremsstrahlung radiation of the electrons in the TPC detector material. Moreover, the J/ψ peak, as seen from the histogram, is superimposed on a significant amount of background. This background observed in the invariant mass region of the J/ψ are dielectron pairs predominantly originating from open heavy-flavour decays (mesons and baryons containing at least one heavy -*c* or *b*- quark) [88].
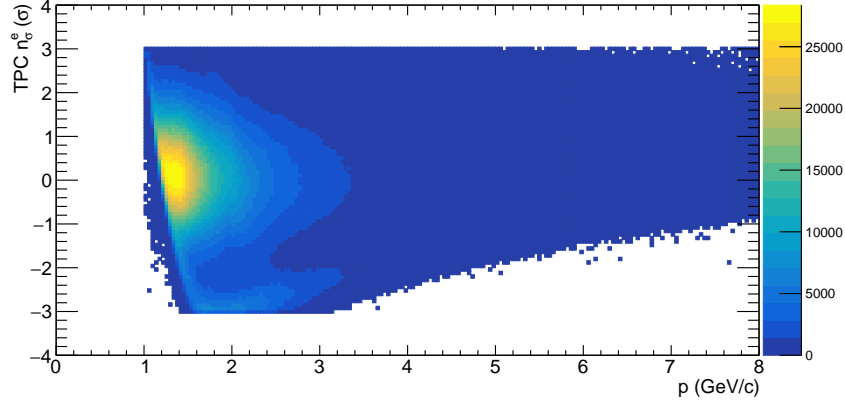
Figure 4.14.: electron-$n\sigma_{TPC}$ values as a function of the momentum of the selected tracks in the analysis.
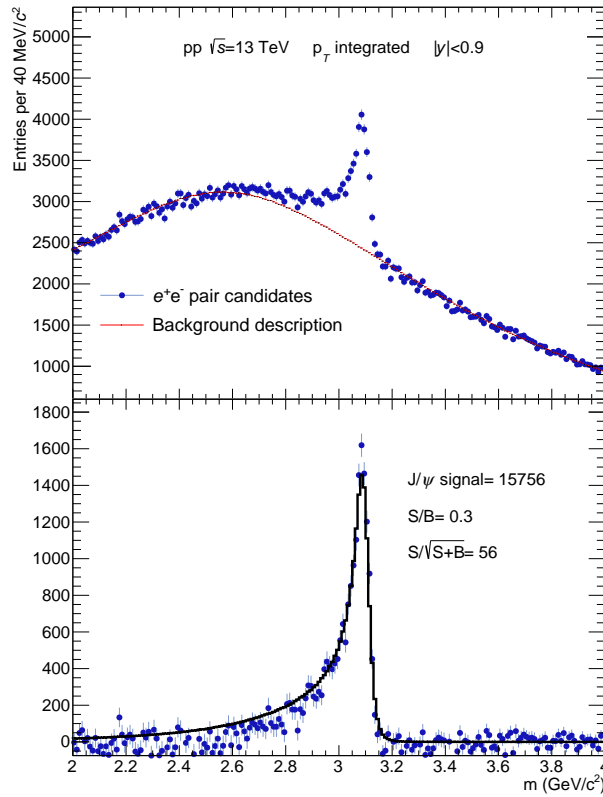
Figure 4.15.: Top: Invariant mass distribution of electron-positron pairs resulting on the J/ψ peak and its background description. **Bottom:** J/ψ signal after background subtraction together with its MC template (black line).

The current analysis aiming to remain with only the J/ψ signal uses the Event Mixing technique and a second-order polynomial to estimate and subtract the background under the peak. The Event Mixing technique involves randomly pairing electrons or positrons from one collision with its corresponding opposite charge particle from a different collision, ensuring that the vertex positions of these collisions are similar (i.e., pairs consisting of one electron and one positron come from two different collisions occurring at the same Vtx_Z distance from the interaction point). The resultant histogram from this technique is then scaled to the dielectron invariant mass histogram (Fig. 4.15-top). The scaling factor is estimated as the ratio of these two histograms in the invariant mass interval 2.2-2.8 GeV/c^2. A second-order polynomial fit is employed after

the Event Mixing technique to subtract the remaining background. The red line in the upper section of Fig. 4.15 represents the combined outcome of these two methods.

The bottom part of Fig. 4.15 represents the histogram obtained after background subtraction. The number of J/ψ mesons in the selected events is the integral of this histogram in the invariant mass range of 2.92 and 3.16 GeV/c^2. The analysis of this thesis considering events triggered MB and HM, detected over fifteen thousand J/ψ mesons, with 60% emitted with a low transverse momentum ($p_{\mathrm{T}} < 4$ GeV/c) and around 40% emitted with high transverse momentum ($p_{\mathrm{T}} > 4$ GeV/c). In case of wishing to increase the high p_{T} J/ψ sample, alongside the TPC signal, additional particle identification detectors such as the DCal and EmCal calorimeters, for example, could be incorporated into the analysis.

4.4. Correlating J/ψ meson yields and N$_{ch}$

The analysis of the produced J/ψ mesons as a function of the charged-particle multiplicity correlates J/ψ yields values on the y-axis and mean charged-particle multiplicity values on the x-axis.

For determining the values in the y-axis of the correlation, the process begins by constructing a two-dimensional histogram of electron-positron pairs invariant mass against the number of produced tracks in the analyzed events, as depicted in Fig. 4.16. This histogram is then segmented along the x-axis and projected onto the y-axis to extract the J/ψ signal within the specified track multiplicity ranges (marked by the black lines). The segmentation criterion is based on the possibility of reconstructing the J/ψ peak and describing its background reasonably in each one of these ranges.
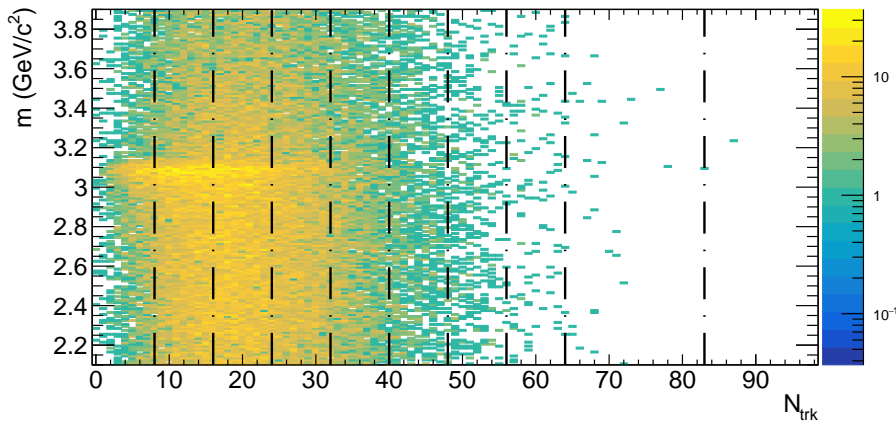
Figure 4.16.: Two-dimensional histogram correlating the J/ψ signal in the y-axis and charged particle multiplicity in the x-axis.

The resulting dielectron invariant mass distributions for each multiplicity bin and the J/ψ mesons obtained after background subtraction using the Event Mixing technique and a second-order polynomial fit are presented in Fig. 4.17. The figure shows that in the first multiplicity interval, which contains fewer tracks than the average amount of produced tracks in MB-triggered collisions, the J/ψs peak appears over minimal background, resulting in the highest

signal-to-background (S/B) ratio. Conversely, this ratio diminishes with increasing multiplicity, reaching its lowest values in the last three intervals. Finally, the number of detected J/ψs in each multiplicity bin is normalized to the number of detected J/ψs in MB-triggered events and the number of analyzed MB-triggered events, obtaining the self-normalized J/ψ yield per multiplicity bin.

The x-axis of the correlation takes its values from unfolding the experimental track multiplicity (N_{trk}) distribution for all analyzed events and not only the N_{trk} distribution corresponding to events where a J/ψ was produced, which is the result of projecting Fig. 4.16 onto its x-axis. Following the multiplicity ranges where the J/ψ mesons were detected, the N_{trk} distribution for the analyzed events is binned as depicted in the upper plot of Fig. 4.18 by the pink lines. Subsequently, according to Eq. 4.6, the corresponding N_{ch} distributions to each of these N_{trk} multiplicity ranges are estimated using the resultant smearing matrix (depicted in Fig 4.12) from the unfolding. The bottom plot of Fig. 4.18 shows, in black lines, the obtained N_{ch} distributions for each multiplicity range. The mean values of each of these distributions normalized to the total number of analyzed MB-triggered events make the final values for the x-axis of the correlation.
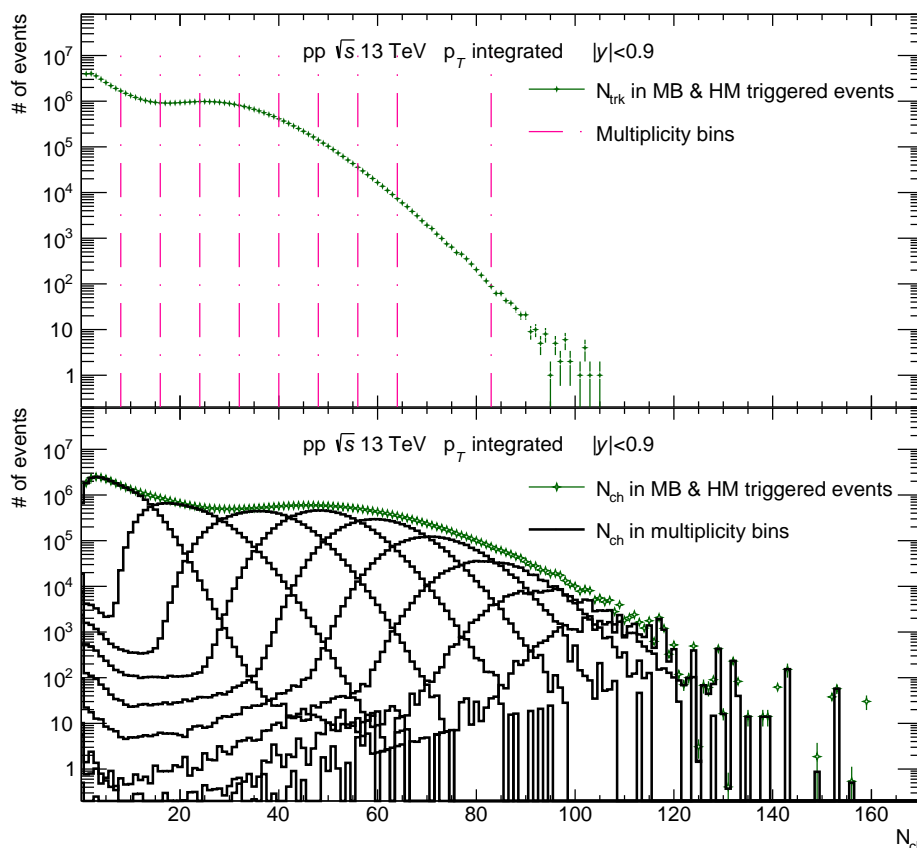
Figure 4.18.: Top: The track multiplicity distribution (N_{trk}), in the simultaneously MB and HM-triggered events, segmented into the multiplicity intervals (pink lines) where the J/ψ mesons are detected. **Bottom:** The charged particle multiplicity distribution, resulting from the unfolding, in the simultaneously MB and HM-triggered events, and the N_{ch} distributions (black lines) obtained for each N_{trk} interval marked by the pink lines.
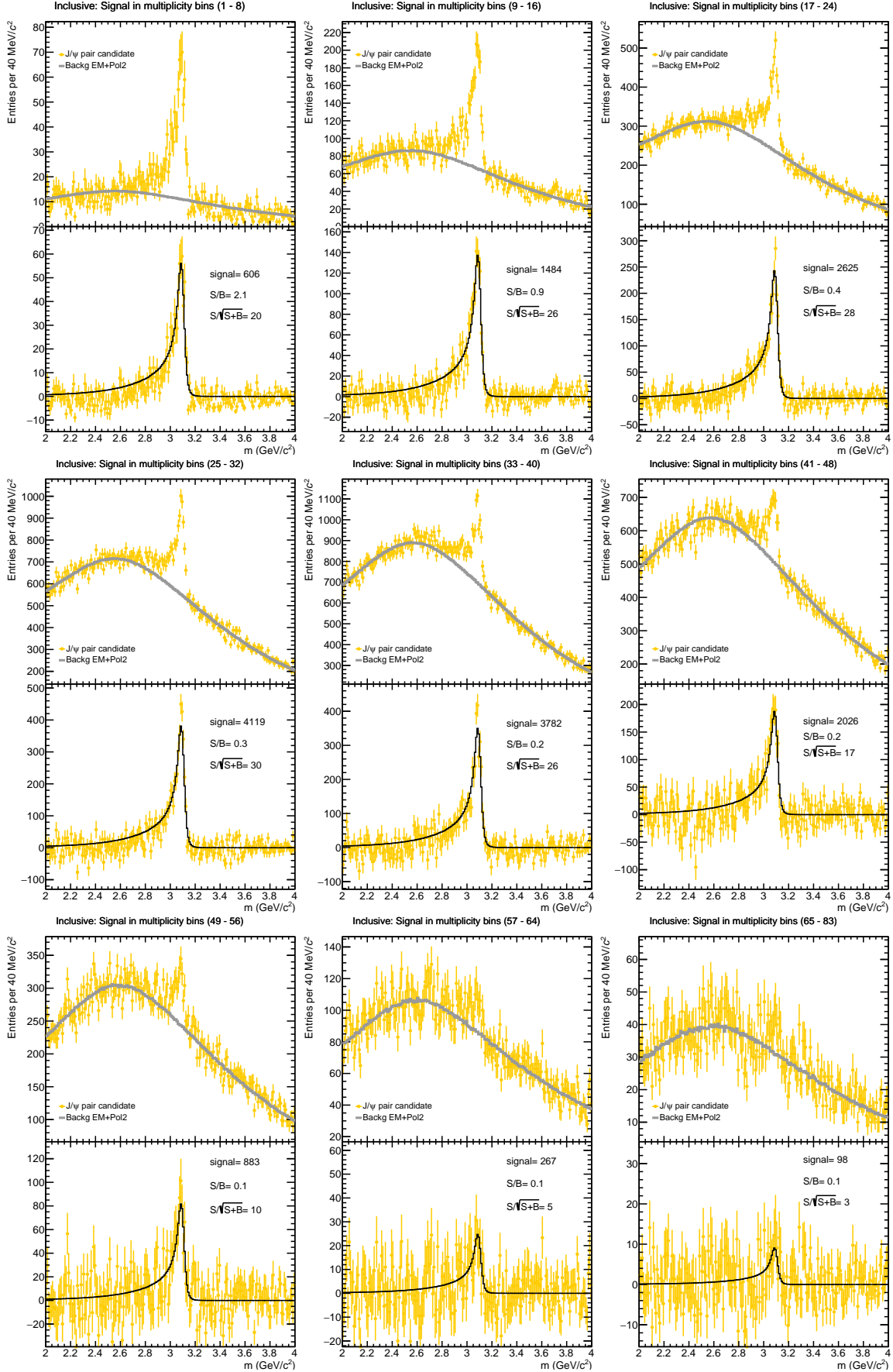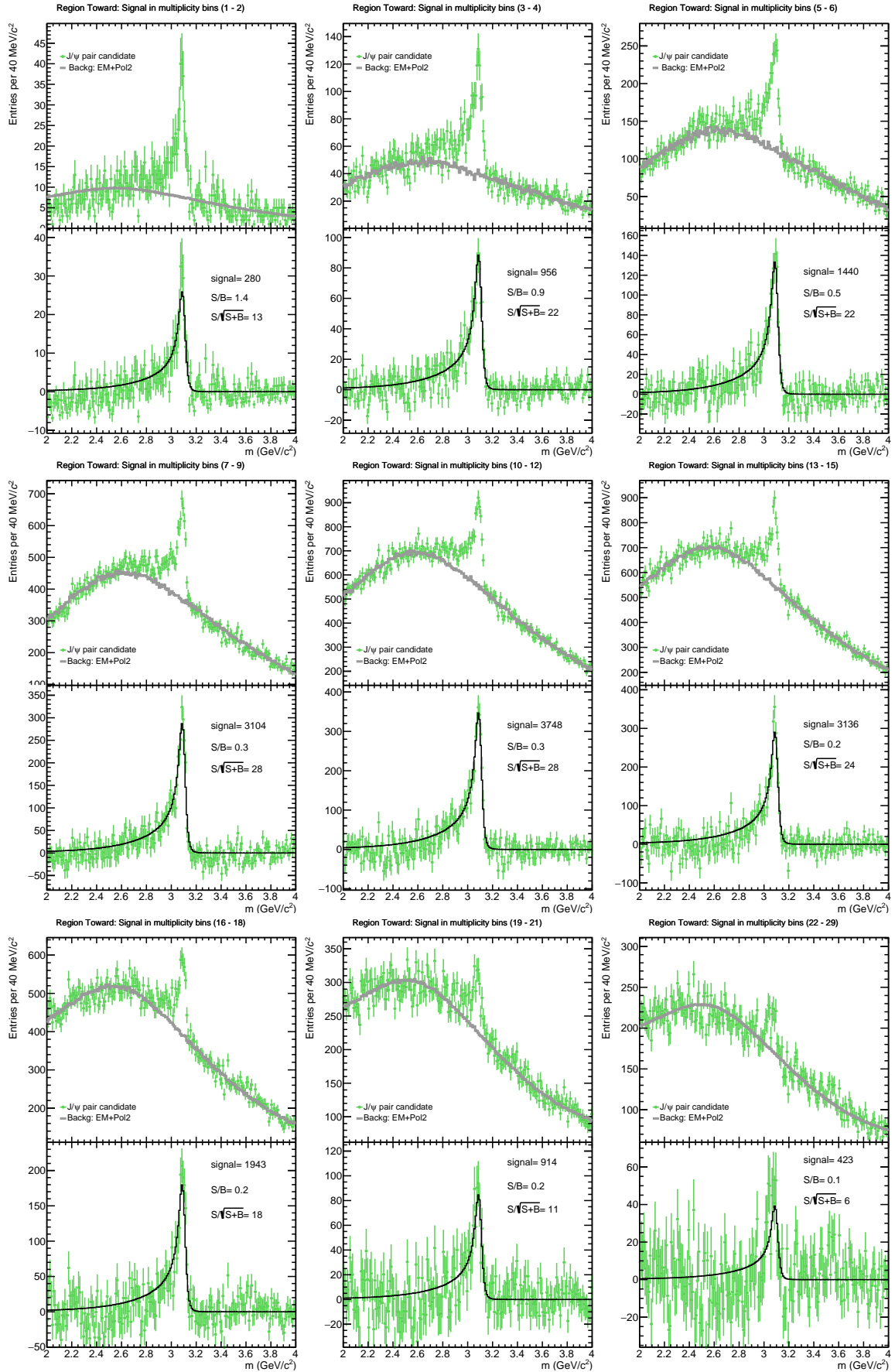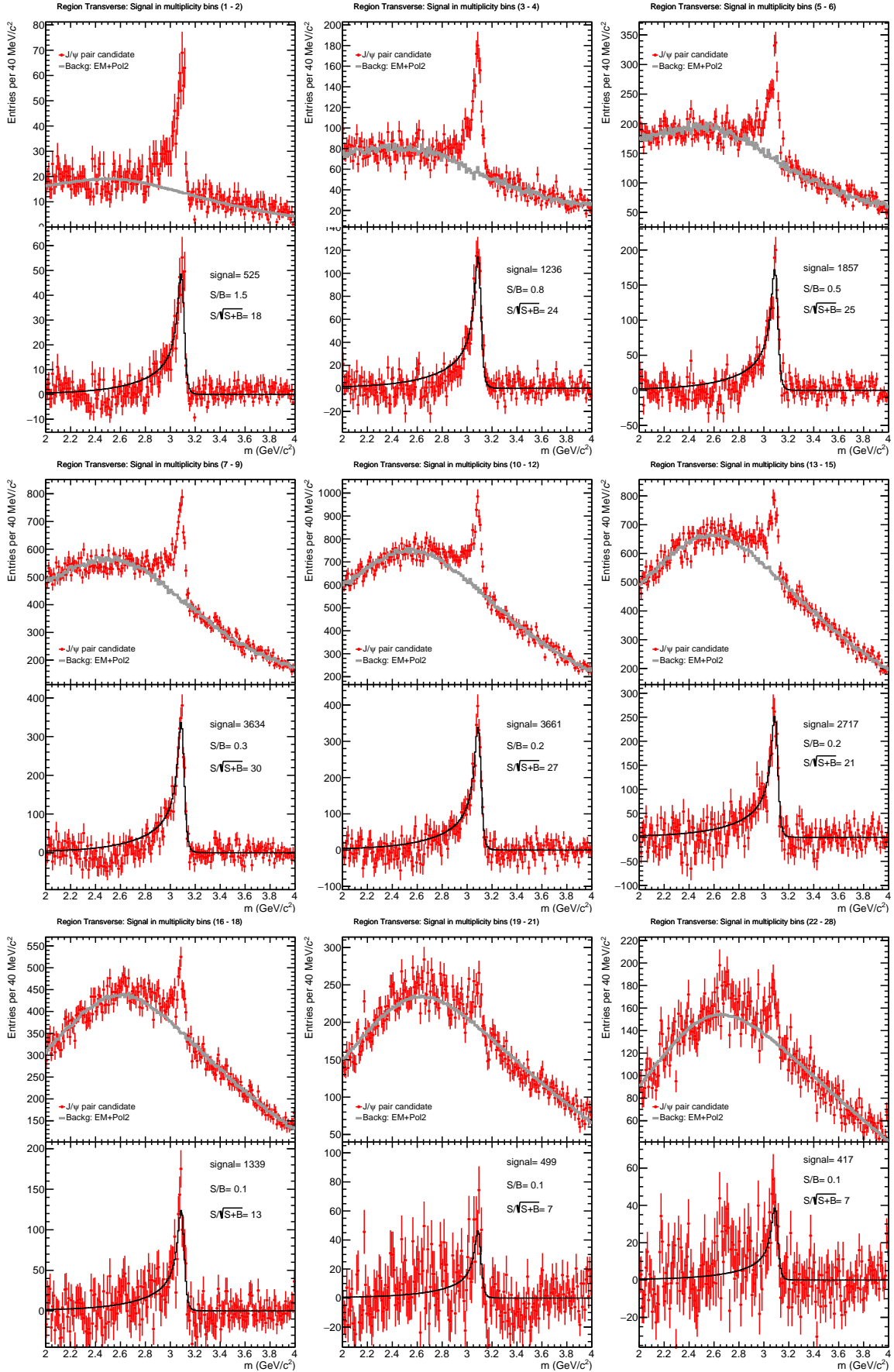
Figure 4.17.: Invariant mass distribution of electron-positron pairs resulting in the J/ψ peak, its background description, and the J/ψ signal after background subtraction in each multiplicity range.

4.4.1. Azimuthal inclusive J/ψ meson yields as a function of N$_{ch}$

The latest published analysis about the J/ψ yield as a function of the charged particle multiplicity at midrapidity in the ALICE experiment used ITS tracks corrected by the vertex and alpha factor method to estimate the charged-particle multiplicity. In contrast, as discussed in previous sections of this chapter, the experimental multiplicity estimator used in this thesis analysis comprises tracks reconstructed in the ITS and TPC detectors, which were corrected using the unfolding technique. Nevertheless, aiming a comparison between the previously published results and the J/ψ-N$_{trk}$ correlations when correcting N$_{trk}$ by the different discussed methods, the vertex plus alpha factor correction was also applied to the ITS-TPC multiplicity estimator. This comparison is in Fig. 4.19 showing, additionally, the resultant non-corrected J/ψ-N$_{trk}$ correlation. When comparing the non-corrected correlation with the corrected ones, it is evident that the increase in multiplicity derived from the corrections leads to a steeper dependency between the self-normalized J/ψ yields and the charged particle multiplicity in the analyzed events. Moreover, when comparing the correlations with N$_{trk}$ corrected either by the unfolding technique or the vertex plus alpha factor method, they are compatible with the latest published results, showing a better agreement when using the unfolding technique. Therefore, these observations allow employing ITS-TPC tracks corrected by the unfolding technique to estimate the charged particle multiplicity in the selected events and validate its use for the subsequent azimuthal analysis of this thesis.
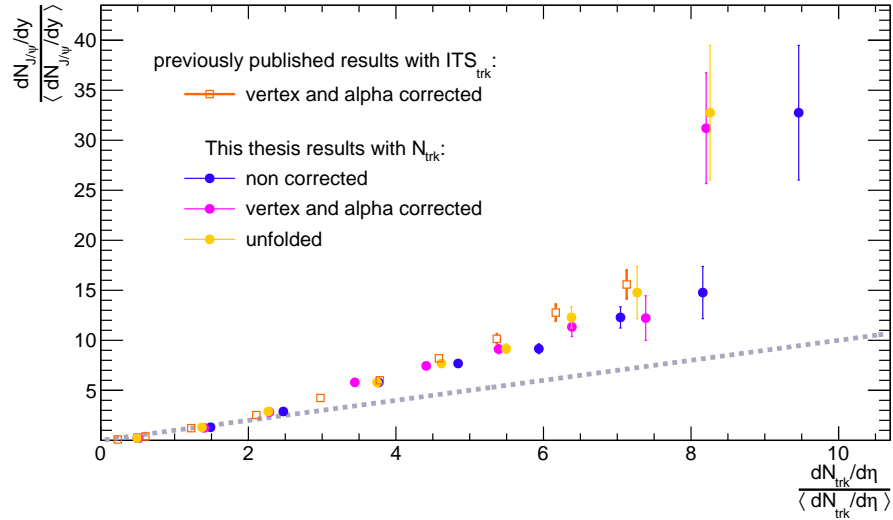
Figure 4.19.: Comparison with previously published results ([48]) of this thesis azimuthal-inclusive and self-normalized J/ψ-N$_{ch}$ correlations, when the charged particle multiplicity is corrected and uncorrected.

4.5. Correlating J/ψ yields and N$_{ch}$ in J/ψ azimuthal regions

The correlation analysis between J/ψ mesons and the charged-particle multiplicity N$_{ch}$ in the azimuthal plane relative to the beam direction begins by defining the specific regions of interest within this plane for estimating the experimental observables. These three regions, the Towards, the Transverse and the Away, as proposed in [1], are as follows:

- Toward: $\frac{5\pi}{3} < \Delta\varphi < \frac{\pi}{3}$

- Transverse: $\frac{\pi}{3} < \Delta\varphi < \frac{2\pi}{3}$ or $\frac{4\pi}{3} < \Delta\varphi < \frac{5\pi}{3}$

- Away: $\frac{2\pi}{3} < \Delta\varphi < \frac{4\pi}{3}$

The detection of J/ψs mesons within these azimuthal regions starts by computing $\Delta\varphi$ as the difference between the azimuthal angle of each electron-positron pair candidate and the azimuthal angle of each charged particle track in the event, resulting in a N_{trk} distribution that characterizes the azimuthal distribution of the charged particle tracks relative to the emitted J/ψ pair candidate ($N_{trk\text{-}regions/J/\psi}$) for the analyzed event. A sketch detailing this idea is shown in Fig. 4.20. Conversely, for determining the N_{ch} distribution in each region, $\Delta\varphi$ is the difference between a randomly selected azimuthal angle and the azimuthal angle of the remaining charged particle tracks in the event, thereby dividing the azimuthal plane of emitted charged particles into three homogeneous regions ($N_{trk\text{-}regions}$).
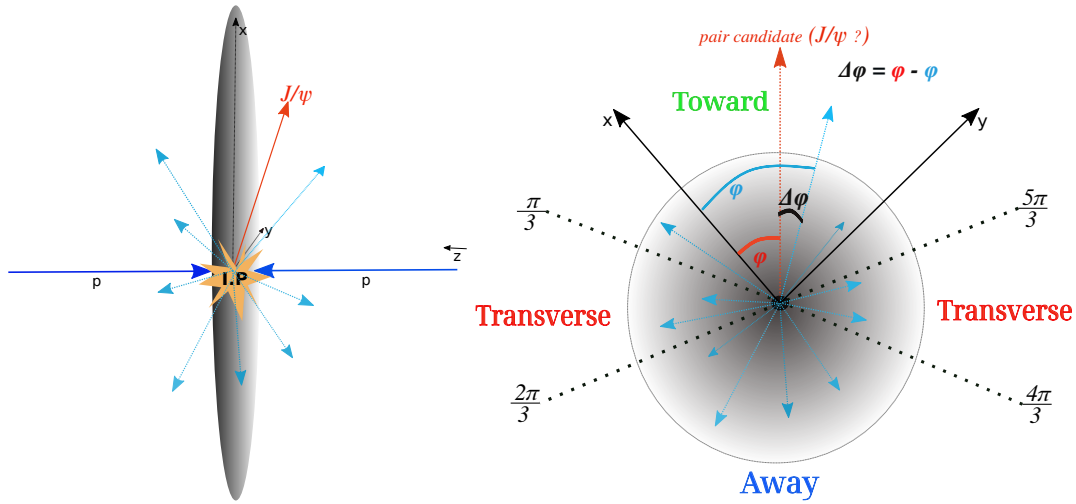
Figure 4.20.: Sketch showing the collision's azimuthal plane where the regions are constructed regarding the emitted J/ψ pair candidate.

For the extraction of J/ψ yields (y-axis of the correlation) in each region, the analysis follows a procedure analogous to that described in the preceding section. A two-dimensional histogram is constructed, correlating the invariant mass of electron-positron pairs with the φ-differential tracks distribution (described by $N_{trk\text{-}regions/J/\psi}$). This histogram is then segmented into multiplicity bins and projected onto its y-axis to extract the J/ψ signal. The extracted values, representing the detected number of J/ψ mesons within each multiplicity bin, are normalized by the total number of detected J/ψ mesons and events that triggered minimum bias (MB). Figures 4.21, 4.22, and 4.23 present the dielectron invariant mass distributions in the selected multiplicity bins for the three regions of interest (Towards, Transverse, and Away respectively), with the corresponding background characterization (top) and the resultant dielectron invariant mass histogram post-background subtraction (bottom).

A similar reasoning to that described in the previous section was employed to determine each region's mean charged particle multiplicity values (x-axis of the correlation). Mainly this implies the segmentation of the corresponding N_{trk} distribution following the multiplicity intervals used in the J/ψ signal extraction, and subsequently the estimation, for each of these N_{trk} segments, of

Figure 4.21.: Toward region: Invariant mass distribution of electron-positron pairs resulting in the J/ψ peak, its background description, and the J/ψ signal after background subtraction in each multiplicity range.

Figure 4.22.: Transverse region: Invariant mass distribution of electron-positron pairs resulting in the J/ψ peak, its background description, and the J/ψ signal after background subtraction in each multiplicity range.
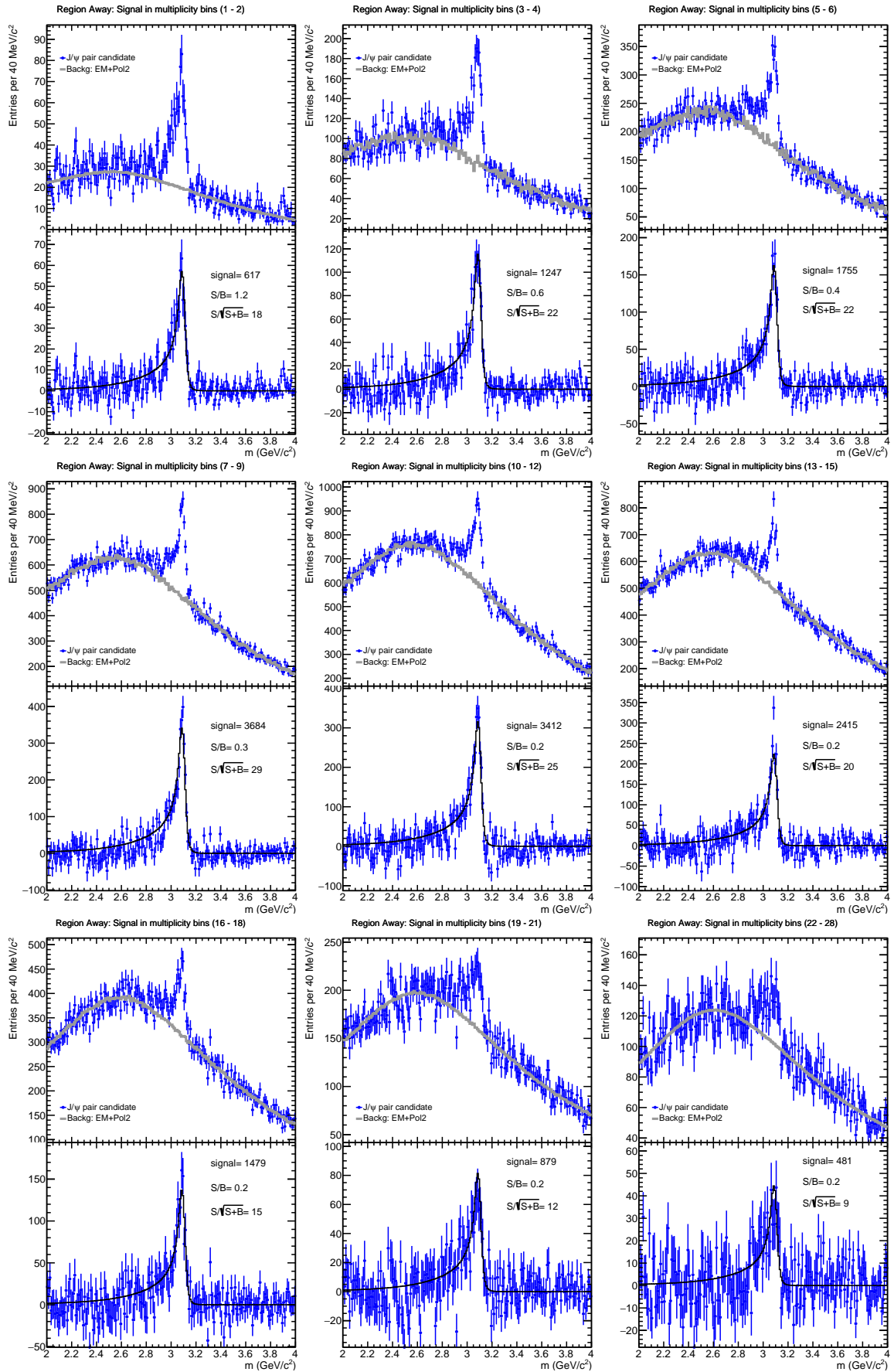
Figure 4.23.: Away region: Invariant mass distribution of electron-positron pairs resulting in the J/ψ peak, its background description, and the J/ψ signal after background subtraction in each multiplicity range.

their true charged particle multiplicity distribution N_{ch} according to Eq. 4.6, to finally take the mean value of each N_{ch} distribution and normalize it to the number of events triggering MB. In the particular case of the regions, the N_{trk} distribution is the previously found $N_{trk-regions}$. This distribution has a mean value accounting for a third of the azimuth inclusive track multiplicity distribution for all the analyzed events. After its unfolding, the resultant unfolding matrix estimates the true charged particle multiplicity with Eq. 4.6 for each multiplicity bin. The top plot in Fig. 4.24 shows the $N_{trk-regions}$ distribution with the taken multiplicity bins marked by the pink lines, while similar to the previous section, the bottom plot shows in black lines the unfolded $N_{trk-regions}$ distribution for simultaneously MB and HM-triggered events with the true charged particle multiplicity distributions corresponding to each multiplicity bin.
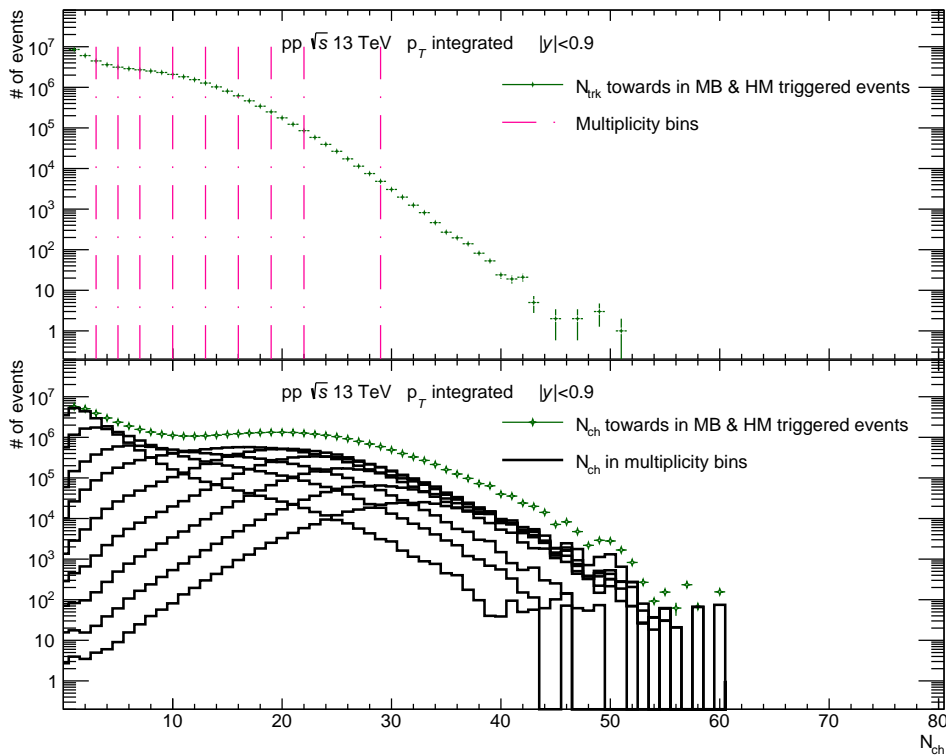
Figure 4.24.: Top: The φ-differential track multiplicity distribution (N_{trk}), in the simultaneously MB and HM-triggered events, segmented into the multiplicity intervals (pink lines) where the J/ψ mesons are detected. **Bottom:** The φ-differential charged particle multiplicity distribution, resulting from unfolding, in the simultaneously MB and HM-triggered events, and the φ-differential N_{ch} distributions (black lines) obtained for each φ-differential N_{trk} interval marked by the pink lines.

5. Systematic Uncertainties

The analysis discussed in this thesis correlates two observables detected by the ALICE experiment: J/ψ mesons and the charged-particle multiplicity, N_{ch}. While the previous chapter detailed the methodology for estimating and correlating these observables, this chapter focuses on quantifying the systematic uncertainties associated with this methodology. The analysis described in the previous chapter identified two possible sources contributing to the systematic uncertainty of each observable. The first is the track selection criteria applied in constructing both observables. The second source differs between the observables: in the case of the charged particle multiplicity, the unfolding procedure could be a contributor, whereas, while determining the J/ψ yields, the signal extraction procedure plays a significant role. The contributions from each source are treated as independent, allowing its calculation to be the square root of adding the squares (sum in quadrature) of the contributions. This chapter is organized into two main sections, each estimating the total systematic uncertainty associated with each observable.

The sources of systematic uncertainty will be investigated by varying the values of its main parameters. The coming sessions comprehensively discuss the introduced variations and detail the methodology used to quantify the impact of these variations on the correlations φ-inclusive and differential between the self-normalized J/ψ yields and the charged-particle multiplicity. In that direction, the values of the parameters yielding the final results of this thesis are consistently referred to as the standard reference values of each systematic uncertainty source. The relative ratio ($|N_{variation} - N_{standard}|/N_{standard}$) of the observable under each varied condition serves as an indicator of the magnitude of the variation. When assessing the systematic uncertainties associated with the J/ψ yields, the Barlow criterion [89] is applied to rule out non-statistically-significant variations, whereas, for systematic uncertainties related to the charged particle multiplicity, this criterion is not applied as the used approach considering continuous functions and distributions does not require it. Finally, the root mean square (RMS), as expressed by Eq. 5.1 where n is always the number of variations and x_n stands for each relative ratio, estimates the contribution to the total systematic uncertainty of each discussed source.

$$x_{RMS} = \sqrt{\frac{1}{n}(x_1^2 + x_2^2 + ... + x_n^2)} \tag{5.1}$$

5.1. N_{ch} systematic uncertainty

The estimation of the charged particle multiplicity for the analyzed events is predominantly influenced by systematic uncertainties arising from the following sources:

- The track selection criteria ($\sigma_{trk-cuts}$)

- The unfolding procedure ($\sigma_{unfolding}$)

The total systematic uncertainty σ_{Nch}, considering each of these sources independent, is then the sum in quadrature of the contributions:

$$\sigma_{Nch} = \sqrt{\sigma_{trk-cuts}^2 + \sigma_{unfolding}^2} \tag{5.2}$$

Next, the impact of these sources of systematic uncertainties is investigated in the context of the azimuthal-inclusive charged particle multiplicity distribution to subsequently assess their impact on the J/ψ- N_{ch} correlation analysis. For this purpose, the azimuthal-inclusive and differential values of the self-normalized charged particle multiplicity per analyzed multiplicity bin are also estimated for all the variations.

5.1.1. Variations to the track selection criteria

Table 5.1 collects the standard values, highlighted in black, and the variations applied to the ITS+TPC track selection criteria to investigate this source of systematic uncertainty. With 27 variations, each variation is incorporated into the analysis while keeping the rest of the parameters at their standard values. The previous analysis developed in [24], which focused on estimating the charged particle multiplicity with the ALICE detector, provided the limiting values for each track selection criterion.

Selection	Value
pseudorapidity	$\lvert\eta\rvert < 0.9$
transverse momentum	$p_{\mathrm{T}} > 0.15$ GeV/c
ITS refit	required
TPC refit	required
geometric length (dead TPC area)	2, **3 cm**, 4
geometric length (track length)	120, **130 cm**, 140
crossed rows/findable clusters	0.7, 0.75, **0.8**, 0.85, 0.9
max. fraction of shared TPC clusters	0.2, **0.4**, 1.0
$\chi^2/N_{cls.TPC}$	< 2, **2.5**, 3
$\chi^2/N_{hit.ITS}$	< 25, **36**, 49
max. $\chi^2_{TPC-ITS}$	25, **36**, 49
DCA_z	< 1, **2cm**, 3, 4, 5
DCA_{xy}	$< 4\sigma_0$, $5\sigma_0$, $6\sigma_0$, **$7\sigma_0$**, $8\sigma_0$, $9\sigma_0$, $10\sigma_0$
Hit in SPD	**required in at least one layer**, non-required
kink topologies	daughters rejected

Table 5.1.: Standard values and variations of ITS+TPC track selection criteria

After applying the specified variations, the resultant track multiplicity distributions for the events triggered MB and HM are depicted in Fig. 5.1, along with their ratio to the standard distribution. Significant divergences from the standard track multiplicity distribution are observed for variations associated with the TPC geometric cut. The most pronounced deviation occurs when increasing by 10 cm the standard value of the track length within the active volume of the TPC, which considerably reduces the resulting distribution by order of magnitude compared to the standard distribution.
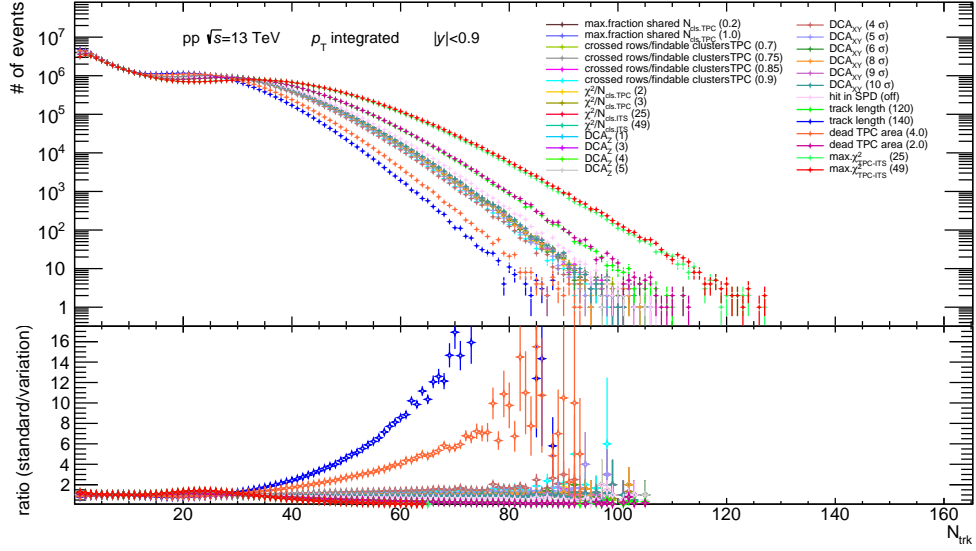
Figure 5.1.: Top: N_{trk} varied-distributions for MB and HM-triggered events. **Bottom:** Ratio N_{trk} varied-distributions to N_{trk} standard-distribution.

The next step is to unfold these varied-track multiplicity distributions to find their true charged particle multiplicity distribution for the analyzed events, which are depicted in Fig. 5.2 together with their ratio to the standard N_{ch} distribution.
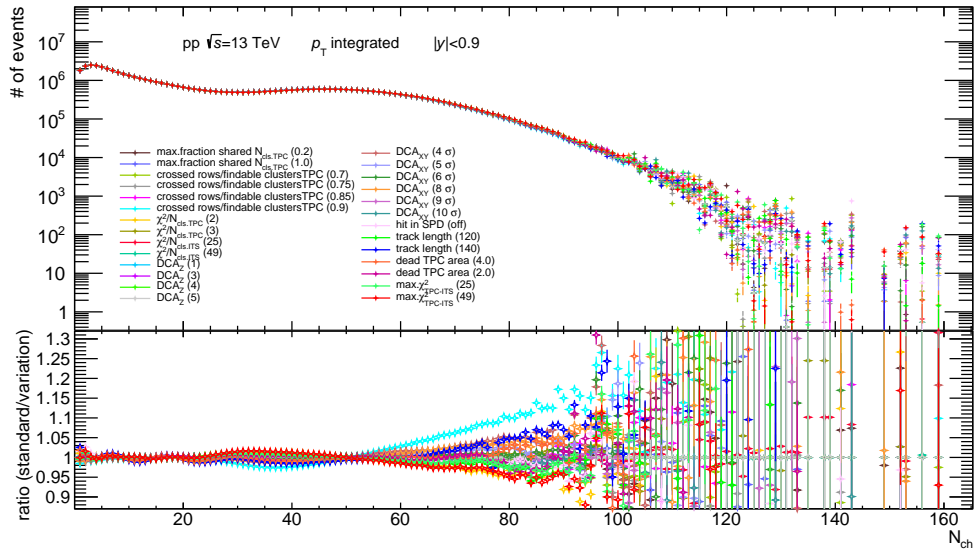
Figure 5.2.: Top: N_{ch} varied-distributions for MB and HM-triggered events. **Bottom:** Ratio N_{ch} varied-distributions to N_{ch} standard-distribution.

After unfolding, the deviations between the varied distributions and the standard distribution become minor, the most significant being the highest value of the criterion quantifying the number of crossed rows over the findable clusters of each track in the TPC. Consequently, even after unfolding, geometrical factors in track reconstruction within the TPC lead to more pronounced deviations from the standard distribution. However, it is remarkable how the unfolding mitigates the detector's influence by retrieving, for all the variations, a true charged particle multiplicity distribution compatible with the MC-true distribution inserted in the algorithm.

To better quantify the influence of varying the standard cut values for selecting tracks, the relative ratios of these varied-unfolded distributions to the standard distribution were estimated and plotted as a function of the charged particle multiplicity in the selected events. These relative ratios were grouped into their corresponding track selection criteria, and the RMS in each group (black dotted line) was determined according to Eq. 5.1, taking n as the number of variations in each group and x_n as the value of each relative ratio. These results are illustrated next in Fig. 5.3. The bump structure that can be observed in some of these relative ratios as a function of the charged particle multiplicity ($20 < N_{ch} < 50$) is due to including the events that trigger HM, where the differences between the varied and standard distributions seem prominent.
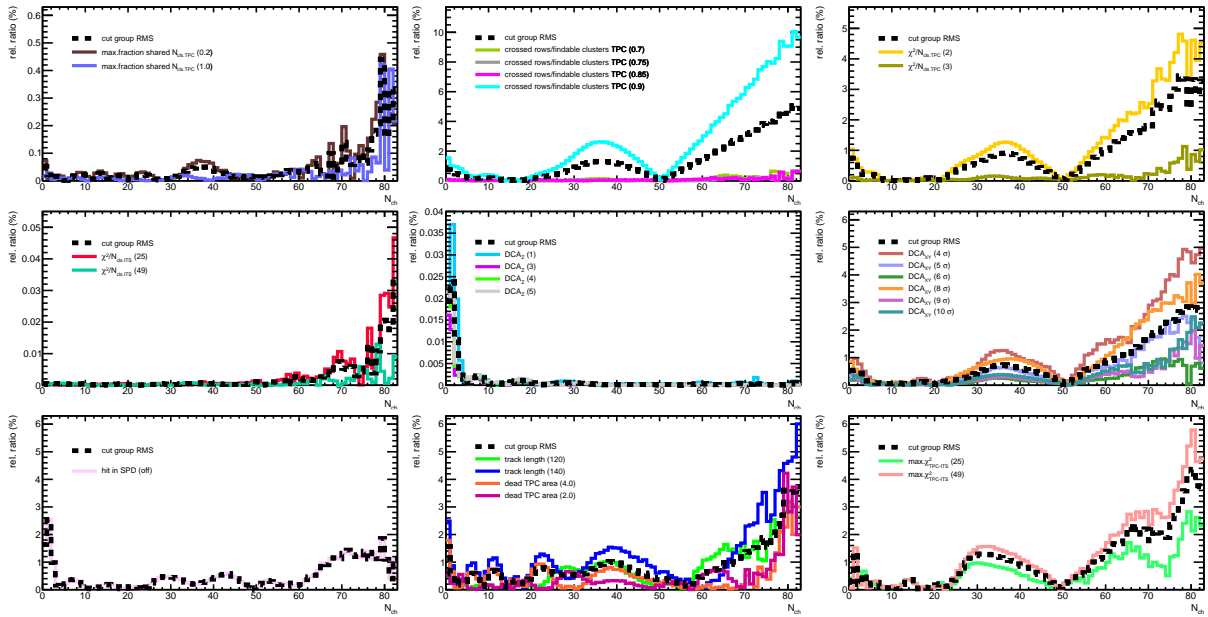
Figure 5.3.: Relative ratios of the varied-charged particle multiplicity distributions to the standard distribution as a function of the charged particle multiplicity in the analyzed events by track selection criteria.

Subsequently, each RMS per cut group was squared and added, considering the contribution of each cut group to the systematic uncertainty as independent. The root square of these sums in each multiplicity bin, of width one, results in the black dotted line depicted in figure Fig. 5.4, plotted with the relative ratio of all the varied-charged particle multiplicity distributions for better visualization. This black dotted line represents the total systematic uncertainties associated with the overall charged-particle multiplicity distribution in the analyzed events.
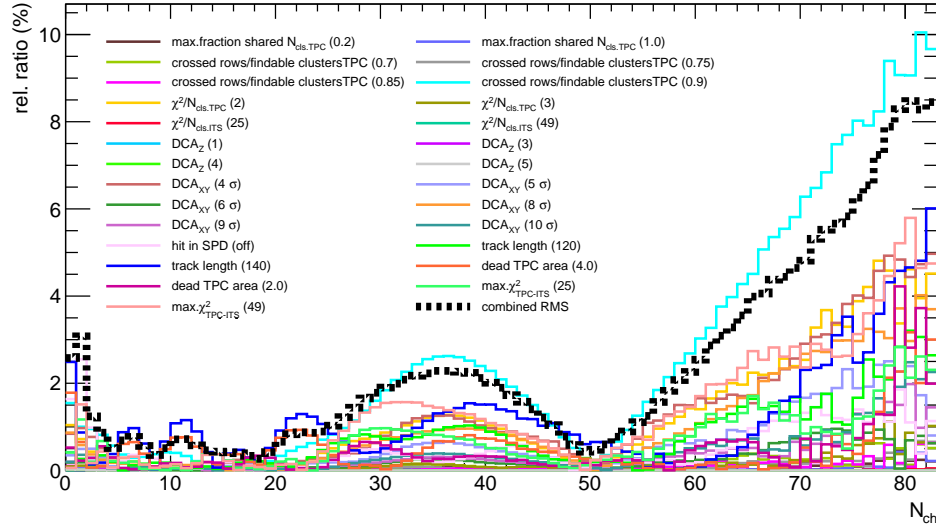
Figure 5.4.: Total systematic uncertainty (black dotted line) along with the relative ratios of the varied-charged particle multiplicity distributions to the standard distribution as a function of the charged particle multiplicity.

However, this analysis aims to assess the systematic uncertainty of the self-normalized charged-particle multiplicity values corresponding to the multiplicity bins where the J/ψ signal is extracted. Therefore, slight modifications, discussed in the following parts, must be introduced to the previously described procedure to quantify these uncertainties accurately.

Systematic uncertainties of the φ-inclusive self-normalized charged-particle multiplicity in the selected multiplcity bins: Assessing the impact of varying the track selection cuts in the correlation analysis implies reproducing the whole procedure with each varied-charged particle multiplicity distribution. When doing this, due to the variation of the track multiplicity per event, there is also a variation in the number of detected J/ψ within the selected multiplicity bins for signal extraction. However, the total number of detected J/ψ in all analyzed events remains constant. These fluctuations of detected J/ψs in bins of multiplicity due to variations of the track selection cut are better visualized in Fig. 5.5 showing the cuts to the TPC geometrical criteria as the variations accounting for the more significant deviations from the standard value, which is compatible with observations from Fig. 5.1. This compatibility is consequent because the process of J/ψ signal extraction in multiplicity bins occurs before unfolding the multiplicity distribution of the analyzed events. These fluctuations of the detected J/ψ in multiplicity bins are a factor to consider when estimating the systematic uncertainties associated with the self-normalized charged-particle multiplicity.

In the meantime, Fig. 5.6 shows the obtained correlation curves of the self-normalized J/ψ yields as a function of the charged-particle multiplicity when reproducing the analysis procedure with each varied-charged particle multiplicity distribution. From this figure, it is essential to highlight that although variations to the track selection criteria imply variations of the J/ψ counts and the mean charged particle multiplicity in bins of multiplicity, the dependency between both observables remains almost constant.

75
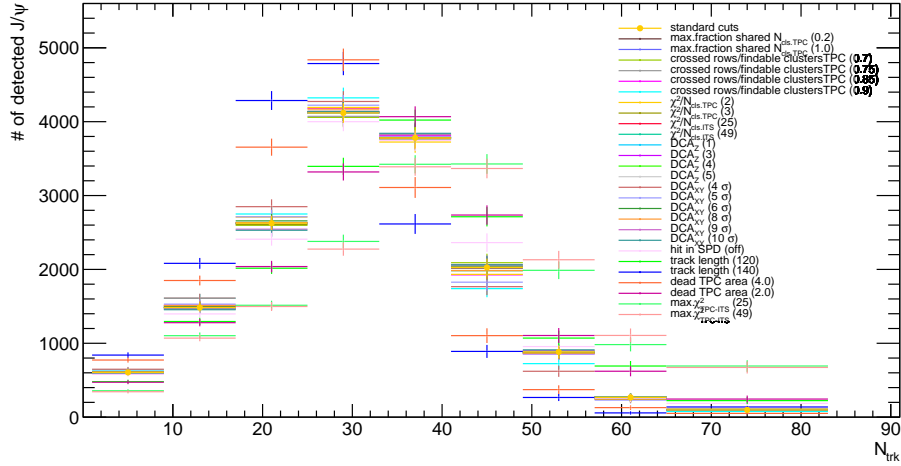
Figure 5.5.: Detected J/ψs in bins of the track multiplicity with standard and varied track selection cuts in the selected events.
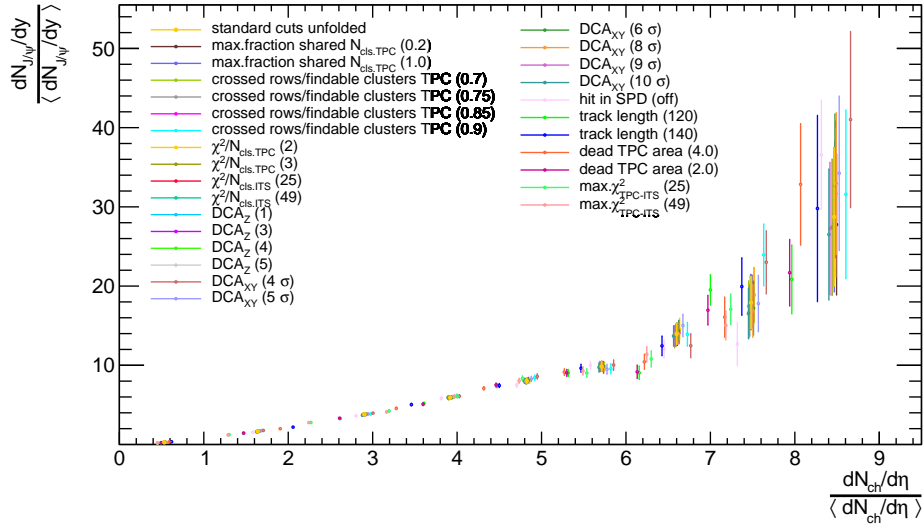
Figure 5.6.: Correlations azimuthal-inclusive and self-normalized J/ψ- N_{ch} with the standard and varied track selection cuts.

Consequently, a more general procedure must be adopted to estimate the relative ratios of the variations to the standard self-normalized charged particle multiplicity values instead of simply using their x-axis values to estimate their relative ratio in each multiplicity bin. The idea is then to calculate a relative ratio of the overall J/ψ- N_{ch} correlation, thus accounting for the fluctuations in the number of J/ψ in bins of multiplicity. The procedure begins by fitting the J/ψ- N_{ch} correlation to a second-order polynomial reasonably characterizing the relationship between these observables. While Fig. 5.7 shows the J/ψ- N_{ch} standard correlation fitted to a second-order polynomial, Fig. 5.8 represents the varied- J/ψ- N_{ch} correlations in logarithmic scale along with their respective second-order polynomial fits.
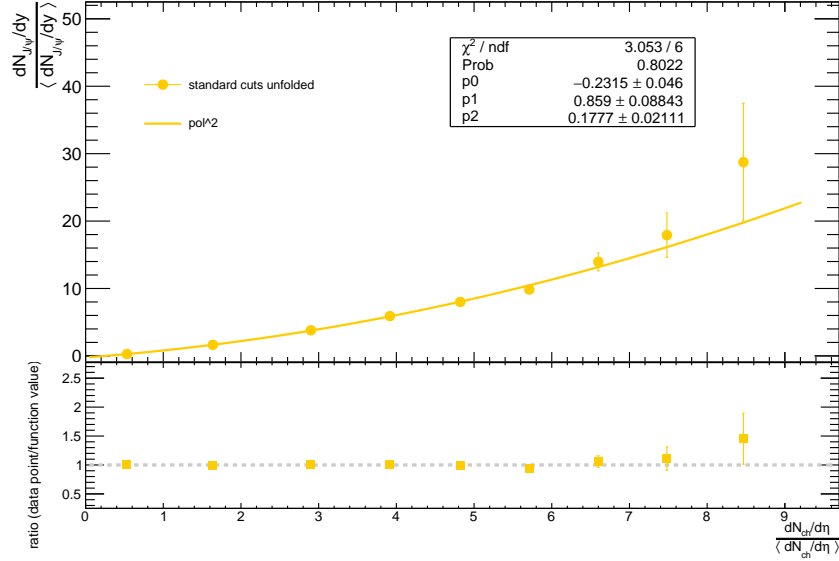
Figure 5.7.: Top: Correlation azimuthal-inclusive and self-normalized J/ψ- N_{ch} with the standard track selection cuts fitted to a second-order polynomial. **Bottom:** Ratio standard correlation point to fit function.
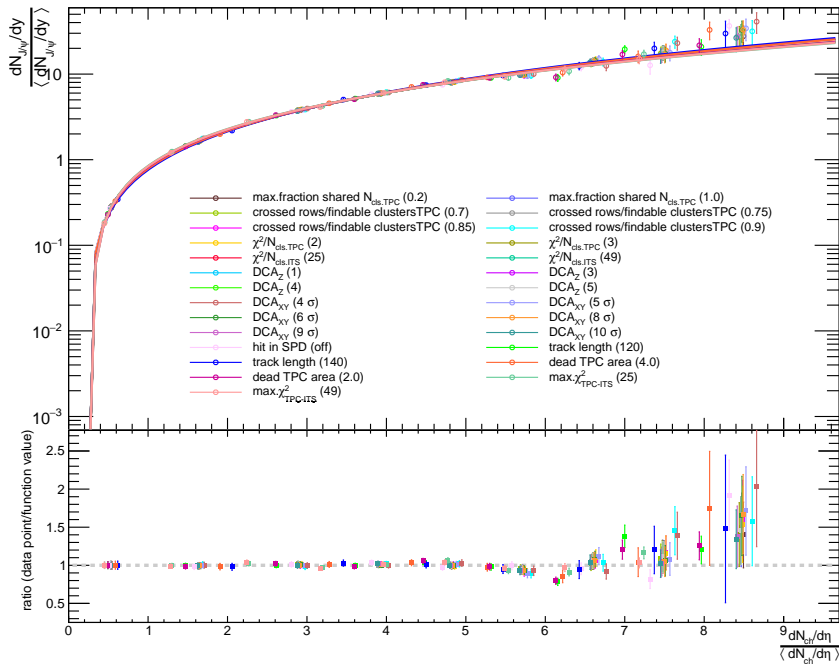
Figure 5.8.: Top: Correlations azimuthal-inclusive and self-normalized J/ψ- N_{ch} with the variations to the track selection cuts fitted to a second-order polynomial in logarithmic scale. **Bottom:** Ratio varied-correlation point to its corresponding fit function.

The figures show an excellent agreement between the correlation curves and their fits in the lower multiplicity bins, while disparities can be observed towards the higher multiplicity bins, especially the last one. Subsequently, the relative ratios (variations to standard) are estimated with the second-order polynomial curves from the fits. The procedure consists of evaluating each second-order polynomial curve in the standard values of the self-normalized J/ψ yields (y-axis of the J/ψ- N_{ch} correlation), thus obtaining a new set of x-axis values for each second-order

polynomial curve corresponding to a variation. The second-order polynomial curve that fits the standard distribution is also evaluated in the standard J/ψ yield values, providing the new standard x-axis values. Finally, the relative ratio is established between each set of new x-axis values found through the fits to the varied correlation and the new set of standard x-axis values found with the fitted curve.

The following steps include grouping the obtained relative ratios by their corresponding track selection criteria and estimating their RMS per group following Eq. 5.1. These groups of relative ratios in bins of multiplicity and their corresponding RMS are represented in Fig. 5.9. Finally, the systematic uncertainty of the self-normalized charged-particle multiplicity values in the selected multiplicity bins is the square root of adding each track selection criteria RMS squared. In Fig. 5.10 this systematic uncertainty is represented by the dotted black line and plotted along with all the relative ratios in the selected bins of multiplcity for better visualization.
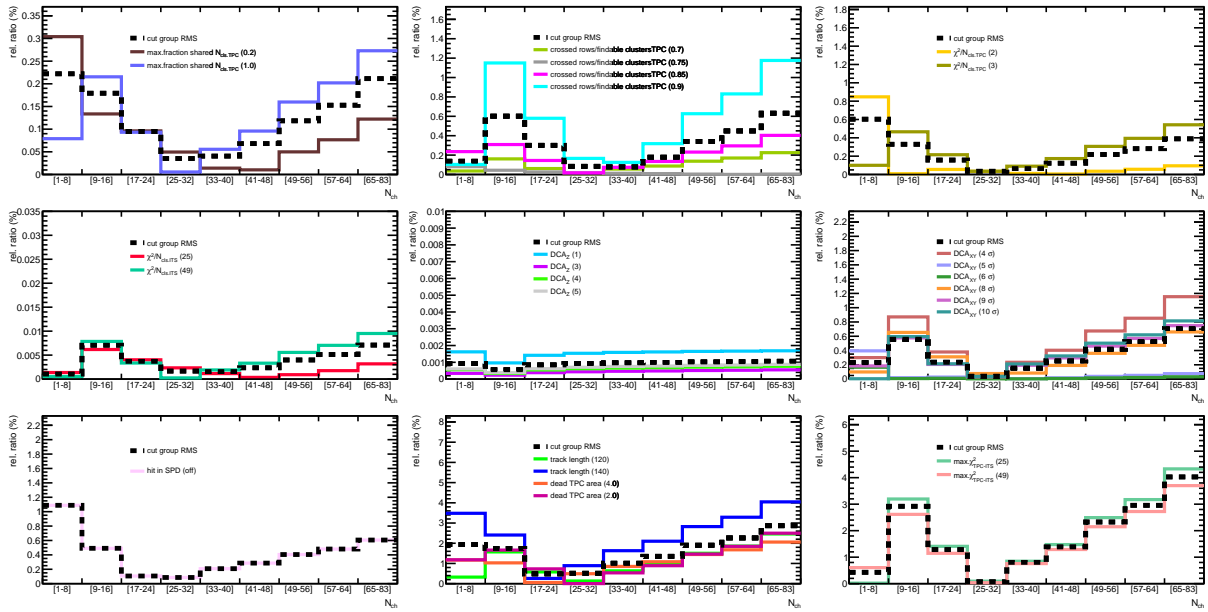
Figure 5.9.: Relative ratios of the varied to the standard-mean charged particle multiplicity values in the selected multiplicity bins, by track selection criteria.
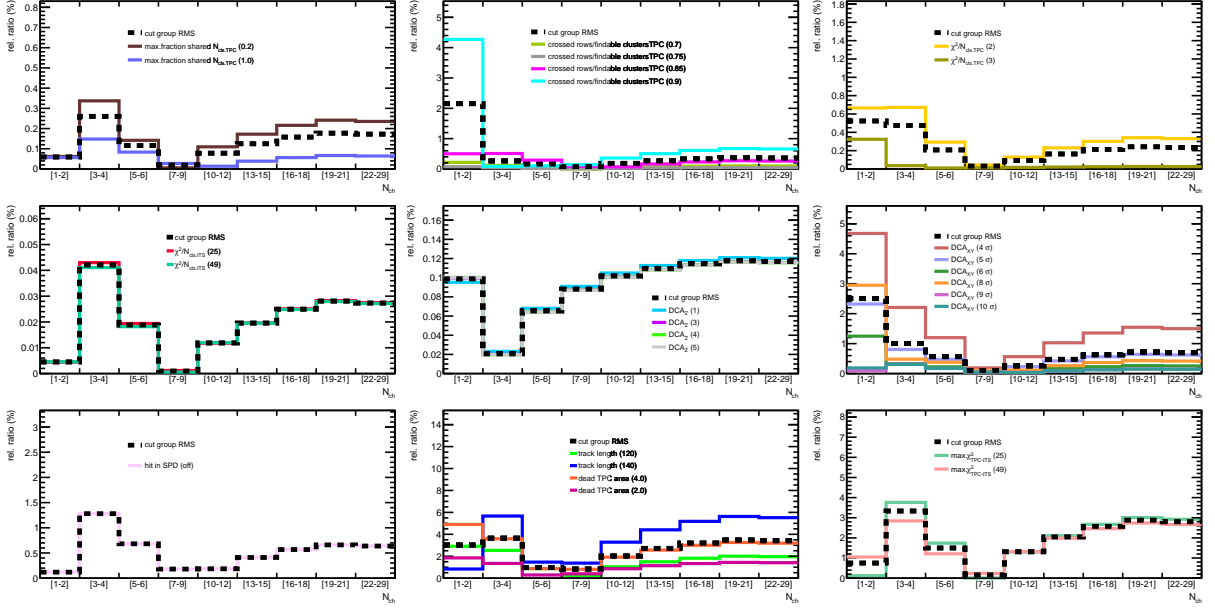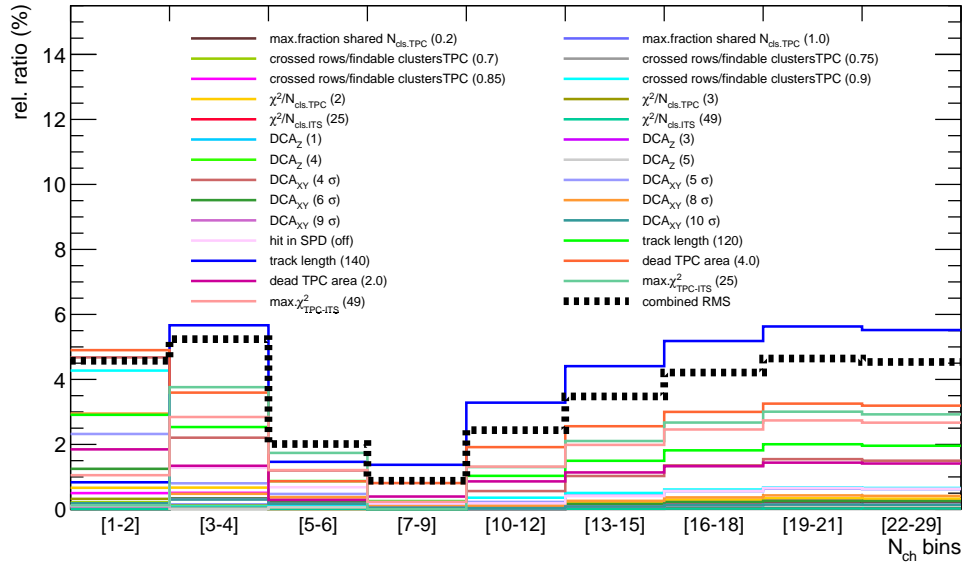
The total systematic uncertainty associated with the φ-inclusive mean charged-particle multiplicity values in the selected multiplicity bins is predominantly driven by the 140 cm track length geometrical cut within the TPC active volume. Although reasonably mitigated after unfolding, this cut remains dominant since the J/ψ signal extraction is performed in raw rather than unfolded multiplicity bins. This cut becomes particularly relevant for the lowest multiplicity bin, which is consequent when observing in Fig. 5.4 the obtained systematics uncertainty for the overall distribution. According to this figure, when setting the crossed raw over findable clusters ratio to 0.9, the uncertainties at higher multiplicities should be around 8%. However, in the selected multiplicity bins, it remains below 1.5%. The systematic uncertainty associated with the first bin accounts for less than 2%, and overall, the systematic uncertainties remain below 5%, reaching their highest value in the last bin.
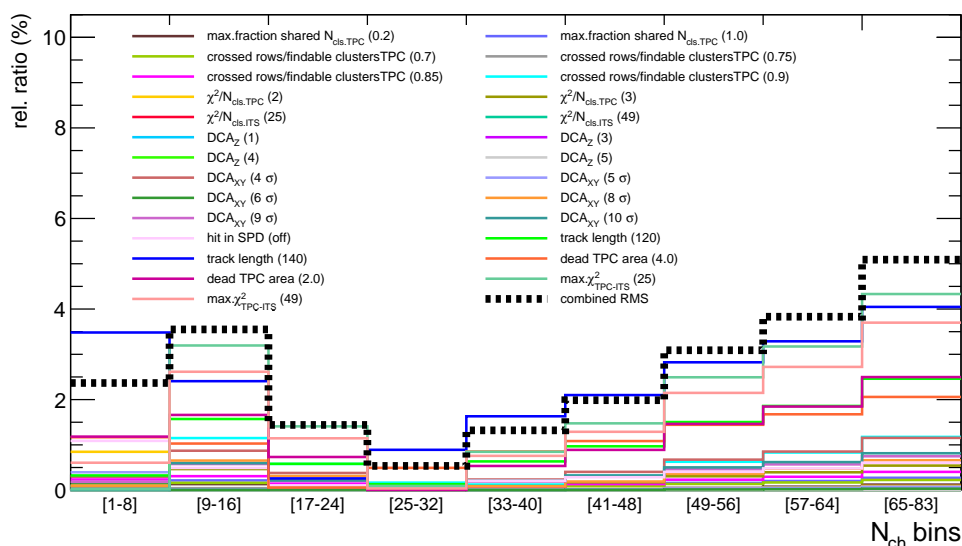
Figure 5.10.: Total systematic uncertainty (black dotted line) and the relative ratios of the φ-inclusive varied-mean charged particle multiplicity to the standard-mean charged particle multiplicity values in the selected multiplicity bins.

Systematic uncertainties for φ-differential mean charged-particle multiplicity in the selected multiplcity bins: The reasoning explained before, when applied to the case of the φ-differential charged particle multiplicity estimator, allows the estimation of the systematic uncertainties associated with the x-axis in the φ-differential J/ψ- N_{ch} correlation. While the plots obtained for the systematic uncertainties associated with the φ-differential N_{ch} distribution are in Appendix B, this section discussed the plots obtained while investigating the systematic uncertainties of the self-normalized charged-particle multiplicity values. In particular, the calculations were made for the toward region and used for the other two regions since the three regions share the same φ-differential charged particle multiplicity estimator.

Similarly to the case of the φ-inclusive N_{ch}, despite the variations to the track selection criteria fluctuating the detected number of J/ψs per multiplicity bin, the dependency of the φ-differential J/ψ- N_{ch} correlation remains almost independent of the variations. This observation is very well displayed in Fig. 5.11 presenting the standard and varied φ-differential J/ψ- N_{ch} correlations. Thus, aiming to include these effects in estimating the relative ratios, the standard and varied correlations are fitted to a second-order polynomial. Fig. 5.12 displays the varied correlations in logarithmic scale and their fits to a second-order polynomial curve. The fits seem to describe the data points with good agreement, although some minor tensions could still be observed, especially in the higher multiplicity bins.

Subsequently, the relative ratios of the values obtained when evaluating the fit functions in the standard self-normalized J/ψ yields quantifying these variations are grouped by track selection criteria and depicted in Fig. 5.13. The figure also includes the RMS of the relative ratios by selection criteria as black dotted lines. The result of adding in quadrature these resultants RMS in the selected bins of multiplicity is the black dotted line in Fig. 5.14 describing the systematic uncertainty of the φ-differential self-normalized charged-particle multiplicity value in the selected multiplicity bins. This uncertainty is also predominantly driven by the 140 cm track length

geometrical cut within the TPC active volume. Unlike the φ-inclusive case, the total systematic uncertainty associated with the φ-differential mean charged-particle multiplicity displays its higher values at low multiplicities. However, overall, the systematic uncertainties are below 6%.
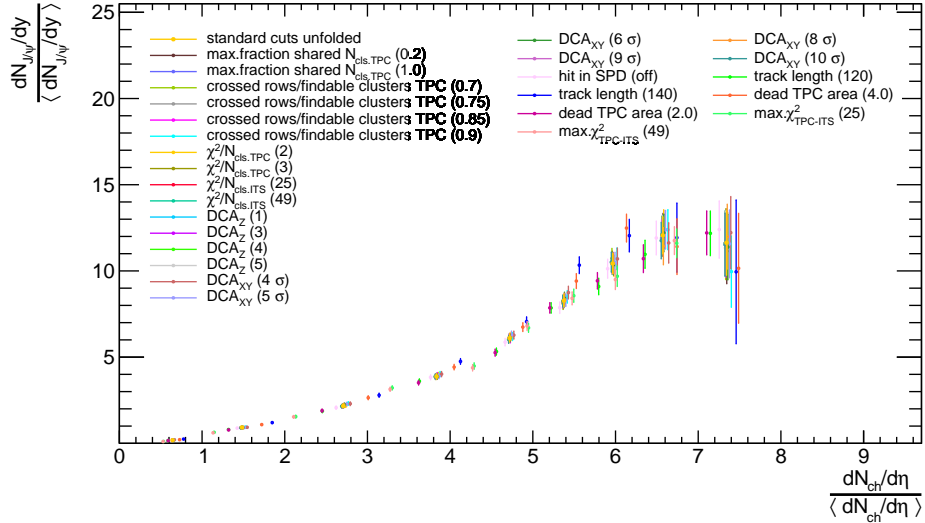
Figure 5.11.: Correlation self-normalized J/ψ- N_{ch} in the Toward azimuthal region with the standard and varied track selection cuts.
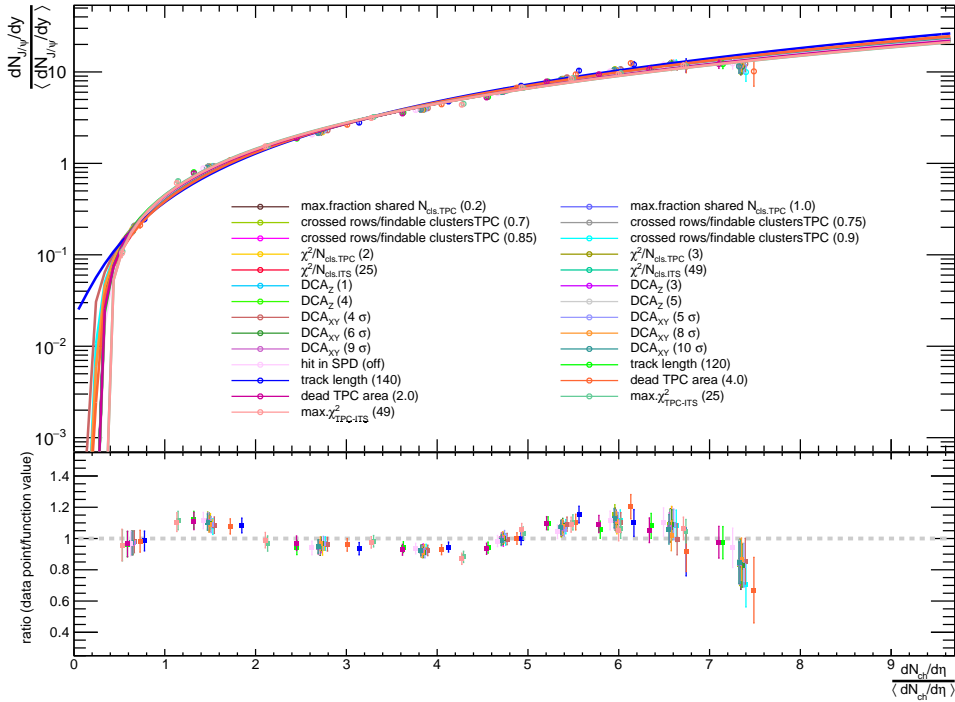
Figure 5.12.: Top: Correlations self-normalized J/ψ- N_{ch} in the Toward azimuthal region with the variations to the track selection cuts fitted to a second-order polynomial in logarithmic scale. **Bottom:** Ratio varied-correlation point to its corresponding fit function.

Figure 5.13.: Relative ratios in the Toward azimuthal region of the varied to the standard-mean charged particle multiplicity values in the selected multiplicity bins, by track selection criteria.

Figure 5.14.: Total systematic uncertainty (black dotted line) and the relative ratios of the φ-differential varied -mean charged particle multiplicity to the standard-mean charged particle multiplicity values in the selected multiplicity bins.

5.1.2. Variations to the Unfolding parameters

The unfolding technique relies on many parameters, which could be varied to explore the stability of the results obtained by this method. In particular, this thesis focused on two aspects that could introduce systematic uncertainties. These are the number of iterations and the use of different unfolding methods.

The number of iterations was set to 50 as the standard parameter, and the unfolding algorithm converged in 14 iterations. While exploring the possible uncertainty associated with the number

of iterations, the standard value varied systematically to explore the performance of the unfolding algorithm with fewer iterations. Applying the unfolding with less than 14 iterations produces large divergencies in the obtained charged particle multiplicity distribution as shown in Fig. 5.15. However, for this method to be valid, it has to converge, so it is not a valid criterion to consider several iterations before the algorithm's convergence. When varying the number of iterations in the unfolding framework above the convergency value, there are no significant differences between the varied and the standard distribution as observed from Fig. 5.16. This figure also includes the ratio between the charged particle multiplicity distribution unfolded with a different unfolding technique: the Iterative Dynamically Stabilized (IDS) Unfolding instead of the standard Iterative Bayesian Unfolding. The variation of this parameter also has no significance on the results. A third aspect involving changing to a different MC generator like EPOS could be a source of uncertainties, but this has not been explored in this thesis.
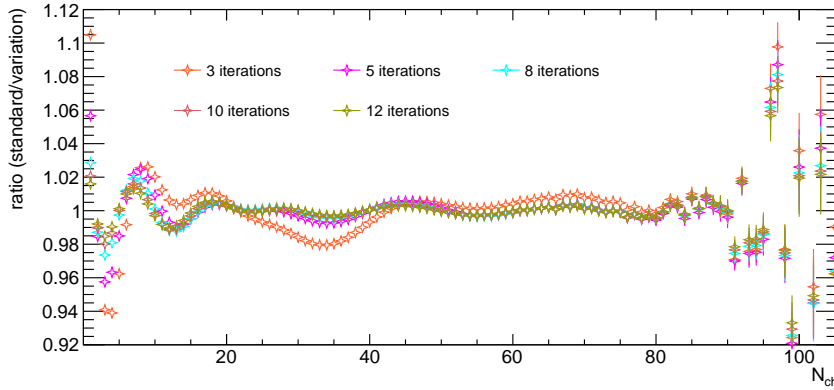
Figure 5.15.: Ratio varied number of iterations N_{ch} distributions to standard number of iterations N_{ch} distribution.
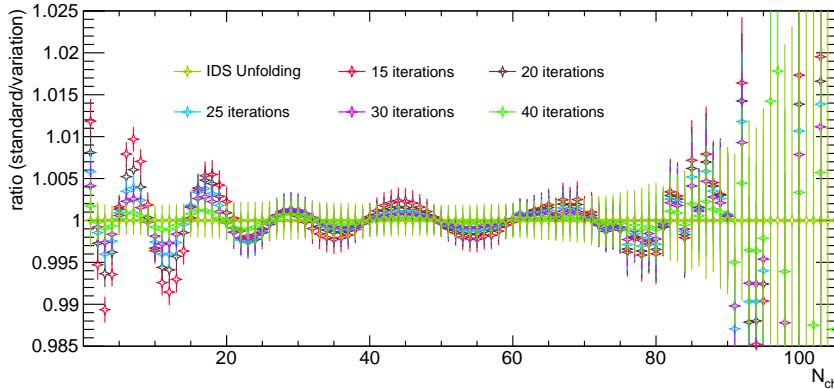
Figure 5.16.: Ratio varied N_{ch} distributions to standard N_{ch} distribution.

Consequently, according to the considerations and analysis discussed in this section, variations to the unfolding technique do not significantly contribute to the total systematic uncertainty associated with the charged particle multiplicity. Therefore, variations to the track selection criteria are taken in this analysis as the sole contributor to the total systematic uncertainty of the self-normalized charged-particle multiplicity values.

5.2. *J/ψ* **yields systematic uncertainty**

The systematic uncertainties of the self-normalized J/ψ yields in bins of multiplicity, are predominantly influenced by the following sources:

- The J/ψ's daughters track selection cuts ($\sigma_{J/\psi-cuts}$)

- The signal extraction method ($\sigma_{J/\psi-SigExt}$)

Considering these sources as independent, the total systematic uncertainty associated with the detected J/ψs in this thesis, $\sigma_{J/\psi}$, is computed as the sum in quadrature of the contributing sources, as in Eq. 5.3:

$$\sigma_{J/\psi} = \sqrt{\sigma_{J/\psi-cuts}^2 + \sigma_{J/\psi-SigExt}^2} \tag{5.3}$$

Both sources of systematic are investigated by varying the values of their standard parameters within reasonable limits, and subsequently the Barlow criterion is used to assess significant variations from non-statistically-significant ones. A variation introducing a deviation below one sigma is considered non-statistically-significant. The Barlow criterion is then applied following the relation:

$$\frac{y_{var} - y_{stand}}{\sqrt{\sigma_{Est.var}^2 - \sigma_{Est.stand}^2}} < 1 \tag{5.4}$$

Where y_{var} and y_{stand} are the varied and standard J/ψ yields, respectively, in each multiplicity bin while in the denominator of the expression $\sigma_{Est.var}$ and $\sigma_{Est.stand}$ are their corresponding statistical uncertainties. Applying this criterion allows for mitigating the effect of the statistical uncertainties accompanying the J/ψ yields in the analyzed events, giving a better estimate of when a variation is significant and not entirely yielded by statistical uncertainties. After applying the Barlow criterion, the impact of the remaining significant variations is quantified by computing their J/ψ yields relative ratios to the standard value. Subsequently, as given by Eq. 5.1, the RMS of these relative ratios measures the systematic uncertainty associated with the investigated source in the analyzed bin of multiplicity.

A clear disclaimer of this procedure is its tendency to bias the results toward higher uncertainty values. This bias arises from applying the Barlow criterion, which excludes non-statistically-significant variations, thereby emphasizing contributions to systematic uncertainties that deviate significantly from the standard value. As a result, interpreting the systematic uncertainties for the J/ψ yield in this thesis must account for this inherent bias. The use of the RMS as an estimator for standard deviation is reasonable, given the expectation of the variations producing outputs that approximate a Gaussian distribution around the standard value, as the parameters are symmetrically varied toward their lower and upper bounds. In the alternative case of dropping the Barlow criterion, the standard deviation could be directly computed from the output values as $(x_{max} - x_{min})/\sqrt{12}$. However, this thesis did not consider this method since it performs well if the number of trials is substantial and the outputs are uniformly distributed, but it

becomes less effective if the outputs follow a Gaussian distribution. An alternative approach that could have been applied, especially in the specific case of this thesis, is to drop the Barlow criterion and reduce the impact of statistical uncertainties by grouping several multiplicity bins to subsequently estimate the RMS of the variations.

The two subsequent subsection in this section will present the detailed results of the systematic uncertainties calculations prposed for this thesis when applied to the case of p_T integrated J/ψ signal in φ-inclusive multiplicity bins, while the same type of results for the remaining signal extraction cases considered in this thesis (φ-inclusive multiplicity bins for J/ψs emitted with high and low p_T as well as the cases of φ-differential low, high and p_T integrated emitted J/ψs) are collected in Appendix C. The last subsection discusses the total systematic uncertainties obtained for all analyzed J/ψ signal extraction cases.

5.2.1. Variations to the J/ψ's daughters track selection cuts

Table 5.2 lists the standard values, highlighted in black, and the variations applied to the J/ψ's daughter track selection criteria to investigate this source of systematic uncertainty.

Selection	Value
pseudorapidity	$\lvert\eta\rvert < 0.9$
transverse momentum	$p_\mathrm{T} > 1.0~\mathrm{GeV}/c$
ITS refit	required
TPC refit	required
DCA_z	< 1.0, **3.0 cm**, 4.0, 5.0
DCA_{xy}	< 0.2, 0.5, **1.0 cm**, 2.0, 3.0
$\chi^2/N_{cls.TPC}$	< 3.0, 2.5, **4.0**, 5.0, 10.0
$N_{cls.TPC}$	> 50, 60, **70**, 80, 90
Hit in SPD	required in at least one layer
kink topologies	daughters **rejected** or accepted
PID electron inclusion	-2.75, -2.5, -2.25, -2.0, **-3.0** $< n\sigma_{TPC,e} <$ **3.0**, 3.5, 3.25, 2.75, 2.5
PID proton exclusion	$n\sigma_{TPC,p} > 2.5$, 2.75, **3.0**, 3.25, 3.5
PID pion exclusion	$n\sigma_{TPC,\pi} > 2.5$, 2.75, **3.0**, 3.25, 3.5

Table 5.2.: Standard values and variations of J/ψ's daughter tracks selection criteria

These selection criteria are not treated as independent in this analysis since they are explicitly optimized for selecting the J/ψ decay electrons while rejecting the remaining particle species. No variations were applied to the kinematic selection criteria (pseudorapidity and transverse momentum), as the focus of this thesis is exclusively on midrapidity events, and selecting electrons with lower p_T would just increase the background. The criterion requiring a hit in the SPD also did not vary, though previous studies have reported deviations when modifying this parameter. Additionally, the ITS and TPC refit requirements are consistently enforced,

as only fully reconstructed tracks are of interest in this study. The J/ψ yields obtained from individually applying the 33 variations are represented in Fig. 5.17. The figure consists of nine plots, each corresponding to a different multiplicity bin for J/ψ signal extraction, with an upper and a lower panel. The upper panel shows the self-normalized J/ψ yields obtained per variation, with the black line representing the standard J/ψ yield value and the grey line indicating its uncertainties. At the same time, the bottom panel shows the calculated Barlow criterion for each variation with a black dotted line at unity distinguishing significant from non-statistically-significant variations.
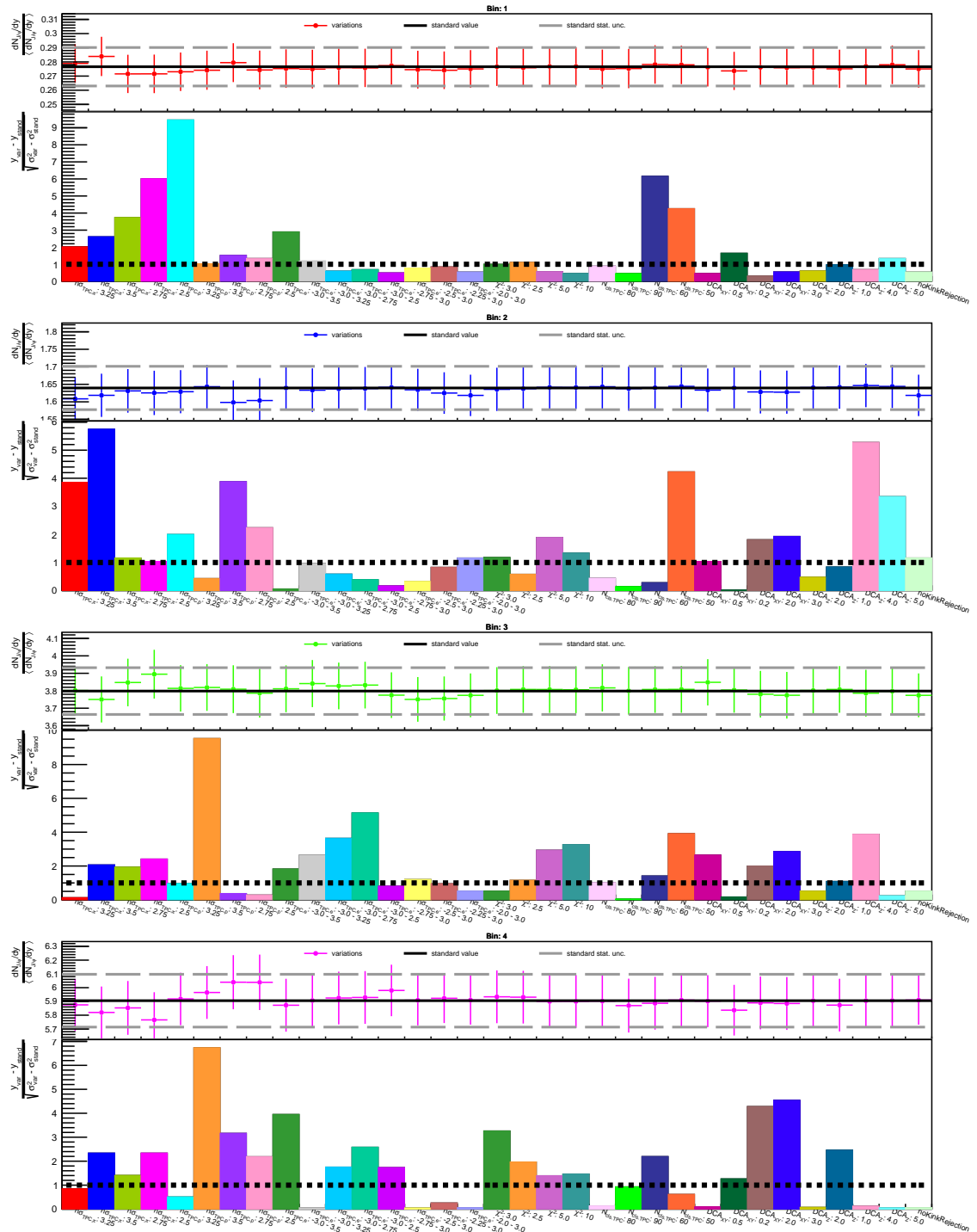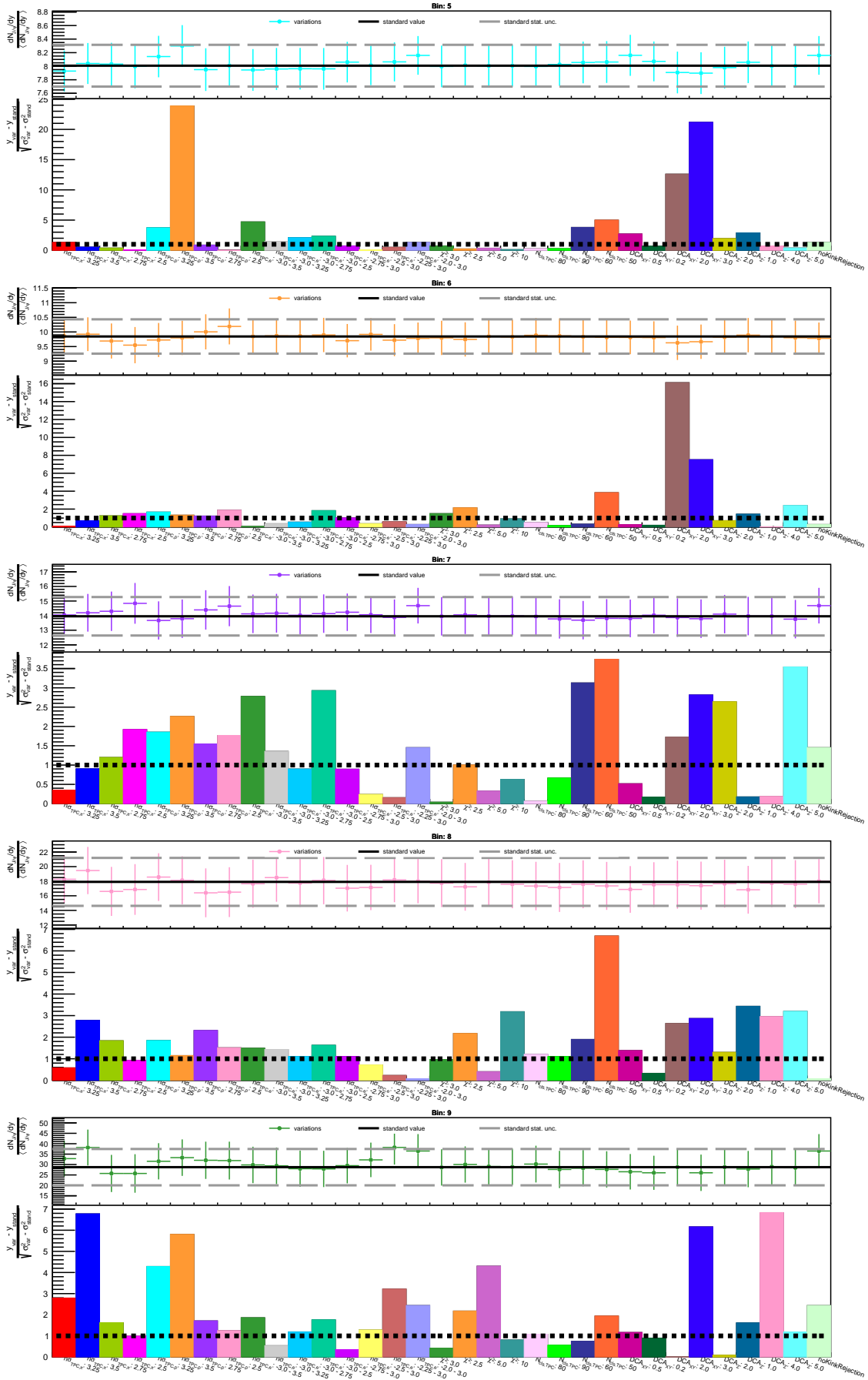
Figure 5.17.: Top: Self-normalized J/ψ yields per variation to the J/ψ's daughter tracks selection criteria. **Bottom:** Barlow criterion of each variation.

In Fig. 5.17 only the variations above the black dotted line are used to estimate the systematic uncertainties by calculating their relative ratios to the standard value and the RMS of these relative ratios. This final calculation is shown and discussed at the end of this section.

The plots of Fig. 5.17 do not indicate any single cut or criterion as the dominant source of systematic uncertainty across the multiplicity bins, although as expected, values belonging to more broad or restrictive cuts result in the higher Barlow criterion values. It is also important to note that, despite the application of the Barlow criterion, the statistical uncertainties of the J/ψ yields may still play a significant role in these systematic uncertainties since the deviations of the variations to the standard J/ψ yield are more prominent in the higher multiplicity bins. These conclusions also hold for the results obtained in φ-differential and the J/ψ-p_{T} differential cases depicted in the appendices.

5.2.2. Variations to the J/ψ signal extraction method

This thesis explores two main factors to assess the reliability of the reported standard J/ψ yields per multiplicity bin due to signal extraction. The first factor involves systematically varying the parameters influencing the primary signal extraction method. These parameters are the lower and upper ranges of the invariant mass histograms per multiplicity bin and the ranges where the J/ψ signal is extracted. The second factor involves comparing two alternative background subtraction techniques: the Like Sign Pairs and a third-order polynomial fit. The Like Sign Pairs method offers a background description by pairing electrons with electrons and positrons with positrons belonging to the same event, while the other signal extraction method describes the background of the dielectron invariant mass histogram by only a third-order polynomial function.

Table 5.3 overviews the parameter variations applied with the primary signal extraction method (Event Mixing technique combined with a second-order polynomial fit) in addition to the two alternatively investigated signal extraction methods.

Signal Extraction	**Event Mixing + 2nd order polynomia**, like sign pairs, 3rd order polynomia
Fit range lower limit	1.8, **2.0**, 2.2
Fit range upper limit	3.6, **4.0**, 4.1
Signal extraction window lower limit	2.88, **2.92**, 2.96
Signal extraction window upper limit	3.12, **3.16**, 3.20

Table 5.3.: signal extraction settings

At the same time, Fig. 5.18 shows the self-normalized J/ψ yields obtained when applying all the variations listed in this table in bins of multiplicity. In the figure, each plot belongs to an analyzed multiplicity bin and is divided into an upper and a bottom panel, showing the J/ψ yields obtained by variation compared to the standard J/ψ yield and the estimated Barlow criterion, respectively. After applying the Barlow criterion, the total systematic uncertainty corresponding to each multiplicity bin due to this source is estimated as the RMS of the significant variations following Eq. 5.1 with n as the number of significant variations and x_n

as the relative ratio per variation. This calculation is depicted per analyzed J/ψ yield cases in the following subsection. Although the plots of Fig. 5.18 do not reveal any single variation as the primary source of systematic uncertainty across the multiplicity bins, the third-order polynomial fit causes significant deviations in the lower multiplicity bins. Moreover, the lower and upper-range variations of the signal extraction method tend to show more significant deviations across all the multiplicity bins. These observations are consistent for the remaining J/ψ signal extraction cases analyzed in this thesis and collected in the appendices.
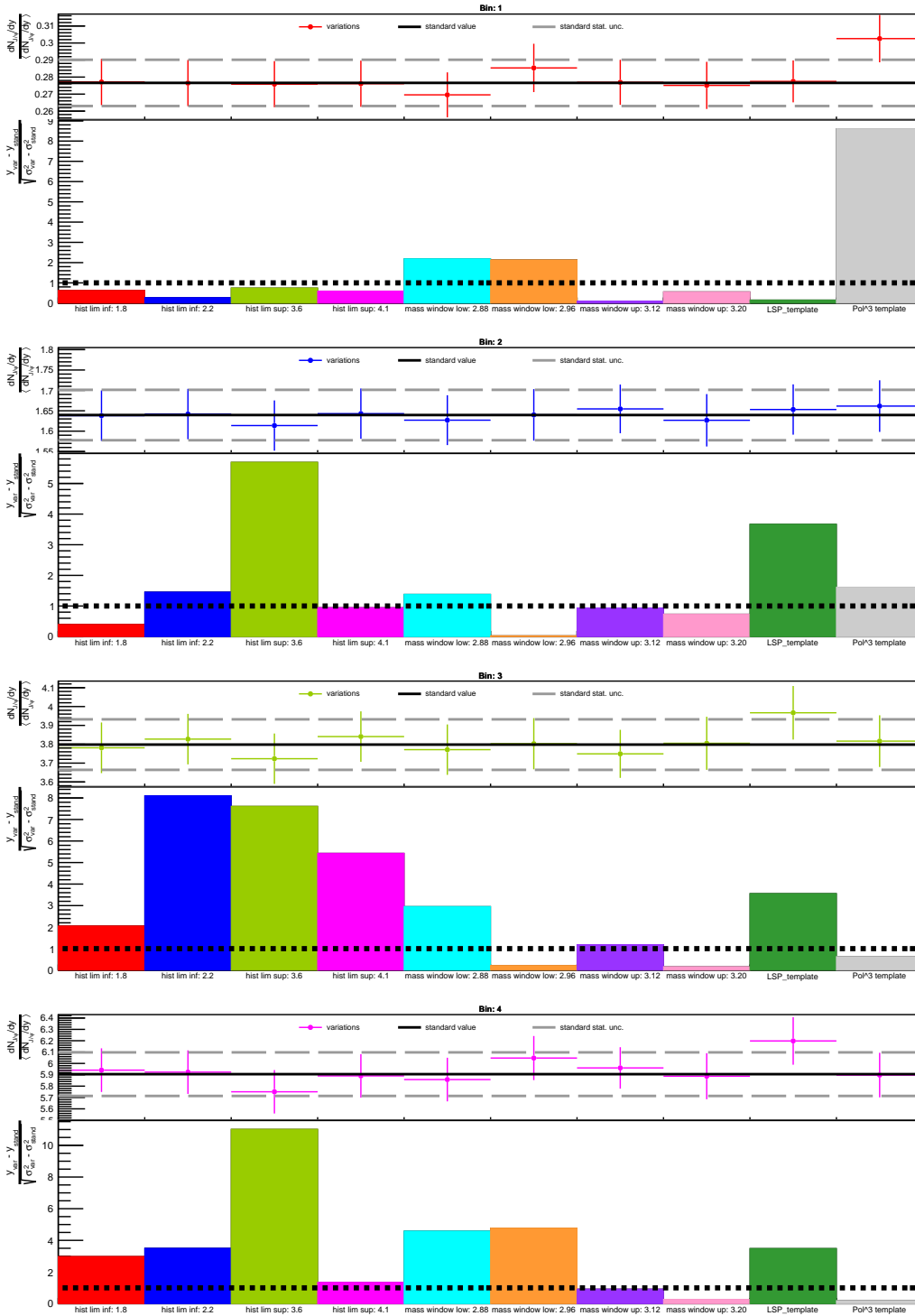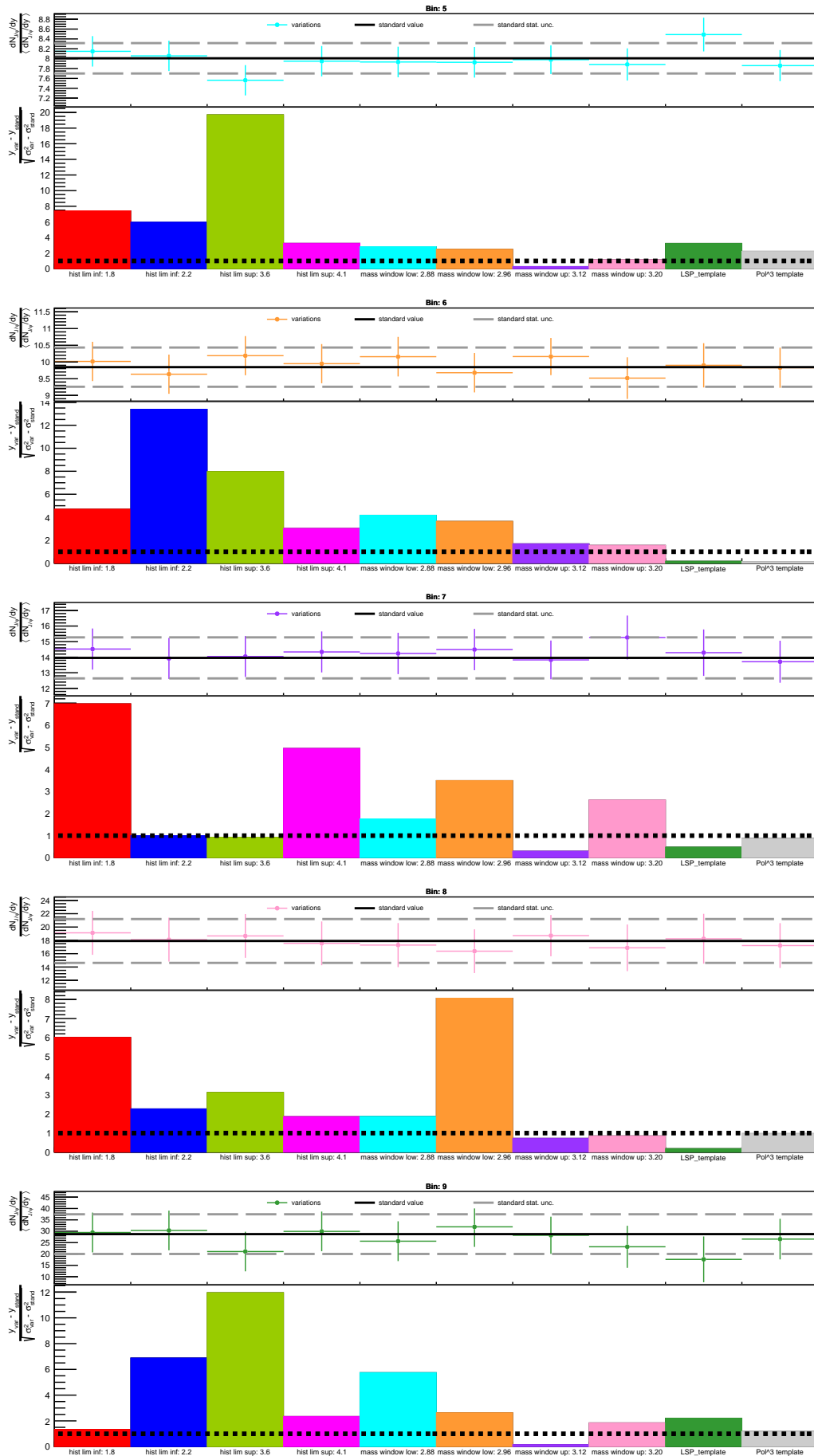
Figure 5.18.: Top: Self-normalized J/ψ yields per variation to the signal extraction method. **Bottom:** Barlow criterion of each variation.

5.2.3. Total J/ψ yields systematic uncertainty

The last two subsections discussed the procedure to estimate the contributions of the two primary sources of systematic uncertainties influencing the total systematic uncertainty associated with the J/ψ yields in multiplicity bins. Finally, Fig. 5.19 shows the estimated contributions of the discussed sources to the systematic uncertainties along with the total systematic uncertainty, given by Eq. 5.3, for J/ψs emitted with integrated, high, and low p_T in the φ-inclusive multiplicity intervals. Figures 5.20, 5.21, and 5.22 show the equivalent results but for the azimuthal regions.

Figure 5.19 depicts values of total systematic uncertainties becoming more prominent in the last multiplicity bin, reaching 25% for inclusive p_T J/ψs, 31% for J/ψs emitted at high p_T, and 12% for low p_T J/ψs. In case of J/ψs detected at low and integrated p_T, the signal extraction accounts as the higher contributing source to the total systematic uncertainty, presumably due to the higher J/ψ's statistical uncertainties in the last multiplicity bin. However, when analyzing the case of the high p_T emitted J/ψs, then varying the J/ψ' daughters track cuts are the principal contribution to the total systematic uncertainty, primarily because of the TPC's restricted capabilities to resolve electrons in high multiplicity environments as their p_T increases.

(a)

(b)

(c)
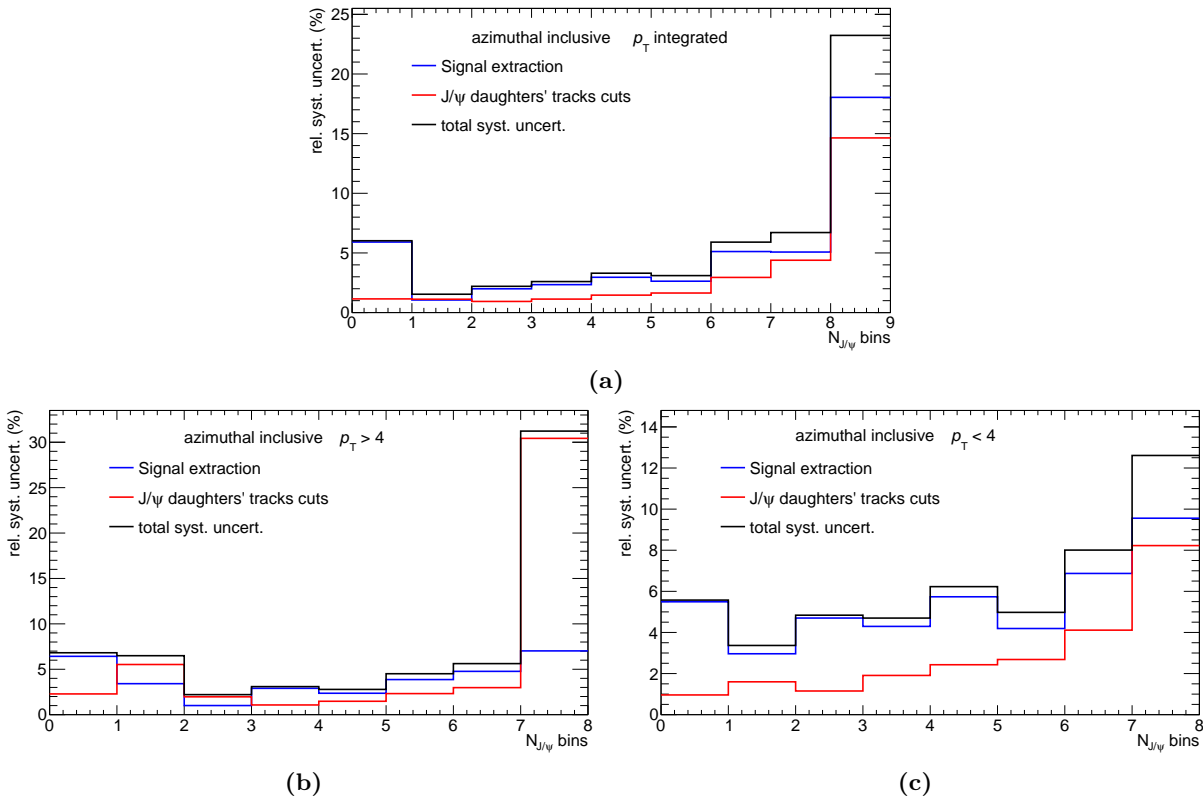
Figure 5.19.: Systematic uncertainties of the azimuthal inclusive self-normalized J/ψ yields.

The figures 5.20, 5.21, and 5.22, show the total systematic uncertainties of J/ψs-p_T integrated cases reaching their higher values in the last multiplicity bin of 13%, 14%, and 11% for the Towards, Transverse, and Away regions, respectively. The systematic uncertainties related to the

signal extraction method mainly contribute to the total systematic uncertainty when analyzing the low and p_T-integrated cases. In contrast, varying the J/ψ' daughters track cuts is the most influential source of systematics when analyzing the results obtained for high-p_T J/ψs case. However, unlike the φ-inclusive multiplicity case, the total systematic of the high-p_T emitted J/ψs show higher values for the first multiplicity bin, which is primarily produced by the signal extraction source of systematics and is due to the lower statistic in those first bins difficulting an accurate background characterization. In the last bin, the total systematic uncertainties in the Toward region reach values of 27% and 18% for high and low-p_T J/ψs, respectively. Meanwhile, the systematic uncertainty in the Transverse region of low-p_T J/ψs sees the highest value of 23% in the penultimate multiplicity bin, unlike the high-p_T J/ψs having a maximum systematic uncertainty of 13% given by the last bin. Finally, in the Away region, for J/ψs emitted at low-p_T the highest value of the total systematic uncertainty is 18%, while for high-p_T J/ψs the total systematic uncertainty in the multiplicity bins does not surpass the value of 7% reached in the first bin.

The reported systematic uncertainties are primarily influenced by, or correlated with, statistical uncertainties. For high-p_T J/ψ mesons, the largest uncertainties typically appear in the last multiplicity bins, where the TPC resolution degrades and the available statistics are limited. Conversely, when the highest systematic uncertainties are observed in the first bins, this is also attributed to low statistics, which makes a reliable background reconstruction difficult.

(a)

(b)

(c)
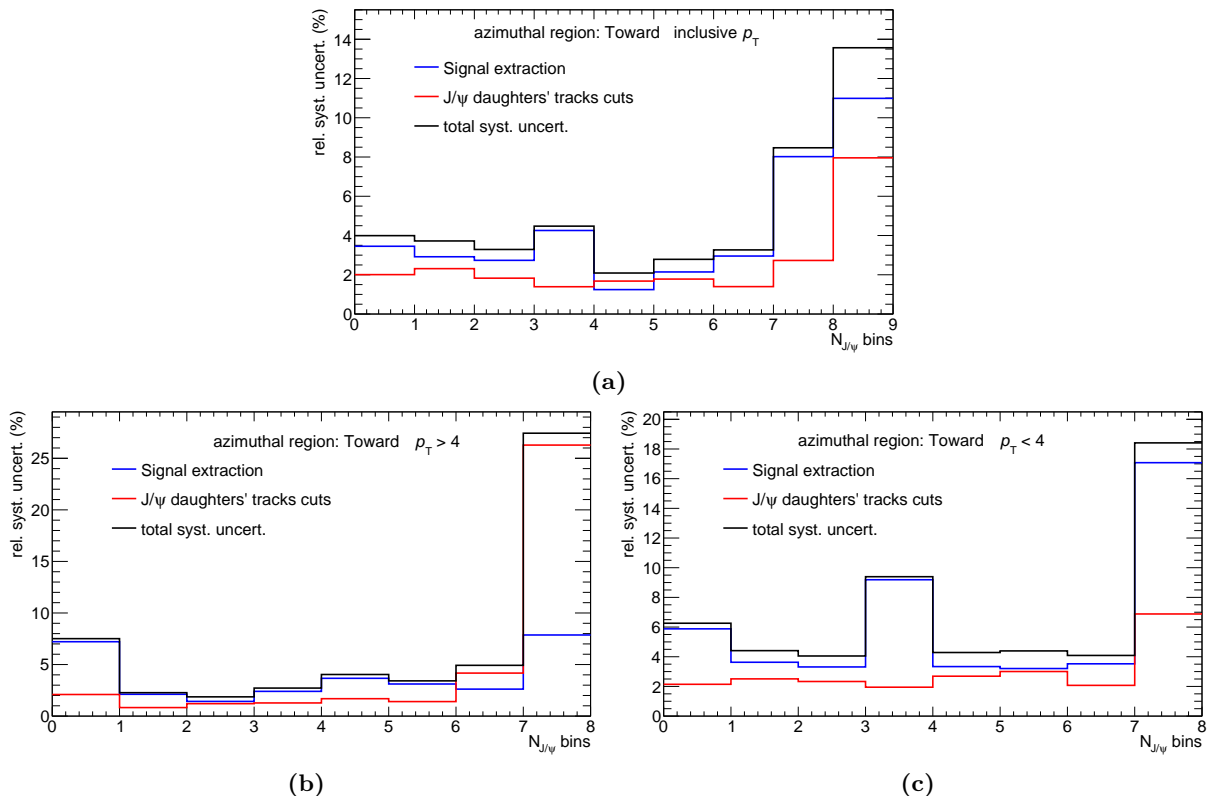
Figure 5.20.: Systematic uncertainties of the Toward region self-normalized J/ψ yields.

(a)

(b)

(c)
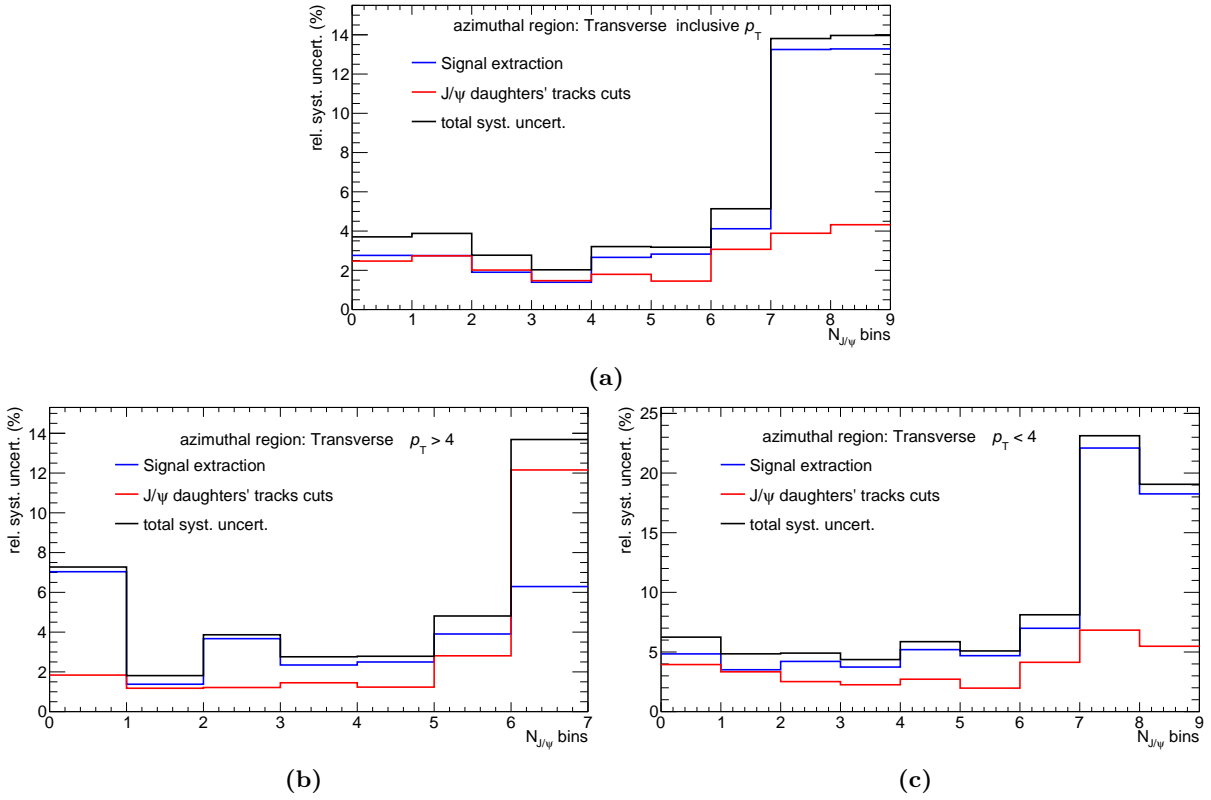
Figure 5.21.: Systematic uncertainties of the Transverse region self-normalized J/ψ yields.

(a)

(b)

(c)
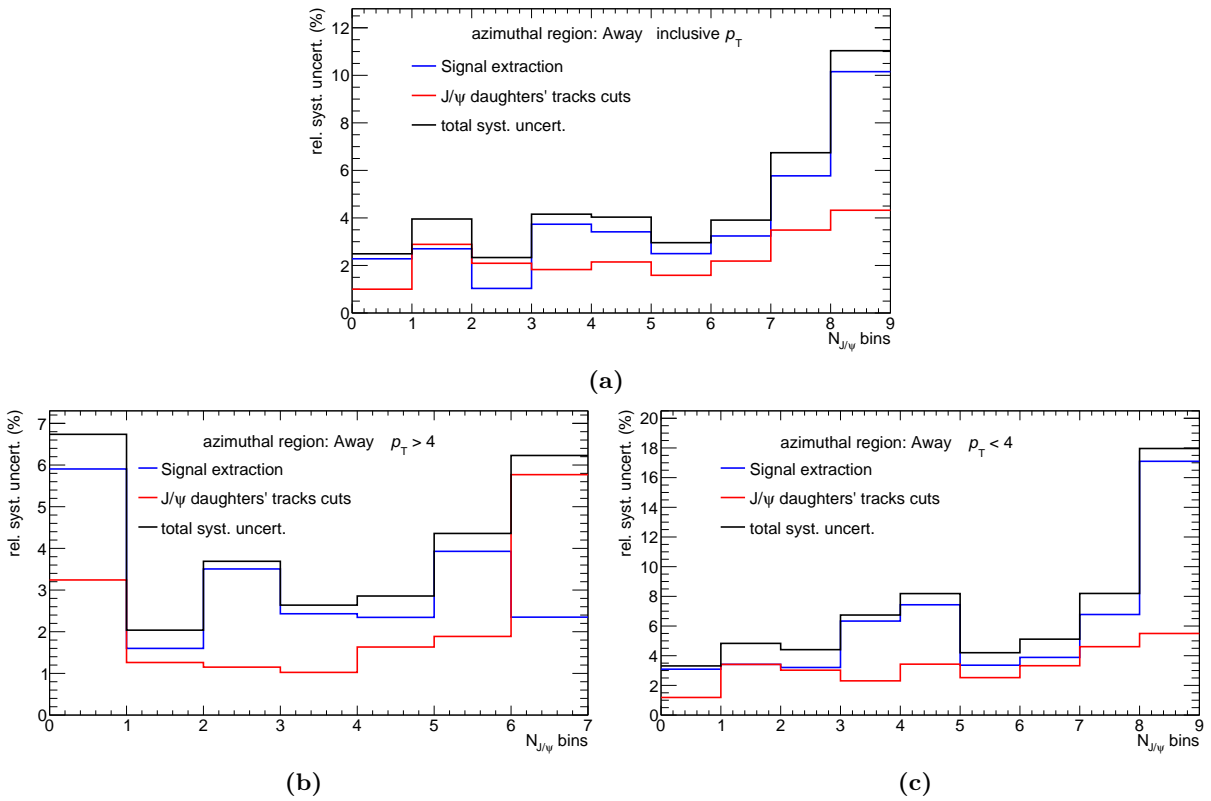
Figure 5.22.: Systematic uncertainties of the Away region self-normalized J/ψ yields.

6. Results

This chapter presents the main contribution of this thesis: the measurement of the J/ψ yield as a function of the charged-particle multiplicity in the three defined azimuthal regions (Toward, Transverse, and Away), following the procedure detailed in Chapter 4. The results are organized into two main sections based on the transverse momentum (p_T) of the emitted J/ψ mesons. The first section presents the J/ψ-N_{ch} correlation for J/ψ mesons integrated over p_T values. Meanwhile, the second section analyses the exact correlation by separating low-p_T and high-p_T J/ψ mesons, thereby offering a differential perspective. Finally, the third section includes a complementary study based on ALICE Monte Carlo simulations exploring the azimuthal J/ψ-N_{ch} correlations in different modeling scenarios.

6.1. J/ψ meson yields as a function of N_{ch} in J/ψ azimuthal regions

Figure 6.1 shows the self-normalized J/ψ yields as a function of the charged-particle multiplicity in pp collisions at $\sqrt{s} = 13$ TeV, for inclusive-p_T J/ψ mesons in the Toward, Transverse, and Away azimuthal regions. Throughout this chapter, the gray dotted line in the plots represents linearity with unit slope ($y = x$) and is depicted only as a reference for what is called "linear behavior". Vertical bars will always indicate statistical uncertainties on each data point, while, when shown, the systematic uncertainties are represented as boxes and estimated as discussed in Chapter 5 .
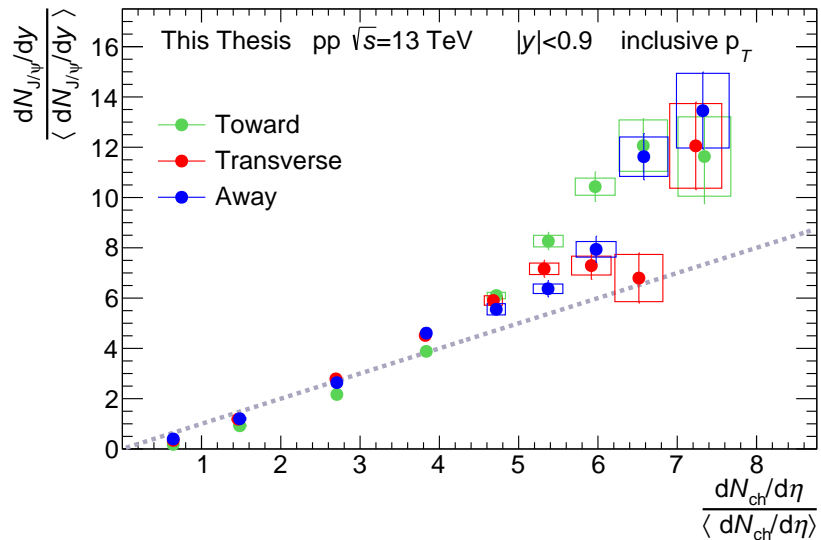
Figure 6.1.: Self-normalized J/ψ yields as a function of the charged particle multiplicity in regions of the azimuthal plane relative to inclusive p_T J/ψ mesons.

The figure shows a similar stronger-than-linear increase of the self-normalized J/ψ yield as a function of the charged particle multiplicity across the Toward, Transverse, and Away regions. Specifically, the J/ψ-N_{ch} correlation evolves from data points lying below the linear trend (in the first two multiplicity intervals) to data points aligning with the diagonal at intermediate multiplicities (approximately 2-5 times the mean multiplicity) and eventually exceeding the linear scaling at the highest multiplicities (above 6 times the mean).

This behavior closely mirrors the trend observed in the azimuthally inclusive J/ψ-N_{ch} correlation, which could be explained within the MPI scenario as follows. The lower J/ψ production in events with low charged-particle multiplicity or collisions with values below the average multiplicity observed in MB-pp collisions at $\sqrt{s} = 13$ TeV hints towards events that are predominantly soft, characterized by low-p_T particle production and minimal hard scatterings. Moreover, heavy quarks production, such as the charm quarks constituting J/ψ mesons, require large momentum transfers or hard partonic interactions; therefore, the probability of forming a J/ψ meson is lower in these soft-dominated pp events. As the multiplicity increases, the correlation between J/ψ yields and the charged-particle multiplicity evolving towards a diagonal and a stronger-than-the-diagonal behavior indicates a progressively larger contribution from hard partonic interactions. At very high multiplicities, five to six times the mean minimum-bias multiplicity, the J/ψ yield increases markedly faster than the charged particle multiplicity, possibly reflecting a saturation of the N_{ch} observable. This scenario signals a regime with an anomalous increase of hard partonic scatterings, or it could point to an underlying mechanism (non-prompt J/ψ, QGP-like medium ...) that selectively enhances J/ψ production cross section relative to charged-hadron production at very high multiplicities.

A comparison between the measured results and the PYTHIA8 Monasch 2013 tune simulations reported by Ref. [1] is presented in Fig. 6.2. The plots reveal notable discrepancies between data and simulations, with PYTHIA8 systematically underestimating the J/ψ yields across the different azimuthal regions. This trend is consistent with PYTHIA8's underprediction of the inclusive J/ψ-N_{ch} correlation at midrapidity, as previously discussed in Sec. 2.2.2.

Given that the azimuthal-inclusive J/ψ-N_{ch} correlation at midrapidity exhibits a stronger-than-linear increase, one might naively expect a similar trend in the azimuthal-dependent results. However, the study presented in [1], and shown in Fig. 6.2, does not support this expectation by predicting a weaker-than-linear increase of the J/ψ yield with the charged particle multiplicity in the Transverse region. This behavior was attributed to the absence of autocorrelation effects from the J/ψ production mechanisms in that region (see Sec. 2.3). In contrast, the Toward and Away regions exhibit a slightly stronger-than-linear and approximately a linear increase, respectively, in the simulation. These trends were explained by contributions from the J/ψ decay daughters and associated non-prompt decay products in the Toward region and by decay products of the recoiling B-jets in the Away region. However, as observed, the ALICE measurements presented in this thesis do not reflect this azimuthal pattern. A stronger-than-linear increase of the J/ψ yields with multiplicity is observed in all three regions, including the Transverse region. These observations challenge the assumptions underlying the PYTHIA8 modeling, particularly the expectation that the Transverse region is free from autocorrelation effects. If autocorrelations associated with the J/ψ production mechanism are indeed responsible for the observed stronger-

than-linear behavior, the presence of such a trend in the Transverse region then suggests that additional mechanisms beyond those modeled in PYTHIA8 Monasch 2013 tune may be contributing to J/ψ-related activity in this region.
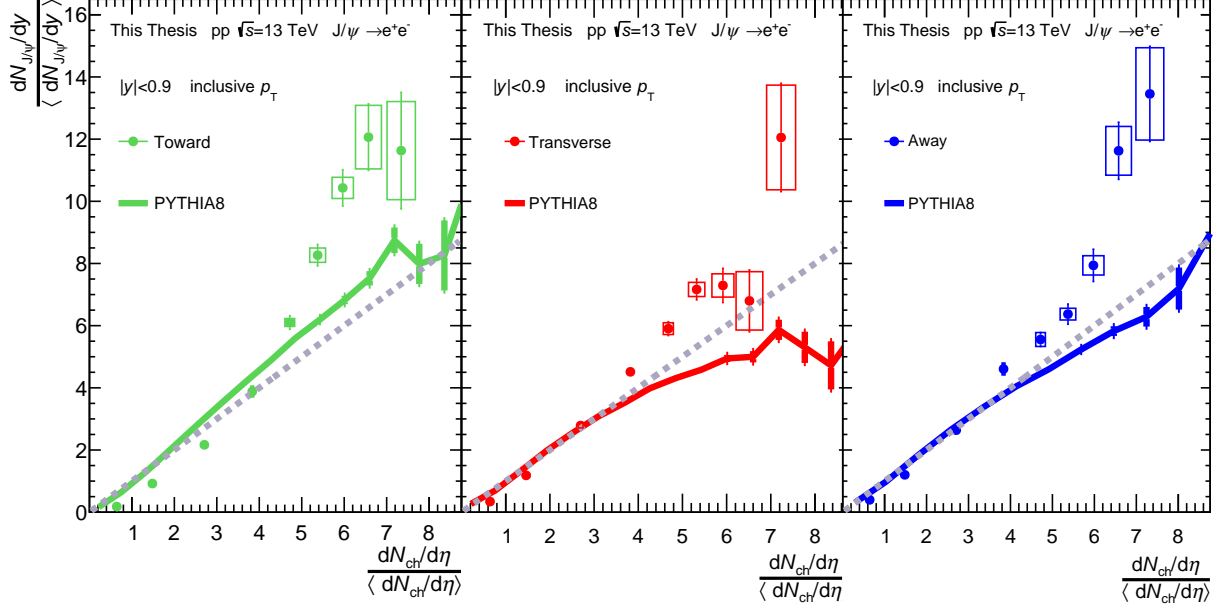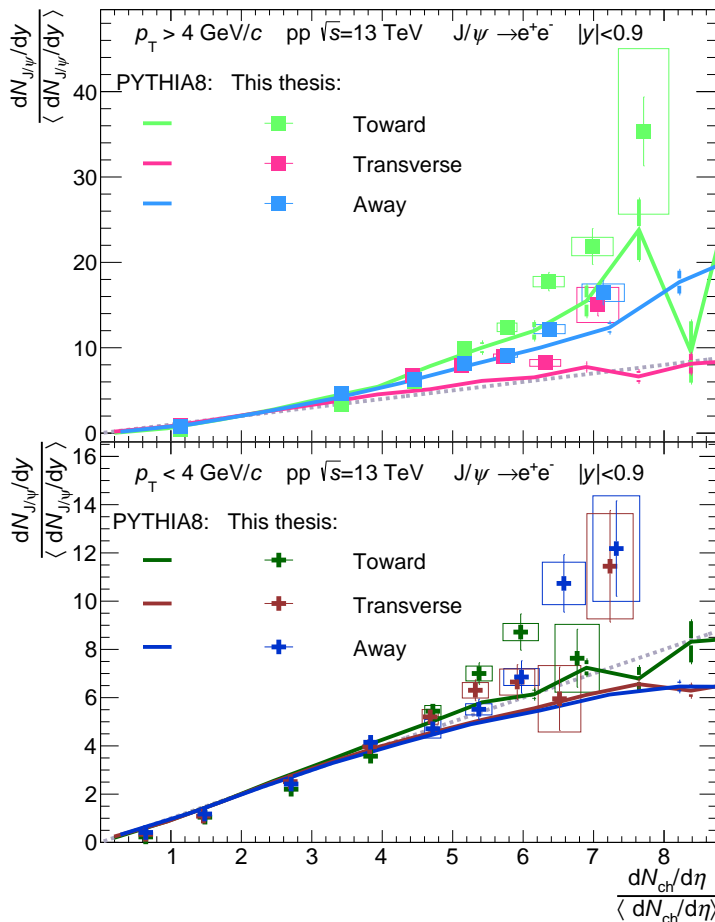

Figure 6.2.: Self-normalized J/ψ yields as a function of the charged particle multiplicity in regions of the azimuthal plane relative to the p_T integrated J/ψs compared with the PYTHIA8 predictions by [1].

6.2. p_T-differential J/ψ meson yields as a function of N_{ch} in J/ψ azimuthal regions

Figure 6.3 shows the azimuthal J/ψ-N_{ch} correlations for two p_T intervals of the J/ψ yield: high-p_T ($p_T > 4$ GeV/c) in the top panel and low-p_T ($p_T < 4$ GeV/c) in the bottom panel. The extracted high- and low-p_T J/ψ signals in the selected bins of the multiplicity estimator N_{trk} can be found in Appendix A. Note that these multiplicity bins differ from those shown in Figures 4.21, 4.22, 4.23 for the Toward, Transverse, and Away regions, respectively, due primarily to statistical limitations, especially affecting high-p_T J/ψs.

The high-p_T J/ψ-N_{ch} correlations in the top panel of Fig. 6.3 show wider bins at low N_{ch} which are consequence of maintaining statistical significance in the high-p_T data where relatively fewer J/ψs at low multiplicities are detected. This can be understood by considering that low-multiplicity events are less likely to produce high-momentum (i.e., highly energetic) J/ψ mesons, leading to suppressed yields in those bins. Meanwhile, the low-p_T J/ψ-N_{ch} correlations, shown in the bottom panel, display a behavior similar to the inclusive azimuthal J/ψ-N_{ch} correlation. This result is expected, as most J/ψ mesons reconstructed in this analysis, relying solely on the TPC detector, are concentrated in the low-p_T region. To enhance statistics in the high-p_T regime, additional input from other detectors, such as the TRD or calorimeters (EMCal and DCal), would be necessary.

The J/ψ-N$_{\mathrm{ch}}$ correlations for high-p_{T} J/ψ mesons, shown in the top panel, exhibit a stronger-than-linear increase, most prominently in the Toward region. Although the systematic uncertainties in the highest multiplicity bin for this p_{T} interval are large, the steeper increase in the Toward region is also reflected clearly from the data point before. On the other hand, for low-p_{T} J/ψs in the Toward region, the correlation shows a more modest stronger-than-linear increase trend, with the highest multiplicity point of the Toward region lying close to the linear reference line.

Figure 6.3.: Self-normalized J/ψ yields as a function of the charged-particle multiplicity in regions of the azimuthal plane relative to the **Top:** $p_{\mathrm{T}} > 4$ GeV/c and **Bottom:** $p_{\mathrm{T}} < 4$ GeV/c J/ψ mesons.

In addition, the plots in Fig. 6.3 include model predictions from the simulation study reported in Ref. [1]. In that study, differences among the azimuthal regions were more pronounced when analyzing the non-prompt J/ψ fraction. Therefore, that analysis was extended to different J/ψ p_{T} intervals, revealing that the weaker-than-linear trend in the Transverse region and the stronger-than-linear trend in the Toward region become more pronounced when focusing on high-p_{T} J/ψ mesons. However, a comparison with the experimental results obtained by this thesis shows that the PYTHIA8 simulations consistently underestimate the measured yields, particularly at high multiplicities. The discrepancies are particularly pronounced in the Transverse region for both low- and high-p_{T} intervals, as well as in the low-p_{T} measurements in the Away region, where the simulated trends fail to capture the behavior of the experimental Jpsi-Nch correlation. These discrepancies might be due to limitations in modeling J/ψ production

mechanisms or in the current treatment of multiparton interactions (MPI) and the interplay between soft and hard components in a collision.

The azimuthally integrated J/ψ-N_{ch} correlations in p_T intervals ($p_T > 4$ GeV/c and $p_T < 4$ GeV/c) are shown in Fig. 6.4. The analysis follows the methodology described in Chapter 4, and the systematic uncertainties are evaluated according to the procedures outlined in Chapter 5. The results are in agreement with previous measurements reported in Ref. [48] with a different multiplicity estimator. As anticipated, the azimuthally integrated self-normalized J/ψ yield as a function of the charged particle multiplicity show a stronger-than-linear increase, which becomes significantly pronounced when analyzing J/ψ mesons with high transverse momentum.
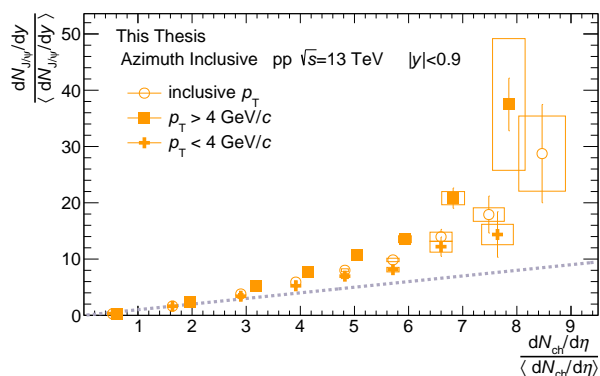
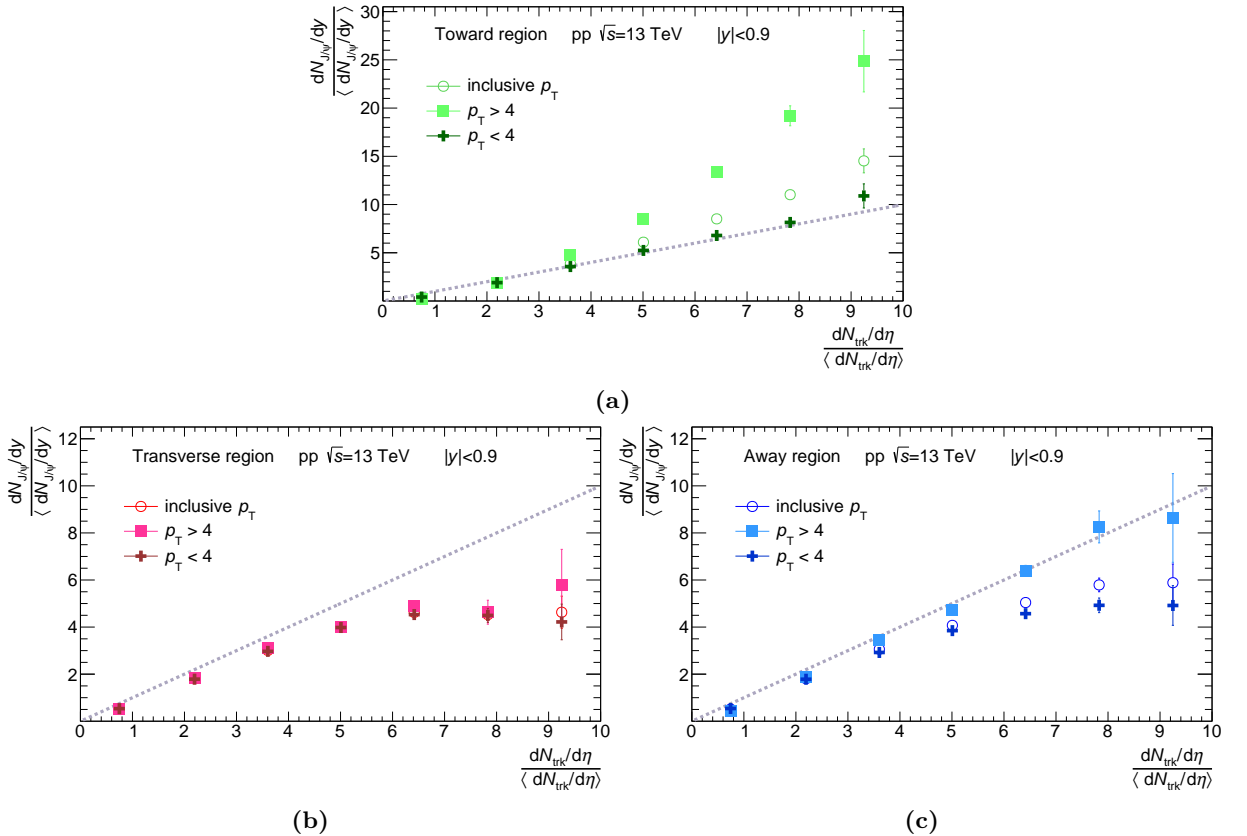**Figure 6.4.:** p_T differential analysis of the self-normalized inclusive J/ψ yields as a function of the charged-particle multiplicity.

To facilitate direct comparison between the azimuthally inclusive (Fig. 6.4) and the azimuthally differential J/ψ-N_{ch} correlation, the experimental measurements presented in figures 6.1 and 6.3 for the three azimuthal regions are depicted following the same format in Fig. 6.5. This similar representation enables a clear visualization of the impact of the p_T-differential analysis on each region individually.

The figure shows that in contrast to the Toward region, where the correlation becomes markedly steeper with increasing p_T, the Transverse and Away regions exhibit a p_T-independent behavior, with the J/ψ-N_{ch} correlations consistently showing a stronger-than-linear trend across all analyzed p_T intervals. This observation suggests that the overall increase observed in the azimuthally integrated J/ψ-N_{ch} correlation may be predominantly influenced by the Toward region. As discussed in Ref. [1], such behavior could be attributed to autocorrelation effects linked to the J/ψ production mechanism. In particular, a substantial fraction of high-p_T J/ψ mesons are non-prompt, originating from B-hadron decays, whose associated decay products can significantly enhance the charged-particle multiplicity, especially in the Toward region. Consequently, performing a dedicated prompt/non-prompt separation analysis is strongly recommended to further support these conclusions and hopefully disentangle potential contributions from the different J/ψ production mechanisms.
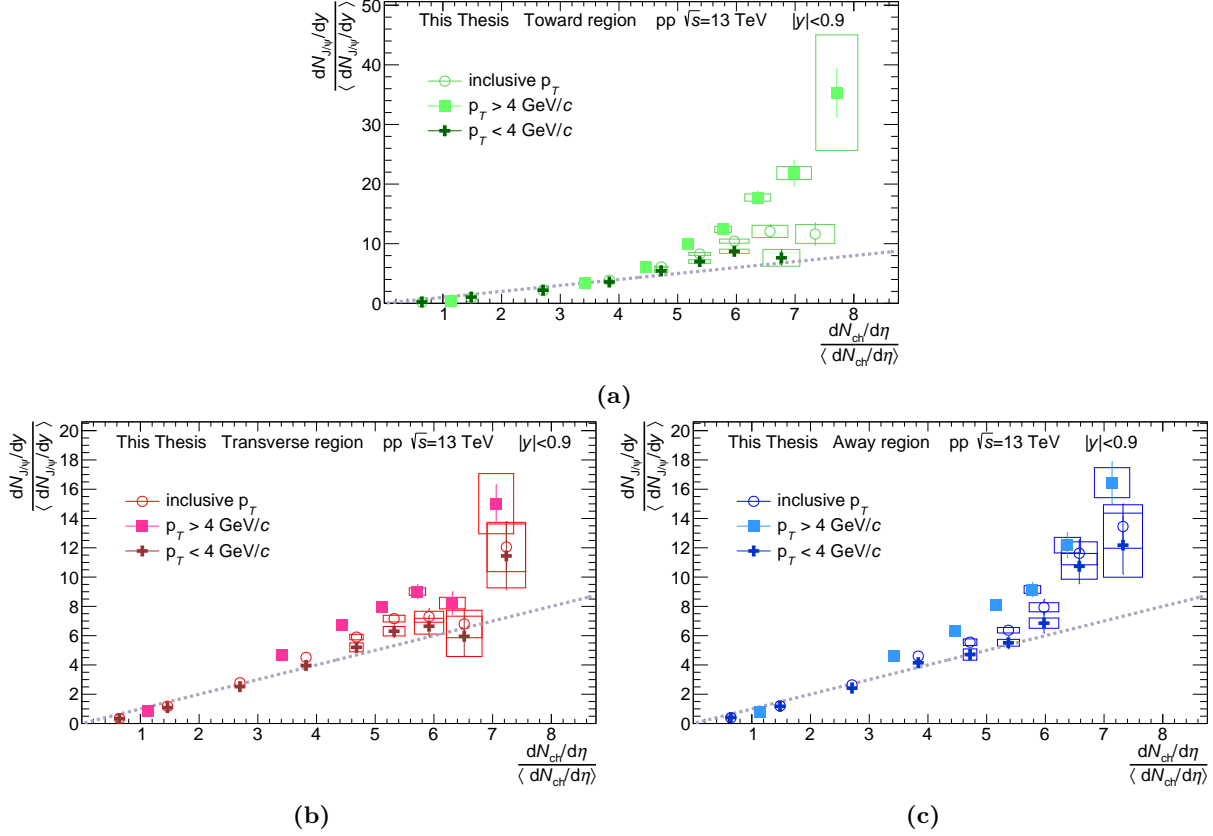
Figure 6.5.: p_T differential analysis of the self-normalized J/ψ yields as a function of the charged-particle multiplicity in the Toward 6.5a, Transverse 6.5b, and Away 6.5c regions.

6.3. Studies with ALICE-MC simulated data

To bridge the gap between the simulation study reported in Ref. [1] and the experimental ALICE measurements discussed above, the PYTHIA8 event generator is coupled with detector simulations via Geant4 to produce ALICE-MC simulated data and replicate the strategy described in Chapter 4 for constructing the azimuthal regions and studying the J/ψ-N_{ch} correlations within those regions. Using the dataset of the general-purpose ALICE-MC simulations, which simulates MB data, the azimuthal regions were defined with respect to several reference points: (i) true emitted J/ψ mesons without any rapidity constraint, (ii) true emitted J/ψ mesons only at midrapidity, and (iii) reconstructed J/ψ mesons from their true midrapidity electron decay products. For each scenario, the J/ψ yields were plotted as a function of the experimental multiplicity estimator (full tracks at midrapidity) and subsequently analyzed. The results of the J/ψ-N_{ch} correlations when using J/ψ mesons detected as explained in Sec. 4.3 are included in Appendix D and compared to experimental MB-triggered data .

Additionally, given that these regions, when using experimental ALICE data, are constructed with respect to pair candidates rather than true J/ψ mesons, background pair candidates were taken as alternative references to construct the regions. This allows for a comparison of the azimuthal analysis for J/ψs as in contrast for the background. Specifically, like-sign pairs in the invariant mass interval 2.92 - 3.16 GeV/c and general opposite-sign pair candidates in the

invariant mass intervals 2 - 2.8 GeV/c and 3.2-4 GeV/c at midrapidity were chosen for the construction of the regions. Subsequently, these pairs were correlated with the experimental multiplicity estimator and the results obtained are presented and discussed below.

p_T differential analysis with true J/ψs

Figure 6.6 presents the J/ψ-N$_{trk}$ correlations obtained using true J/ψ mesons, i.e., particles directly retrieved from the PYTHIA8 event generator rather than reconstructed from their detected decay products, thus, J/ψ mesons without detector-related effects and additionally no rapidity constraints. The observed trends are consistent with those reported in Ref. [1]. Specifically, the Toward region exhibits a pronounced stronger-than-linear increase of the J/ψ yield with the charged-particle multiplicity, particularly evident at high-p_T. The Away region shows a nearly linear dependence at high-p_T, transitioning to a weaker-than-linear trend at lower and inclusive p_T values. On the other hand, unlike the Toward and Away regions that depict a p_T differential behavior, the Transverse region consistently displays a weaker-than-linear increase of the correlation in all p_T intervals, remarkably even for high-p_T J/ψ mesons.

(a)

(b)

(c)

Figure 6.6.: MC simulations: p_T differential analysis of the self-normalized true J/ψ yields as a function of the charged-particle multiplicity in the Toward 6.6a, Transverse 6.6b, and Away 6.6c regions.

The repeated analysis for each region when using true J/ψ mesons restricted to midrapidity J/ψs is shown in Fig. 6.7. Although the general features observed in the previous case persist, the trends appear less pronounced. Notably, the Transverse region continues to exhibit the predicted by [1] weaker-than-linear increase in J/ψ yield with multiplicity. However, it is difficult to

draw definitive conclusions due to the significant statistical uncertainties at higher multiplicities, specially for high-p_T J/ψs.

Lastly, the results for the correlation when using midrapidity decay electrons to reconstruct J/ψ mesons, rather than directly selecting the true J/ψ mesons, are depicted in Fig. 6.8. The statistical uncertainties increase significantly, especially for high-p_T J/ψs, where a considerable data reduction leads to fewer available data points in the correlation. Nevertheless, the previously observed weaker-than-linear trend in the Transverse region is no longer reproduced, as highlighted particularly by the deviation in the highest multiplicity bin of the correlations for low and inclusive p_T J/ψs.

(a)

(b)

(c)
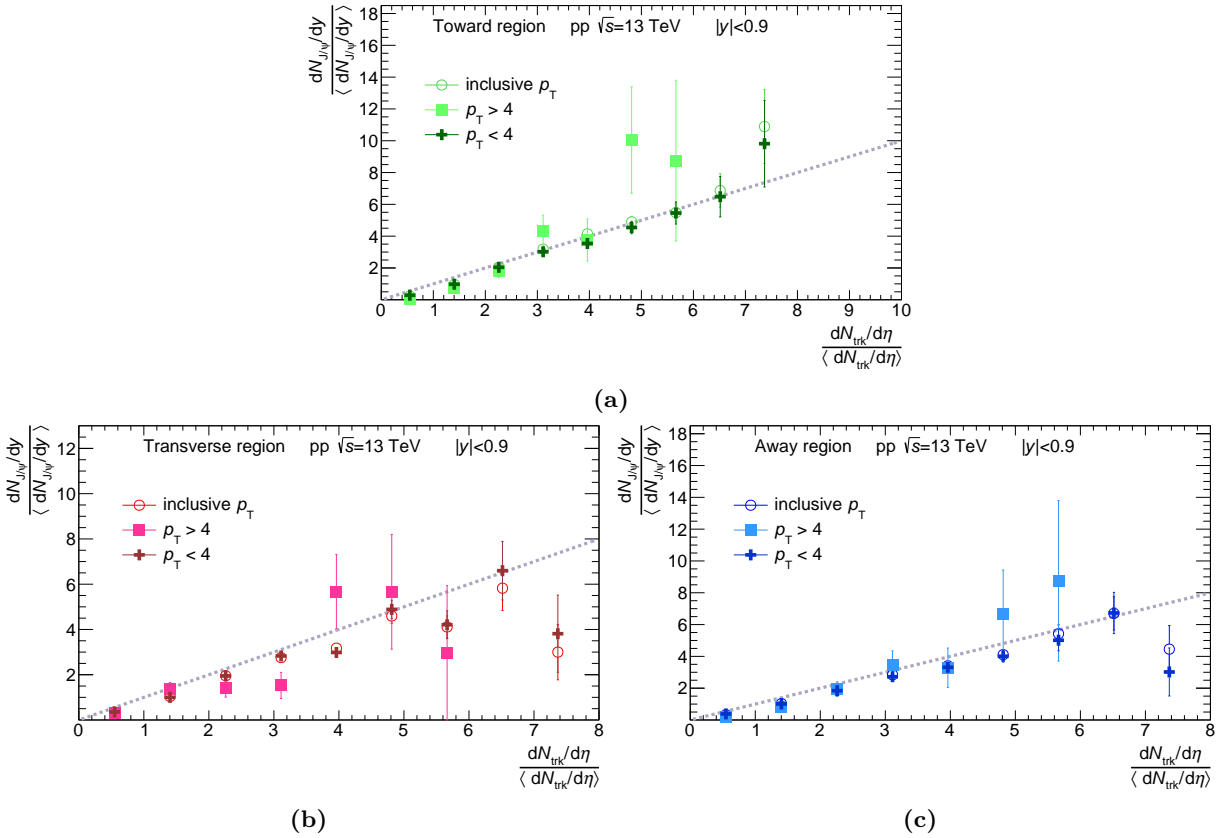
Figure 6.7.: MC simulations: p_T differential analysis of the self-normalized midrapidity true J/ψ yields as a function of the charged-particle multiplicity in the Toward 6.7a, Transverse 6.7b, and Away 6.7c regions.

(a)
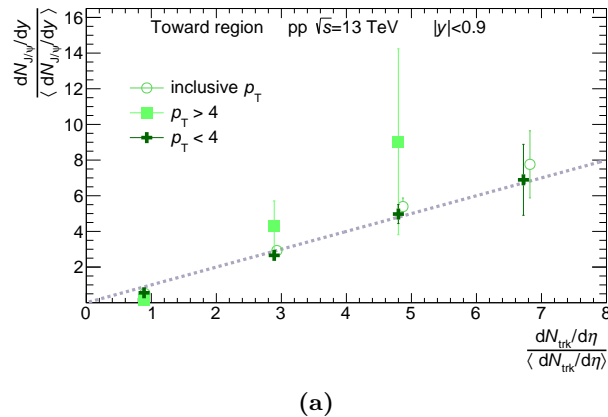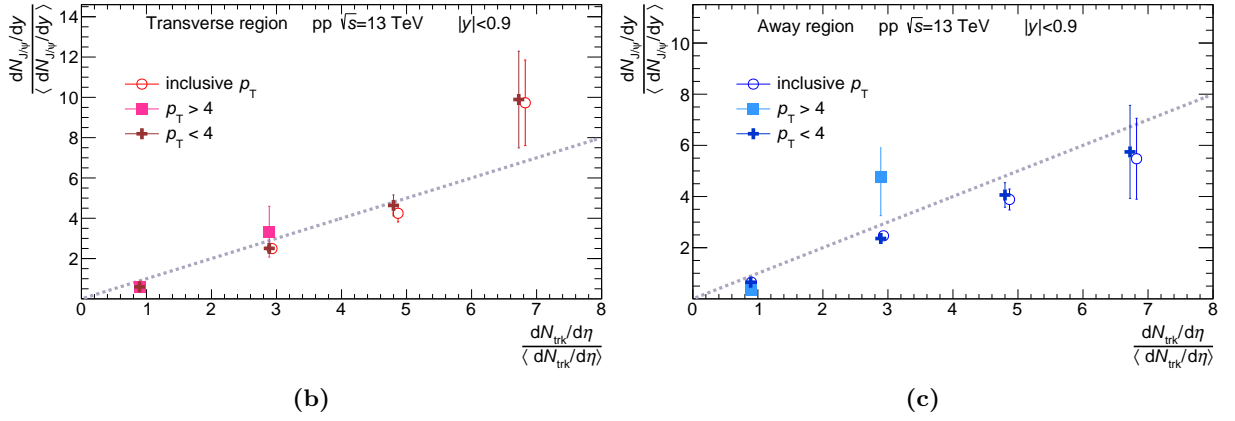
Figure 6.8.: MC simulations: p_T differential analysis of the self-normalized midrapidity true reconstructed J/ψ yields as a function of the charged-particle multiplicity in the Toward 6.8a, Transverse 6.8b, and Away 6.8c regions.

Summarizing: The trends of the J/ψ-N_{ch} correlations observed using true J/ψ mesons (J/ψs free from detector effects) show the azimuthal region-dependent behavior predicted by [1]: a stronger-than-linear increase in the Toward region, an almost linear to weaker-than-linear increase in the Away region and a weaker-than-linear increase in the Transverse region of the J/ψ yield with the charged particle multiplicity. Limiting the analysis to midrapidity true J/ψ mesons introduces large statistical uncertainties, especially for high-p_T J/ψs. Additionally, it attenuates the strength of the predicted trends for the regions. However, the qualitative weaker-than-linear increase in the Transverse region remains somehow visible. On the other hand, when reconstructing the J/ψ mesons directly from their decay electrons at midrapidity, the weaker-than-linear increase in the Transverse region is no longer evident, implying that detector effects could dilute the genuine correlation features predicted at the generator level. However, due to limited statistics reflected in large uncertainties, particularly in the highest multiplicity bins, it is challenging to draw firm conclusions about how large the effects are (or if there are any at all) introduced by the detectors when constructing the azimuthal regions.

p_T differential analysis with background pairs

Due to the implications that could represent to the experimental analysis, it is meaningful for this thesis to evaluate the background-N_{ch} correlation behavior. In real data, the azimuthal regions are constructed around pair candidates, which include both signal and background, rather than exclusively around true J/ψ mesons. Although the signal extraction method discussed in Chapter 4, such as event mixing plus a second-order polynomial fitting, is employed to subtract the background under the J/ψ peak, these methods may not fully eliminate background contributions. Consequently, it is instructive to explicitly investigate how the background itself correlates with the charged-particle multiplicity in the different azimuthal regions. This study is further motivated by the physical origin of the background under the J/ψ peak, which is not entirely random. A significant component of the background, especially in the signal mass region, is composed of correlated dielectron pairs from semileptonic decays of mesons and baryons containing at least one heavy -*c* or *b*- quark [88]. Since the p_T-differential analysis shows distinct

azimuthal patterns for J/ψ-N$_{\text{ch}}$ correlations, a careful study of background behavior can help determine whether these trends are unique to J/ψ mesons or could be shared with other heavy-flavor decay products. Previously discussed in Sec. 2.2.3, as observed for J/ψ mesons, the recent ALICE results at midrapidity show a stronger-than-linear increase of the self-normalized yield of electrons from heavy-flavor hadron decays as a function of the charged particle multiplicity, with the slope of the increase becoming steeper at higher p_{T}. This observation adds further motivation to probe whether background electrons reflect similar behaviors in different azimuthal regions.

In this context, two representative background samples are analyzed. The first consists of like-sign (LS) electron pairs within the J/ψ invariant mass window, presented in Fig. 6.9. The second, shown by Fig. 6.10, consists of unlike-sign (US) electron pairs located in the side band regions of the dielectron invariant mass spectrum, specifically within the invariant mass intervals of 2.0–2.8 GeV/c^2 and 3.2–4.0 GeV/c^2. These intervals are chosen since they are considered a reflection of the background adjacent to the J/ψ peak. In both cases, the yield of these background pair candidates is analyzed as a function of the experimental charged-particle multiplicity estimator across Toward, Away, and Transverse azimuthal regions.

The results, as presented in figures 6.9 and 6.10, reveal a stronger-than-linear increase of background yields with charged-particle multiplicity for high-p_{T} pairs across all three azimuthal regions. However, notable differences emerge when compared with the J/ψ results. In the Toward region, background pair candidates do not exhibit the p_{T}-dependent steepening seen for J/ψ mesons, indicating that the strong p_{T} dependence observed in J/ψ-N$_{\text{ch}}$ correlations may be specific to the signal. In the Away region, the background continues to show a consistently stronger-than-linear trend across all p_{T} intervals, qualitatively similar to J/ψ results. However, the most significant divergence is observed in the Transverse region. While the J/ψ-N$_{\text{ch}}$ correlation in this region is characterized by a consistently stronger-than-linear behavior across the analyzed p_{T} bins, the background shows a markedly stronger-than-linear increase at low and inclusive p_{T}, transitioning to an approximately linear scaling at high p_{T}, particularly for unlike-sign (US) side-band pairs. In the case of like-sign (LS) background pairs in the Transverse region, the trend is less conclusive due to large statistical uncertainties in the highest multiplicity bin. These findings suggest that, in contrast to the J/ψ analysis, where the Toward region is found to be transverse momentum sensitive, the Transverse region appears more affected in the background case, hinting towards an azimuthally distinct behavior for genuine J/ψ mesons compared to their background.
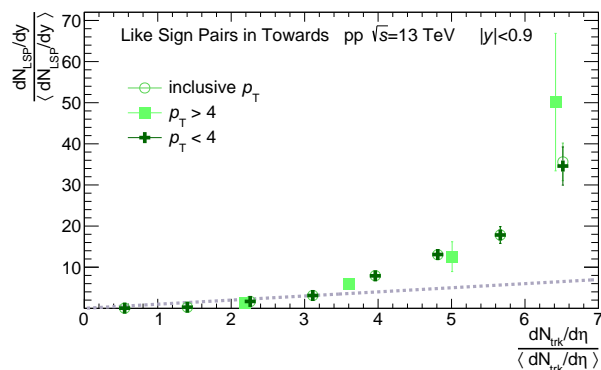
(a)
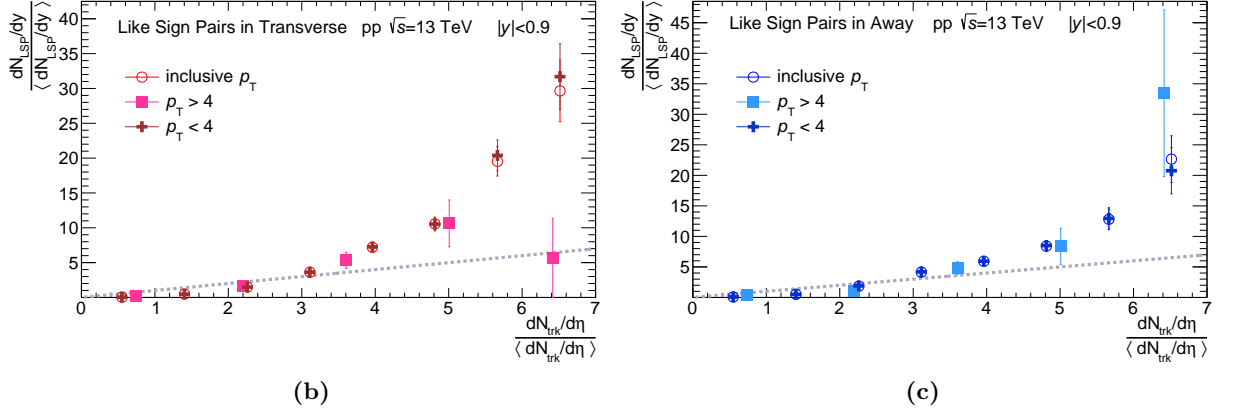
Figure 6.9.: MC simulations: p_T differential analysis of the self-normalized Like Sign Pairs yields (in the invariant mass interval 2.92 - 3.16 GeV/c) as a function of the charged-particle multiplicity in the Toward 6.9a, Transverse 6.9b, and Away 6.9c regions.
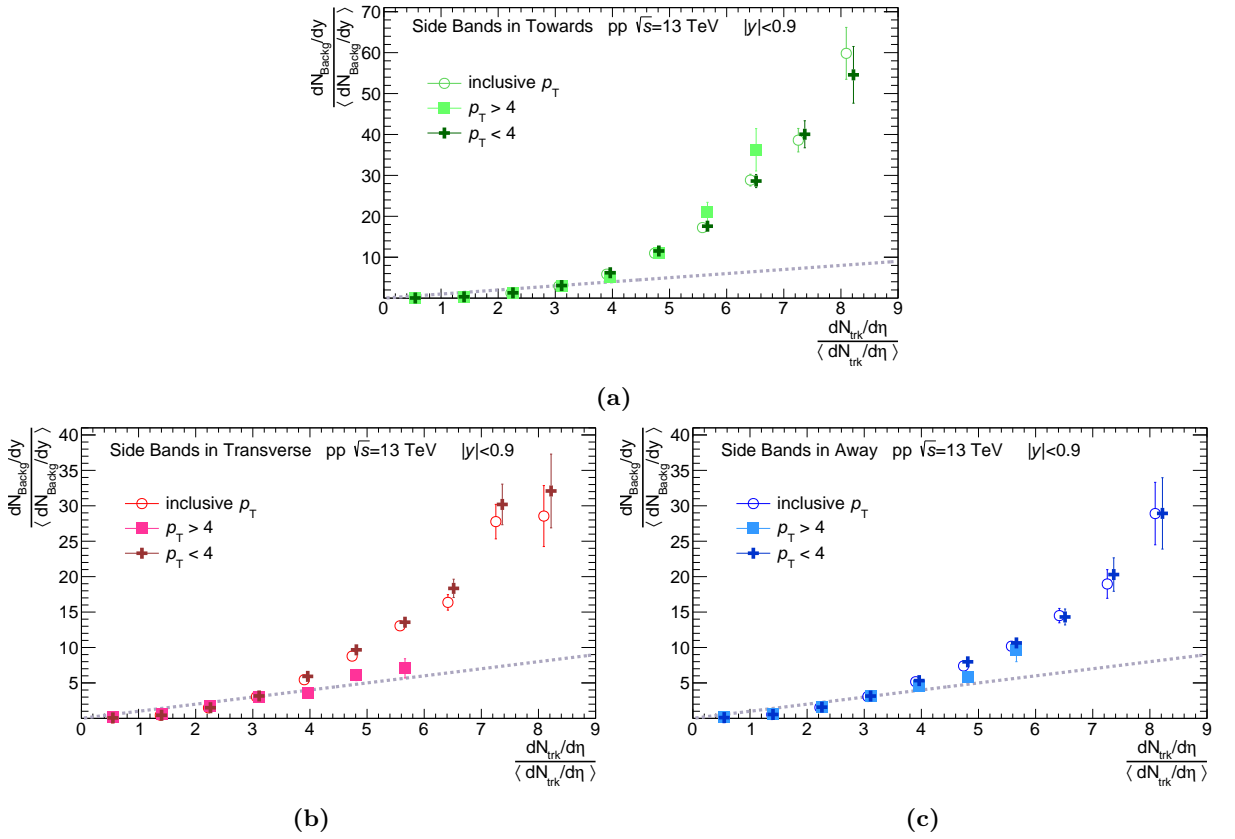
Figure 6.10.: MC simulations: p_T differential analysis of the self-normalized side bands unlike-sign pairs (2 - 2.8 GeV/c and 3.2-4 GeV/c) yields as a function of the charged-particle multiplicity in the Toward 6.10a, Transverse 6.10b, and Away 6.10c regions.

7. Conclusions and Outlook

This thesis presents measurements of the self-normalized J/ψ yield as a function of the charged-particle multiplicity (N_{ch}) in three azimuthal regions—Toward, Transverse and Away—defined relative to the direction of the reconstructed J/ψ mesons. The analysis focuses on J/ψ mesons decaying into dielectrons at midrapidity ($|\eta| < 0.9$), considering p_T-integrated yields and two transverse momentum intervals: $p_T < 4$ GeV/c and $p_T > 4$ GeV/c. Additionally, this thesis reported the azimuthal inclusive J/ψ-N_{ch} correlation using an alternative experimental multiplicity estimator. The results are consistent with previously published ALICE measurements, further validating this analysis.

For inclusive-p_T J/ψ mesons, the results reveal a consistently stronger-than-linear increase of the self-normalized yield with charged-particle multiplicity in all three azimuthal regions. However, a p_T-differential analysis exposes distinct behavior: in the Toward region, the J/ψ–N_{ch} correlation shows a clear p_T dependence, with high-p_T J/ψ mesons exhibiting a significantly steeper stronger-than-linear increase with multiplicity. In contrast, the correlations in the Transverse and Away regions appear independent of p_T, maintaining a stronger-than-linear increase across the analyzed intervals.

When compared with PYTHIA8 Monasch 2013 tune predictions, notable discrepancies are observed. PYTHIA8 anticipates a region-dependent behavior attributed to autocorrelation effects from the J/ψ production mechanism. Specifically, it predicts a weaker-than-linear increase of the J/ψ yield with multiplicity in the Transverse region, where such effects are expected to be minimal, and a stronger-than-linear trend in the Toward region. These effects are expected to be more pronounced in a p_T-differential context, with high-p_T J/ψ mesons producing a steeper increase in the Toward region, while the Transverse region should show an even more suppressed correlation. Although the experimental results of this thesis do not support this predicted suppression of the J/ψ-N_{ch} correlation in the Transverse region, they are consistent with the model predictions for the Toward region, where a steeper stronger-than-linear increase at high-p_T and a pronounced dependence on the J/ψ transverse momentum of the J/ψ-N_{ch} correlation were the anticipated behaviors. Since PYTHIA8 attributes the enhanced correlation in the Toward region to the decay products of B-hadrons, where non-prompt J/ψ mesons are accompanied by additional charged particles potentially contributing to the multiplicity, a natural extension of this analysis is to perform a prompt/non-prompt separation of the J/ψ mesons; which would allow for a more precise characterization regarding the J/ψ production mechanisms and their role in the observed multiplicity dependence.

Additional studies were performed using ALICE Monte Carlo data to assess the role of detector effects and background correlations. First, simulations using true J/ψ mesons as a function

of the multiplicity estimator in the azimuthal regions did not yield a definitive conclusion on whether detector effects influence the observed correlation trends in the regions, primarily due to the limited statistical precision at high multiplicities in the minimum-bias (MB) dataset. To address this limitation, a key recommendation is to repeat the analysis using simulated datasets incorporating the high-multiplicity (HM) trigger to enhance statistical reach and investigate potential detector-related biases. Second, studies of the background pairs as a function of the multiplicity estimator reveal a qualitatively different behavior compared to analyses involving J/ψ mesons. While confirming the role of proper background subtraction, these studies also suggest a possible azimuthal-region dependence specific to the physics of J/ψ production.

In conclusion, the observables constructed and analyzed in this thesis have enabled a deeper investigation of J/ψ production as a function of charged-particle multiplicity at midrapidity. The azimuthally differential approach has provided novel insights into the interplay between multiplicity and J/ψ production dynamics, confirming that potential autocorrelation effects linked to the J/ψ production mechanism could indeed contribute to the observed stronger-than-linear increase of the azimuthally inclusive J/ψ-N_{ch} correlation at midrapidity. The correlation behavior in the Toward region appears dominant, driving the overall trend of the azimuthally inclusive measurement. Therefore, these findings represent a meaningful step toward understanding the interplay between hard and soft processes in high-energy collisions. Looking ahead, future measurements incorporating prompt/non-prompt separation and improved model comparisons will be fundamental for advancing our understanding of J/ψ production mechanisms, particle production, and the role of multiparton interactions in small collision systems.

Appendices

A. High and low-p_T J/ψ signal in bins of N$_{trk}$
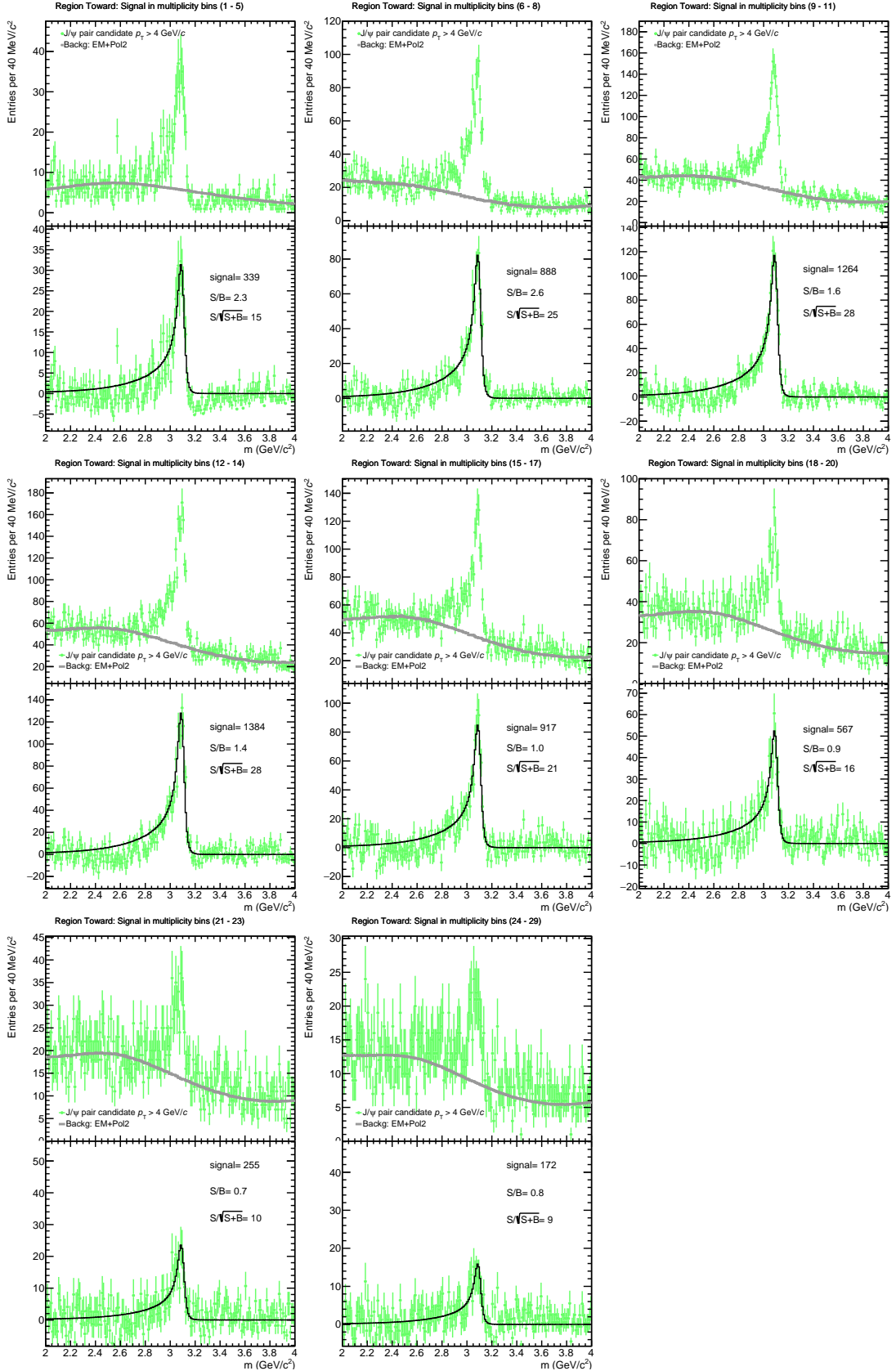
Figure A.1.: Toward region: Invariant mass distribution of high-p_T ($p_T > 4$ GeV/c) electron-positron pairs resulting in the J/ψ peak, its background description, and the J/ψ signal after background subtraction in each multiplicity range.
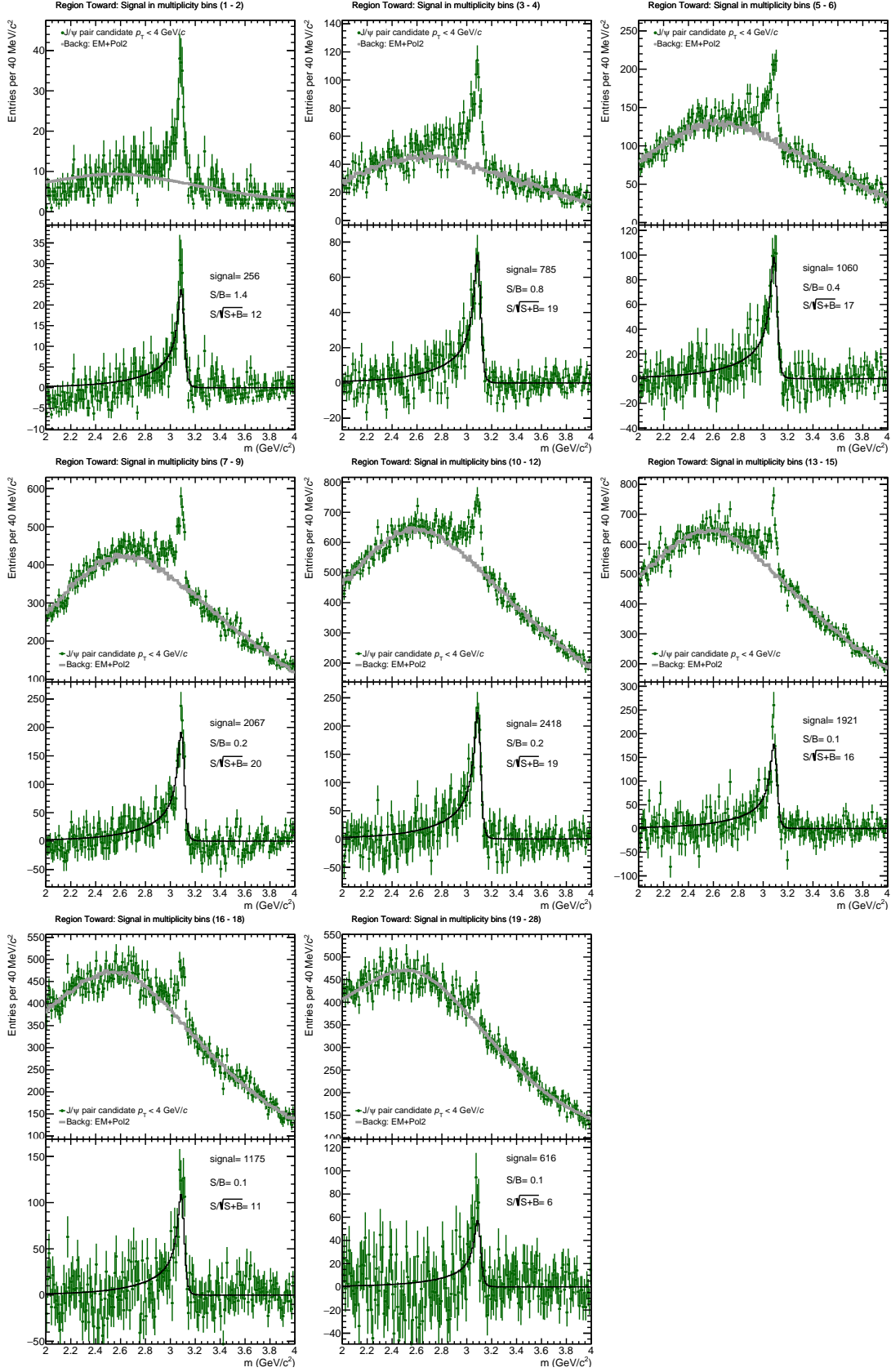
Figure A.2.: Toward region: Invariant mass distribution of low-p_T ($p_\mathrm{T} < 4$ GeV/c) electron-positron pairs resulting in the J/ψ peak, its background description, and the J/ψ signal after background subtraction in each multiplicity range.
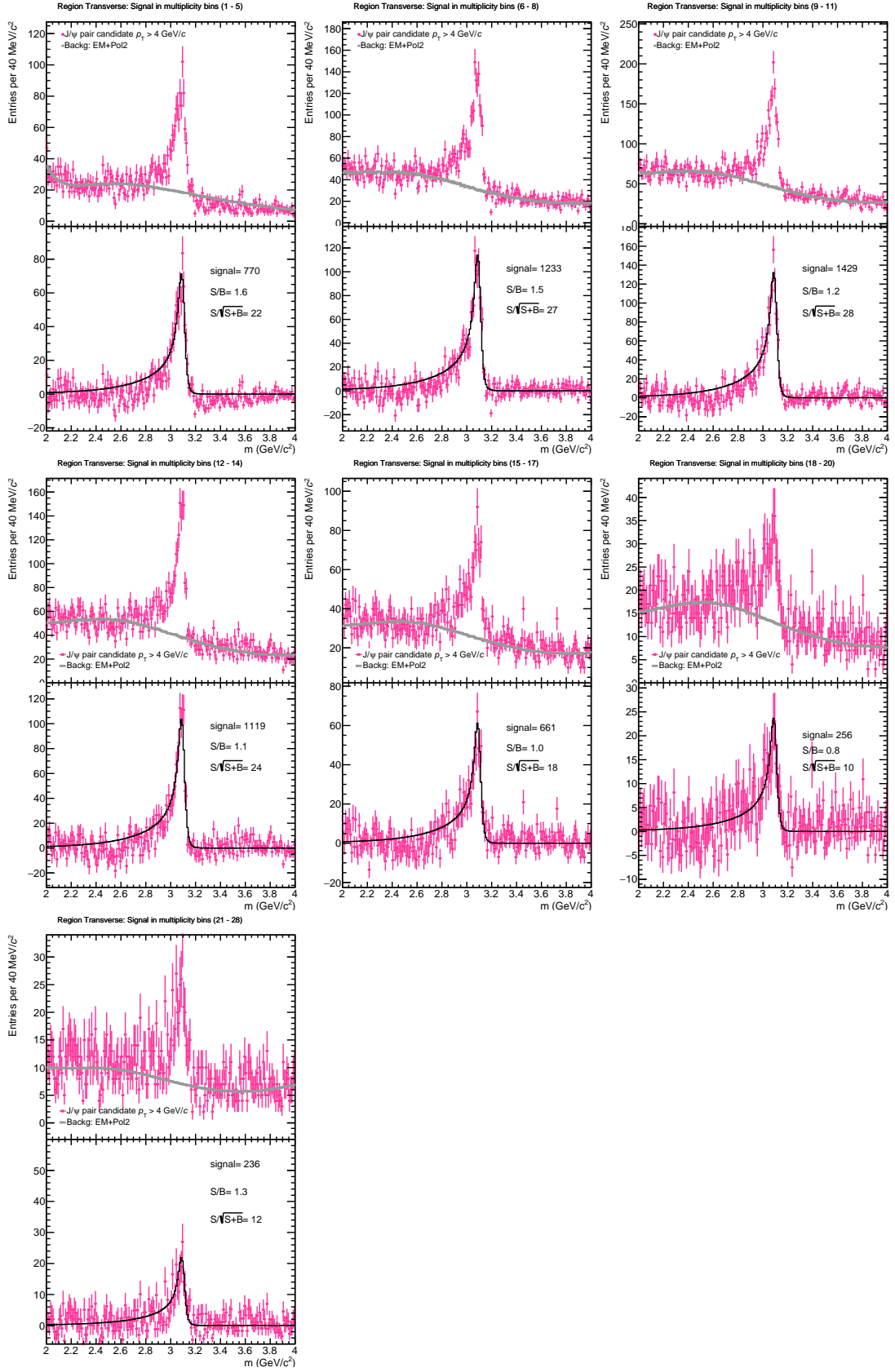
Figure A.3.: Transverse region: Invariant mass distribution of high-p_T ($p_T > 4$ GeV/c) electron-positron pairs resulting in the J/ψ peak, its background description, and the J/ψ signal after background subtraction in each multiplicity range.
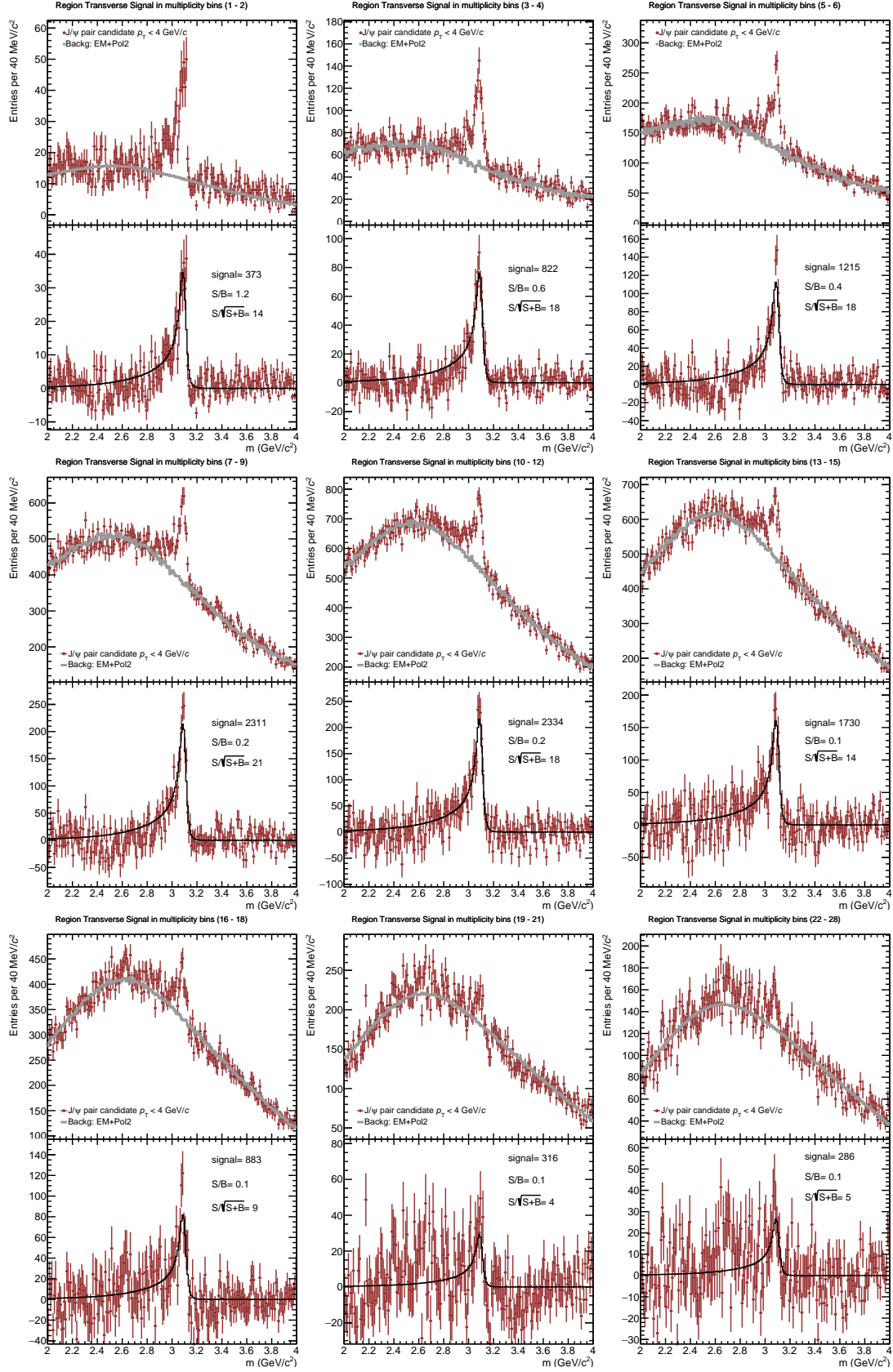
Figure A.4.: Transverse region: Invariant mass distribution of low-p$_T$ ($p_T < 4$ GeV/c) electron-positron pairs resulting in the J/ψ peak, its background description, and the J/ψ signal after background subtraction in each multiplicity range.
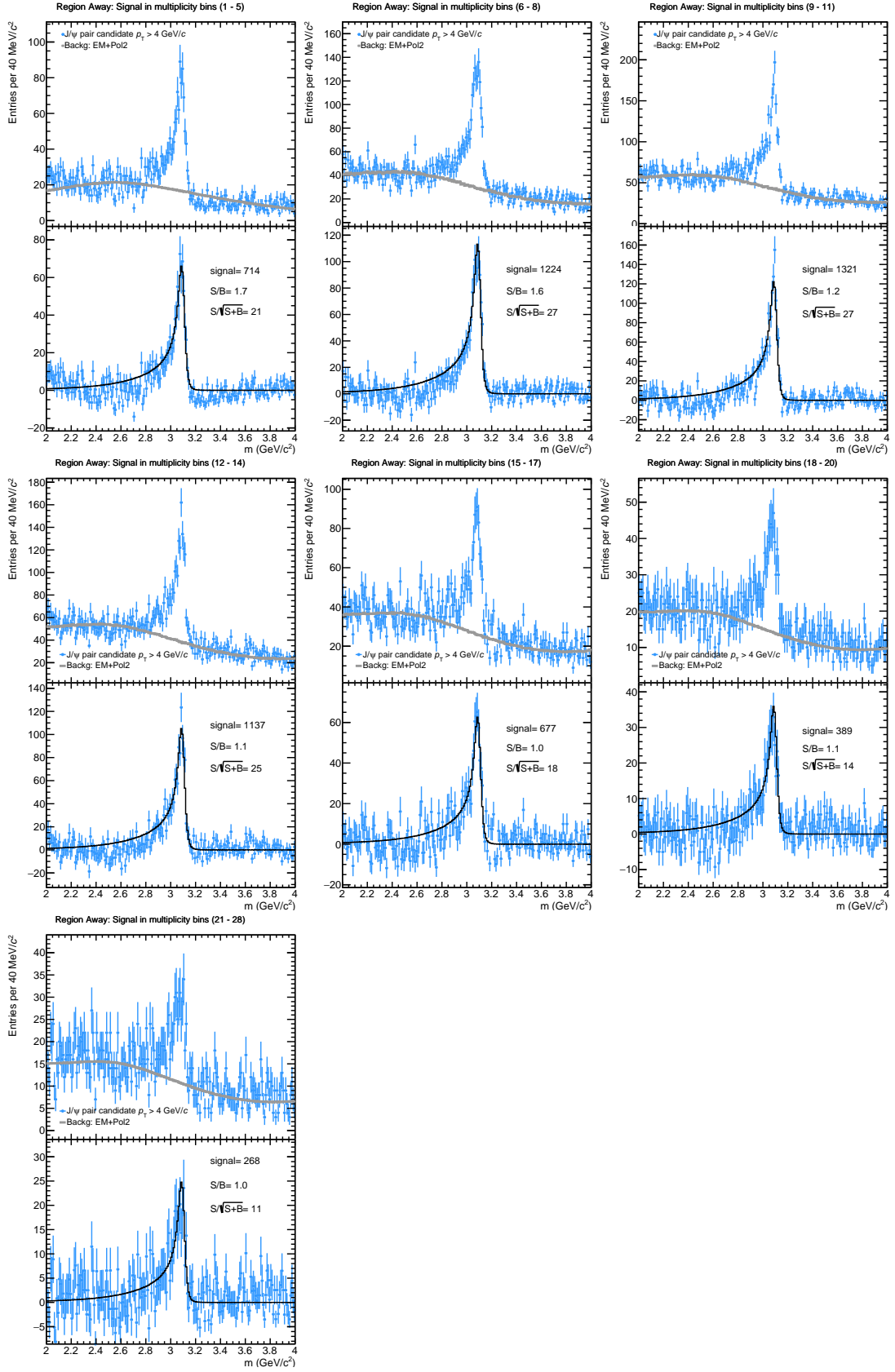
Figure A.5.: Away region: Invariant mass distribution of high-p_T ($p_T > 4$ GeV/c) electron-positron pairs resulting in the J/ψ peak, its background description, and the J/ψ signal after background subtraction in each multiplicity range.
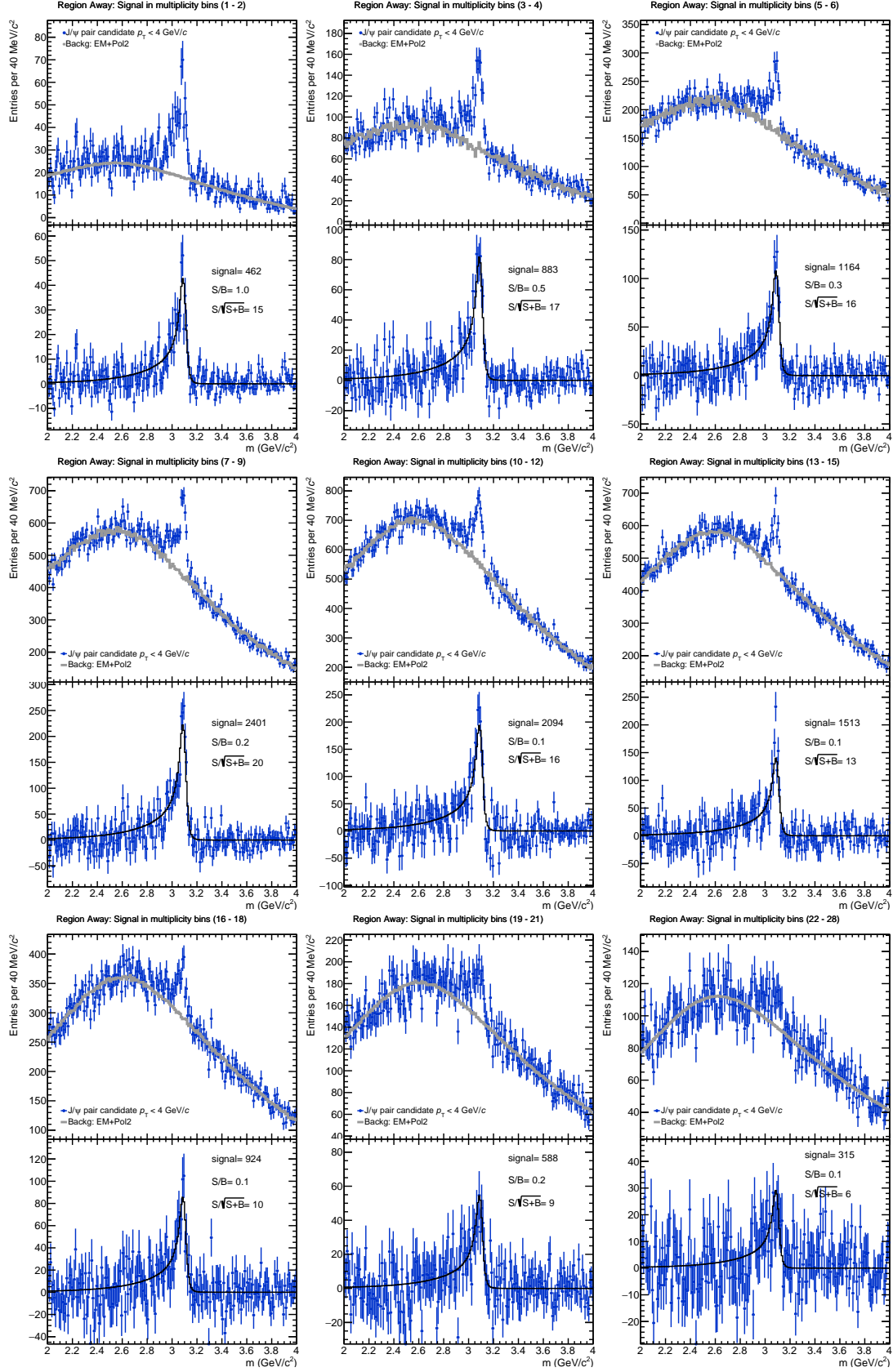
Figure A.6.: Away region: Invariant mass distribution of low-p_T ($p_T < 4$ GeV/c) electron-positron pairs resulting in the J/ψ peak, its background description, and the J/ψ signal after background subtraction in each multiplicity range.

B. Systematic uncertainties of the φ-differential N_{ch} distribution
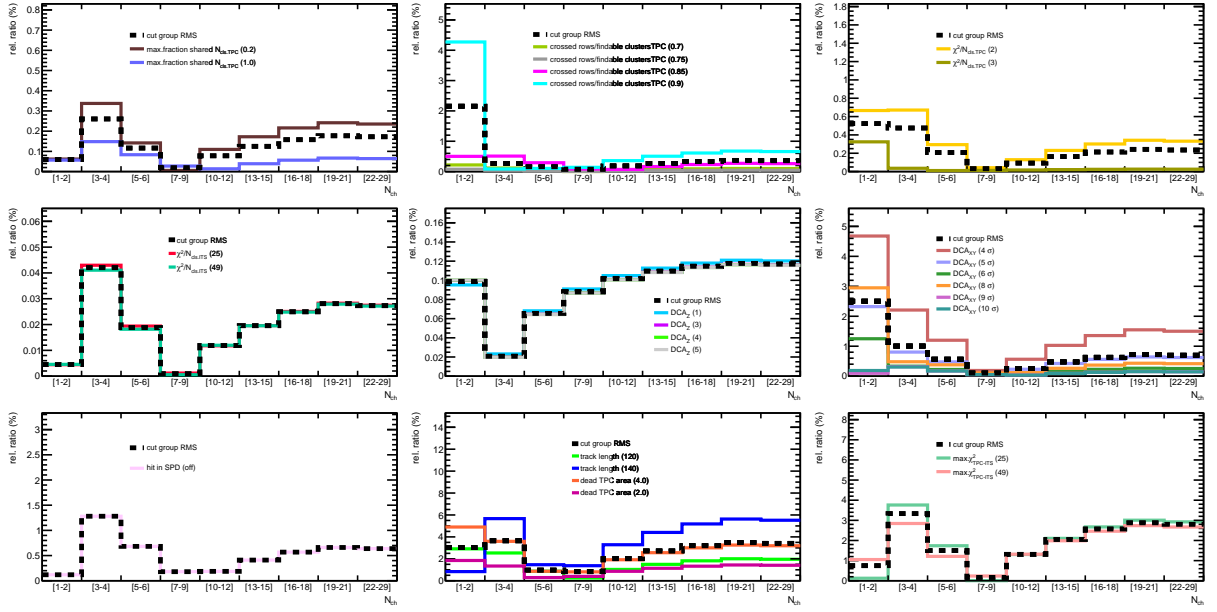
Figure B.1.: Relative ratios of the varied-charged particle multiplicity distributions to the standard distribution as a function of the charged particle multiplicity in the analyzed events by track selection criteria.
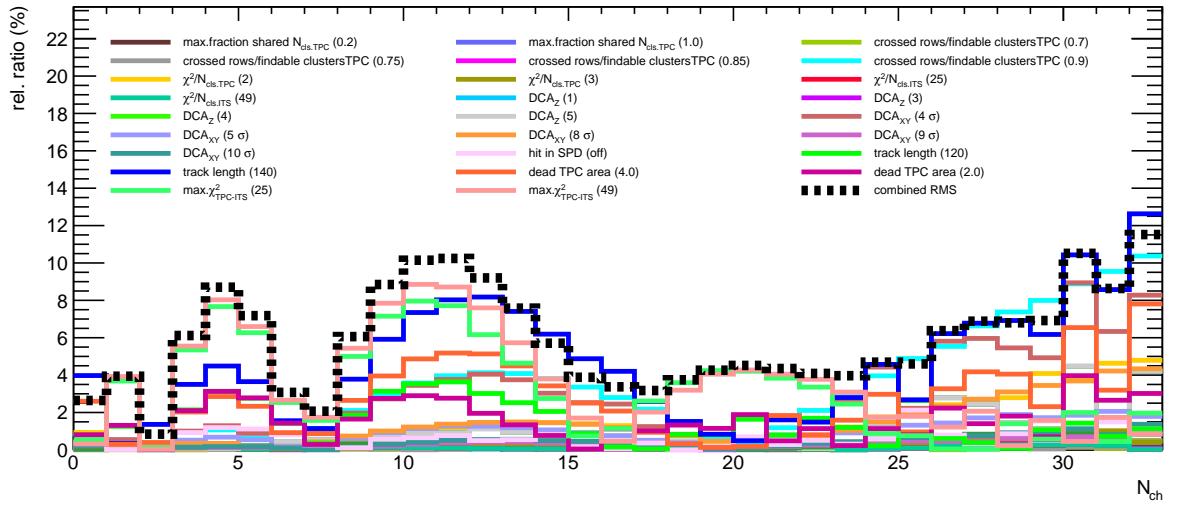
Figure B.2.: Total systematic uncertainty (black dotted line) along with the relative ratios of the varied-charged particle multiplicity distributions to the standard distribution as a function of the charged particle multiplicity.
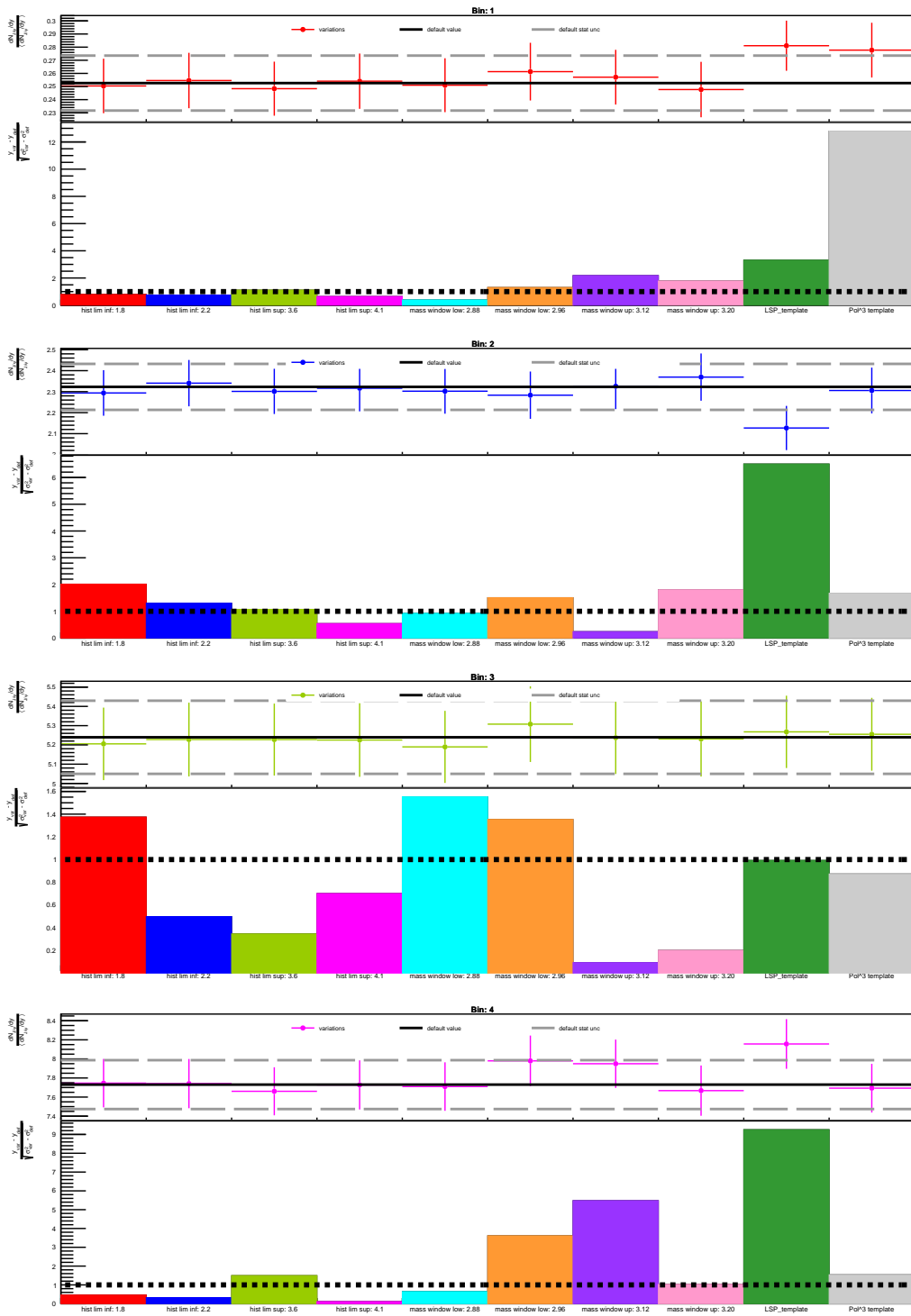
C. Systematic uncertainties of the φ and p_T differential self-normalized J/ψ yields

C.1. Azimuth inclusive

Azimuth inclusive: High-p_T J/ψ bins. Variations to J/ψ's daughter tracks selection criteria

Figure C.1.: Azimuth inclusive **Top:** High-p_T self-normalized J/ψ yields per variation to the J/ψ's daughter tracks selection criteria. **Bottom:** Barlow criterion of each variation.

Azimuth inclusive: High-p_T J/ψ bins. Variations to signal extraction method
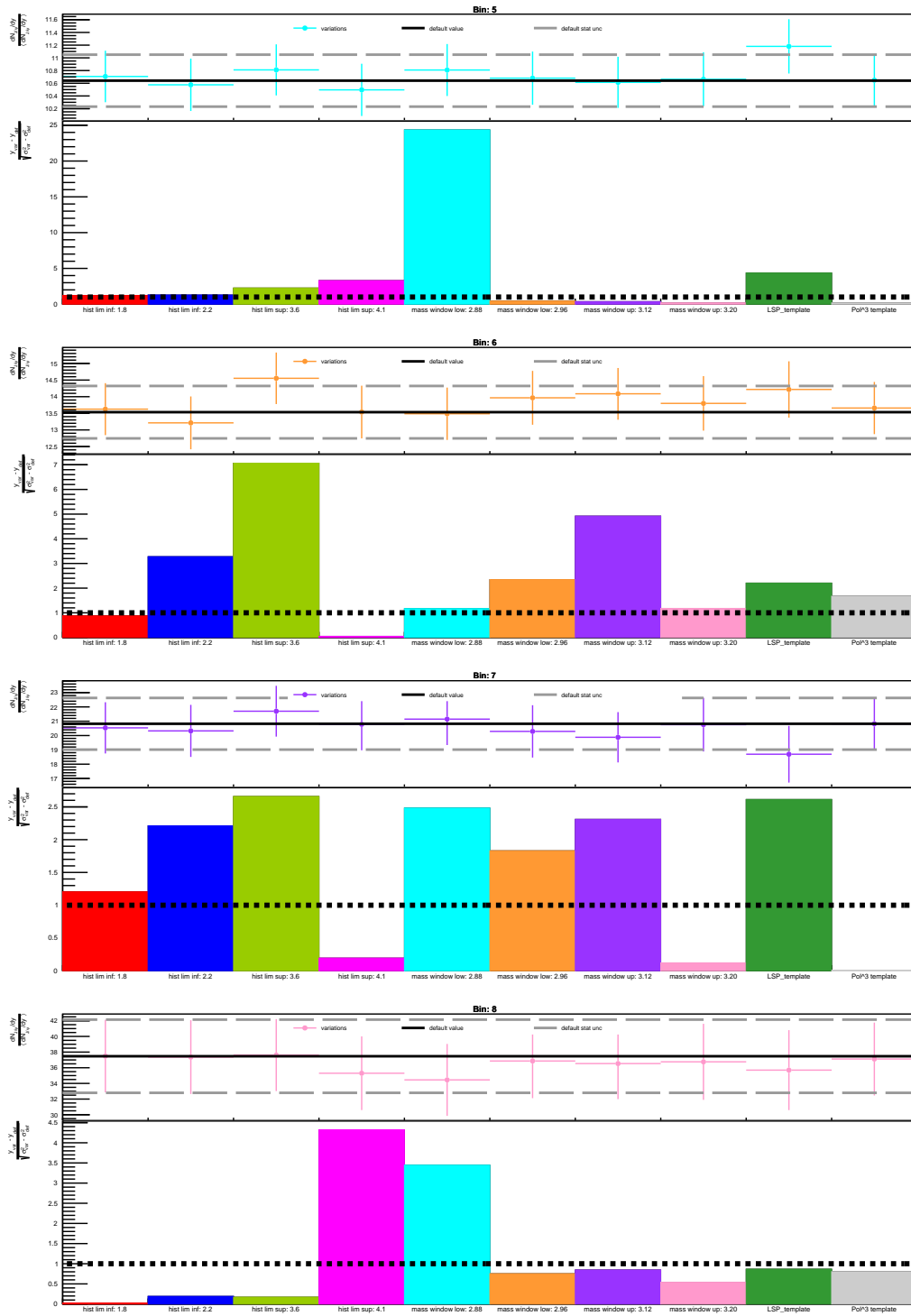
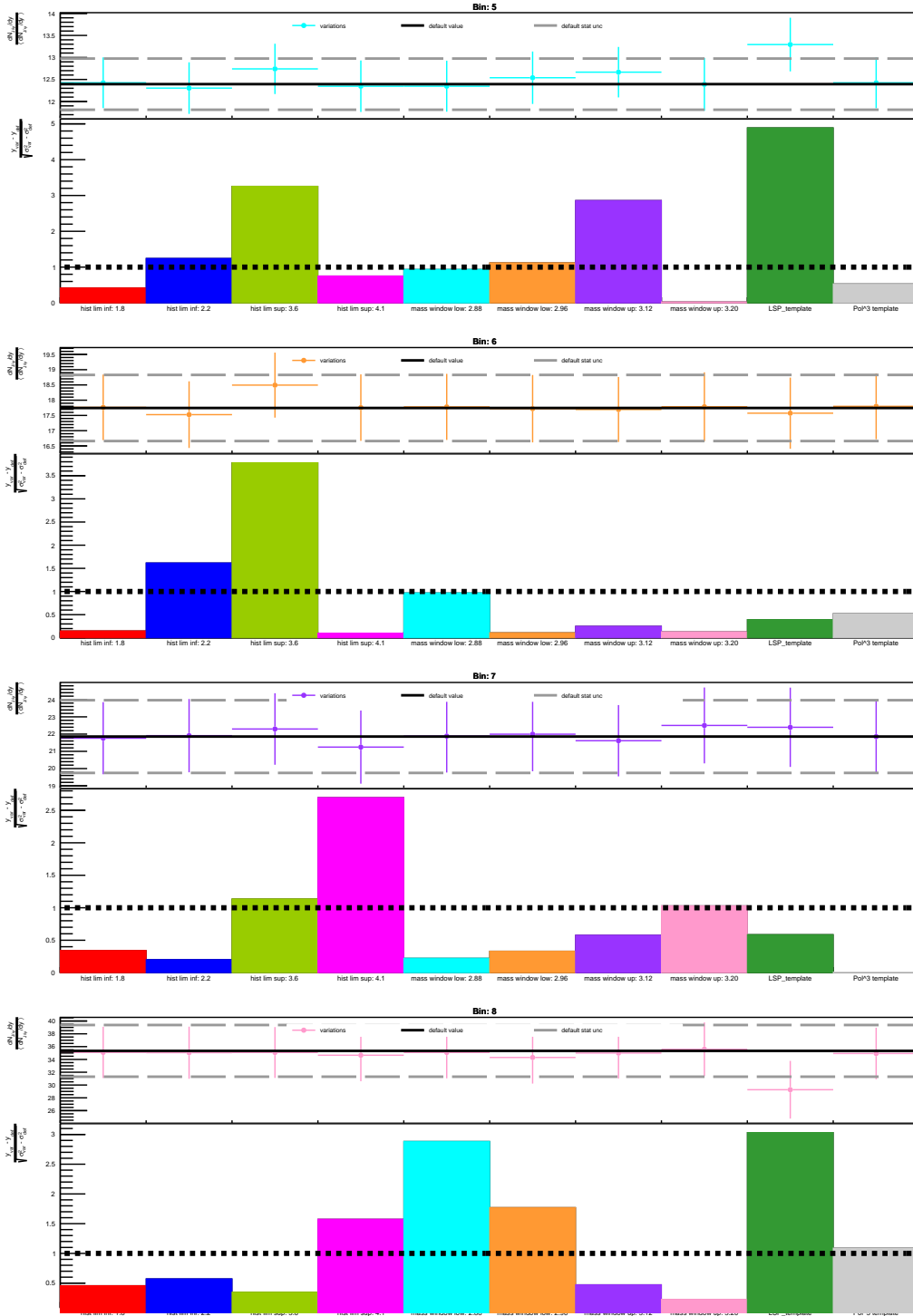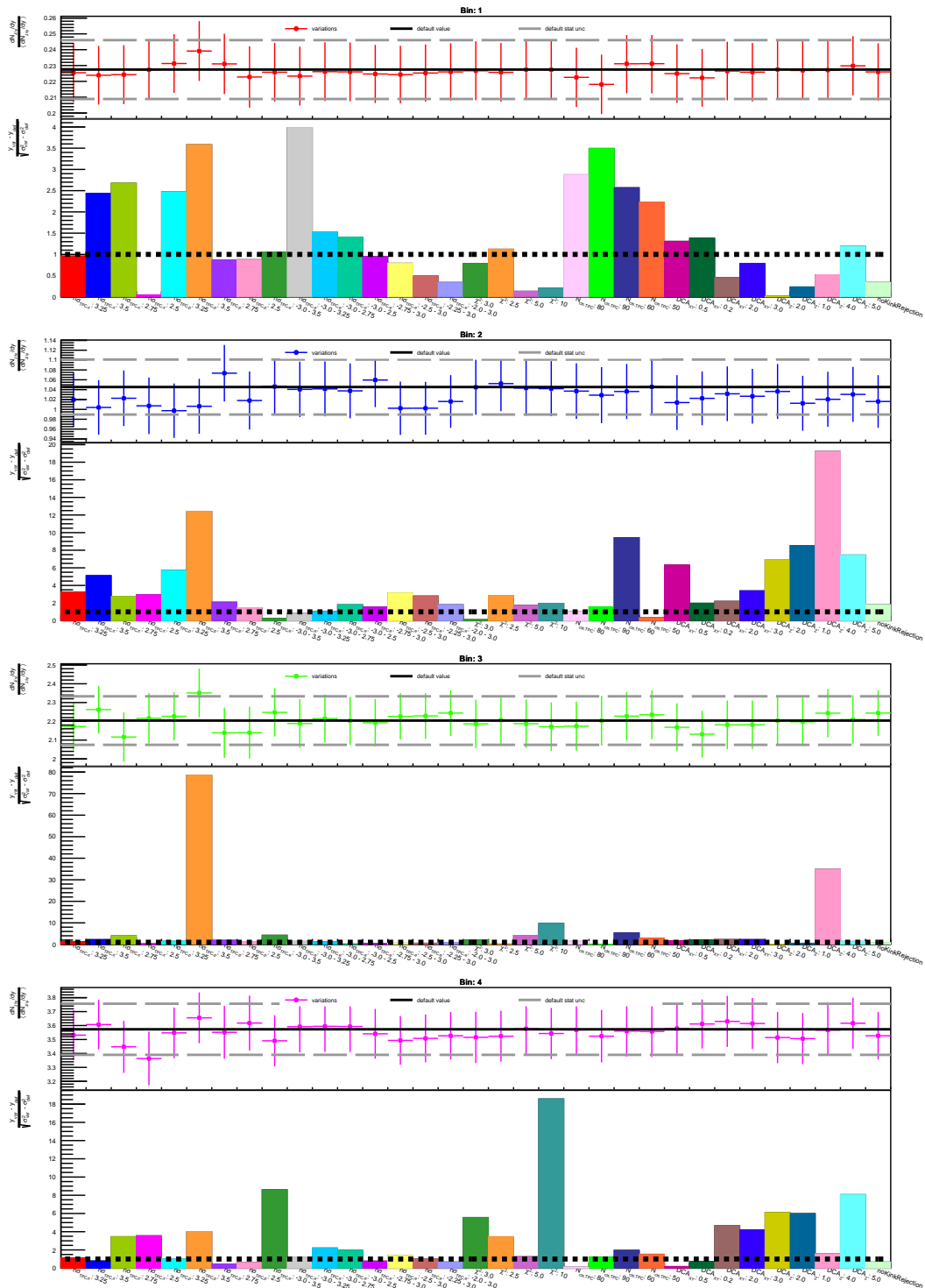**Figure C.2.:** Azimuth inclusive **Top:** High-p_T self-normalized J/ψ yields per variation to the signal extraction method. **Bottom:** Barlow criterion of each variation.

Azimuth inclusive: Low-p_T J/ψ bins. Variations to J/ψ's daughter tracks selection criteria

Figure C.3.: Azimuth inclusive **Top:** Low-p_T self-normalized J/ψ yields per variation to the J/ψ's daughter tracks selection criteria. **Bottom:** Barlow criterion of each variation.

Azimuth inclusive: Low-p_T J/ψ bins. Variations to signal extraction method

Figure C.4.: Azimuth inclusive **Top:** Low-p_T self-normalized J/ψ yields per variation to the signal extraction method. **Bottom:** Barlow criterion of each variation.

C.2. Toward region

Toward region: Integrated-p_T J/ψ bins. Variations to J/ψ's daughter tracks selection criteria

Figure C.5.: Toward region **Top:** Integrated-p_T self-normalized J/ψ yields per variation to the J/ψ's daughter tracks selection criteria. **Bottom:** Barlow criterion of each variation.

Toward region: Integrated-p_T J/ψ bins. Variations to signal extraction method
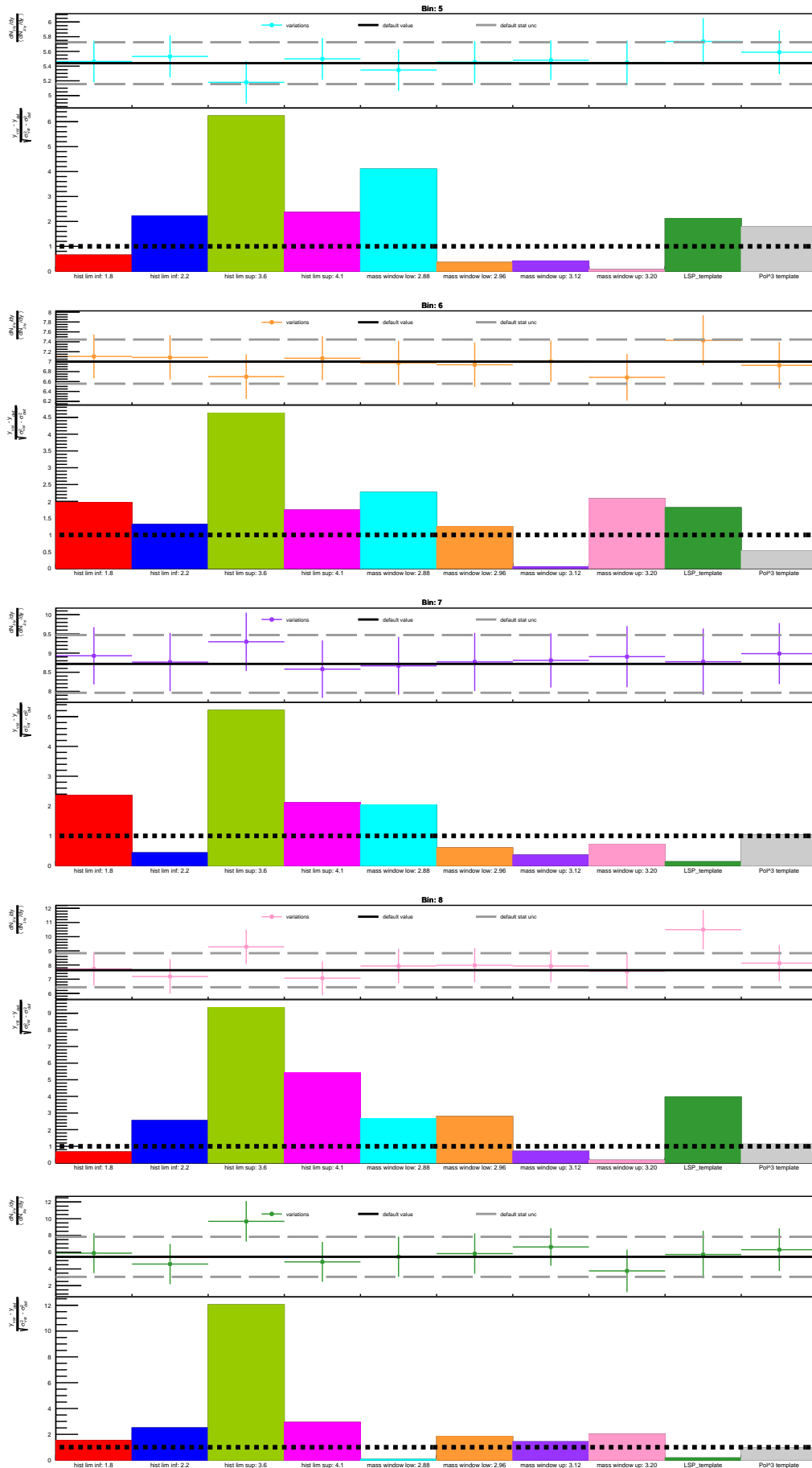
Figure C.6.: Toward region **Top:** Integrated-p_T self-normalized J/ψ yields per variation to the signal extraction method. **Bottom:** Barlow criterion of each variation.

Toward region: High-p_T J/ψ bins. Variations to J/ψ's daughter tracks selection criteria

Figure C.7.: Toward region **Top:** High-p_T self-normalized J/ψ yields per variation to the J/ψ's daughter tracks selection criteria. **Bottom:** Barlow criterion of each variation.
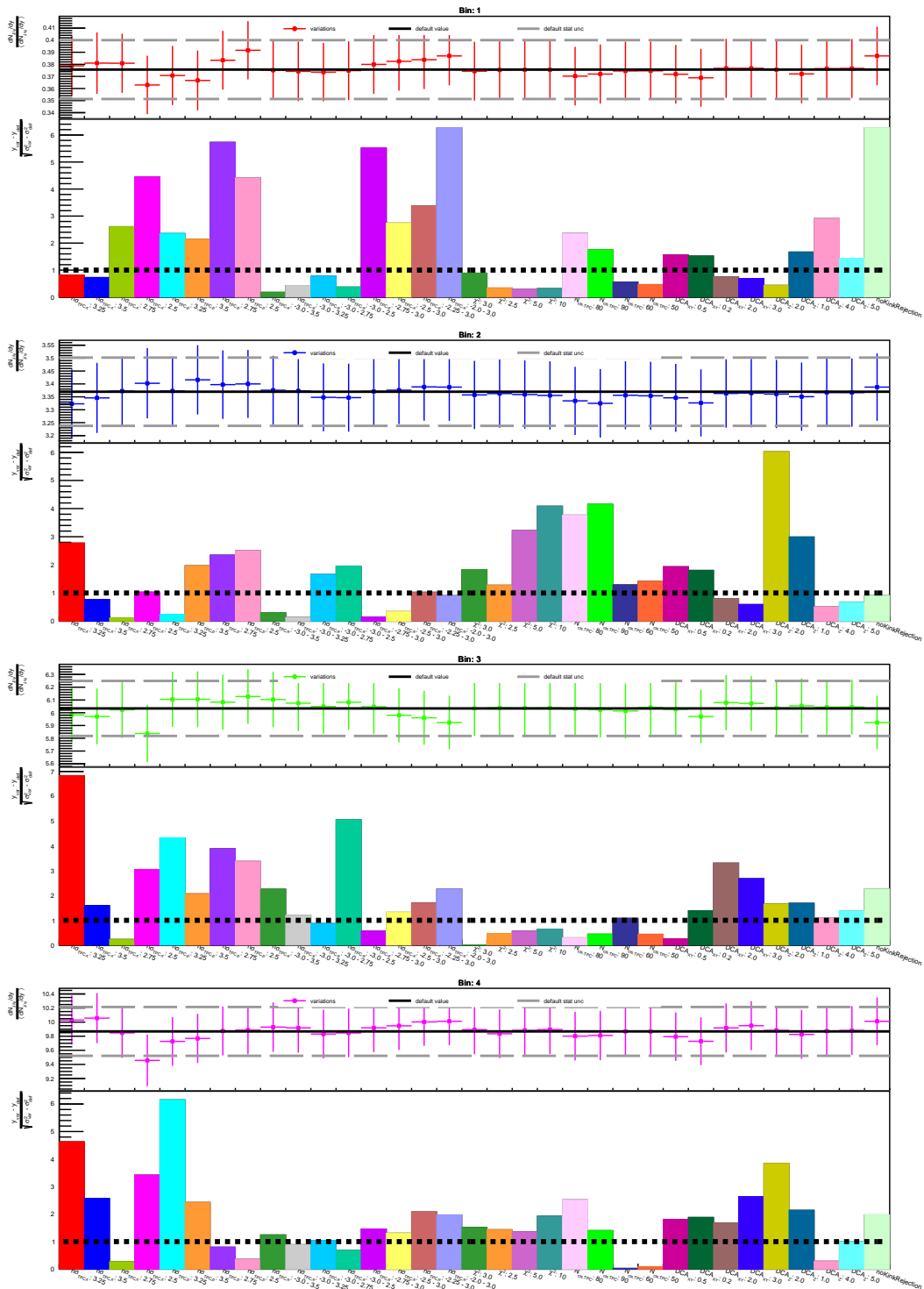
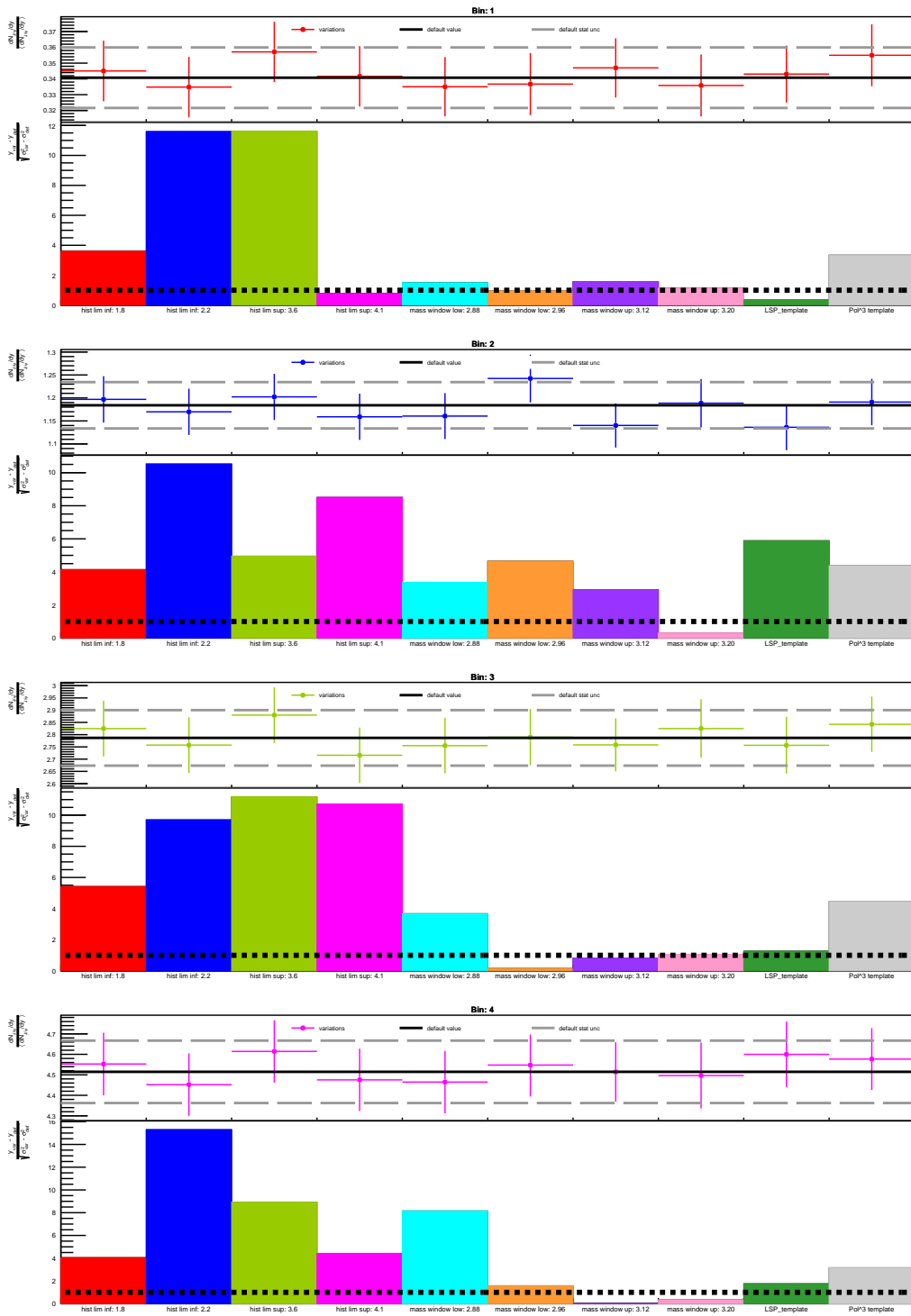**Toward region: High-p_T J/ψ bins. Variations to signal extraction method**
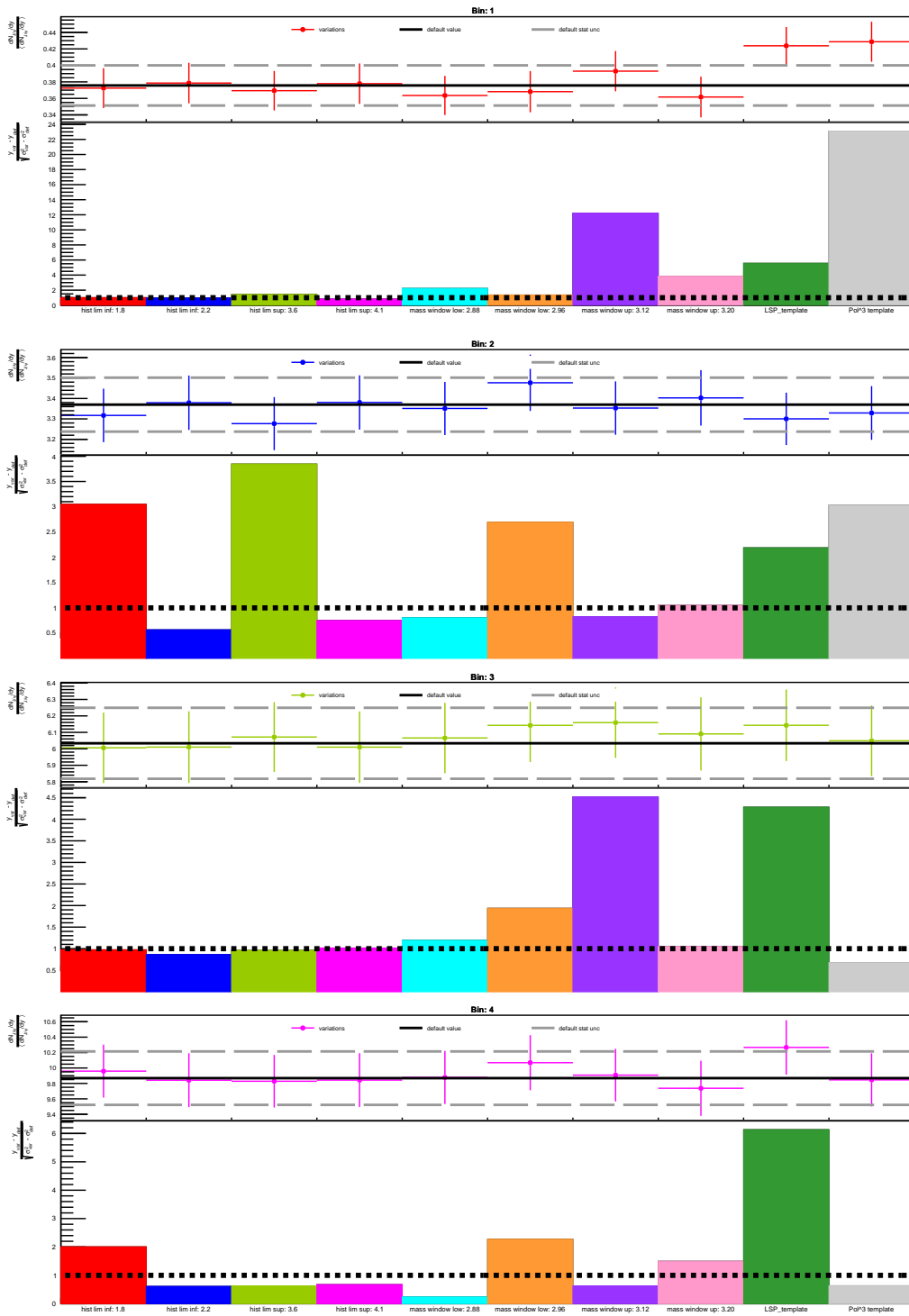
Figure C.8.: Toward region **Top:** High-p_T self-normalized J/ψ yields per variation to the signal extraction method. **Bottom:** Barlow criterion of each variation.

Toward region: Low-p_T J/ψ bins. Variations to J/ψ's daughter tracks selection criteria
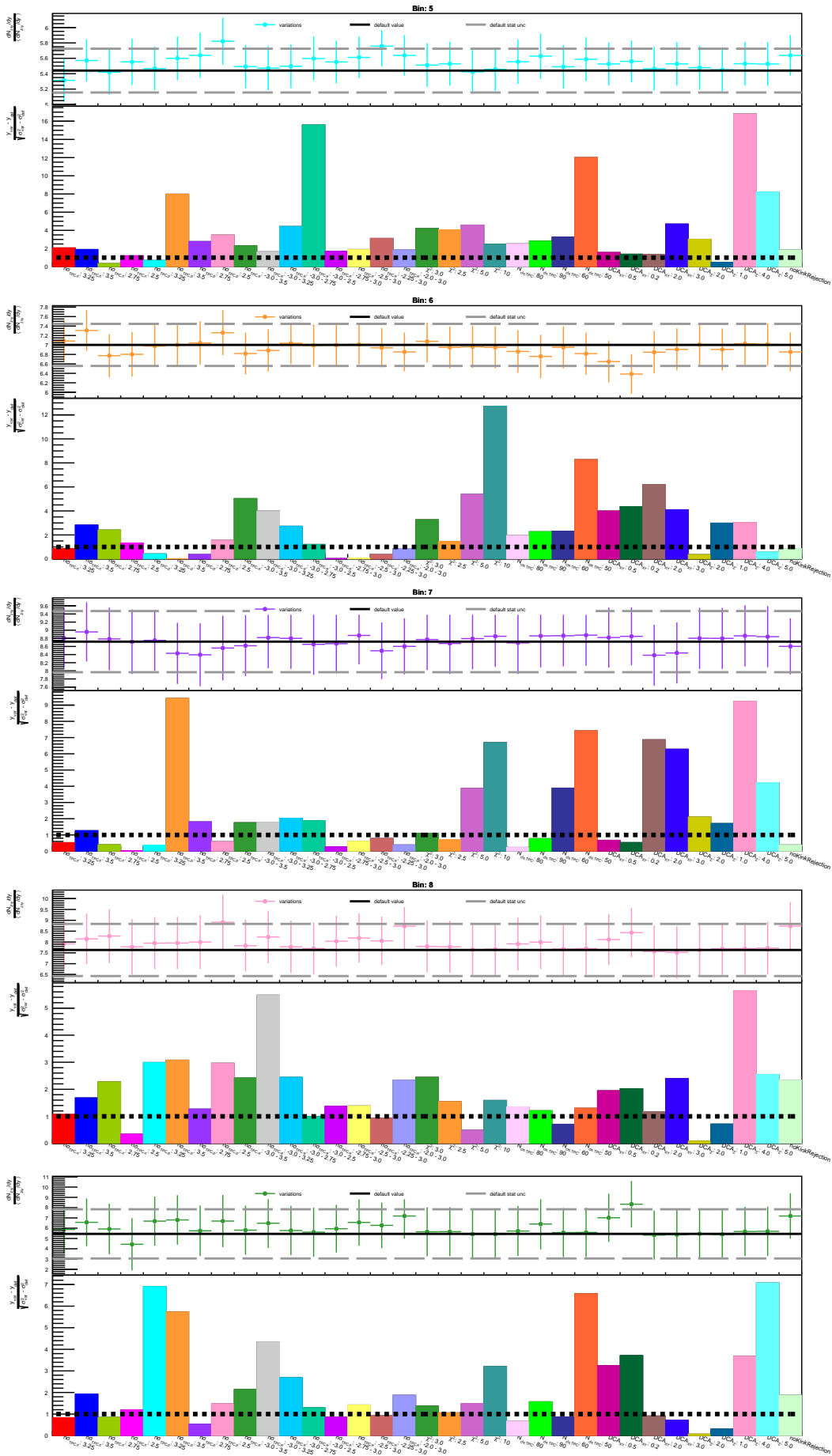
Figure C.9.: Toward region **Top:** Low-p_T self-normalized J/ψ yields per variation to the J/ψ's daughter tracks selection criteria. **Bottom:** Barlow criterion of each variation.

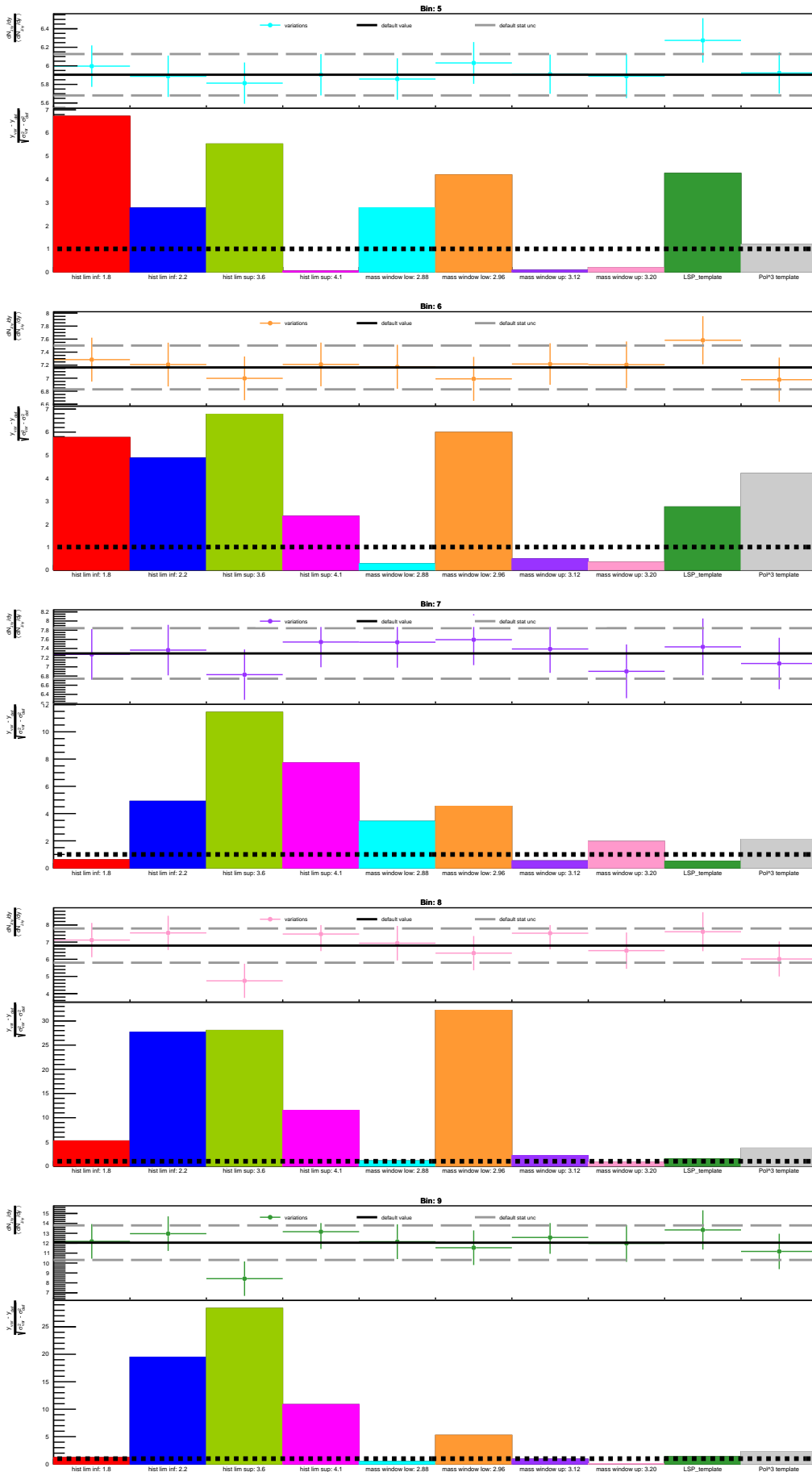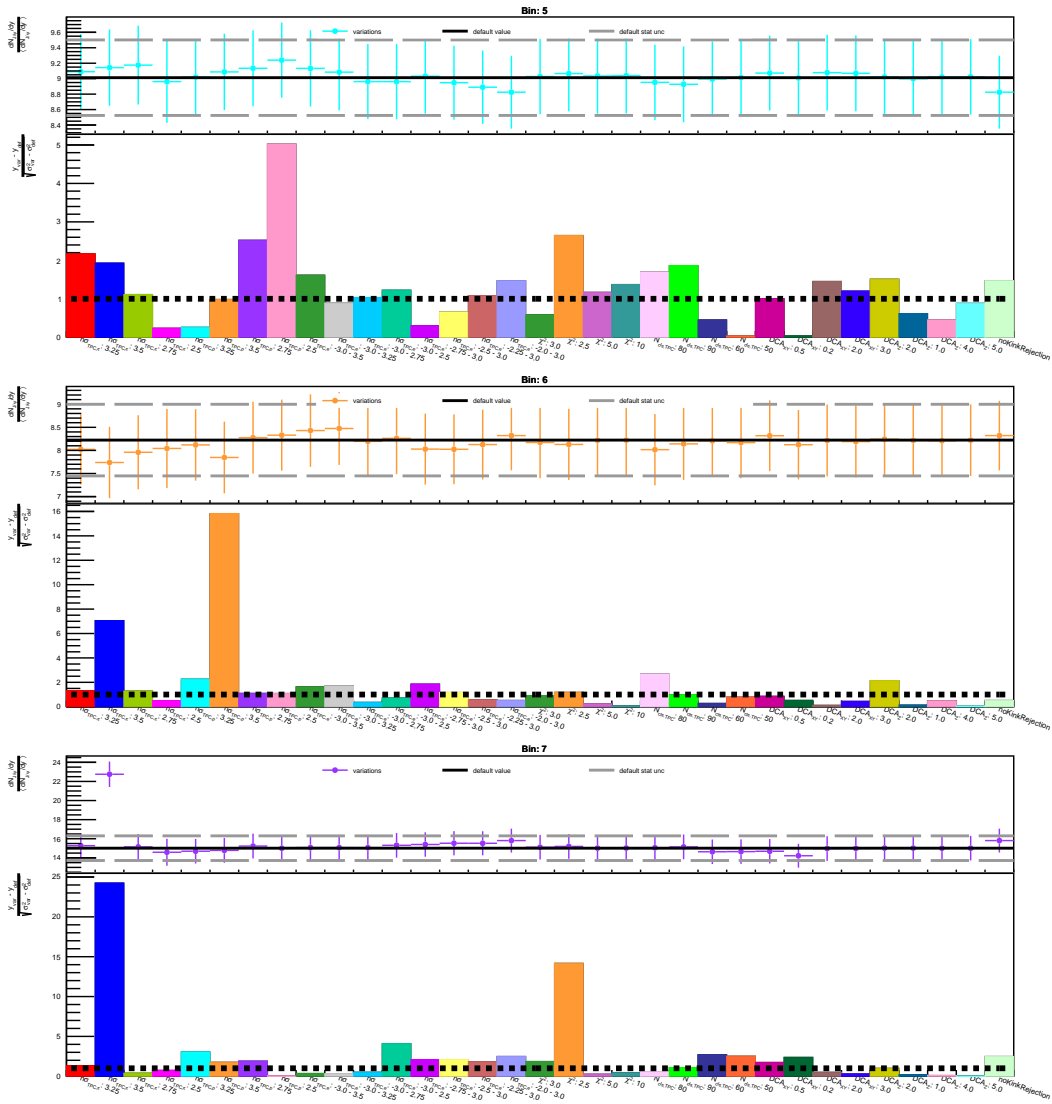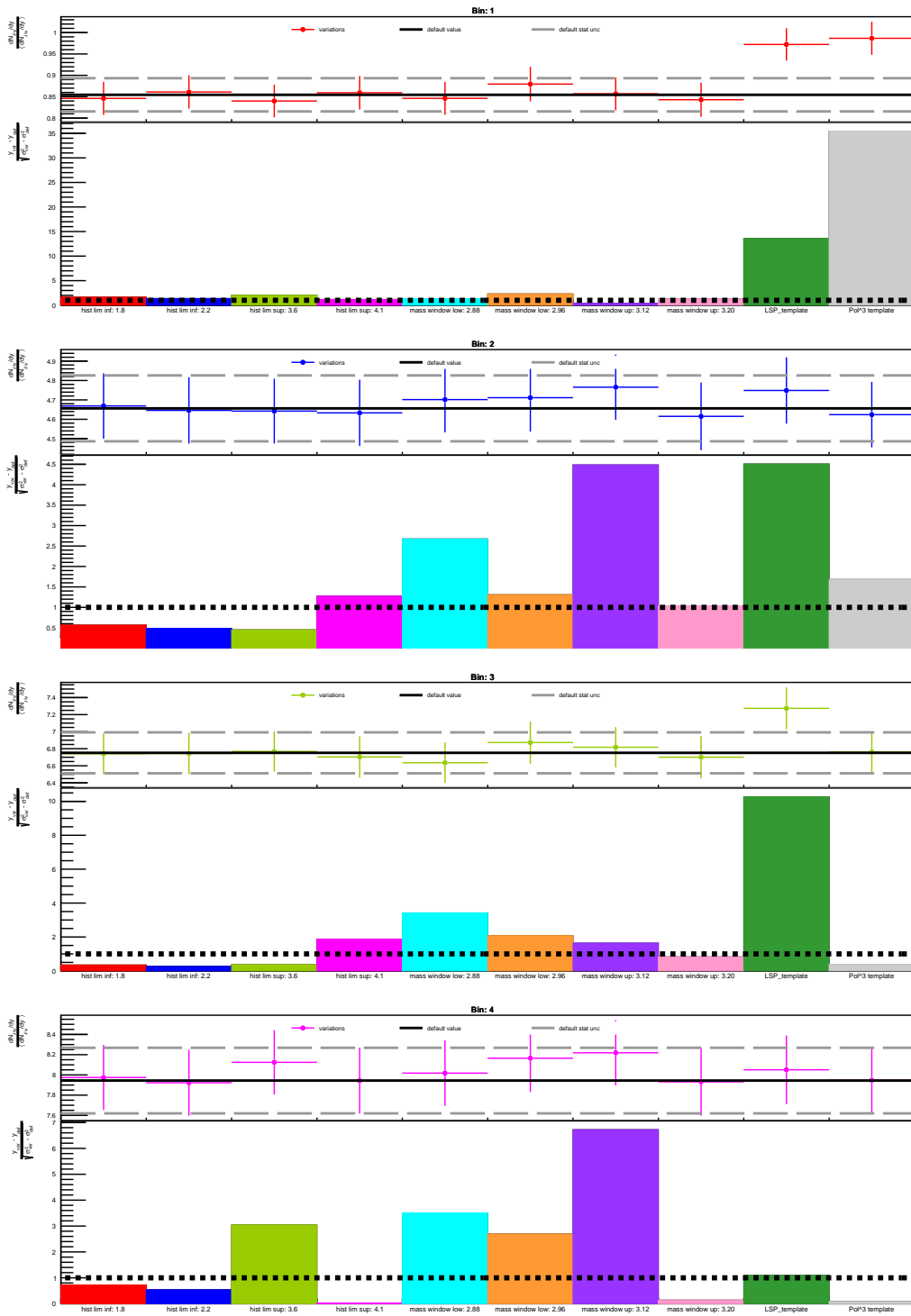**Toward region: Low-p_T J/ψ bins. Variations to signal extraction method**
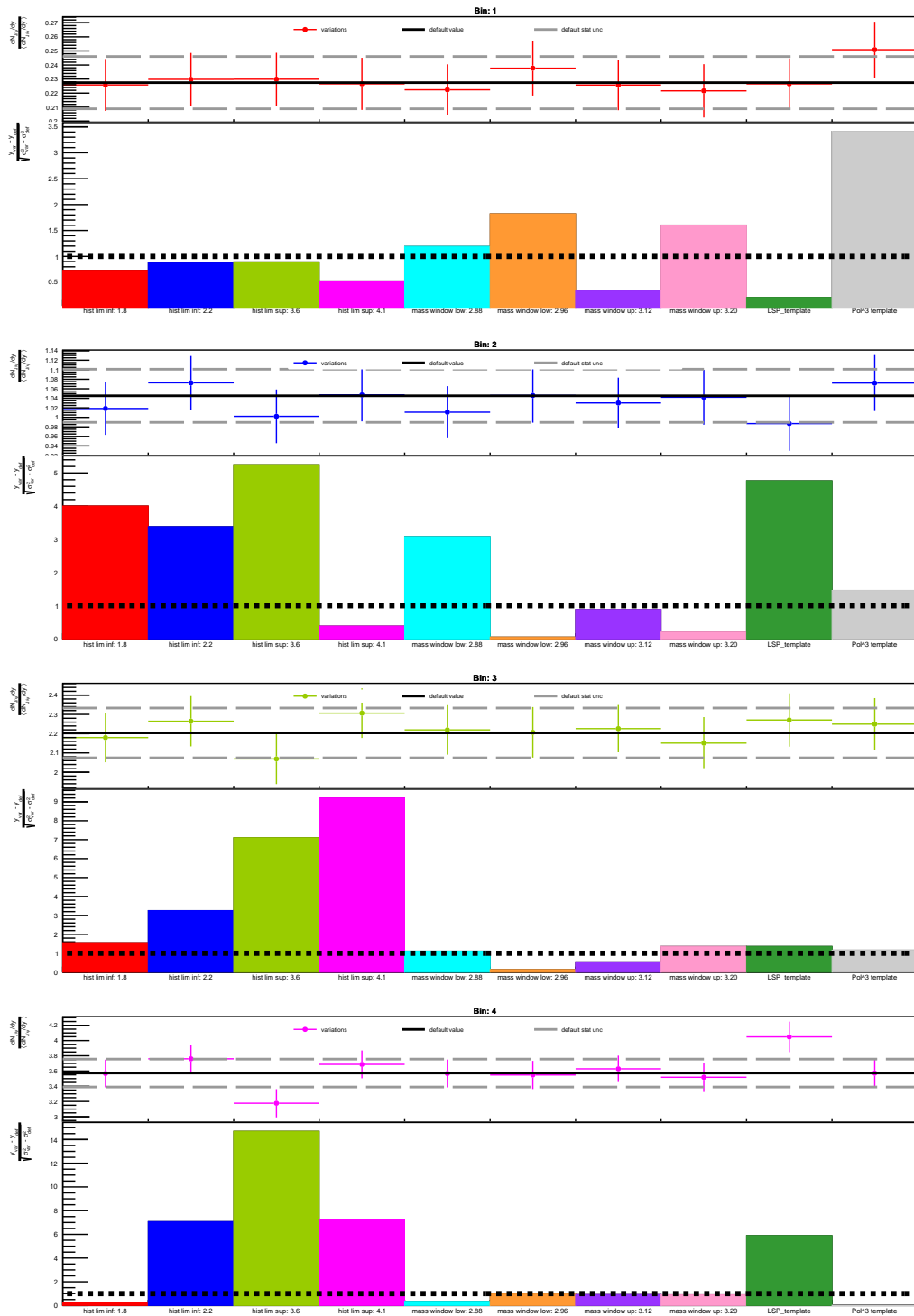
Figure C.10.: Toward region **Top:** Low-p_T self-normalized J/ψ yields per variation to the signal extraction method. **Bottom:** Barlow criterion of each variation.

C.3. Transverse region

Transverse region: Integrated-p_T J/ψ bins. Variations to J/ψ's daughter tracks selection criteria

Figure C.11.: Transverse region **Top:** Integrated-p_T self-normalized J/ψ yields per variation to the J/ψ's daughter tracks selection criteria. **Bottom:** Barlow criterion of each variation.

Transverse region: Integrated-p_{T} J/ψ bins. Variations to signal extraction method
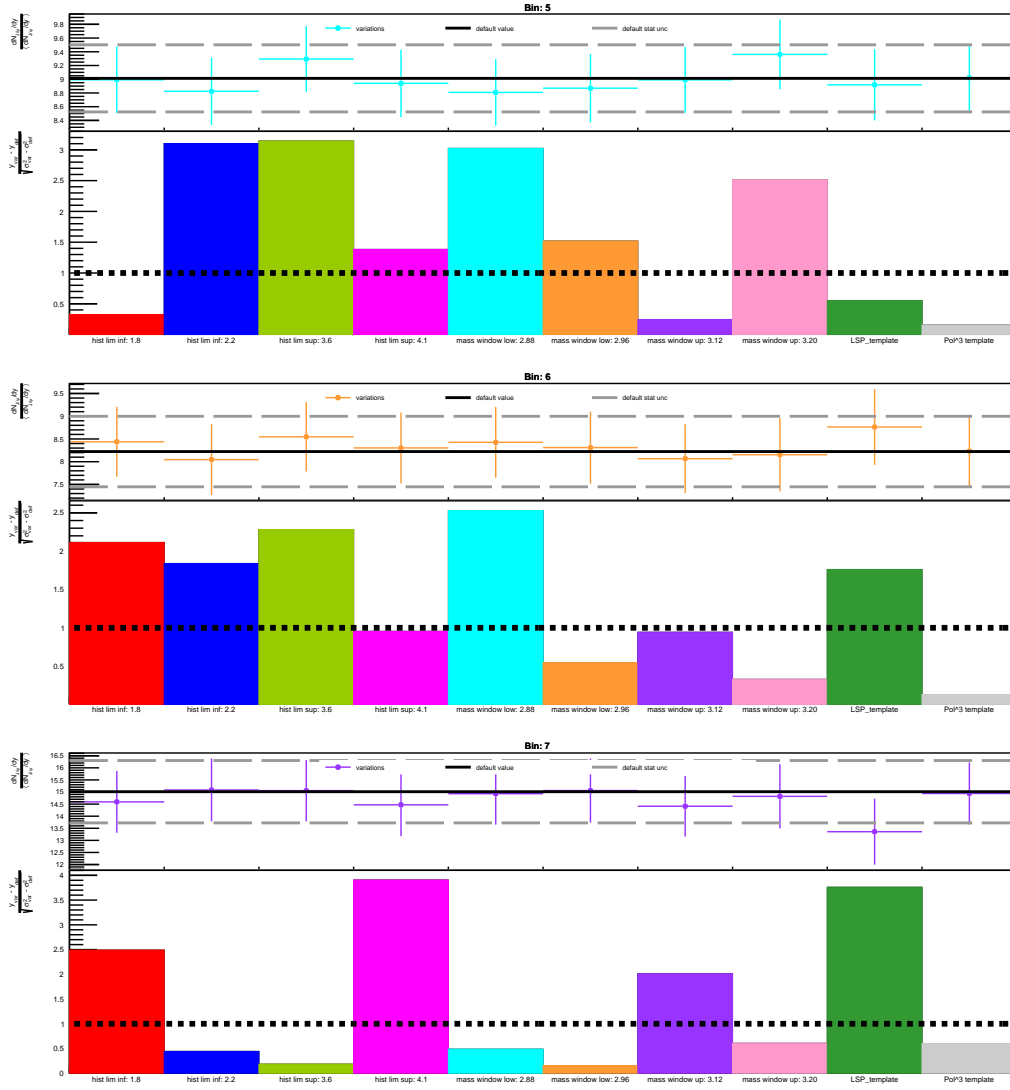
Figure C.12.: Transverse region **Top:** Integrated-p_T self-normalized J/ψ yields per variation to the signal extraction method. **Bottom:** Barlow criterion of each variation.

Transverse region: High-p_T J/ψ bins. Variations to J/ψ's daughter tracks selection criteria
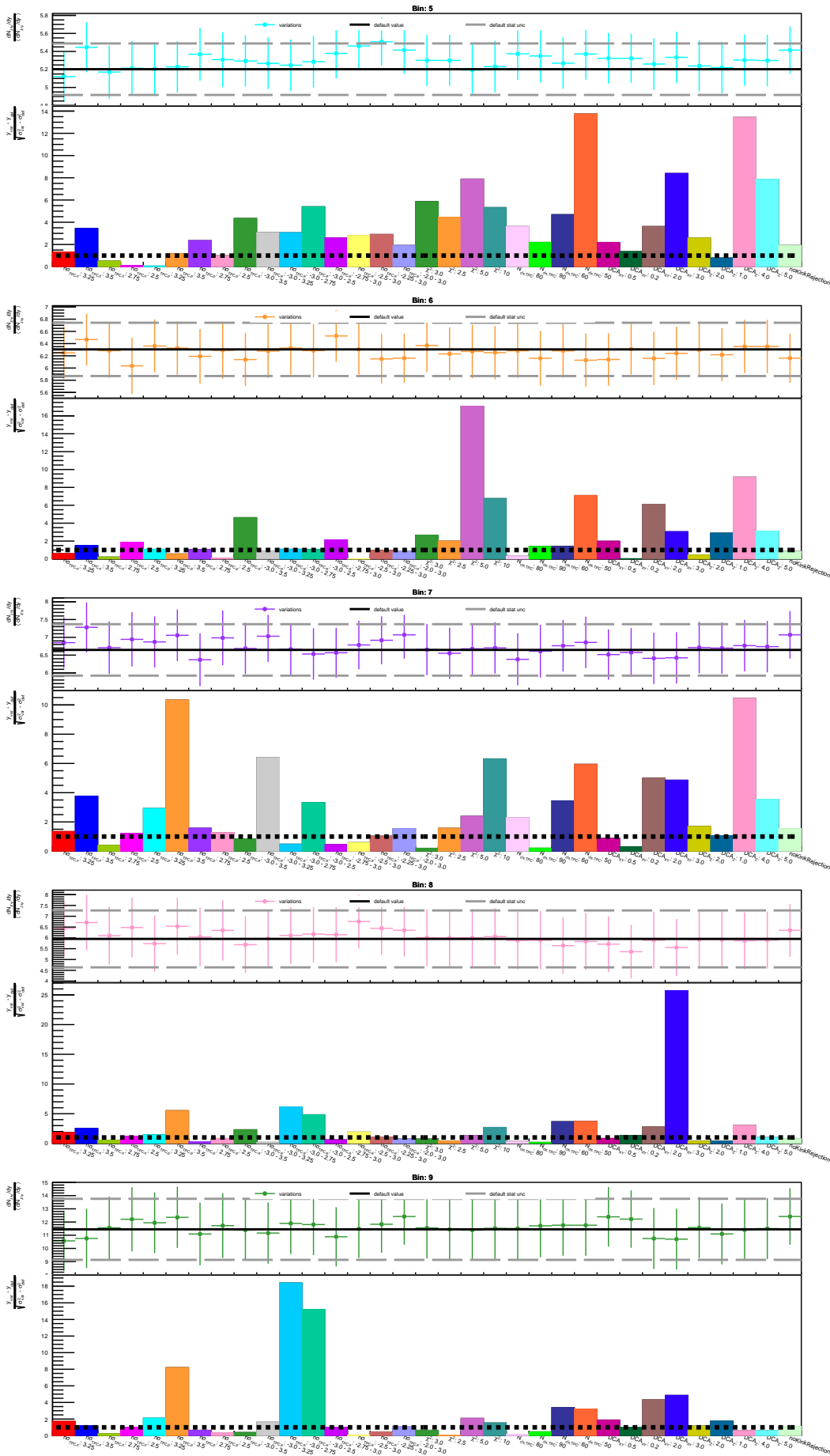
Figure C.13.: Transverse region **Top:** High-p_T self-normalized J/ψ yields per variation to the J/ψ's daughter tracks selection criteria. **Bottom:** Barlow criterion of each variation.

Transverse region: High-p_T J/ψ bins. Variations to signal extraction method

Figure C.14.: Transverse region **Top:** High-p_T self-normalized J/ψ yields per variation to the signal extraction method. **Bottom:** Barlow criterion of each variation.

Transverse region: Low-p_T J/ψ bins. Variations to J/ψ's daughter tracks selection criteria
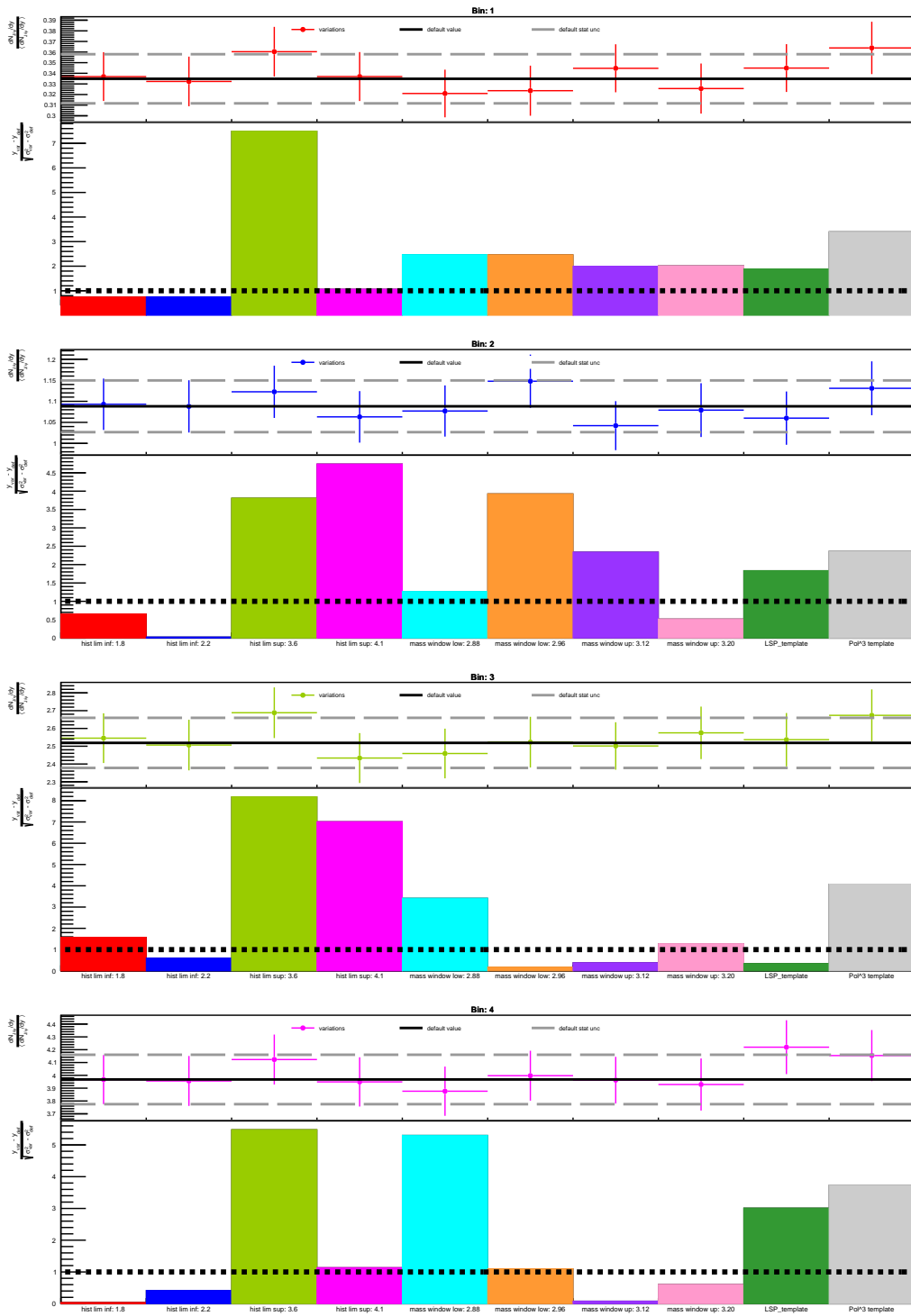
Figure C.15.: Transverse region **Top:** Low-p_T self-normalized J/ψ yields per variation to the J/ψ's daughter tracks selection criteria. **Bottom:** Barlow criterion of each variation.

Transverse region: Low-p_T J/ψ bins. Variations to signal extraction method
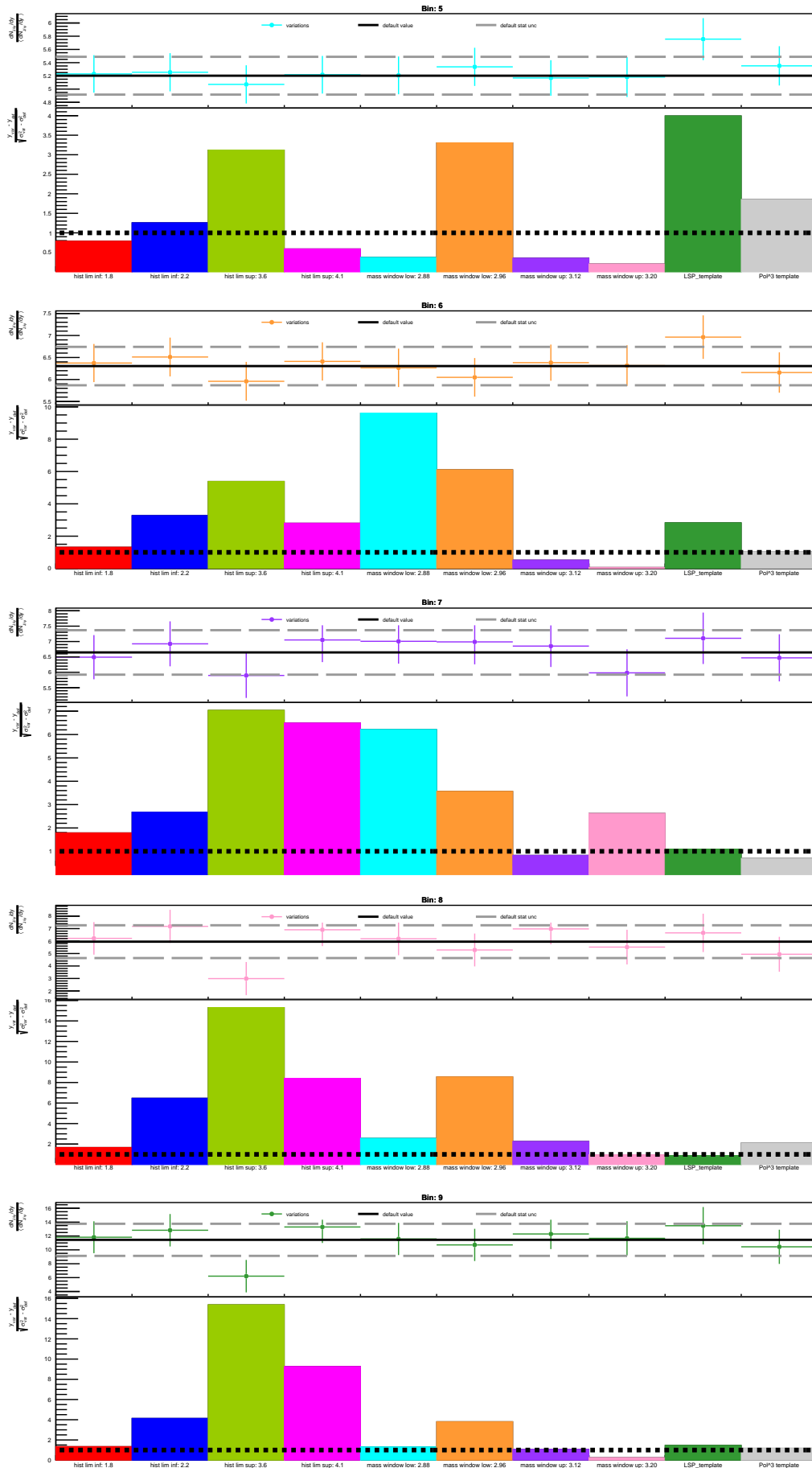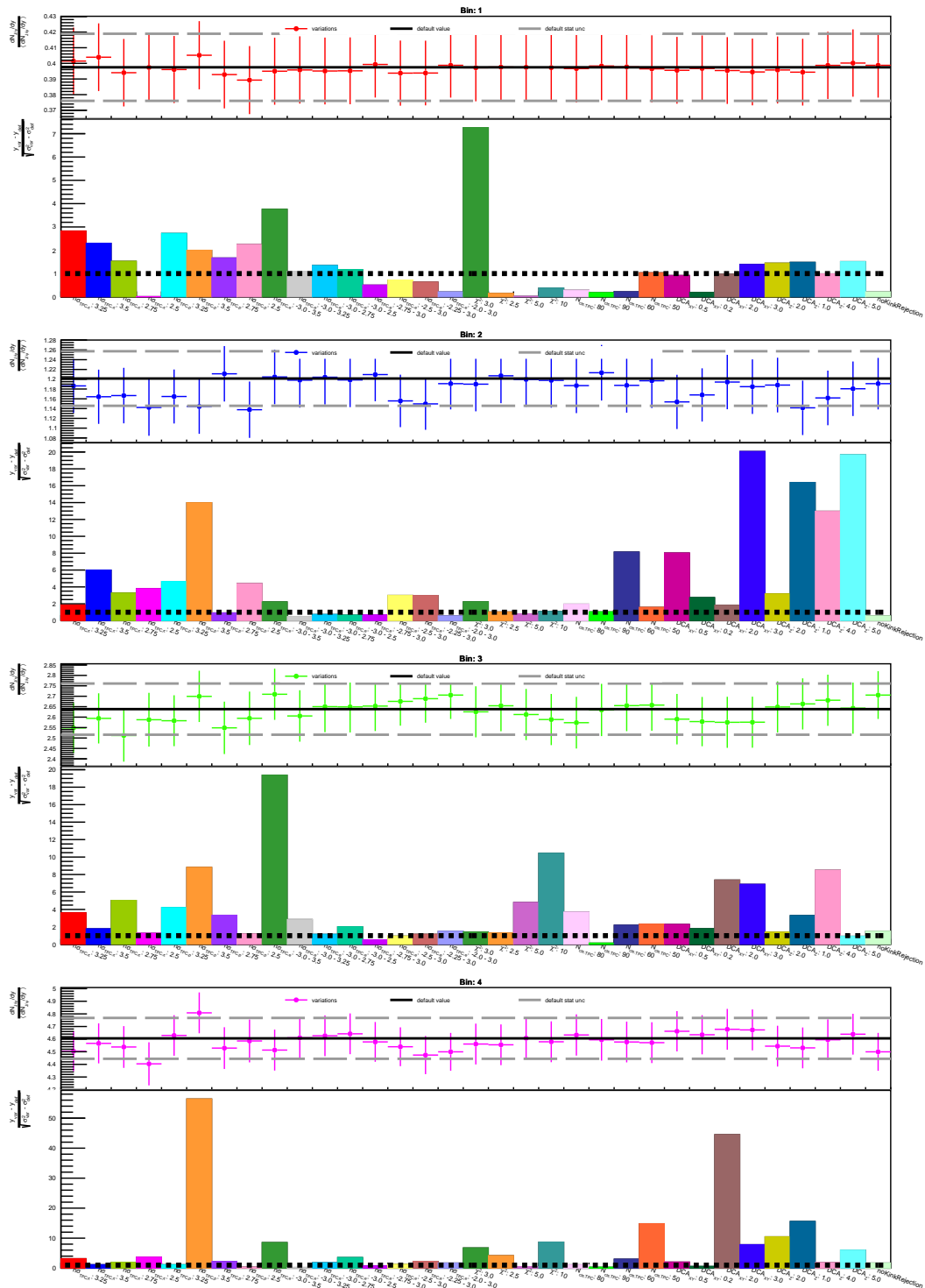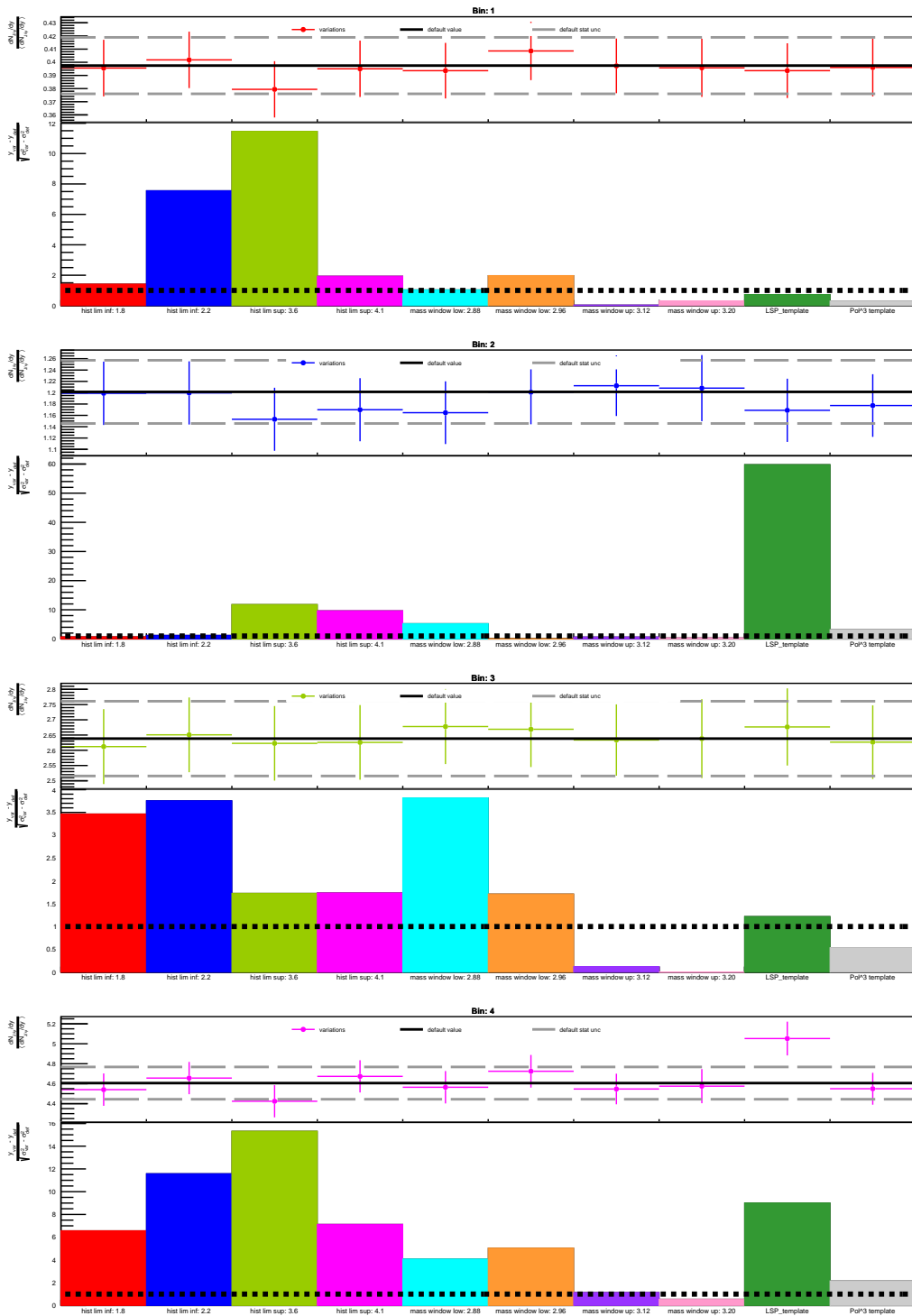
Figure C.16.: Transverse region **Top:** Low-p_T self-normalized J/ψ yields per variation to the signal extraction method. **Bottom:** Barlow criterion of each variation.

C.4. Away region

Away region: Integrated-p_T J/ψ bins. Variations to J/ψ's daughter tracks selection criteria

Figure C.17.: Away region **Top:** Integrated-p_T self-normalized J/ψ yields per variation to the J/ψ's daughter tracks selection criteria. **Bottom:** Barlow criterion of each variation.

Away region: Integrated-p_T J/ψ bins. Variations to signal extraction method

Figure C.18.: Away region **Top:** Integrated-p_T self-normalized J/ψ yields per variation to the signal extraction method. **Bottom:** Barlow criterion of each variation.

Away region: High-p_T J/ψ bins. Variations to J/ψ's daughter tracks selection criteria

Figure C.19.: Away region **Top:** High-p_T self-normalized J/ψ yields per variation to the J/ψ's daughter tracks selection criteria. **Bottom:** Barlow criterion of each variation.

Away region: High-p_T J/ψ bins. Variations to signal extraction method
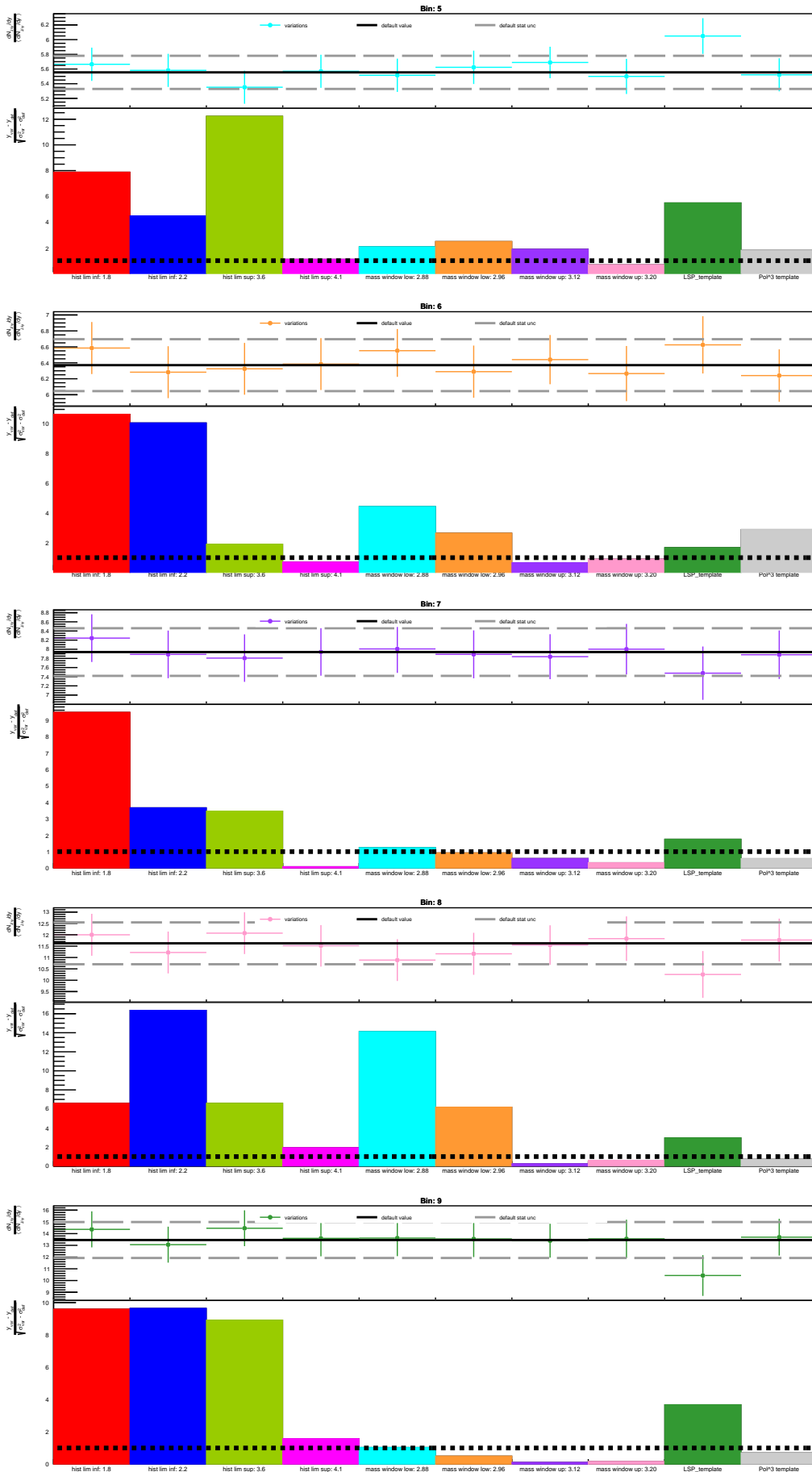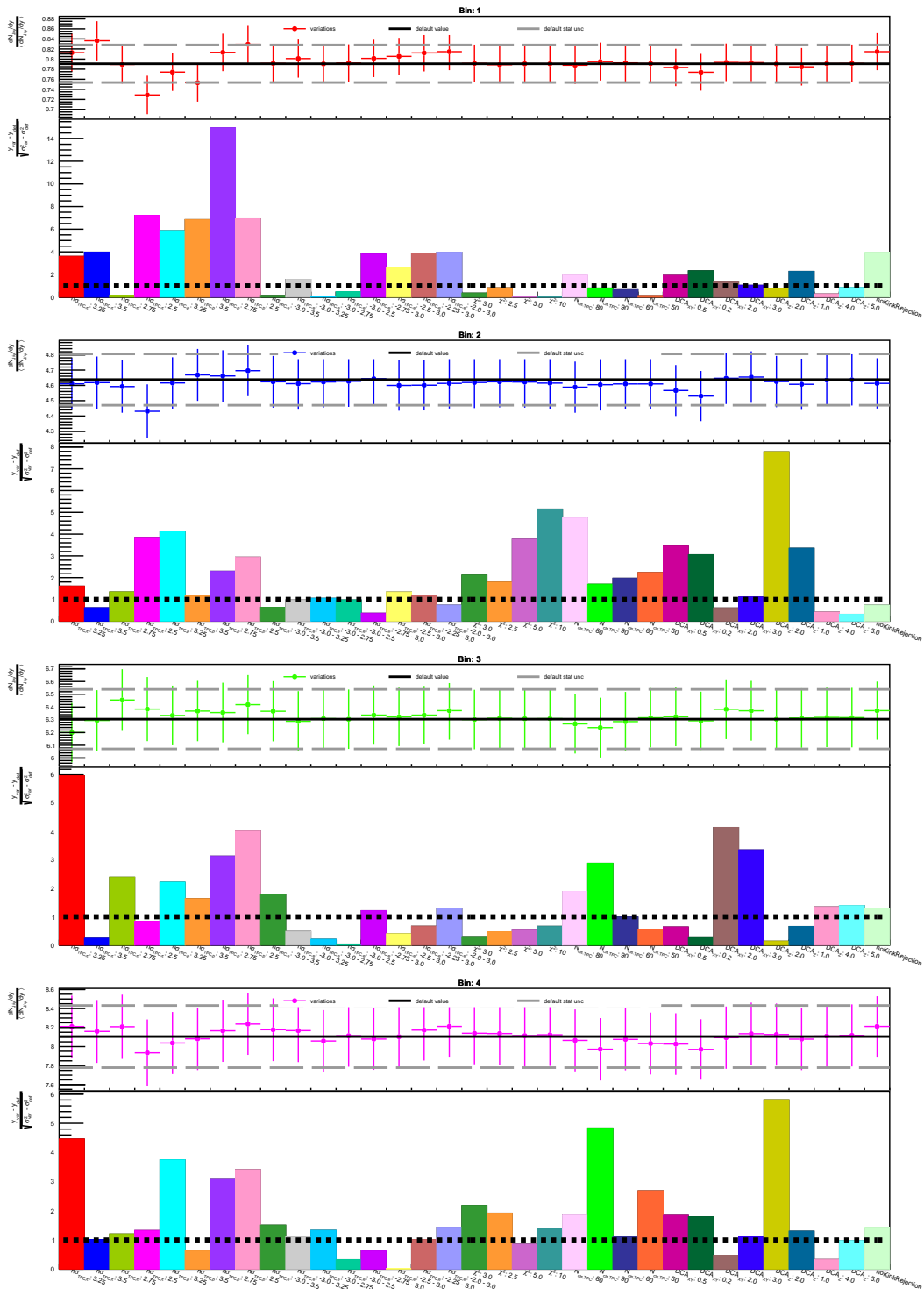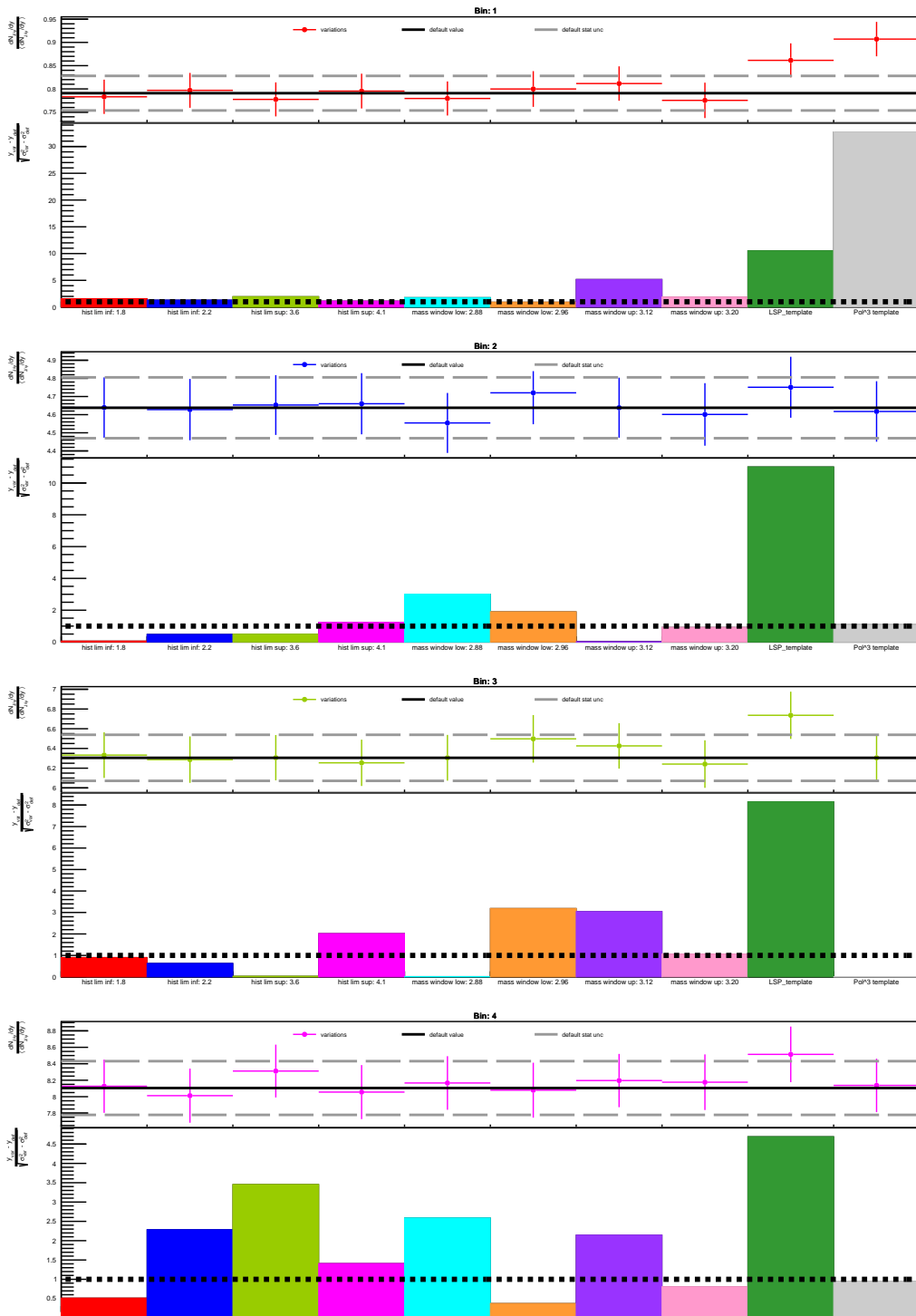
Figure C.20.: Away region **Top:** High-p_T self-normalized J/ψ yields per variation to the signal extraction method. **Bottom:** Barlow criterion of each variation.

Away region: Low-p_T J/ψ bins. Variations to J/ψ's daughter tracks selection criteria

Figure C.21.: Away region **Top:** Low-p_T self-normalized J/ψ yields per variation to the J/ψ's daughter tracks selection criteria. **Bottom:** Barlow criterion of each variation.

Away region: Low-p_T J/ψ bins. Variations to signal extraction method
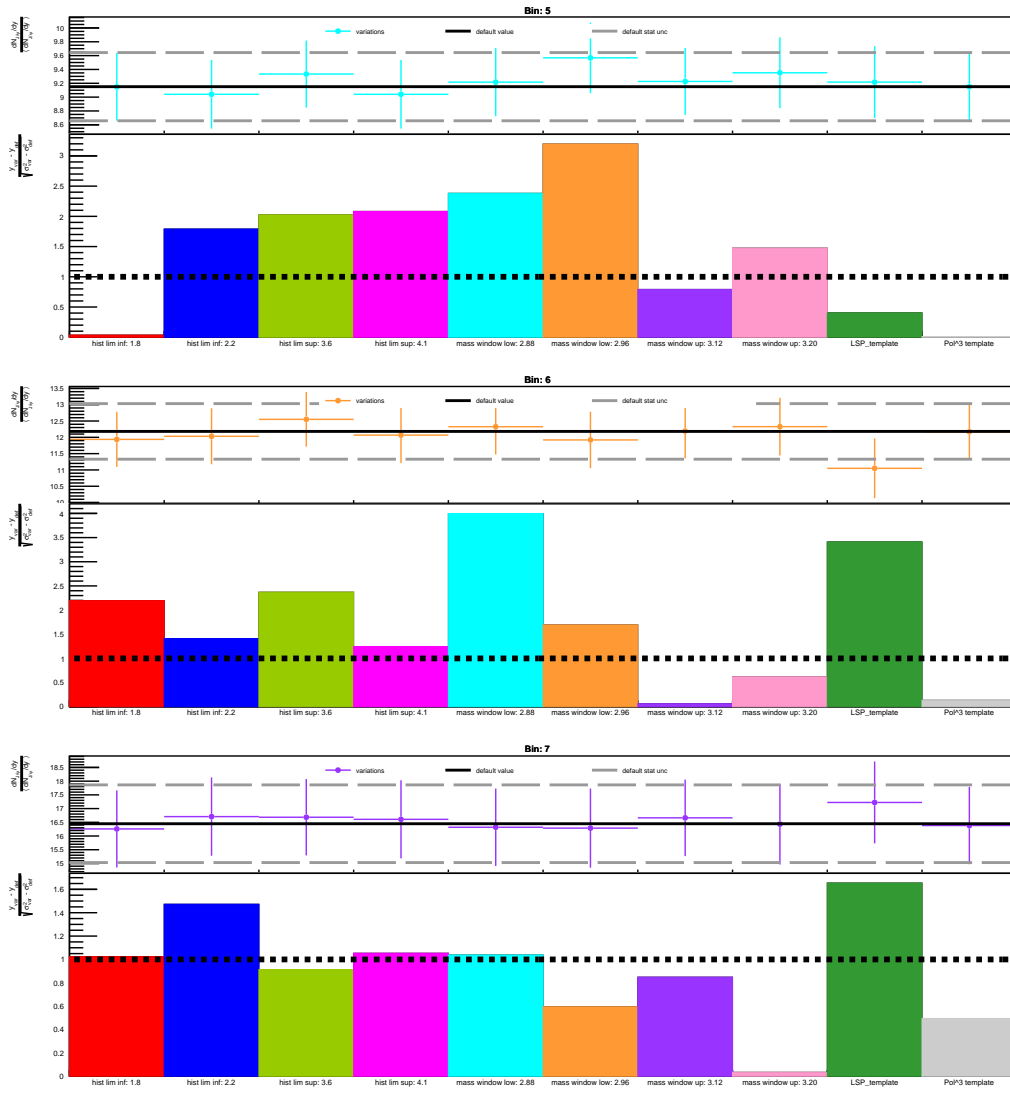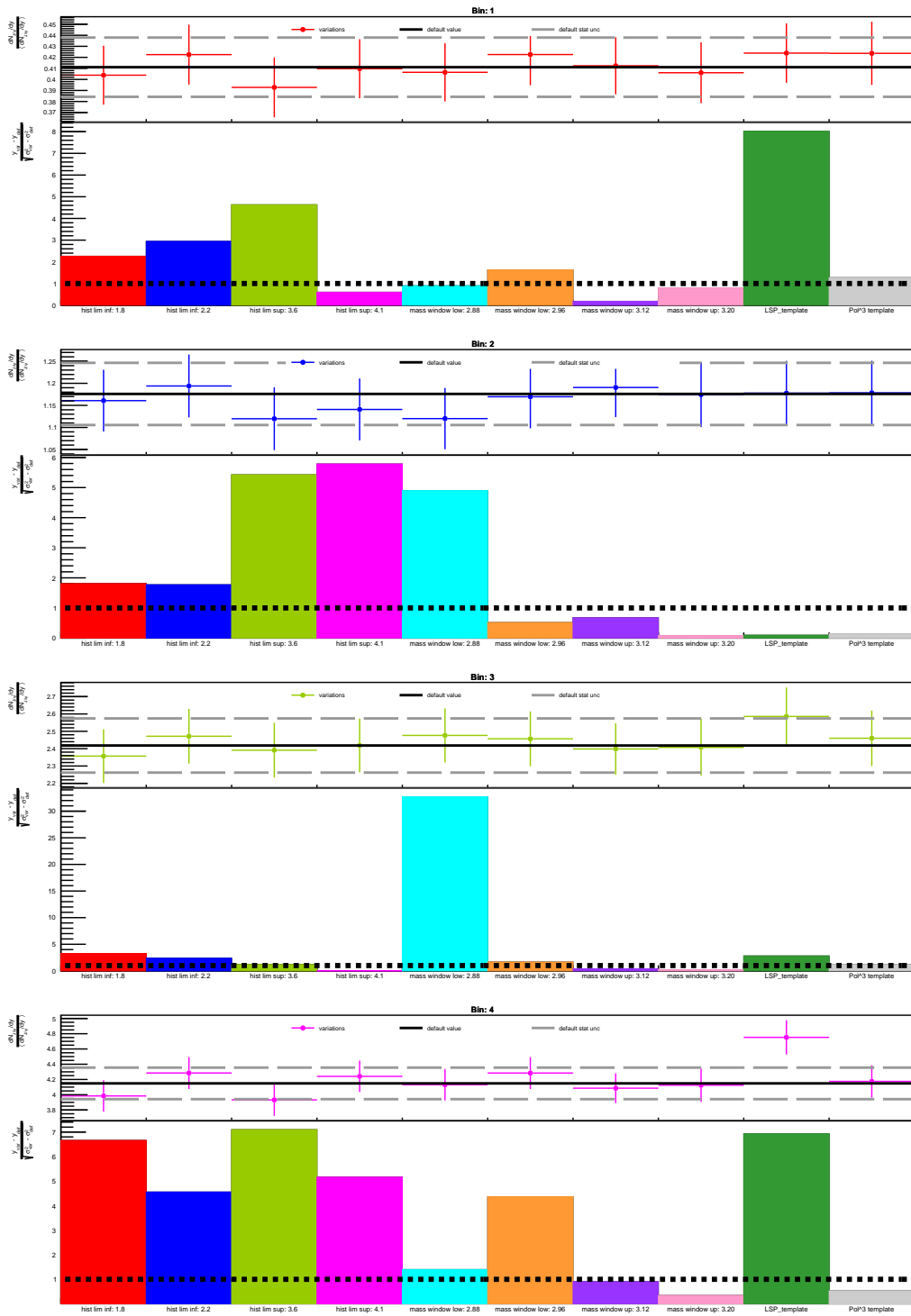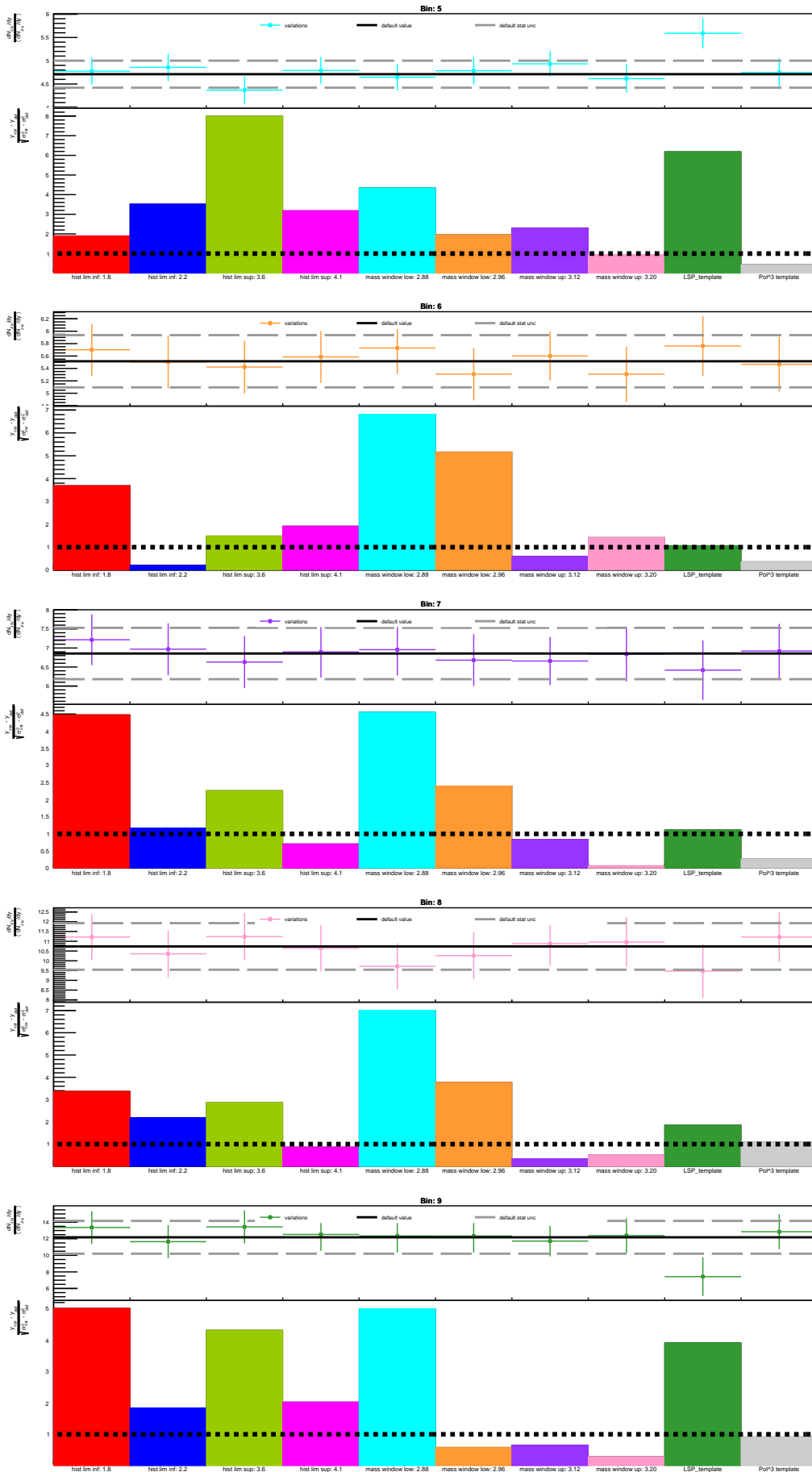
Figure C.22.: Away region **Top:** Low-p_T self-normalized J/ψ yields per variation to the signal extraction method. **Bottom:** Barlow criterion of each variation.

D. ALICE-MC J/ψ-N$_{\text{ch}}$ dependency compared to experimental results

(a)

(b)

(c)

Figure D.1.: Toward region: Comparison between ALICE-MC data and ALICE data of the self-normalized J/ψ yields as a function of the charged particle multiplicity for inclusive p_{T} D.1a, high-p_{T} D.1b, and low-p_{T} D.1c J/ψs.

(a)

(b)

(c)

Figure D.2.: Transverse region: Comparison between ALICE-MC data and ALICE data of the self-normalized J/ψ yields as a function of the charged particle multiplicity for inclusive p_T D.2a, high-p_T D.2b, and low-p_T D.2c J/ψs.
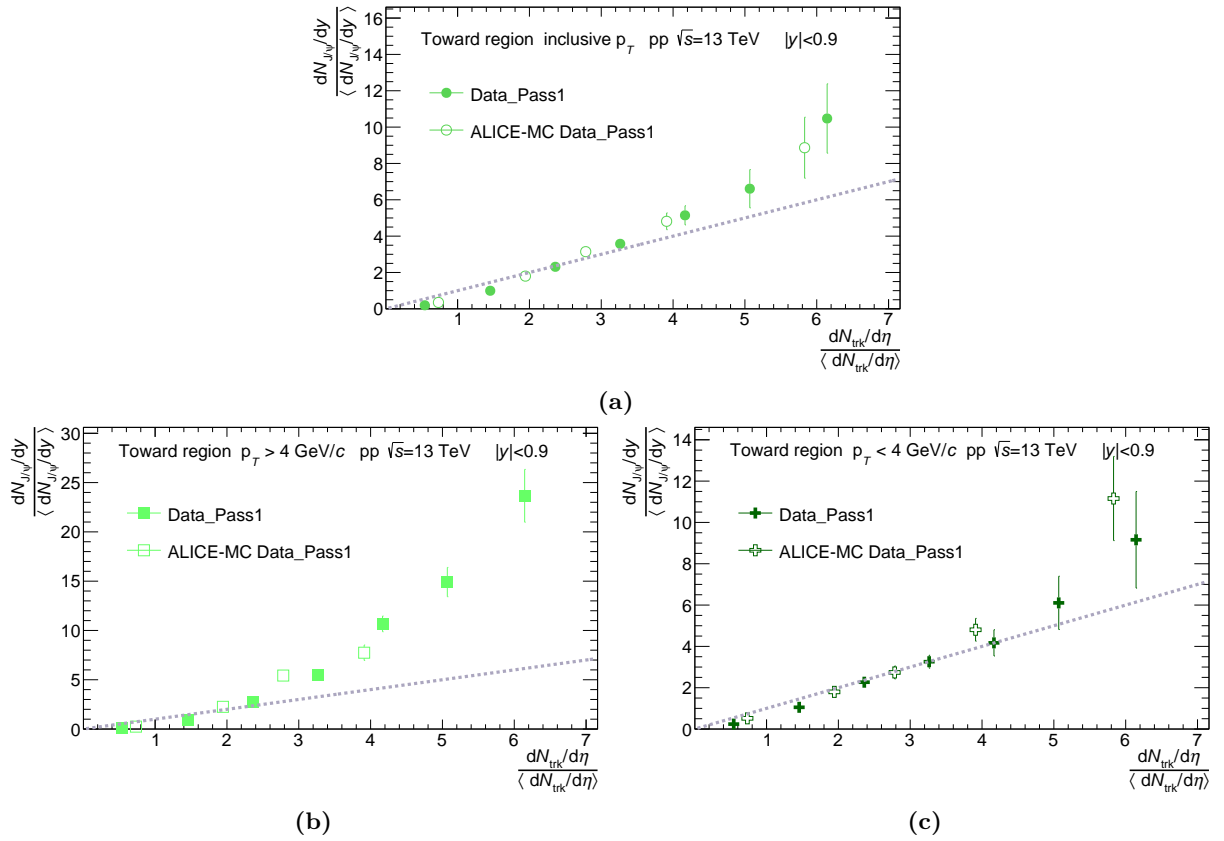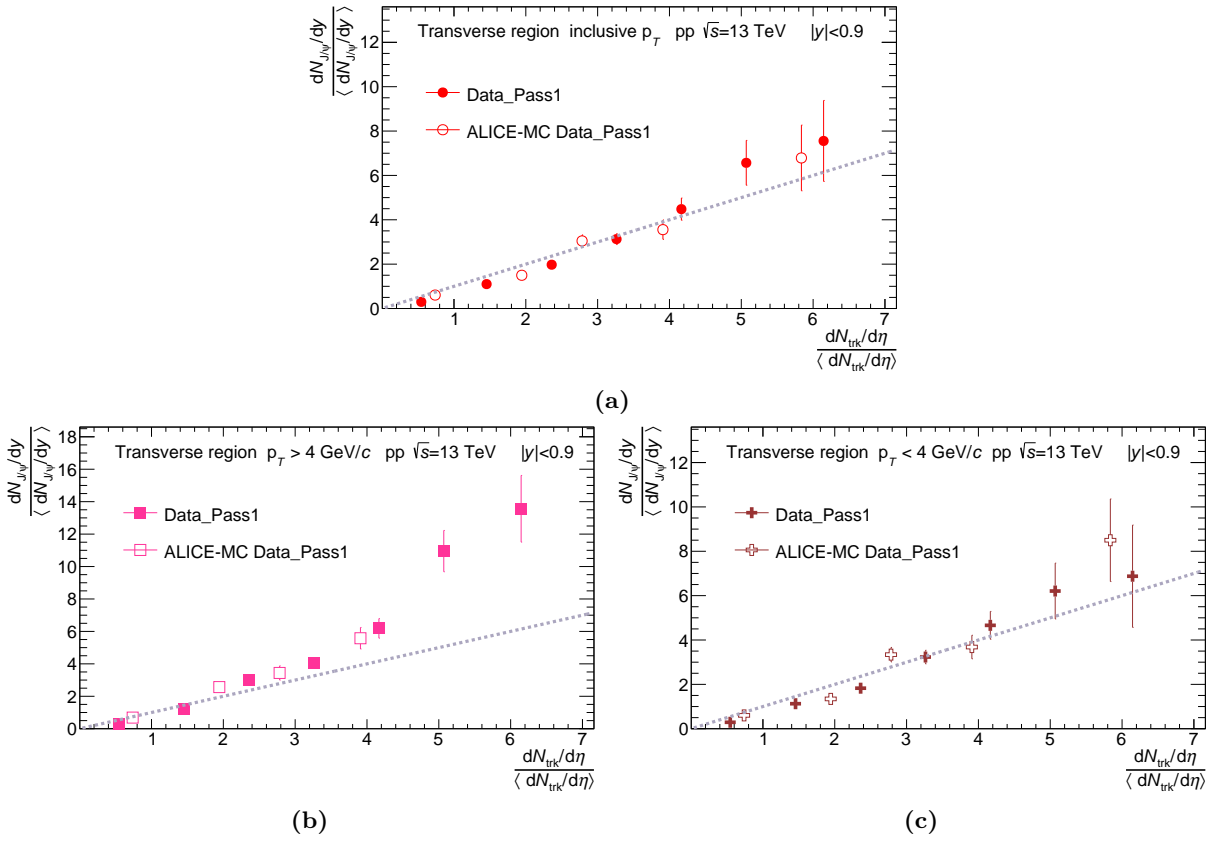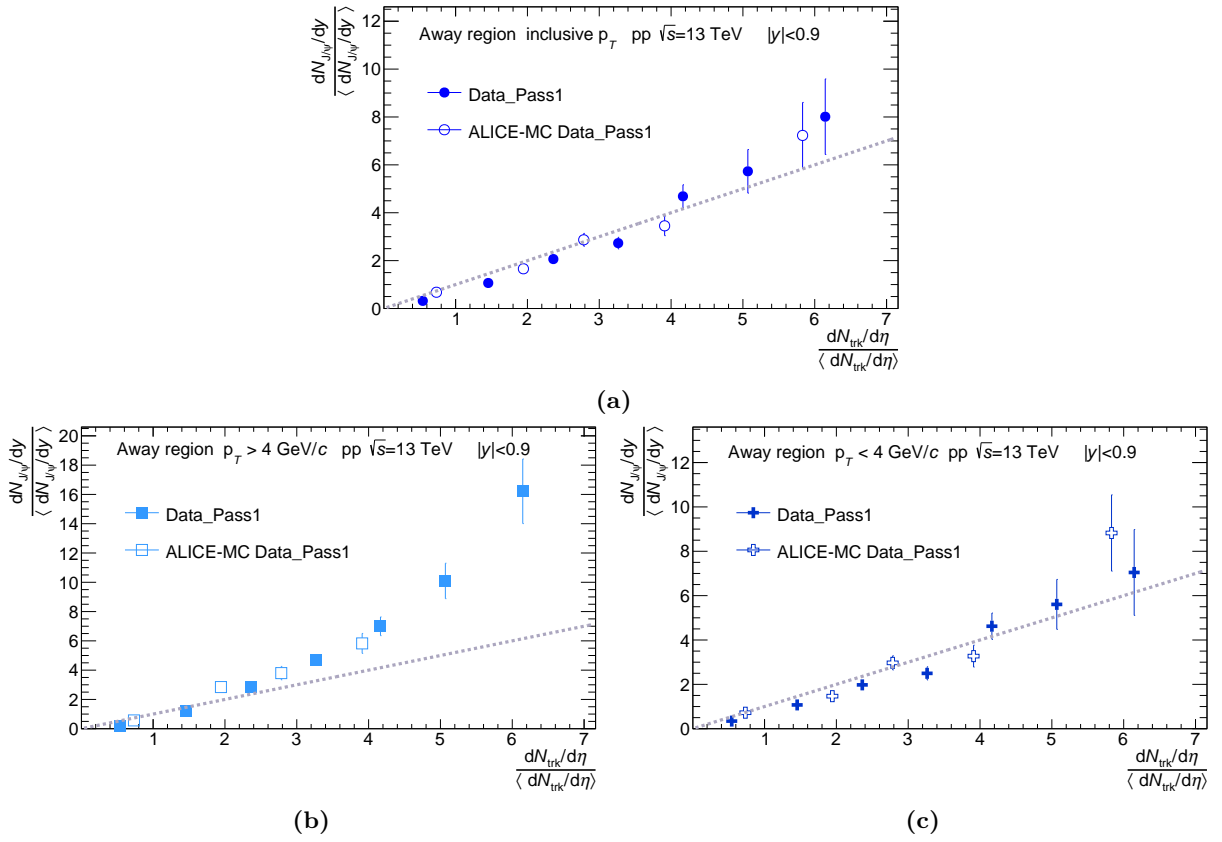
Figure D.3.: Away region: Comparison between ALICE-MC data and ALICE data of the self-normalized J/ψ yields as a function of the charged particle multiplicity for inclusive p_T D.3a, high-p_T D.3b, and low-p_T D.3c J/ψs.

References

[1] S. G. Weber et al. "Elucidating the multiplicity dependence of J/ψ production in proton–proton collisions with PYTHIA8". In: *Eur. Phys. J. C* 79.1 (2019), p. 36. DOI: 10.1140/epjc/s10052-018-6531-4. arXiv: 1811.07744 [nucl-th].

[2] Luis Álvarez-Gaumé and Miguel Á. Vázquez-Mozo. "Field theory and the Standard Model: A symmetry-oriented approach". In: *CERN Yellow Rep. School Proc.* 1 (2025), p. 1. DOI: 10.23730/CYRSP-2025-001.1. arXiv: 2306.08097 [hep-th].

[3] W. Buchmuller and C. Ludeling. "Field Theory and Standard Model". In: *2005 European School of High-Energy Physics*. Sept. 2006. arXiv: hep-ph/0609174.

[4] Shreyasi Acharya et al. "The ALICE experiment: a journey through QCD". In: *Eur. Phys. J. C* 84.8 (2024), p. 813. DOI: 10.1140/epjc/s10052-024-12935-y. arXiv: 2211.04384 [nucl-ex].

[5] John W. Harris and Berndt Müller. ""QGP Signatures" Revisited". In: *Eur. Phys. J. C* 84.3 (2024), p. 247. DOI: 10.1140/epjc/s10052-024-12533-y. arXiv: 2308.05743 [hep-ph].

[6] Michael L. Miller et al. "Glauber modeling in high energy nuclear collisions". In: *Ann. Rev. Nucl. Part. Sci.* 57 (2007), pp. 205–243. DOI: 10.1146/annurev.nucl.57.090506.123020. arXiv: nucl-ex/0701025.

[7] Xiaojian Du and Ralf Rapp. "Sequential Regeneration of Charmonia in Heavy-Ion Collisions". In: *Nucl. Phys. A* 943 (2015), pp. 147–158. DOI: 10.1016/j.nuclphysa.2015.09.006. arXiv: 1504.00670 [hep-ph].

[8] Anton Andronic et al. "Transverse momentum distributions of charmonium states with the statistical hadronization model". In: *Phys. Lett. B* 797 (2019), p. 134836. DOI: 10.1016/j.physletb.2019.134836. arXiv: 1901.09200 [nucl-th].

[9] Shreyasi Acharya et al. "Multiplicity dependence of π, K, and p production in pp collisions at $\sqrt{s} = 13$ TeV". In: *Eur. Phys. J. C* 80.8 (2020), p. 693. DOI: 10.1140/epjc/s10052-020-8125-1. arXiv: 2003.02394 [nucl-ex].

[10] Sandra S. Padula. "Flow and correlation phenomena measurements in pp, pPb and PbPb collisions at CMS". In: *EPJ Web Conf.* 172 (2018). Ed. by A. Ayala Mercado and E. Cuautle Flores, p. 05005. DOI: 10.1051/epjconf/201817205005.

[11] Vardan Khachatryan et al. "Measurement of long-range near-side two-particle angular correlations in pp collisions at $\sqrt{s} =$13 TeV". In: *Phys. Rev. Lett.* 116.17 (2016), p. 172302. DOI: 10.1103/PhysRevLett.116.172302. arXiv: 1510.03068 [nucl-ex].

[12] J. M. Campbell et al. "Event generators for high-energy physics experiments". In: *SciPost Phys.* 16.5 (2024), p. 130. DOI: 10.21468/SciPostPhys.16.5.130. arXiv: 2203.11110 [hep-ph].

[13] Torbjörn Sjostrand, Stephen Mrenna, and Peter Z. Skands. "PYTHIA 6.4 Physics and Manual". In: *JHEP* 05 (2006), p. 026. DOI: `10.1088/1126-6708/2006/05/026`. arXiv: `hep-ph/0603175`.

[14] Torbjörn Sjostrand, Stephen Mrenna, and Peter Z. Skands. "A Brief Introduction to PYTHIA 8.1". In: *Comput. Phys. Commun.* 178 (2008), pp. 852–867. DOI: `10.1016/j.cpc.2008.01.036`. arXiv: `0710.3820 [hep-ph]`.

[15] Torbjörn Sjöstrand et al. "An introduction to PYTHIA 8.2". In: *Comput. Phys. Commun.* 191 (2015), pp. 159–177. DOI: `10.1016/j.cpc.2015.01.024`. arXiv: `1410.3012 [hep-ph]`.

[16] Christian Bierlich et al. "A comprehensive guide to the physics and usage of PYTHIA 8.3". In: *SciPost Phys. Codeb.* 2022 (2022), p. 8. DOI: `10.21468/SciPostPhysCodeb.8`. arXiv: `2203.11601 [hep-ph]`.

[17] S. Porteboeuf, T. Pierog, and K. Werner. "Producing Hard Processes Regarding the Complete Event: The EPOS Event Generator". In: *45th Rencontres de Moriond on QCD and High Energy Interactions.* Gioi Publishers, 2010, pp. 135–140. arXiv: `1006.2967 [hep-ph]`.

[18] T. Pierog et al. "EPOS LHC: Test of collective hadronization with data measured at the CERN Large Hadron Collider". In: *Phys. Rev. C* 92 (3 Sept. 2015), p. 034906. DOI: `10.1103/PhysRevC.92.034906`. URL: `https://link.aps.org/doi/10.1103/PhysRevC.92.034906`.

[19] Tanguy Pierog and Klaus Werner. "EPOS LHC-R : up-to-date hadronic model for EAS simulations". In: *PoS* ICRC2023 (2023), p. 230. DOI: `10.22323/1.444.0230`.

[20] A. V. Efremov et al. "Production of cumulative particles and quark - gluon strings model". In: *Phys. Atom. Nucl.* 57 (1994), pp. 874–880.

[21] A. Capella et al. "Dual parton model". In: *Physics Reports* 236.4 (1994), pp. 225–329. ISSN: 0370-1573. DOI: `https://doi.org/10.1016/0370-1573(94)90064-7`. URL: `https://www.sciencedirect.com/science/article/pii/0370157394900647`.

[22] P. D. B. Collins. In: Cambridge Monographs on Mathematical Physics (2023).

[23] Jaroslav Adam et al. "Charged-particle multiplicities in proton–proton collisions at $\sqrt{s} = 0.9$ to 8 TeV". In: *Eur. Phys. J. C* 77.1 (2017), p. 33. DOI: `10.1140/epjc/s10052-016-4571-1`. arXiv: `1509.07541 [nucl-ex]`.

[24] Shreyasi Acharya et al. "Multiplicity dependence of charged-particle production in pp, p-Pb, Xe-Xe and Pb-Pb collisions at the LHC". In: *Phys. Lett. B* 845 (2023), p. 138110. DOI: `10.1016/j.physletb.2023.138110`. arXiv: `2211.15326 [nucl-ex]`.

[25] Peter Skands, Stefano Carrazza, and Juan Rojo. "Tuning PYTHIA 8.1: the Monash 2013 Tune". In: *Eur. Phys. J. C* 74.8 (2014), p. 3024. DOI: `10.1140/epjc/s10052-014-3024-y`. arXiv: `1404.5630 [hep-ph]`.

[26] Jaroslav Adam et al. "Pseudorapidity and transverse-momentum distributions of charged particles in proton–proton collisions at $\sqrt{s} = 13$ TeV". In: *Phys. Lett. B* 753 (2016), pp. 319–329. DOI: `10.1016/j.physletb.2015.12.030`. arXiv: `1509.08734 [nucl-ex]`.

[27] Richard P. Feynman. "Very high-energy collisions of hadrons". In: *Phys. Rev. Lett.* 23 (1969). Ed. by L. M. Brown, pp. 1415–1417. DOI: `10.1103/PhysRevLett.23.1415`.

[28] Eric Braaten, Sean Fleming, and Tzu Chiang Yuan. "Production of heavy quarkonium in high-energy colliders". In: *Ann. Rev. Nucl. Part. Sci.* 46 (1996), pp. 197–235. DOI: 10.1146/annurev.nucl.46.1.197. arXiv: hep-ph/9602374.

[29] Eric Braaten. "Color and spin in quarkonium production". In: *Nucl. Phys. B Proc. Suppl.* 71 (1999). Ed. by X. N. Wang and B. Jacak, pp. 441–450. DOI: 10.1016/S0920-5632(98)00376-4. arXiv: hep-ph/9810390.

[30] Geoffrey T. Bodwin, Eric Braaten, and Jungil Lee. "Comparison of the color-evaporation model and the NRQCD factorization approach in charmonium production". In: *Phys. Rev. D* 72 (2005), p. 014004. DOI: 10.1103/PhysRevD.72.014004. arXiv: hep-ph/0504014.

[31] Jean-Philippe Lansberg. "New Observables in Inclusive Production of Quarkonia". In: *Phys. Rept.* 889 (2020), pp. 1–106. DOI: 10.1016/j.physrep.2020.08.007. arXiv: 1903.09185 [hep-ph].

[32] R. Vogt. "Quarkonium Production and Polarization in an Improved Color Evaporation Model". In: *Nucl. Phys. A* 982 (2019). Ed. by Federico Antinori et al., pp. 751–754. DOI: 10.1016/j.nuclphysa.2018.08.003.

[33] Yan-Qing Ma and Ramona Vogt. "Quarkonium Production in an Improved Color Evaporation Model". In: *Phys. Rev. D* 94.11 (2016), p. 114029. DOI: 10.1103/PhysRevD.94.114029. arXiv: 1609.06042 [hep-ph].

[34] Edmond Iancu and Raju Venugopalan. "The Color glass condensate and high-energy scattering in QCD". In: *Quark-gluon plasma 4*. Ed. by Rudolph C. Hwa and Xin-Nian Wang. Mar. 2003, pp. 249–3363. DOI: 10.1142/9789812795533_0005. arXiv: hep-ph/0303204.

[35] Jamal Jalilian-Marian et al. "The Wilson renormalization group for low x physics: Towards the high density regime". In: *Phys. Rev. D* 59 (1998), p. 014014. DOI: 10.1103/PhysRevD.59.014014. arXiv: hep-ph/9706377.

[36] L. V. Gribov, E. M. Levin, and M. G. Ryskin. "Semihard Processes in QCD". In: *Phys. Rept.* 100 (1983), pp. 1–150. DOI: 10.1016/0370-1573(83)90022-4.

[37] Jean Paul Blaizot, Francois Gelis, and Raju Venugopalan. "High-energy pA collisions in the color glass condensate approach. 2. Quark production". In: *Nucl. Phys. A* 743 (2004), pp. 57–91. DOI: 10.1016/j.nuclphysa.2004.07.006. arXiv: hep-ph/0402257.

[38] Hirotsugu Fujii and Kazuhiro Watanabe. "Heavy quark pair production in high energy pA collisions: Quarkonium". In: *Nucl. Phys. A* 915 (2013), pp. 1–23. DOI: 10.1016/j.nuclphysa.2013.06.011. arXiv: 1304.2221 [hep-ph].

[39] Zhong-Bo Kang, Yan-Qing Ma, and Raju Venugopalan. "Quarkonium production in high energy proton-nucleus collisions: CGC meets NRQCD". In: *JHEP* 01 (2014), p. 056. DOI: 10.1007/JHEP01(2014)056. arXiv: 1309.7337 [hep-ph].

[40] Shreyasi Acharya et al. "Inclusive J/ψ production at midrapidity in pp collisions at $\sqrt{s} =$ 13 TeV". In: *Eur. Phys. J. C* 81.12 (2021), p. 1121. DOI: 10.1140/epjc/s10052-021-09873-4. arXiv: 2108.01906 [nucl-ex].

[41] Shreyasi Acharya et al. "Energy dependence of forward-rapidity J/ψ and ψ(2S) production in pp collisions at the LHC". In: *Eur. Phys. J. C* 77.6 (2017), p. 392. DOI: 10.1140/epjc/s10052-017-4940-4. arXiv: 1702.00557 [hep-ex].

[42] Biswarup Paul. "Recent ALICE results on quarkonium production in nuclear collisions". In: *J. Phys. Conf. Ser.* 2586.1 (2023), p. 012007. DOI: 10.1088/1742-6596/2586/1/012007. arXiv: 2210.04356 [nucl-ex].

[43] S. Porteboeuf and R. Granier de Cassagnac. "J/Ψ yield vs. multiplicity in proton-proton collisions at the LHC". In: *Nucl. Phys. B Proc. Suppl.* 214 (2011). Ed. by Zaida Conesa del Valle et al., pp. 181–184. DOI: 10.1016/j.nuclphysbps.2011.03.082. arXiv: 1012.0719 [hep-ex].

[44] Serguei Chatrchyan et al. "Event Activity Dependence of Y(nS) Production in $\sqrt{s_{NN}}$=5.02 TeV pPb and $\sqrt{s}$=2.76 TeV pp Collisions". In: *JHEP* 04 (2014), p. 103. DOI: 10.1007/JHEP04(2014)103. arXiv: 1312.6300 [nucl-ex].

[45] Vardan Khachatryan et al. "Υ(nS) polarizations versus particle multiplicity in pp collisions at $\sqrt{s} = 7$ TeV". In: *Phys. Lett. B* 761 (2016), pp. 31–52. DOI: 10.1016/j.physletb.2016.07.065. arXiv: 1603.02913 [hep-ex].

[46] Jaroslav Adam et al. "J/ψ production cross section and its dependence on charged-particle multiplicity in $p+p$ collisions at $\sqrt{s} = 200$ GeV". In: *Phys. Lett. B* 786 (2018), pp. 87–93. DOI: 10.1016/j.physletb.2018.09.029. arXiv: 1805.03745 [hep-ex].

[47] B. Abelev et al. "J/ψ Production as a Function of Charged Particle Multiplicity in *pp* Collisions at $\sqrt{s} = 7$ TeV". In: *Phys. Lett. B* 712 (2012), pp. 165–175. DOI: 10.1016/j.physletb.2012.04.052. arXiv: 1202.2816 [hep-ex].

[48] Shreyasi Acharya et al. "Multiplicity dependence of J/ψ production at midrapidity in pp collisions at $\sqrt{s} = 13$ TeV". In: *Phys. Lett. B* 810 (2020), p. 135758. DOI: 10.1016/j.physletb.2020.135758. arXiv: 2005.11123 [nucl-ex].

[49] Shreyasi Acharya et al. "Forward rapidity J/ψ production as a function of charged-particle multiplicity in pp collisions at $\sqrt{s} = 5.02$ and 13 TeV". In: *JHEP* 06 (2022), p. 015. DOI: 10.1007/JHEP06(2022)015. arXiv: 2112.09433 [nucl-ex].

[50] K. Werner et al. "Analysing radial flow features in p-Pb and p-p collisions at several TeV by studying identified particle production in EPOS3". In: *Phys. Rev. C* 89.6 (2014), p. 064903. DOI: 10.1103/PhysRevC.89.064903. arXiv: 1312.1233 [nucl-th].

[51] E. G. Ferreiro and C. Pajares. "High multiplicity *pp* events and J/ψ production at LHC". In: *Phys. Rev. C* 86 (2012), p. 034903. DOI: 10.1103/PhysRevC.86.034903. arXiv: 1203.5936 [hep-ph].

[52] Eugene Levin, Iván Schmidt, and Marat Siddikov. "Multiplicity dependence of quarkonia production in the CGC approach". In: *Eur. Phys. J. C* 80.6 (2020), p. 560. DOI: 10.1140/epjc/s10052-020-8086-4. arXiv: 1910.13579 [hep-ph].

[53] Yan-Qing Ma et al. "Event engineering studies for heavy flavor production and hadronization in high multiplicity hadron-hadron and hadron-nucleus collisions". In: *Phys. Rev. D* 98.7 (2018), p. 074025. DOI: 10.1103/PhysRevD.98.074025. arXiv: 1803.11093 [hep-ph].

[54] B. Z. Kopeliovich et al. "Heavy quarkonium in the saturated environment of high-multiplicity *pp* collisions". In: *Phys. Rev. D* 101.5 (2020), p. 054023. DOI: 10.1103/PhysRevD.101.054023. arXiv: 1910.09682 [hep-ph].

[55] Shreyasi Acharya et al. "Measurement of ψ(2S) production as a function of charged-particle pseudorapidity density in pp collisions at $\sqrt{s} = 13$ TeV and p-Pb collisions at $\sqrt{s_{NN}} = 8.16$

TeV with ALICE at the LHC". In: *JHEP* 06 (2023), p. 147. DOI: 10.1007/JHEP06(2023)147. arXiv: 2204.10253 [nucl-ex].

[56] Shreyasi Acharya et al. "Multiplicity dependence of Υ production at forward rapidity in pp collisions at s=13 TeV". In: *Nucl. Phys. B* 1011 (2025), p. 116786. DOI: 10.1016/j.nuclphysb.2024.116786. arXiv: 2209.04241 [nucl-ex].

[57] E. G. Ferreiro. "Excited charmonium suppression in proton–nucleus collisions as a consequence of comovers". In: *Phys. Lett. B* 749 (2015), pp. 98–103. DOI: 10.1016/j.physletb.2015.07.066. arXiv: 1411.0549 [hep-ph].

[58] Angelo Esposito et al. "The nature of X(3872) from high-multiplicity pp collisions". In: *Eur. Phys. J. C* 81.7 (2021), p. 669. DOI: 10.1140/epjc/s10052-021-09425-w. arXiv: 2006.15044 [hep-ph].

[59] Shreyasi Acharya et al. "Inclusive and multiplicity dependent production of electrons from heavy-flavour hadron decays in pp and p-Pb collisions". In: *JHEP* 08 (2023), p. 006. DOI: 10.1007/JHEP08(2023)006. arXiv: 2303.13349 [nucl-ex].

[60] Albert M Sirunyan et al. "Investigation into the event-activity dependence of $\Upsilon(\text{nS})$ relative production in proton-proton collisions at $\sqrt{s} = 7$ TeV". In: *JHEP* 11 (2020), p. 001. DOI: 10.1007/JHEP11(2020)001. arXiv: 2007.04277 [hep-ex].

[61] The ATLAS Collaboration et al. "The ATLAS Experiment at the CERN LHC". In: *Journal of Instrumentation* 3:S08003 (2008). DOI: 10.1088/1748-0221/3/08/S08003.

[62] The CMS Collaboration et al. "The CMS Experiment at the CERN LHC". In: *Journal of Instrumentation* 3:S08003 (2008). DOI: 10.1088/1748-0221/3/08/S08004.

[63] The LHCb Collaboration. "The LHCb Detector at the LHC". In: *Journal of Instrumentation* 3:S08003 (2008). DOI: 10.1088/1748-0221/3/08/S08005.

[64] CERN Communication Group. "CERN LHC: the guide, frequently asked questions". In: *Nuclear Instruments and Methods in Physics Research* (2006). URL: http://cds.cern.ch/record/999421.

[65] F. Carminati et al. "ALICE: Physics Performance Report, Volume I". In: *Journal of Physics G: Nuclear and Particle Physics* 30 1517 (2004). DOI: 10.1088/0954-3899/30/11/001.

[66] The ALICE Collaboration et al. "The ALICE experiment at the CERN LHC". In: *Journal of Instrumentation* 3:S08003 (2008). DOI: 10.1088/1748-0221/3/08/S08002.

[67] P Cortese et al. "ALICE technical design report on forward detectors: FMD, T0 and V0". In: (2004).

[68] A. Gheata. "ALICE analysis framework". In: *PoS* ACAT08 (2008). Ed. by Thomas Speer, Federico Carminati, and Monique Werlen, p. 028. DOI: 10.22323/1.070.0028.

[69] M. Zimmermann. "The ALICE analysis train system". In: *Journal of Physics: Conference Series 16th International workshop on Advanced Computing and Analysis Techniques in physics research (ACAT2014) 1–5 September 2014, Prague, Czech Republic* 608 012019 (2015). DOI: 10.1088/1742-6596/608/1/012019.

[70] I. Legrand et al. "MonALISA: An agent based, dynamic service system to monitor, control and optimize distributed systems". In: *Computer Physics Communications* 180.12 (2009), pp. 2472–2498. ISSN: 0010-4655. DOI: https://doi.org/10.1016/j.cpc.2009.08.003. URL: https://www.sciencedirect.com/science/article/pii/S0010465509002410.

[71] V. Altini et al. "Commissioning and initial experience with the ALICE on-line". In: *Journal of Physics: Conference Series* Volume 219, Online Computing (2010). DOI: 10.1088/1742-6596/219/2/022022.

[72] Xin-Nian Wang and Miklos Gyulassy. "HIJING: A Monte Carlo model for multiple jet production in p p, p A and A A collisions". In: *Phys. Rev. D* 44 (1991), pp. 3501–3516. DOI: 10.1103/PhysRevD.44.3501.

[73] Stefan Roesler, Ralph Engel, and Johannes Ranft. "The Monte Carlo event generator DPMJET-III". In: *International Conference on Advanced Monte Carlo for Radiation Physics, Particle Transport Simulation and Applications (MC 2000)*. Dec. 2000, pp. 1033–1038. DOI: 10.1007/978-3-642-18211-2_166. arXiv: hep-ph/0012252.

[74] R. et al Brun. "GEANT3". In: (Sept. 1987).

[75] S. Agostinelli et al. "Geant4: A simulation toolkit". In: *Nuclear Instruments and Methods in Physics Research Section A: Accelerators, Spectrometers, Detectors and Associated Equipment* 506.3 (2003), pp. 250–303. ISSN: 0168-9002. DOI: https://doi.org/10.1016/S0168-9002(03)01368-8. URL: https://www.sciencedirect.com/science/article/pii/S0168900203013688.

[76] Alfredo Ferrari et al. "FLUKA: A multi-particle transport code (Program version 2005)". In: (Oct. 2005). DOI: 10.2172/877507.

[77] E Bruna et al. *Vertex reconstruction for proton-proton collisions in ALICE*. Tech. rep. 2009.

[78] P. Billoir. "Track fitting with multiple scattering: a new method". In: *Nuclear Instruments and Methods in Physics Research* 225 (1984), pp. 352–366. DOI: https://doi.org/10.1016/0167-5087(84)90274-6.

[79] Betty Bezverkhny Abelev et al. "Performance of the ALICE Experiment at the CERN LHC". In: *Int. J. Mod. Phys. A* 29 (2014), p. 1430044. DOI: 10.1142/S0217751X14300440. arXiv: 1402.4476 [nucl-ex].

[80] ALICE Collaboration et al. "The ALICE experiment at the CERN LHC". In: *Journal of Instrumentation 1430044* 3 (2008). DOI: 10.1088/1748-0221/3/08/S08002.

[81] Alexander Kalweit. "Production of light flavor hadrons and anti-nuclei at the LHC". Darmstadt, Tech. U., 2012. URL: https://cds.cern.ch/record/2119440.

[82] Walter Blum, Luigi Rolandi, and Werner Riegler. *Particle detection with drift chambers*. Particle Acceleration and Detection. 2008. ISBN: 978-3-540-76683-4, 978-3-540-76684-1. DOI: 10.1007/978-3-540-76684-1.

[83] Mesut Arslandok. "Event-by-Event Identified Particle Ratio Fluctuations in Pb–Pb Collisions with ALICE". Presented 04 Dec 2017. Frankfurt U., 2017. URL: https://cds.cern.ch/record/2308311.

[84] ALICE Collaboration. "The ALICE definition of primary particles". In: *ALICE-PUBLIC-2017-005* (2017). URL: https://cds.cern.ch/record/2270008.

[85] ALICE Collaboration. "Transverse momentum spectra and nuclear modification factors of charged particles in pp, p-Pb and Pb-Pb collisions at the LHC". In: *J. High Energ. Phys.013* (2018). URL: https://doi.org/10.1007/JHEP11(2018)013.

[86] Javier Martin Blanco. "Study of J/ψ production dependence with the charged particle multiplicity in p-Pb collisions at $\sqrt{s_{\mathrm{NN}}} = 5.02$ TeV and pp collisions at $\sqrt{s} = 8$ TeV with the ALICE experiment at the LHC". PhD thesis. Nantes U., Jan. 2016.

[87] G. D'Agostini. "A Multidimensional unfolding method based on Bayes' theorem". In: *Nucl. Instrum. Meth. A* 362 (1995), pp. 487–498. DOI: 10.1016/0168-9002(95)00274-X.

[88] Shreyasi Acharya et al. "Dielectron and heavy-quark production in inelastic and high-multiplicity proton-proton collisions at $\sqrt{s} = 13$ TeV". In: *Phys. Lett. B* 788 (2019). 23 pages, 5 captioned figures, 3 tables, authors from page 18, published version, figures at http://aliceinfo.cern.ch/ArtSubmission/node/4291, pp. 505–518. DOI: 10.1016/j.physletb.2018.11.009. arXiv: 1805.04407. URL: https://cds.cern.ch/record/2316934.

[89] Roger Barlow. "Systematic errors: Facts and fictions". In: *Conference on Advanced Statistical Techniques in Particle Physics*. July 2002, pp. 134–144. arXiv: hep-ex/0207026.

Lebenslauf / Curriculum Vitae

Persönliche Daten / Personal Data

Name:	Ailec de la Caridad Bell Hechavarria
Geburtsdatum:	21.03.1992
Geburtsort:	Havanna, Kuba
Staatsangehörigkeit:	Kubanisch

Schulausbildung / Education

2007–2010   **Gymnasium**, *Vladimir I. Lenin*, Arroyo Naranjo, Havanna.
Notendurchschnitt: 98,60 von 100

Studium /Higher Education

2010–2015   **Bachelorstudium in Kernphysik**, *Instituto Superior de Ciencias y Tecnologías Aplicadas (InSTEC)*, Havanna, Kuba.
Titel der Bachelorarbeit: *"Calibración de la Actividad de ^{18}F por Espectrometría Gamma"*
Note: 4,44 auf einer Skala von 5,0

2015-2018   **M.Sc. in Kernphysik**, *Instituto Superior de Ciencias y Tecnologías Aplicadas (InSTEC), Universidad de La Habana*, Havanna, Kuba.
Titel der Masterarbeit: *"Modelo de Coalescencia Superficial en Colisión Nucleón-Núcleo"*
Note: 5,0 auf einer Skala von 5,0

Promotionsstudium / Ph. D. Studies

11/2018   **Beginn der Dissertation am**, *Institut für Kernphysik, Universität Münster (bis Oktober 2023: Westfälische Wilhelms-Universität Münster)*, Münster, Deutschland.
Unter der Betreuung von: Prof. Dr. Anton Andronic

Forschungserfahrung / Research Experience

Sommer 2018   **Praktikum**, *LHCb-Gruppe, Centre de Physique des Particules de Marseille (CPPM).*, Marseille, Frankreich.

2015–2017   **Wissenschaftliche Mitarbeiterin**, *Abteilung für Radionuklidmetrologie, Centro de Isótopos (CENTIS).*, Havanna, Kuba.

2013–2015   **Praktikum**, *Abteilung für Radionuklidmetrologie, Centro de Isótopos (CENTIS).*, Havanna, Kuba.

2012–2013   **Praktikum**, *Abteilung für Nuklearmedizin, Krankenhaus "Hermanos Ameijeiras".*, Havanna, Kuba.